

Statistical Mechanics
of
Supramolecular Self Assembly
in
Soft Matter Systems

William Stuart Fall

The University of Sheffield
Faculty of Science
Department of Physics & Astronomy

A thesis submitted in partial fulfilment of the
requirements for the degree of Doctor of Philosophy



The
University
Of
Sheffield.

September 7, 2020

Declaration

I declare that this thesis was composed by myself and that the work contained herein is my own, except where explicitly stated otherwise in the text.

To my parents Susan & Stuart Fall

and

In memory of Audrey J. O'Nions my beloved

grandmother 30.08.1931 - 04.09.2020.

Abstract

In this thesis, unusual phase transitions in liquid crystals formed from compounds with novel shapes and polymers are investigated using different techniques including, statistical modelling, Monte Carlo and molecular dynamics simulation.

An unusual phase transition, between two columnar phases of the same hexagonal symmetry, has been discovered in a liquid crystal formed from taper-shaped Minidendrons. This unique transition requires a quantised drop in the number of molecules in the columnar cross-section on heating. A mean field theory is developed which models a single self-assembled column as a one-dimensional Ising spin chain. Dominant energetic terms are calculated and fed into the theory, accompanied by small mean field terms. Close quantitative agreement is found between theory and experiment, providing an elegant description of the first-order nature of the transition.

Next, a nanometre-scale square tiling in X-shaped liquid crystal compounds has been achieved with zero in-plane expansion. A previously unseen order-disorder transition, between a two-colour segregated chessboard phase and a single-colour mixed phase, has been observed on heating. The transition is a close real-life example of the 3d Ising model. Monte Carlo simulation is performed, considering important interactions inside the nano-compartments. The results for different lattice sizes in simulation, when compared to experimental data, show how kinematic effects dominate within the liquid crystal.

Then the newly observed crystallisation behaviour of isotactic polypropylene, at large undercoolings, has indicated an additional mesophase appears which overtakes the ordered-phase growth. Their competition results in a kinetic barrier, similar to that observed in folded n-alkanes, whereby the extended form is blocked by the attachment of folded chains. This process is called self-poisoning. Using a 1d solid-on-solid model the two-step process of mesophase attachment and subsequent meso-order conversion required to grow the ordered form is studied. Monte Carlo simulation is used to study the importance of neighbouring interactions and better fit the experimental data.

Finally, it is well known that a two-dimensional crystal melts before a three-dimensional one. Adsorbed model polyethylene monolayers however are exceptional and are found recently to melt up to 80K above the bulk melting temperature. Atomic force microscopy studies have shown unusual pre-melting behaviour in graphite adsorbed ultra-long n-alkanes. The monolayers resist melting by gradually disordering from their ends inwards, to over half their extended length, before finally melting. Molecular dynamics simulations are performed, at different temperatures, by leveraging a new coarse-grained model of bulk polyethylene. The results show remarkable agreement with AFM images, providing new insights into polymer melting.

Publications

- [1] William S Fall, Constance Nürnberger, Xiangbing Zeng, Feng Liu, Stephen J Kearney, Gillian A Gehring, Carsten Tschierske, and Goran Ungar. An ising transition of chessboard tilings in a honeycomb liquid crystal. *Molecular Systems Design & Engineering*, 4(2):396–406, 2019.
- [2] William S Fall, Ming-Huei Yen, Xiangbing Zeng, Liliana Cseh, Yongsong Liu, Gillian A Gehring, and Goran Ungar. Molecular ejection transition in liquid crystal columns self-assembled from wedge-shaped minidendrons. *Soft Matter*, 15(1):22–29, 2019.
- [3] Ruibin Zhang, William S Fall, Kyle Wm Hall, Gillian A Gehring, Xiangbing Zeng, and Goran Ungar. Reinterpreting bulk polymer melting: Insights from quasi-continuous melting in model polymer monolayers. *Phys. Rev. Lett. (Submitted)*, 2020.
- [4] Ruibin Zhang, William S Fall, Kyle Wm Hall, Gillian A Gehring, Xiangbing Zeng, and Goran Ungar. Quasi-continuous melting and a roughening transition in monolayers of ultra-long alkanes: new insights into polymer melting. *Phys. Rev. B. (Submitted)*, 2020.

Collaborating Author

Declarations

This alternative format thesis contains both published and recently submitted articles as well as work written in a format suitable for publication. Each chapter therefore comprises of a single piece of published/publishable work, for which my contribution is significant. All co-authors have read and agreed the following and their agreement can be provided upon request.

I, a collaborating author on publication(s) used in this thesis, agree that the theoretical/numerical work and/or the analysis and interpretation of work and/or the text within these publication(s) is primarily completed by William Stuart Fall and suitable for use in his thesis.

Dr Ming-Huei Yen

Prof Goran Ungar

Dr Xiangbing Zeng

Prof Feng Liu

Dr Liliana Cseh

Mr Stephen J. Kearney

Dr Yongsong Liu

Prof Carsten Tschierske

Dr Constance Nürnberger

Dr Ruibin Zhang

Prof Gillian A. Gehring

Dr Kyle Wm. Hall

Mr Thomas H. Sexton

Conference Presentations

Talks

Invited Speaker: William S. Fall, Constance Nürnberger, Xiangbing Zeng, Feng Liu, Stephen J. Kearney, Gillian A. Gehring, Carsten Tschierske and Goran Ungar, *An ising transition of chessboard tilings in a honeycomb liquid crystal*, US Army Research Lab: Strategic Materials Meeting, Temple University, Philadelphia, USA, August 20-21, 2019.

William S. Fall, Ming-Huei Yen, Xiangbing Zeng, Liliana Cseh, Yongsong Liu, Gillian A. Gehring and Goran Ungar, The Col_h - Col_h transition in LC columns self-assembled from wedge-shaped minidendrons, Departmental Research Day, The University of Sheffield, UK, April 25, 2019.

William S. Fall, Ming-Huei Yen, Xiangbing Zeng, Liliana Cseh, Yongsong Liu, Gillian A. Gehring and Goran Ungar, The Col_h - Col_h transition in LC columns self-assembled from wedge-shaped minidendrons; insights from theory and simulation. British Liquid Crystal Society: Annual General Meeting, University of Leeds, UK, April 15-17, 2019.

Posters

William S. Fall, Constance Nürnberger, Xiangbing Zeng, Feng Liu, Stephen J. Kearney, Gillian A. Gehring, Carsten Tschierske and Goran Ungar, *An ising transition of chessboard tilings in a honeycomb liquid crystal*, Milestones in Molecular Simulation, Imperial College London, London, UK, June 21, 2019.

William S. Fall, Constance Nürnberger, Xiangbing Zeng, Feng Liu, Stephen J. Kearney, Gillian A. Gehring, Carsten Tschierske and Goran Ungar, *An ising transition of chessboard tilings in a honeycomb liquid crystal*, Institute of Physics: Theory of Condensed Matter, Warwick University, Warwick, UK, June 13, 2019.

William S. Fall, Ming-Huei Yen, Xiangbing Zeng, Liliana Cseh, Yongsong Liu, Gillian A. Gehring and Goran Ungar, *The $Col_h - Col_h$ transition in LC columns self-assembled from wedge-shaped minidendrons*, LAMMPS Workshop and Symposium: Modelling Supramolecular Structures Using LAMMPS, Temple University, Philadelphia, USA, July 9-13, 2018.

William S. Fall, Ming-Huei Yen, Xiangbing Zeng, Liliana Cseh, Yongsong Liu, Gillian A. Gehring and Goran Ungar, *Quantised molecular ejection transition in liquid crystal columns self-assembled from wedge-shaped minidendrons*, Graduate School Showcase, The University of Sheffield, April 17, 2018.

William S. Fall, Ming-Huei Yen, Xiangbing Zeng, Liliana Cseh, Yongsong Liu, Gillian A. Gehring and Goran Ungar, *Quantised molecular ejection transition in liquid crystal columns self-assembled from wedge-shaped minidendrons*, Institute of Physics: Soft Matter School - 'Solutions in the Spring', Durham University, Durham, April 9-12, 2017.

Acknowledgements

I would like to thank my primary research supervisor Prof Gillian A. Gehring, in the Dept of Physics and Astronomy at the University of Sheffield for her continual support and guidance throughout my PhD.

I also wish to thank Prof Goran Ungar and Dr Xiangbing Zeng, in the Dept of Materials Science at the University of Sheffield, for sharing many fascinating experiments with us and Prof Goran Ungar for his enduring financial support. Thanks to Dr Kyle Hall at Temple University for many useful discussions across timezones.

Thanks to my best friend Dr Ahmad Saeedi for showing me there is more to life than Physics, this includes many adventures, office lunches and coffee trips. I am still trying to find the right work-life balance.

Finally thanks to my financial sponsors, EPSRC, ZSTU, XJTU and Prof Goran Ungar for providing financial support. Thanks to the Dept of Physics and Astronomy and Dept of Materials Science at the University of Sheffield for providing additional funding for publication costs. Thank you to the much undervalued Learned Societies Fund and also to Prof Gillian Gehring for donating me her non-staff-budget to cover the cost of more than one conference visit.

List of Figures

1.1	Professor Pierre-Gilles de Gennes.	2
1.2	Number of molecules vs temperature and experiment vs theory fitting . .	7
1.3	Sample configurations of the ordered segregated chessboard tiling at low temperature vs the more disordered mixed tiling at high temperature reproduced from MC simulation.	8
1.4	Progressive snapshots of the growth front for a series of interacting 1d growth stems from MC simulation.	10
1.5	Binned maps of average squared displacement for all temperatures simulated below the melt calculated from MD simulation.	11
2.1	Oriental snapshots of molecules in two different type of smectic phases. Director is perpendicular to the layers in Smectic A and at an angle other than 90 degrees in Smectic C, in this case 45 degrees.	19
2.2	Example mesogens: rod-shaped, taper-shaped, disc-shaped, cross-shaped and chevron-shaped.	22
2.3	Paul Stern (Left) and Nick Metropolis (Right) playing chess with MANIAC.	31
2.4	Boundary conditions for $d = 2$ Ising Model on a square lattice, arrows indicate periodic interactions across the boundary.	37

2.5	Coarse-grained schematic of a single Alkane chain ($C_{12}H_{26}$), blue beads represent terminal groups (CT) and blue central groups (CM).	37
2.6	Lennard-Jones potential functions for the interactions between all possible bead types.	39
2.7	Assigning the local crystallinity, P_2 order parameter, of a single coarse-grained bead.	40
2.8	Example order parameter (left) and associated scaling plot for a 3d Ising like liquid crystal model system reproduced from [7].	42
2.9	Torsional potential energy of C-C bond in n-Alkane chain, Newman projections and schematic configurations.	43
2.10	Polarising optical microscopy setup and experimental textures.	45
2.11	X-ray Scattering schematic from parallel planes and Xenocs Genix 3d instrument at ZSTU.	47
2.12	Basic AFM operation and AFM instrumentation.	49
2.13	Appropriate techniques across different length and timescales.	51
3.1	Unprocessed synchrotron XRD data for compounds 12Na, 14Na and 12K.	79
3.2	All possible modes for 12Na, other cations are not shown.	81
3.3	Model predictions with and without vibrations included.	84
4.1	Example tilings found in X-shaped compounds.	88
5.1	Optical micrograph showing spherulites and schematic model of a spherulite.	94
5.2	Phases of i-PP: α, β and γ	95
5.3	Inverse time-to-peak as a function of temperature for i-PP, lines are drawn for clarity, reproduced with permission from [7].	96
5.4	Allowed processes in the self-poisoning model for i-PP.	98
5.5	The growth rate, in arbitrary units for the 1d model using the estimated parameters for i-PP.	103

5.6	Illustration of the allowed processes in the 2d self-poisoning model for i-PP.	106
5.7	Growth rate as a function of temperature measured from 2d simulation and schematic of mesophase adsorption.	108
5.8	AFM image of i-PP at 60°C reproduced with permission from [7].	110
7.1	Electron density map showing the suggested structure of the frustrated p4gm phase.	125
7.2	Growth rate of high molar mass polyethylenes with bromine atoms substituted on every 21st carbon.	126
7.3	AFM image taken at the tilt to perpendicular transition reproduced from [4], yellow/white areas indicate soft amorphous regions.	127

List of Tables

2.1	Properties of crystalline solid vs isotropic liquid, ordering of the constituent molecules and corresponding WAXS patterns.	17
2.2	Properties of nematic, smectic and columnar phases, ordering of the constituent molecules and corresponding WAXS patterns.	18
2.3	Critical exponent values for the 2d and 3d Ising Models on a square lattice. Exponents for the 2d model are exact, 3d calculated numerically from MC simulations [16].	27
3.1	Parameters as calculated for 12Na (green) and 12K (blue), mean field terms were not calculated. Fitted parameters with and without vibrations included for 12Na (fitted), 12K (estimated) and 14Na. Calculations were performed as described in Publication 3.2, see SI.	83
5.1	Parameters used in the 1d model for i-PP. Entropy is given per monomer, side and end surface energies are per end.	103

Contents

Declaration	ii
Abstract	v
Publications	vi
Collaborating Author Declarations	vii
Conference Presentations	ix
Acknowledgments	x
List of Figures	xiii
List of Tables	xiv
1 Introduction	1
1.0.1 Project Aims	2
1.0.2 Thesis Outline	5
2 General Considerations	16
2.1 What Are Liquid Crystals?	16
2.1.1 Mesogens	20

2.2	Statistical Physics	23
2.2.1	Principal Ensembles	23
2.2.2	The Canonical Partition Function \mathcal{Z}	24
2.2.3	Essential Thermodynamic Quantities	24
2.2.4	The Ising Model	25
2.2.5	Phase Transitions and Critical Phenomena	26
2.2.6	Fluctuations	28
2.3	Computer Simulations	30
2.3.1	Markov Chain Monte Carlo	31
2.3.2	Molecular Dynamics	34
2.3.3	Standard Computational Procedures	36
2.3.3.1	Periodic Boundary Conditions	36
2.3.3.2	Interaction Potentials	37
2.3.3.3	Local Order Parameter	40
2.3.3.4	Tensor Order Parameter	41
2.3.3.5	Finite Size Scaling	41
2.3.3.6	Rotational Isomeric State Model	42
2.4	Experimental Techniques	44
2.4.1	Polarising Optical Microscopy	44
2.4.2	X-ray Diffraction	45
2.4.3	Atomic Force Microscopy	47
2.5	Computer Simulations of Liquid Crystals and Polymers	50
2.5.1	Highly Complex Liquid Crystals	52
2.5.2	Polymers	56
3	Wedge-Shaped Minidendrons	74
3.1	Introduction	74

3.2	Published Article 1	77
3.3	Additional Experimental Work & Model Predictions	78
4	X-Shaped Bolapolyphiles	87
4.1	Introduction	87
4.2	Published Article 2	90
5	Self-Poisoning in Isotactic Polypropylene	92
5.1	Introduction	93
5.2	Theory and Model Description	97
5.3	Simulation	104
5.4	Results and Discussion	107
6	Ultralong n-Alkanes Adsorbed on Graphite	114
6.1	Introduction	114
6.2	Published Article 3	116
6.3	Published Article 4	117
7	Conclusions and Future Work	119
7.1	Conclusions	120
7.2	Future Work	123

Chapter 1

Introduction

Condensed matter physics and the study of many-body states of matter, has kept theorists busy for a very long time. In this broad area, the physical laws governing quantum mechanics, electromagnetism and statistical mechanics are all leveraged in order to understand the behaviour of condensed phases. Soft matter physics is a subfield and the materials falling under this description often have diverse properties and many important technological applications. Pierre-Gilles de Gennes was awarded the nobel prize in Physics in 1991 “for discovering that methods developed for studying order phenomena in simple systems can be generalised to more complex forms of matter, in particular to liquid crystals and polymers.” He demonstrated how order-disorder transitions in simple condensed matter systems can be used to understand complex ordering phenomena in softer, more flexible ones. Theory has long played an important part in contributing to the understanding and prediction of liquid crystal phase transitions. Computer simulations are now widely accepted as an intermediary step between experiment and theory. Simulations allow us to refine and numerically solve theoretical models, which are not analytically solvable and probe the important interactions responsible for the formulation of liquid crystals and the subsequent phase transitions in these systems. They may be used not only to understand experimental

results but also to predict the results of new experiments without the need for difficult synthesis, albeit on much shorter timescales. This thesis will follow much the same theme with the primary goal of furthering the understanding of phase transitions in these wonderfully rich materials.

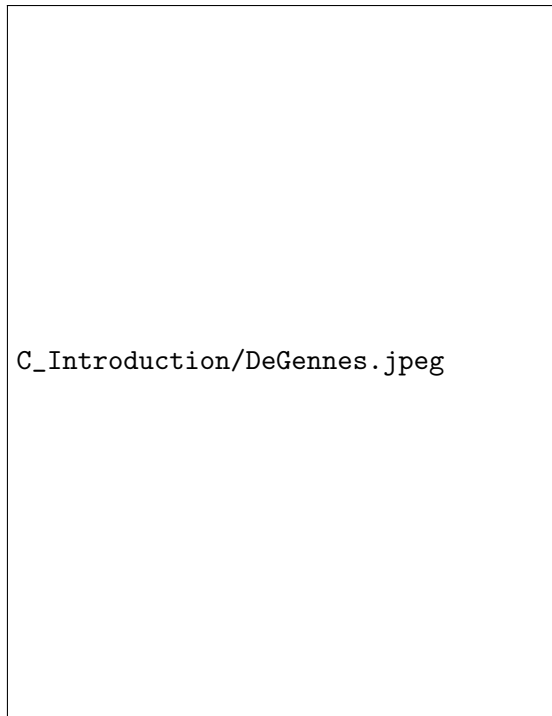


Figure 1.1: Professor Pierre-Gilles de Gennes.

1.0.1 Project Aims

This section is dedicated to setting out what the works presented in this thesis aim to achieve. The primary goal of each of the chapters presented in this thesis are to both complement and, in some cases, predict new experimental results in soft matter systems through a multi-scale modelling approach. The systems studied in this thesis have been cherry-picked from the rich and diverse experimental works performed by Ungar and Zengs groups in the Dept of Materials Science at the University of Sheffield. Prof Goran

Ungar and Dr Xiangbing Zeng co-supervise this project with Prof Gillian Gehring in the Physics Dept. Together myself and Prof Gehring form the theoretical arm of this unusual collaboration and the chapters in this work are representative of this. In Ungar and Zeng’s respective groups liquid crystalline systems and polymers, often synthesised for the first time are studied using popular techniques such as X-Ray Diffraction (XRD), Polarising Optical Microscopy (POM), Differential Scanning Calorimetry (DSC) and Atomic Force Microscopy (AFM). Using these methods, they have revealed the interesting properties of these compounds for the first time often discovering new liquid crystalline phases and transitions between them [1–7] and tackling important questions in model polymer systems [8–11]. Prof Gehring has been in an active collaboration with Prof Ungar and Dr Zeng since 2011 [12–15].

We find that collaboration between experimentalists on the one hand and the theory/simulation community on the other has been lacking in some areas of soft matter. E.g. while the nematic liquid crystal phase has been covered very extensively by physicists, the more complex LC phases, particularly those with 2D and 3D periodicity, i.e. columnar and cubic/pseudocubic phases, often referred to as supramolecular LCs, have been mostly left to be analysed by the chemists who synthesised the compounds. Thus many fascinating aspects of their phase behaviour have been either ignored or tackled somewhat superficially and in a speculative hand-waving way. A close collaboration such as between the above two groups is relatively rare, especially where fundamental physics is being pursued simultaneously with the experiments. Concomitance of this kind allows theory/simulation to influence and direct further experiments and chemical synthesis in a tight feedback loop. Being able to respond to experimental discoveries in a timely way can sometimes come at a price of not being able to follow a rigid, long-term path prescribed in detail in advance. A decision favouring the flexible approach has been made at the beginning of this project. Nevertheless,

the project still follows a general aim of understanding novel and unsolved phenomena in structure, thermodynamics and kinetics of soft matter by applying simulation and theories of condensed matter physics to “chemical” systems.

The aims of this thesis are as follows:

1. To take soft matter systems studied experimentally, understand those systems and identify areas in which theory and/or simulation can be used to further their understanding.
2. To develop theoretical models in close collaboration with experimental colleagues and refine those models through any means necessary into tractable problems.
3. To critically evaluate the model hypotheses or assumptions by solving these models analytically and/or numerically and comparing the results with experiment.
4. To design and carry out computer simulations by identifying the most appropriate computational techniques available and where none exists to develop those computational techniques.
5. To demonstrate an up-to-date awareness of pre-existing theoretical, computational and experimental studies on similar systems and utilise them.

“I have emphasised experiments more than theory. Of course, we need some theory when thinking of soft matter.”

Pierre Gilles de Gennes, Nobel Lecture, December 9 1991, College de France, Paris, France.

1.0.2 Thesis Outline

In Chapter 2 of this work a short overview of liquid crystals is given, and the compounds described in this thesis are presented for the first time. Then important aspects of statistical mechanics are outlined and the simulation techniques used throughout this thesis are discussed, such as Monte Carlo (MC) and molecular dynamics (MD) simulation, with reference to the previous section. A brief section outlining the common experimental techniques used to study liquid crystal systems such as X-ray diffraction (XRD), and atomic force microscopy (AFM) then follows. Throughout some discussion is given regarding how to interpret experimental results and important links with theory and simulations.

In Chapter 3 of this work the aim is to shed some light on the columnar phases in taper-shaped Minidendrons. Dendrimers and the liquid crystals that they form have been subject to declining interest, surprisingly not because they are well understood from a theoretical standpoint, quite the opposite in fact but because they are considered nothing new among materials scientists [16]. Minidendrons can be thought of as one branch of their much larger parent dendrimers and they are of significant interest because they show an impressive number of phases [1, 17], which are normally observed singularly in larger compounds in the same family [18]. The focus of Chapter 3 is to explain a puzzling phase transition between two columnar phases of the same hexagonal ($p6mm$) symmetry. In columnar phases an integer number of molecules, 3 or 4 in the cases studied here, self-assemble and form discs which then stack to form columns as shown in Figure 1.2. On heating the symmetry of the packing remains the same but the columnar shrinkage appears to be first-order in nature which suggests a sudden drop in the number of molecules comprising the many-molecule columns. This behaviour is explained through a simple self-consistent theory, drawing analogy with magnetic spin systems, inspired to some extent by the work of de Gennes, including only the

interactions thought to be most important such as the free energy of the terminal chains, Coulomb interactions both between and inside the core of cations and phonon vibrations inside the core. Numerical calculations of the component terms in the theory are performed and fed into the theory with small additional mean field terms required to tip the transition over into the first-order regime. It is demonstrated that the driving force behind the temperature controlled molecular-expulsion is the increased disordering of the terminal chains and consequent increase in sideways expansion. The model provides a remarkably close quantitative description of the experimental findings and is published in [14], see Section 3.2 for the published article. Further simulations also demonstrate the experimentally found smoothing of the transition at larger chain lengths and the importance of the mass of the metal cations in lowering the transition temperature, this is discussed in Section 3.3. It is suggested that adding free alkane into the mix could change the nature of the transition altogether, from discontinuous to continuous as shown in previous experiments [19] and this is discussed in terms of the theoretical model parameters. In this Chapter, a poorly understood LC system is identified and a thorough understanding of the experiments so far performed is demonstrated. Using these results a theoretical model is developed, in close collaboration with experimental colleagues and computer simulations are then used to inform the parameters of this theory employing both standard and new techniques. The calculated parameters are then fed into the model and the results are directly compared to experiment providing a new understanding of this system for the first time.

In Chapter 4 the focus is on amphiphilic compounds, which are attracting increasing interest at the moment, specifically newly synthesised tetraphilic (X-shaped) molecules called bolaamphiphiles [5, 20–23]. They usually consist of a π -conjugated rod-like core with terminal glycerol groups at either end with the X-shape being provided by two, sometimes incompatible, lateral alkyl chains on either side of the backbone. These

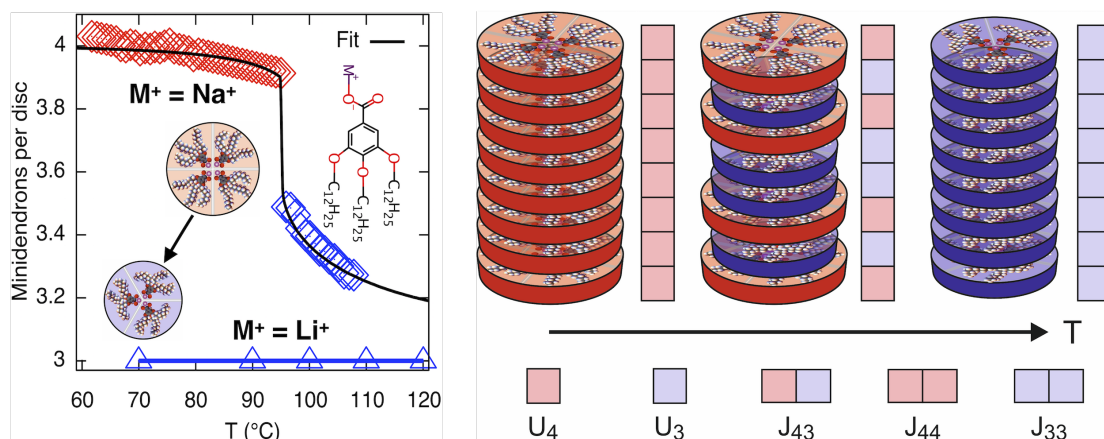


Figure 1.2: Number of molecules vs temperature and experiment vs theory fitting (left) and schematic of columnar shedding of Minidendrons with temperature, including model parameters.

molecules form columnar phases with unique tiling patterns [3, 12, 24–27] often on a sub 5nm scale and are considered promising candidates for use in nano-electronics [28]. This is because of the 2d stacked square array formed by them which is rare in itself, previously only observed in block-copolymers [29], the temperature range over which the array remains intact with little expansion and the ability to form chemically distinct patterns such as a chessboard. In this work, the phase transition between two columnar chessboard phases formed from molecules with a single perfluoralkyl and carbosilane chain attached on opposing sides of the backbone is investigated. The system undergoes a unique transition from a two-colour tiling, where like chains segregate into their respective nano-compartments to a single-colour tiling at higher temperatures where the chains are mixed as illustrated by Figure 1.3. Both grazing incidence and small-angle X-ray scattering (GISAXS and SAXS) studies show critical behaviour above and below the transition indicating that this system is a close real-life example of the 3d Ising model. Monte Carlo simulation is used to assess the critical behaviour by modelling the system on a 3d cubic lattice. Direct comparisons made between how susceptible the system is to spontaneous ordering under an external stimulus (susceptibility) measured from

simulation and experiment (diffuse peak height) indicate a smaller domain size above the transition. This agreement between finite sized MC simulations and experimental observations suggest that kinetic effects are dominating inside the liquid crystal. It was found that large scale fluctuations are suppressed in reality likely due to the kinetic barrier present at the border between local two-colour patches. The results have been published in [13]. In this Chapter, an opportunity to perform a theoretical study of a new LC system is identified and a thorough understanding of the experiments so far performed is demonstrated. Using these results a theoretical model is developed, in close collaboration with experimental colleagues and computer simulations are then used to solve the model in 3d using MC simulation. The results are then directly compared with experiment through scaling arguments yielding new theoretical insights.

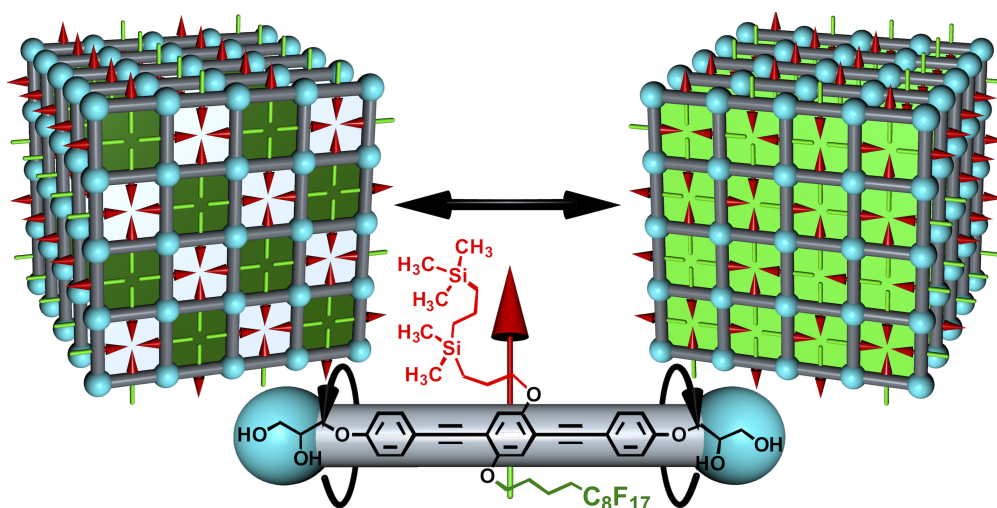


Figure 1.3: Sample configurations of the ordered segregated chessboard tiling at low temperature vs the more disordered mixed tiling at high temperature reproduced from MC simulation. Red arrows heads indicate carboxilane chains and green tails illustrate fully fluorinated chains. Terphenyl backbone is drawn in grey with blue terminating glycerol groups at either end.

In Chapter 5 the crystallisation behaviour of isotactic polypropylene (i-PP) at large undercooling is investigated. Recent works have revealed the presence of a metastable mesophase which forms rapidly in comparison to the more stable α -phase form of

i-PP [30]. The α -phase unit cell is highly ordered and contains alternating left and right-handed helices (2 left and 2 right) and chains in the melt must first acquire this conformation before joining the growing α -phase crystal. At large undercoolings the metastable mesophase forms faster and overtakes the α -phase crystal likely due to the two-step process required for a chain in the melt to join the α -phase crystal. An additional problem arises where there is competition between two phases, in that the presence of a metastable phase may seriously reduce the rate of crystallisation. This is thought to be an example of self-poisoning analogous to that studied in long chain n-alkanes where metastable folded chains block the formation of the extended chain crystal [31]. In this work a 1d solid-on-solid model is devised by considering the free energy change of adsorbing or desorbing mesophase chains onto the surface of the α -phase chain crystal. Once attached chains may either desorb or convert fast or slow depending on whether the meso- α interface is buried or not, the reverse of these processes are also allowed. Hoffman nucleation theory is employed to account for the growth rate dependence on chain length below the poisoning temperature by considering the free energy of primary nuclei and the Williams-Landel-Ferry equation is used to factor in the changing viscosity of the polymer as the glass transition is approached. Semi-quantitative agreement is found and provides clear evidence of self-poisoning in i-PP, despite the model's simplicity. In order to achieve better quantitative agreement with experimental data, neighbouring interactions are introduced by designing an interaction scheme for a pseudo-2d line of interacting 1d growth stems. The results point to two crucial model adjustments required to better describe the experiment, the direct attachment of α -phase chains above the mesophase melt temperature and a variable crystal width. Examples of self-poisoning on cleaner model polymer systems are also discussed [32]. In this Chapter, an understanding of a newly reported experimental study as well as a pre-existing joint experimental and theoretical one in a similar system is demonstrated. An existing theoretical model is extended in close collaboration with experimental colleagues. The

model is solved analytically in 1d and studied in 2d and using MC simulation. The model is then critically evaluated against experimental data, areas for improvement are identified and other examples in pre-existing literature are highlighted.

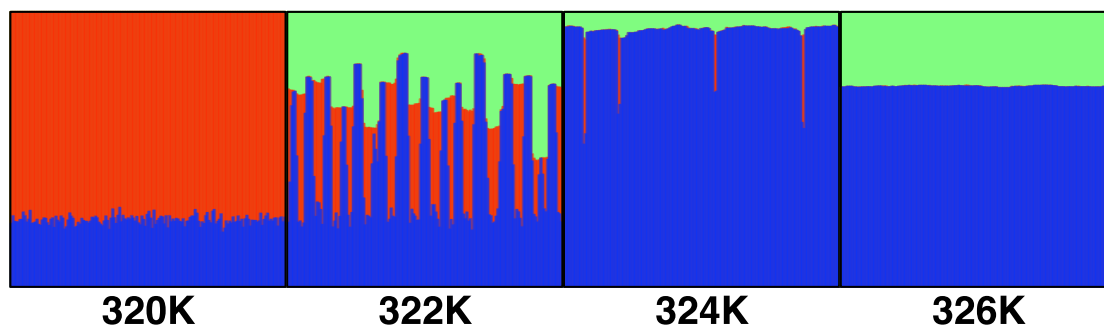


Figure 1.4: Progressive snapshots of the growth front for a series of interacting 1d growth stems from MC simulation. Green areas indicated liquid, blue the α -phase and red the mesophase which poisons the α -phase growth front.

In Chapter 6 molecular dynamics simulation is employed in order to provide additional insight into the unusual pre-melting behaviour, captured by atomic force microscopy, in a series of ultra-long n -alkanes, up to $C_{390}H_{782}$, as monolayers adsorbed on graphite. Specifically the monolayers are found by AFM to melt at nearly 81K above their bulk melting temperature and melt from their ends inwards, until more than half the overall chain length has melted. At higher temperatures the rest of the chains melt altogether, the transition is also fully reversible. This behaviour is surprising because it is well known that a 2d crystal should melt well below the melting temperature of the 3d bulk crystal due to the lower number of neighbouring interactions available in a 2d crystal when compared to the 3d one. Molecular dynamics simulation is used to model a 6 lamellae monolayer structure, formed from 1800 coarse-grained $C_{390}H_{782}$ molecules adsorbed on graphite, by leveraging the CG-SDK model [33]. The model has recently been demonstrated as a viable coarse-grained model for performing simulations of bulk polyethylene in LAMMPS [34]. This coarse-graining approach approximates 3 methylene units as a single bead or atom, using a Lennard-Jones 9-6 potential. We explore the behaviour of

the systems over a range of temperatures from 350K to 600K at 25K intervals calculating observables including average z-displacement away from the graphite surface, local and global estimates of crystallinity and the average squared displacement of beads as shown in Figure 1.5. Lamellae profiles, averaged observables and binned surface maps are reconstructed from the simulations and despite the coarse-grained limitations of the model, agree remarkably well with the experimental AFM images. The results showed differing degrees of pre-melting at all temperatures below the melt temperature of the monolayers and have been submitted for publication [35]. In this Chapter, a poorly understood polymeric system is identified and a detailed understanding of experiment is demonstrated. A theoretical model is developed in close collaboration with experimental colleagues and solved in 1d. Pre-existing computational studies in similar systems are identified and used to form the foundation of new molecular dynamics simulations, which ultimately provide molecular level insights as well as a stringent test of the theoretical model.

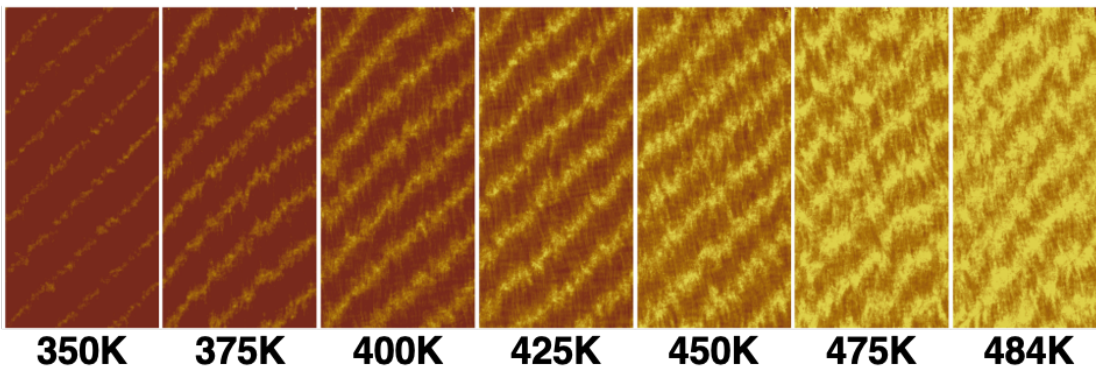


Figure 1.5: Binned maps of average squared displacement for all temperatures simulated below the melt calculated from MD simulation. Surface binning of (1 nm^2) bins over 50 instantaneous configurations (at 20ps intervals) for each simulated temperature, between 350K and 484K.

In Chapter 7 we summarise the findings in this thesis and discuss possible future work, including motivation for further experimental studies and computer simulations.

Bibliography

- [1] X. Zeng, G. Ungar, Y. Liu, V. Percec, A. E. Dulcey, and J. K. Hobbs. *Nature*, 428(6979):157–160, 2004.
- [2] G. Ungar, Y. Liu, X. Zeng, V. Percec, and W.-D. Cho. *Science*, 299(5610):1208–1211, 2003.
- [3] G. Ungar and X. Zeng. *Soft Matter*, 1(2):95–106, 2005.
- [4] V. Percec, C. M. Mitchell, W.-D. Cho, S. Uchida, M. Glodde, G. Ungar, X. Zeng, Y. Liu, V. S. Balagurusamy, and P. A. Heiney. *Journal of the American Chemical Society*, 126(19):6078–6094, 2004.
- [5] S. Poppe, X. Cheng, C. Chen, X. Zeng, R.-b. Zhang, F. Liu, G. Ungar, and C. Tschierske. *Journal of the American Chemical Society*, 142(7):3296–3300, 2020.
- [6] L. Wang, B. E. Partridge, N. Huang, J. T. Olsen, D. Sahoo, X. Zeng, G. Ungar, R. Graf, H. W. Spiess, and V. Percec. *Journal of the American Chemical Society*, 142(20):9525–9536, 2020.
- [7] C. Chen, R. Kieffer, H. Ebert, M. Prehm, R.-b. Zhang, X. Zeng, F. Liu, G. Ungar, and C. Tschierske. *Angewandte Chemie*, 132(7):2747–2751, 2020.
- [8] G. Ungar and X.-b. Zeng. *Chemical reviews*, 101(12):4157–4188, 2001.
- [9] X. Zeng and G. Ungar. *Polymer*, 39(19):4523–4533, 1998.
- [10] X. Zeng, G. Ungar, S. Spells, G. Brooke, C. Farren, and A. Harden. *Physical review letters*, 90(15):155508, 2003.
- [11] X. Zeng and G. Ungar. *Macromolecules*, 34(20):6945–6954, 2001.

-
- [12] X. Zeng, R. Kieffer, B. Glettner, C. Nürnberger, F. Liu, K. Pelz, M. Prehm, U. Baumeister, H. Hahn, H. Lang, et al. *Science*, 331(6022):1302–1306, 2011.
- [13] W. S. Fall, C. Nürnberger, X. Zeng, F. Liu, S. J. Kearney, G. A. Gehring, C. Tschierske, and G. Ungar. *Molecular Systems Design & Engineering*, 4(2):396–406, 2019.
- [14] W. S. Fall, M.-H. Yen, X. Zeng, L. Cseh, Y. Liu, G. A. Gehring, and G. Ungar. *Soft Matter*, 15(1):22–29, 2019.
- [15] S. George, C. Bentham, X. Zeng, G. Ungar, and G. A. Gehring. *Physical Review E*, 95(6):062126, 2017.
- [16] V. Balagurusamy, G. Ungar, V. Percec, and G. Johansson. *Journal of the American Chemical Society*, 119(7):1539–1555, 1997.
- [17] V. Percec, M. N. Holerca, S. Uchida, W.-D. Cho, G. Ungar, Y. Lee, and D. J. Yeardley. *Chemistry—A European Journal*, 8(5):1106–1117, 2002.
- [18] B. M. Rosen, D. A. Wilson, C. J. Wilson, M. Peterca, B. C. Won, C. Huang, L. R. Lipski, X. Zeng, G. Ungar, P. A. Heiney, et al. *Journal of the American Chemical Society*, 131(47):17500–17521, 2009.
- [19] M.-H. Yen, J. Chairapra, X. Zeng, Y. Liu, L. Cseh, G. H. Mehl, and G. Ungar. *Journal of the American Chemical Society*, 138(18):5757–5760, 2016.
- [20] C. Tschierske. *Chemical Society Reviews*, 36(12):1930–1970, 2007.
- [21] R. Zhang, Z. Su, X.-Y. Yan, J. Huang, W. Shan, X.-H. Dong, X. Feng, Z. Lin, and S. Z. Cheng. *Chemistry—A European Journal*, 2020.

-
- [22] R.-b. Zhang, X.-b. Zeng, C. Wu, Q. Jin, Y. Liu, and G. Ungar. *Advanced Functional Materials*, 29(3):1806078, 2019.
- [23] C. Nürnberger, H. Lu, X. Zeng, F. Liu, G. Ungar, H. Hahn, H. Lang, M. Prehm, and C. Tschierske. *Chemical Communications*, 55(29):4154–4157, 2019.
- [24] C. Tschierske, C. Nürnberger, H. Ebert, B. Glettner, M. Prehm, F. Liu, X.-B. Zeng, and G. Ungar. *Interface Focus*, 2(5):669–680, 2012.
- [25] B. Chen, X. Zeng, U. Baumeister, G. Ungar, and C. Tschierske. *Science*, 307(5706):96–99, 2005.
- [26] G. Ungar, V. Percec, X. Zeng, and P. Leowanawat. *Israel Journal of Chemistry*, 51(11-12):1206–1215, 2011.
- [27] B. Glettner, F. Liu, X. Zeng, M. Prehm, U. Baumeister, M. Walker, M. A. Bates, P. Boesecke, G. Ungar, and C. Tschierske. *Angewandte Chemie International Edition*, 47(47):9063–9066, 2008.
- [28] S. Sergeyev, W. Pisula, and Y. H. Geerts. *Chemical Society Reviews*, 36(12):1902–1929, 2007.
- [29] C. Tang, E. M. Lennon, G. H. Fredrickson, E. J. Kramer, and C. J. Hawker. *Science*, 322(5900):429–432, 2008.
- [30] D. Cavallo, L. Zhang, G. Portale, G. Alfonso, H. Janani, and R. Alamo. *Polymer*, 55(15):3234–3241, 2014.
- [31] P. G. Higgs and G. Ungar. *The Journal of Chemical Physics*, 100(1):640–648, 1994.
- [32] X. Zhang, W. Zhang, K. B. Wagener, E. Boz, and R. G. Alamo. *Macromolecules*, 51(4):1386–1397, 2018.

-
- [33] W. Shinoda, R. DeVane, and M. L. Klein. *Molecular Simulation*, 33(1-2):27–36, 2007.
- [34] K. W. Hall, T. W. Sirk, M. L. Klein, and W. Shinoda. *The Journal of Chemical Physics*, 150(24):244901, 2019.
- [35] R. Zhang, W. S. Fall, K. W. Hall, G. A. Gehring, X. Zeng, and G. Ungar. *Submitted To: Science*, 2020.

Chapter 2

General Considerations

2.1 What Are Liquid Crystals?

A liquid crystal possesses some of the properties of both a liquid and a crystalline solid [1]. Molecules inside a crystal are both positionally and orientationally ordered in the long range whereas liquids have only short range order, their constituent molecules are randomly distributed. Molecular arrangements that lie between these two distinct phases, with greater order than a liquid but less than a crystalline solid, are called liquid crystals [2] or mesophases [3, 4] (*mesomorphic*: of intermediate form).

Liquid crystals are most often identified using X-ray diffraction (XRD) and it is important to be able to distinguish them from their crystal or liquid counterparts. Crystal structures are characterised by their Bravais lattice, which are formed from an infinite number of discrete translation operations, from an arbitrary position x_0 , in 3d space such that

$$x = x_0 + n_1\mathbf{a}_1 + n_2\mathbf{a}_2 + n_3\mathbf{a}_3 \quad (2.1)$$

Where $\{\mathbf{a}_i\}$ represent the lattice basis vectors and n_i are integers. The probability of finding the equivalent crystal pattern at the point x , is finite for $|x - x_0| \rightarrow \infty$ and so the resulting XRD pattern will yield sharp Bragg reflections characteristic of the lattice in question. This means that the density-density correlation function for a crystal can be expressed a periodic function of the basis vectors in the following limit. Here $\langle \rho(\mathbf{x})\rho(\mathbf{x}') \rangle$ is the density-density correlation function and $F(\mathbf{x} - \mathbf{x}')$ is a periodic function of the basis vectors $\{\mathbf{a}_i\}$.

$$\lim_{|\mathbf{x}-\mathbf{x}'|\rightarrow\infty} \langle \rho(\mathbf{x})\rho(\mathbf{x}') \rangle = F(\mathbf{x} - \mathbf{x}') \quad (2.2)$$

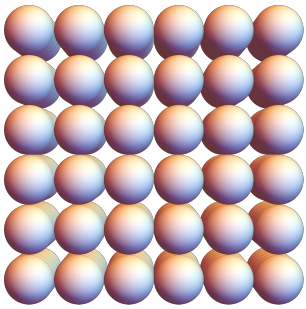
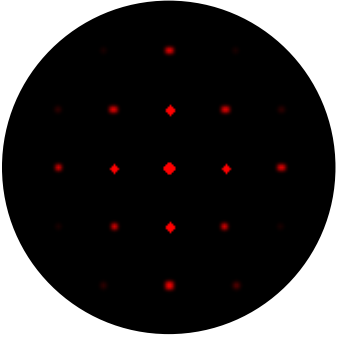
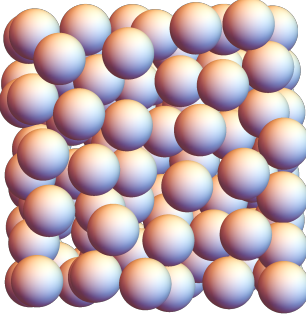

Phase	Ordering	WAXS Pattern
Crystalline Solid		
Isotropic Liquid		

Table 2.1: Properties of crystalline solid vs isotropic liquid, ordering of the constituent molecules and corresponding WAXS patterns.

For an isotropic liquid on the other hand it is only possible to express the probability of locating a similar pattern at some distance, x far from x_0 , through the average particle density $\bar{\rho}$.

$$\lim_{|\mathbf{x}-\mathbf{x}'|\rightarrow\infty} \langle \rho(\mathbf{x})\rho(\mathbf{x}') \rangle \simeq \bar{\rho}^2 \quad (2.3)$$

2.1. WHAT ARE LIQUID CRYSTALS?

There exists an isotropic length scale ξ , over which correlations are lost. Typically XRD patterns for liquids give rise to diffuse peaks of width ξ^{-1} .

Liquid crystals then are systems in which liquid-like order exists, at least in one direction of space and in which some degree of anisotropy is present [4]. More precisely the density-density correlation function depends both on the orientation of $\mathbf{x} - \mathbf{x}'$ w.r.t some axis and its modulus, $|\mathbf{x} - \mathbf{x}'|$.

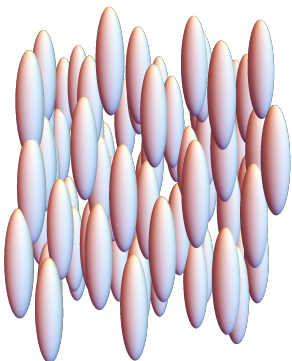

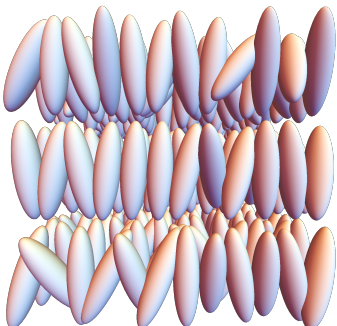

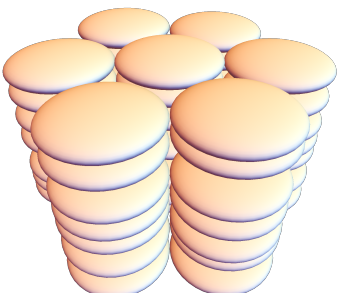
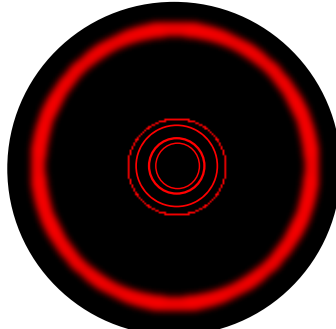
LC Phase	Ordering	WAXS Pattern
<p>Nematic phases: Orientational order and no positional order, the correlation function must be anisotropic such that at least two distinct length scales exist, for example ξ_{\perp} and ξ_{\parallel}, over which correlations decay.</p>		
<p>Smectic: 1d order exists in 3d such that 2d liquid layers appear stacked with well-defined spacing.</p>		
<p>Columnar: 2d order exists in 3d such that a 2d array of liquid tubes exist.</p>		

Table 2.2: Properties of nematic, smectic and columnar phases, ordering of the constituent molecules and corresponding WAXS patterns.

According to de Gennes it is possible to create liquid crystals by doing either of the following:

1. Imposing no positional order, or imposing positional order in one or two rather than three dimensions. This is achieved often through designing molecules which are non-spherical such as prolate or oblate ellipsoids, see Table 2.2.
2. Introducing degrees of freedom that are distinct from the localisations of the centres of gravity. By freezing out orientational degrees of freedom in an isotropic liquid, anisotropy is created such that correlations along the preferred direction are not equivalent to those in the perpendicular plane. This falls under the nematic definition and is the most transparent way of obtaining nematics.

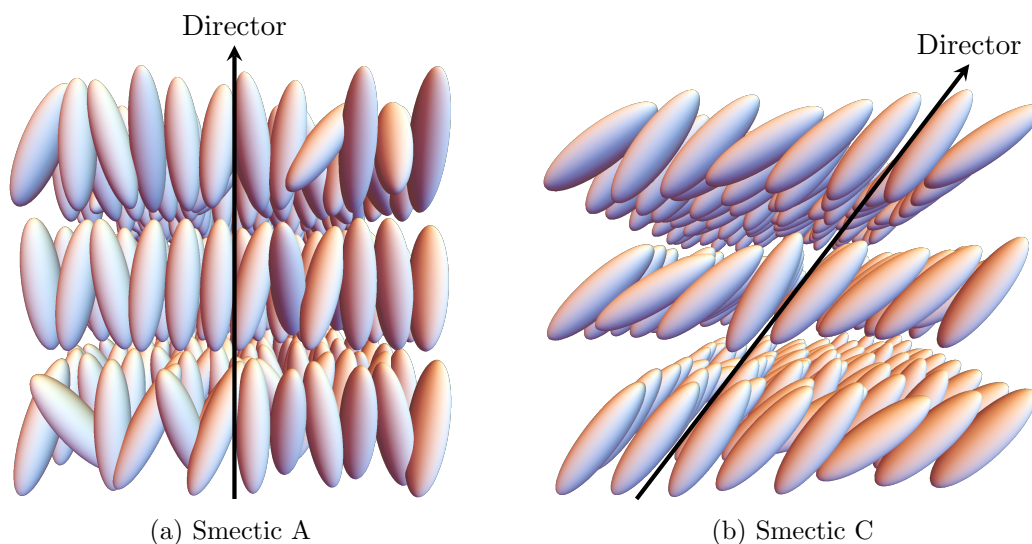


Figure 2.1: Orientational snapshots of molecules in two different type of smectic phases. Director is perpendicular to the layers in Smectic A and at an angle other than 90 degrees in Smectic C, in this case 45 degrees.

The ordering of a liquid crystal is normally defined as a temporal and spatial average as follows

$$S = \langle P_2 \cos \theta \rangle = \left\langle \frac{3 \cos^2 \theta - 1}{2} \right\rangle \quad (2.4)$$

where θ is the angle formed by the axis of the molecule and the local director. For a crystalline solid or isotropic liquid, see Table 2.1, there is 3d order or none at all hence $S = 1$ or $S = 0$ respectively, a liquid crystal falls between these two values. Figure 2.1 depicts two different smectic phases called smectic A and smectic C. In smectic A the molecules generally order at 90 degrees to the layers whereas in smectic C they generally order at some angle other than 90 degrees, in either case S remains the same in both phases, the local director is indicated in both phases.

Molecules that form LC phases (mesogens) come in all shapes and sizes and can generally be grouped into 3 categories, we do so here giving some famous examples and illustrating structures particularly relevant to this work. It is important to stress that, throughout this thesis we are only concerned with liquid crystals brought about by thermal processes as opposed to the influence of solvents, i.e. thermotropic not lyotropic.

2.1.1 Mesogens

For a liquid crystal to form some anisotropy must be introduced and this was traditionally achieved by designing molecules that are either rod-like in shape (calamitics) (Figure 2.2 A) or disc-like (discotics) (Figure 2.2 B). These molecules form the well known liquid crystalline phases such as nematic, smectic and columnar. However in recent years compounds with novel shapes such as, taper-shaped or conical dendrons (Figure 2.2 C), T-shaped or X-shaped amphiphiles (Figure 2.2 D), banana-shaped bent core molecules and even chiral variations of them are being synthesised (Figure 2.2 E). This has brought about the discovery of numerous new phases previously unseen in thermotropic liquid crystals, for example the first quasi-crystalline phase was reported in a dendritic liquid crystal recently and even a new twist-bend nematic phase in bent-core achiral molecules. The molecules all usually have common attributes such as

π -conjugation and flexible terminal chains and with good reason. Firstly π -conjugation allows for the lowering of the overall energy of the molecule and subsequently increases its stability through the sharing of delocalised p-orbital electrons. However π -conjugated systems alone are not soluble and melt at high temperatures, e.g. graphene/graphite, hence the attachment of flexible terminal chains lowers the melting temperature and protects the rigid part of the molecule from oxidisation. Thus carefully controlling attributes such as polarisability, π - π interactions and van der Waals interactions from the flexible terminal chains as well as the size and overall shape of the molecule itself allows for the tuning of the desirable properties of LC's.

In this thesis we are concerned with mesogens which are either taper-shaped, cross-shaped and polymers including ultra-long n-alkanes and isotactic polypropylene. This discussion is continued in the respective Chapters 3, 4, 5 and 6. We are not concerned with the more traditional rod-like liquid crystals or the highly complex chevron-shaped molecules.

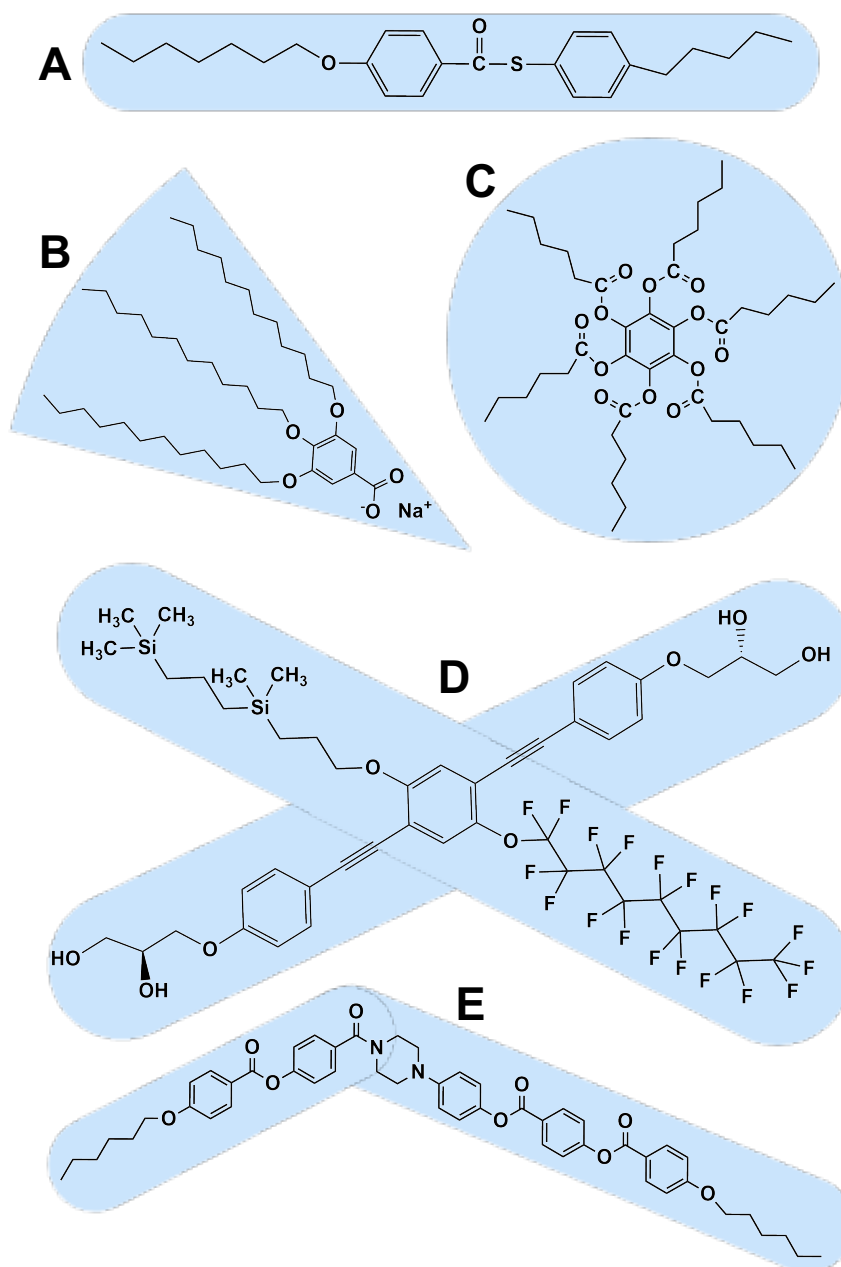


Figure 2.2: Example mesogens (a) Rod-shaped 4-n-pentylbenzenethio-4'-n-heptyloxybenzoate (Sm-C \rightarrow N); (b) Taper-shaped Na-salt of 3,4,5-tris-dodecyloxy benzoic acid (Col_r \rightarrow Col_{h1} \rightarrow Col₂ \rightarrow Pm3n \rightarrow BCC) [5]; (c) Disc-shaped hexa-n-alkanoates of benzene [6]; (d) Cross-shaped bolaamphiphiles [7]; (e) Chevron-shaped (bent core) achiral molecule, forms the twist-bend nematic phase [8].

2.2 Statistical Physics

Statistical Physics describes the behaviour of systems of many particles in equilibrium. It may be used to predict the macroscopic properties of many-body systems arising from the fundamental microscopic properties or interactions.

2.2.1 Principal Ensembles

There are several ensembles in statistical mechanics which are required to group many-body systems. Each ensemble is made up of a large (or theoretically infinite) number of states of a system; which are categorised according to their macroscopic observables. The first three ensembles, as defined by Gibbs, are: (a) the *microcanonical* ensemble which describes a series of isolated states each characterised by a fixed number of particles N , volume V and total energy E . Systems must remain completely isolated such that they reside in statistical equilibrium, this is known as the NVE ensemble. (b) The *canonical* ensemble consists of member states for which the energy is not known but instead the temperature T , is specified. For a canonical system, the number of particles N , volume V and temperature T , is fixed such that the system is closed and only energy may be exchanged with a heat reservoir, this is known as the NVT ensemble. It is most suitable for Monte Carlo simulations of lattice models as discussed in Section 2.3.1 and is the chosen ensemble used in Chapter 3. (c) Finally the *grand-canonical* ensemble groups states in which neither energy nor particle number are fixed but instead both the temperature T and chemical potential μ , are specified. This describes an open system where both energy and particles can be exchanged with the reservoir, this is referred to as the μVT ensemble. (d) A fourth *isothermal-isobaric* ensemble describes an ensemble of states where the number of particles N , pressure P and temperature T , are fixed. This is referred to as the NPT ensemble and is representative of chemical systems which

are often studied under these conditions, this particular ensemble is often used in MD simulations, see Section 2.3.2 and is the chosen ensemble used in Chapter 6.

2.2.2 The Canonical Partition Function \mathcal{Z}

The partition function is the fundamental concept upon which equilibrium statistical mechanics is based; it contains all the information about the system. In its classical form it may be written as

$$\mathcal{Z} = \sum_i e^{-\beta E_i} \quad (2.5)$$

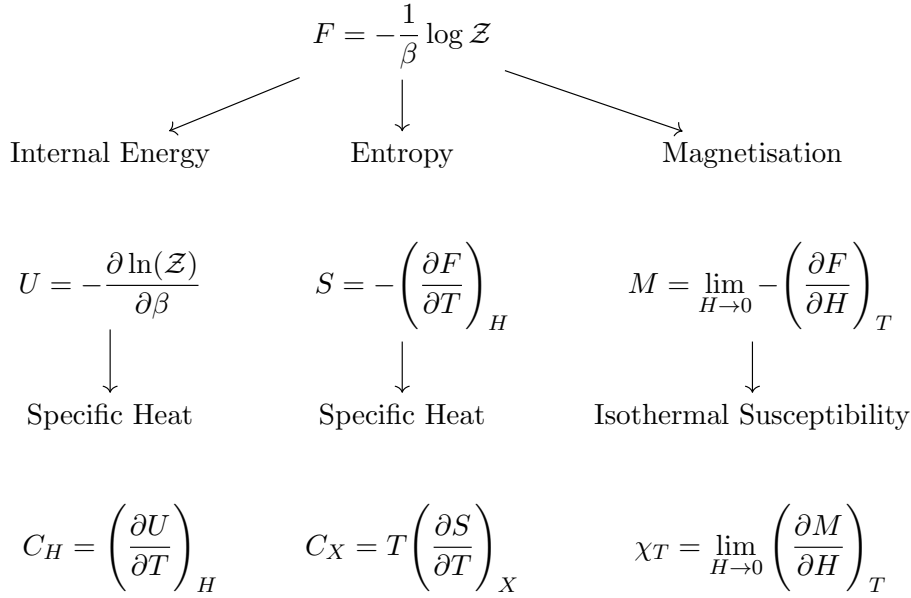
where E_i is the energy of the state and $\beta = 1/k_B T$ where T , is the temperature and k_B is Boltzmann's constant. It is a summation over all possible states for a particular system and is dependent on system size and number of degrees of freedom [9]. For a small system the solution may be written down and equilibrium properties may be calculated in closed form. The probability, P_i of a particular state, i existing is determined from \mathcal{Z} and may be written as

$$P_i = \frac{e^{-\beta E_i}}{\mathcal{Z}} \quad (2.6)$$

where E_i is the energy of the state (or Hamiltonian) and $\beta = \frac{1}{k_B T}$ where T , is the temperature and k_B is Boltzmann's constant. Whilst for large systems calculating \mathcal{Z} may be inaccessible even with modern compute times, Monte Carlo methods may be used to estimate probabilities, P_i and expectation values of system observables.

2.2.3 Essential Thermodynamic Quantities

All other observable quantities may be calculated by differentiation of the free energy. The variables for magnetic systems are described here since they are most relevant to the work carried out in Chapters 3 and 4. Note throughout that H denotes an external magnetic field.



2.2.4 The Ising Model

The Ising Model was originally proposed to describe ferromagnetism in statistical mechanics. It is probably the simplest lattice model imaginable and yet has been studied now for a century since original inception by Wilhelm Lenz in 1920. In fact this year marks it's 100 year anniversary. In the model spins are confined to a lattice and can take values of +1 or -1 and interact with their nearest neighbours through the interaction coupling \mathcal{J} . The model is described by the Hamiltonian:

$$\mathcal{H} = - \sum_{\langle i,j \rangle} \sigma_i \sigma_j - H \sum_i \sigma_i \tag{2.7}$$

where $\sigma_i = \pm 1$. It was first solved analytically in 1d by Lenz PhD student Ernst Ising in 1925 [10] and showed no phase transition. Later in 1936 Rudolph Peierls showed that for $d \geq 2$ spontaneous magnetisation occurs and there is an order-disorder transition [11], this became known as Peierls Argument. In 1941 Hendrik Kramers and Gregory Wannier successfully predicted the critical point by relating the free energy of the 2d

square Ising Model at low temperature to another at higher temperature by considering the 2d square lattice is the dual of itself, this is known as Kramers-Wannier duality [12]. The model was solved exactly on a 2d square lattice by Onsager in 1945 [13] using the transfer matrix method. There is no exact solution in 3d but much is known from approximate theories and MC studies.

2.2.5 Phase Transitions and Critical Phenomena

Close to a phase transition, in the region where the temperature is close to the critical temperature ($T \approx T_c$), the correlation length in the system is much larger than the range of interactions between constituent atoms or spins. System observables in this region can be described according to a simple power law believed to be universal, this power is known as a critical exponent. Many experiments and simple statistical models support this idea and demonstrate how thermodynamic properties can be described around the critical point by a simple power law. Universality provides a framework where multiple systems with the same degrees of freedom and dimensions can be grouped under one class with the same set of critical exponents, this is known as a universality class. In this thesis we are primarily concerned with liquid crystal systems which are analogous to one magnetic system in particular, the Ising Model, see Section 2.2.4. In the case of the Ising ferromagnet thermodynamic properties such as the magnetisation m , specific heat C , susceptibility χ and correlation length ξ vary as follows [14, 15].

$$m = m_0 \tau^\beta \quad (T < T_c) \quad (2.8)$$

$$\chi = \chi_0^\pm \tau^{-\gamma} \quad (2.9)$$

$$C = C_0^\pm \tau^{-\alpha} \quad (2.10)$$

$$\xi = \xi_0^\pm \tau^{-\nu} \quad (2.11)$$

where $\tau = |1 - \frac{T}{T_c}|$ and β, α, γ and ν are the critical exponents. These scaling relationships are only valid close to the critical point, i.e. as $\tau \rightarrow 0$ and the amplitudes are usually different for $T > T_c$ or $T < T_c$. Close to T_c one can also define the magnetisation in terms of another exponent δ and an applied uniform magnetic field such that $m = DH^{\frac{1}{\delta}}$. The density-density correlation function $\Gamma(x)$, see Section 2.1 can similarly be described introducing another exponent η such that $\Gamma(\mathbf{x} - \mathbf{x}') = \Gamma_0 x^{-(d-2-\eta)}$ as $\mathbf{x} - \mathbf{x}' \rightarrow \infty$ which describes a power law decay at T_c . Critical exponents are rarely known exactly and only for a very small number of statistical models, the most famous of which is the exactly solvable 2d square lattice Ising Model [13], see Table 2.3 for a list of exponents.

Universality Class	α	β	γ	δ	ν	η
2d Ising	0	$\frac{1}{8}$	$\frac{7}{4}$	15	1	$\frac{1}{4}$
3d Ising	0.10	0.33	1.24	4.8	0.63	0.04

Table 2.3: Critical exponent values for the 2d and 3d Ising Models on a square lattice. Exponents for the 2d model are exact, 3d calculated numerically from MC simulations [16].

Further important scaling relations exist and they will be discussed here briefly, for a detailed account see refs [17–19]. Close to T_c the singular portion of the free energy $F(H, T)$ may be expressed as

$$F_s = \tau^{2-\alpha} \mathcal{F}^{\pm} \left(\frac{H}{\tau^{\Delta}} \right) \quad (2.12)$$

where H is a small magnetic field, $\Delta = \frac{1}{2}(2 - \alpha - \gamma)$ is the gap exponent and $\mathcal{F}^{\pm} \left(\frac{H}{\tau^{\Delta}} \right)$ is a scaling function. As such all other important quantities can be written in terms of this scaling relation by taking the appropriate derivatives as discussed in Section 2.2.2. The correlation function may be expressed in a similar fashion in terms of two exponents as

$$\Gamma(r, \xi, \tau) = r^{-(d-2-\eta)} \mathcal{G} \left(\frac{r}{\xi}, \frac{H}{\tau^{\Delta}} \right) \quad (2.13)$$

where $\mathcal{G}(\frac{t}{\xi}, \frac{H}{\tau^\Delta})$ is a scaling function of two variables. A number of important scaling relations can now be shown, taking the derivative of Equation 2.12 with respect to the field for example gives

$$M = \tau^{2-\alpha-\Delta} \mathcal{F}'\left(\frac{H}{\tau^\Delta}\right) \quad (2.14)$$

which may be directly compared with Equation 2.13 to show

$$\beta = 2 - \alpha - \delta \quad (2.15)$$

Then using a scaling relation for the magnetic susceptibility

$$\chi = \tau^{-\gamma} C\left(\frac{H}{\tau^\Delta}\right) \quad (2.16)$$

and integrating to find the magnetisation it can be found that for $H = 0$

$$m \propto \tau^{\Delta-\gamma} \quad (2.17)$$

Combining Equation 2.15 with Equation 2.17 results in the Rushbrooke inequality [14] which holds for all models.

$$\alpha + 2\beta + \gamma = 2 \quad (2.18)$$

Finite size scaling will be discussed in the proceeding Section 2.3.3.5 as an extension of this important topic.

2.2.6 Fluctuations

The Fluctuation-Dissipation Theorem describes response functions in terms of correlation functions in physical variables measured at equilibrium without a perturbing field. It is a very general theorem first proven by Herbert Callen and Theodore Welton

in 1951 [20] and later extended by Ryogo Kubo in 1957 [21, 22]. It can be applied to classical and quantum systems, both time-dependent and time-independent and some general relations applicable to magnetic systems are used in this thesis. It is particularly useful for solved models that obey detailed balance i.e MC simulations of Ising like systems as described in Section 2.2.4.

For the Ising Model of a ferromagnet, the magnetic susceptibility may be written in terms of spin correlations in the following way. Beginning by combining Equations 2.5 and 2.7 the partition function for the Ising Model may be written as

$$\mathcal{Z} = \text{Tr}(e^{-\beta\mathcal{H}+\beta h\sum_i\sigma_i}) \quad (2.19)$$

The average magnetisation may then be written by taking the ensemble average as follows

$$\langle\sigma\rangle = \frac{\text{Tr}(\sigma_i e^{-\beta\mathcal{H}+\beta h\sum_i\sigma_i})}{\text{Tr}(e^{-\beta\mathcal{H}+\beta h\sum_i\sigma_i})} \quad (2.20)$$

Using the definition of susceptibility as defined in Section 2.2.3. We can write the susceptibility as follows by taking the derivative with respect to the field

$$\chi = \frac{\beta \text{Tr}(\sum_{\langle i,j\rangle} \sigma_i \sigma_j e^{-\beta\mathcal{H}})}{\mathcal{Z}} - \frac{\beta \text{Tr}(\sum_{\langle i,j\rangle} \sigma_i \sigma_j e^{-\beta\mathcal{H}}) \text{Tr}(\sigma_i e^{\beta\mathcal{H}})}{\mathcal{Z}^2} \quad (2.21)$$

Which may be written as

$$\chi = \beta \left(\sum_{\langle i,j\rangle} \langle\sigma_i\sigma_j\rangle - \langle\sigma_i\rangle\langle\sigma_j\rangle \right) \quad (2.22)$$

This relates the magnitude of fluctuations in the magnetisation to its susceptibility in its conjugate field and is also known as the linear response theorem. It allows for the calculation of susceptibilities in MC simulations by measuring the size of fluctuations in a given variable.

2.3 Computer Simulations

Since the advent of the Atanasoff-Berry Computer in 1937, designed solely to solve systems of linear equations, physicists have been armed with a powerful tool for numerically solving problems without oversimplification. Some early famous examples include ENIAC, a reprogrammable computer used to study the feasibility of thermonuclear weapons and MANIAC famously used during the Manhattan Project to study thermonuclear processes more precisely. Today Apple's iPhone can perform over 50 times the number of calculations than MANIAC could in its day. Up to the present day the number of transistors on an integrated circuit chip approaches 50 trillion and continues to double every 2 years although this cannot continue indefinitely [23], in fact the scale of components is already approaching the limit of the size of individual atoms. The first mass produced supercomputer ever sold (Cray-1) boasted 160 Mega FLOPS of computing power in 1975 and this was exceeded by a single microprocessor unit long ago. These days the top desktop computers can perform 100's of Tera FLOPS on a single chip and the largest supercomputer in the world, SUMMIT at Oak Ridge National Labs USA, can manage 148.6 Peta FLOPS. This decade marks the moment that peak supercomputer performance will enter the Exa scale, with either the USA, China, Japan or the EU in the running to finish first, China is rumoured to unveil theirs this year. This is a significant landmark because this is of the order of the number of calculations theoretically estimated to be achievable by the human brain [24]. The rapid increase in computational power is allowing scientists to tackle ever larger problems. In this section we cover two powerful computational techniques used throughout this thesis, Monte Carlo Importance Sampling and Molecular Dynamics. The key difference between these two techniques is that the former studies an ensemble of representative configurations at fixed time whereas the latter studies the time evolution of a given starting configuration i.e. ensemble average or time average.



Figure 2.3: Paul Stern (Left) and Nick Metropolis (Right) playing chess with the MANIAC computer. [25, 26]

2.3.1 Markov Chain Monte Carlo

In Monte Carlo (MC) simulation the aim is to generate a trajectory in phase space and correctly sample from a chosen statistical ensemble i.e. canonical. This can be performed on lattice or off lattice but the same rules apply in both cases, in this thesis we are primarily concerned with lattice models when using MC. The go to example of MC importance sampling, on lattice, is the simple Ising Model as described previously in Section 2.2.4 using the Metropolis method [27]. The method produces a trajectory by generating new states based only on their immediate predecessors according to some

transition probability, this is known as a Markovian process. The resulting sequence of states are ordered in MC time but not in real time because it is non-deterministic, i.e. the time dependence of a spin flip is zero. For simple models such as the Ising Model the time-dependent behaviour can be described by a master equation

$$\frac{\partial P_n(t)}{\partial t} = - \sum_{n \neq m} [P_n(t)W_{n \rightarrow m} - P_m(t)W_{m \rightarrow n}] \quad (2.23)$$

where $P_n(t)$ is the probability of the system being in a given state n at time t and $W_{n \rightarrow m}$ is the transition rate for $n \rightarrow m$. By considering the equilibrium condition that $\frac{\partial P_n(t)}{\partial t} = 0$ we obtain the important and required condition known as detailed balance

$$P_n(t)W_{n \rightarrow m} = P_m(t)W_{m \rightarrow n} \quad (2.24)$$

The probability of the n th state occurring was defined previously in Equation 2.6 and cannot usually be determined since the partition function is normally too difficult to calculate due to the large number of accessible states. MCMC gets around this problem by producing the m th state from the n th one and removing the partition function altogether by considering the ratio of their individual probabilities. This means that only the energy difference between the two states need be known

$$\Delta E = E_n - E_m \quad (2.25)$$

The metropolis rate is then given by the Metropolis form

$$W_{n \rightarrow m} = \begin{cases} \tau_0^{-1} \exp(-\frac{\Delta E}{k_B T}) & \Delta E > 0 \\ \tau_0^{-1} & \Delta E < 0 \end{cases} \quad (2.26)$$

where τ_0 is the time required to attempt a spin flip, normally set to unity. Thus we arrive at the algorithm itself.

1. Choose a starting configuration.
2. Choose a site i .
3. Calculate ΔE for a given spin flip.
4. Generate a random number r in the interval $0 < r < 1$.
5. If $r < W_{n \rightarrow m}$ flip the spin.
6. Go to the next site and go to (3).

Metropolis dynamics [27] is not the only solution that exists which satisfies detailed balance, others include Glauber[28] and Kawasaki [29] dynamics. In Glauber dynamics the single spin flip method is used with the following transition rate

$$W_{n \rightarrow m} = (2\tau_0)^{-1} [1 + \sigma_i \tanh(\frac{E_i}{k_B T})] \quad (2.27)$$

where $\sigma_i E_i$ is the energy of the i th spin in state n . It differs from Metropolis dynamics only at very high temperatures since the Glauber transition rate approaches $\frac{1}{2}$ as opposed to 1 in the Metropolis case. Hence at high temperatures the Metropolis system becomes non-ergodic because every spin flip is accepted and the system will oscillate between two states, this is not the case for Glauber dynamics which remains ergodic. This means that the behaviour or average over time is the same as that over probability space, i.e. the ensemble average. Kawasaki dynamics have the same transition rate as Metropolis as given in Equation 2.26 except that a pair of neighbouring spins are swapped instead of a single spin. This can be done locally or non-locally where the latter option allows for faster equilibration times. Note that changing the dynamics in this way does not

change the critical exponents, see Section 2.2.5.

The Metropolis algorithm is the simplest algorithm to implement but also the most inefficient particularly at criticality due to the formation of domains and long-ranged correlations leading to a high number of rejections. This is known as critical slowing down [30], a number of different methods have been developed to overcome this problem such as cluster flipping algorithms which flip clusters of like spins at once [31–33] and density of states methods [34]. For the work carried out in this thesis the Metropolis algorithm was used so the discussion of other algorithms ends here.

2.3.2 Molecular Dynamics

For classical many-body systems, MD may be used to model the system in question much in the same way as an experiment, albeit usually on much shorter timescales. For liquid crystals and polymers, at a nuclear level, the assumption is that constituent particles obey the laws of classical mechanics. This means that quantum mechanical effects resulting from the translational or rotational motion of light atoms or molecules such as molecular hydrogen, helium or heavy hydrogen as well as vibrational motion with frequency ν such that $h\nu > k_B T$ can be ignored.

In a normal MD simulation the position, $r_i(t)$ and velocity $v_i(t)$, of the particles at time t are recorded in memory. The forces acting on each particle are computed according to some chosen potential $\mathbf{F}_i = -\nabla_i U$ i.e. Lennard-Jones [35] for a detailed description of the potentials used in this thesis see Section 2.3.3.2. The equation of motion $\mathbf{F}_i = m\mathbf{a}_i$ is then integrated over the chosen time-step Δt using an algorithm such as the Velocity-Verlet algorithm [36] in order to calculate the position of the particles at time $t + \Delta t$ [37, 38].

In this thesis LAMMPS [39] is the chosen MD program which by default integrates Newton's equations of motion using Verlet integration [40], this is the simplest choice and for our purposes the best one. It is important to understand how this algorithm works since it is the foundation upon which any MD simulation is built. In order to derive it we first consider the Taylor expansion of a particle, around time t

$$r(t + \Delta t) = r(t) + v(t)\Delta t + \frac{f(t)}{2m}\Delta t^2 + \frac{\Delta t^2}{3!}\ddot{r} + \mathcal{O}(\Delta t^4) \quad (2.28)$$

$$r(t - \Delta t) = r(t) - v(t)\Delta t + \frac{f(t)}{2m}\Delta t^2 - \frac{\Delta t^2}{3!}\ddot{r} + \mathcal{O}(\Delta t^4) \quad (2.29)$$

Where $f(t)$ is the acceleration of the particle at time t . Summing Equations 2.28 and 2.29 and rearranging gives

$$r(t + \Delta t) \approx 2r(t) - r(t - \Delta t) + \frac{f(t)}{m}\Delta t^2 + \mathcal{O}(\Delta t^4) \quad (2.30)$$

It is important to note that this new estimate of position contains an error of the order of δt^4 which is dependent on the size of time-step chosen in the simulation. The velocity can then be calculated as follows

$$v(t) = \frac{r(t + \Delta t) - r(t - \Delta t)}{2\Delta t} + \mathcal{O}(\Delta t^2) \quad (2.31)$$

however this is only accurate to the order of δt^2 . In order to get around this large error the Velocity-Verlet algorithm is used [36] where the proceeding coordinate update is expressed as

$$r(t + \Delta t) = r(t) + v(t)\Delta t + \frac{f(t)}{2m}\Delta t^2 \quad (2.32)$$

With the velocity now more accurately given as

$$v(t + \Delta t) = v(t) + \frac{f(t + \Delta t) + f(t)}{2m}\Delta t \quad (2.33)$$

The error in the velocity is now of the order of δt^4 , this method originates from calculating the velocities at time $t + \frac{\Delta t}{2}$ and at $t + \Delta t$.

The most time-consuming part in any MD simulation however is not integrating Newton's equations of motion, it is in fact calculating the forces on each particle with respect to all others, the standard computational tricks for dealing with this are covered in Section 2.3.3.2. Standard MD simulations use the microcanonical ensemble but can also be performed at constant temperature in the canonical or isothermal-isobaric ensembles by coupling to a heat-bath, for a detailed description of statistical ensembles see Section 2.2.1.

2.3.3 Standard Computational Procedures

2.3.3.1 Periodic Boundary Conditions

The primary reason for using periodic boundary conditions is that the number of degrees of freedom in any simulation is limited by the available resources. Even simulations done with today's computing power are still far removed from the thermodynamic limit. Most often periodic boundary conditions are chosen to simulate an infinite bulk surrounding the model system. Without periodic boundary conditions, large errors are introduced due to interfacial effects which dominate system behaviour. For the simplest d -dimensional Ising Model, see Section 2.2.4 this is done by simply wrapping the lattice of spins onto a $(d + 1)$ -dimensional torus so that the last spin in any given row feels the first and *visa versa*, illustrated in Figure 2.4.

This is the same procedure for a simulation of molecules off lattice, any molecule which drifts out of the simulation cell comes back in from the opposite side. Interestingly the correlation length on the periodic lattice is still limited by the finite size of the lattice.

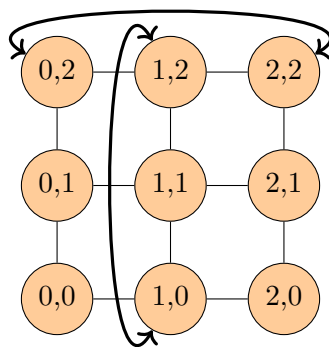


Figure 2.4: Boundary conditions for $d = 2$ Ising Model on a square lattice, arrows indicate periodic interactions across the boundary.

Getting around this problem requires performing finite size scaling as discussed in detail in Section 2.3.3.5.

2.3.3.2 Interaction Potentials

The coarse-grained Shinoda-DeVane-Klein [41] model used in Chapter 6 has recently been demonstrated as a viable model for performing simulations of bulk polyethylene [42] and is described here for reference.

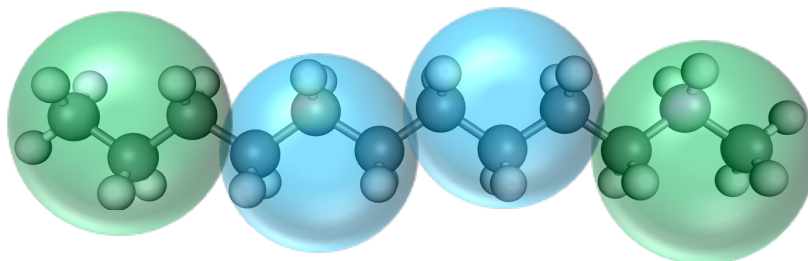


Figure 2.5: Coarse-grained schematic of a single Alkane chain ($C_{12}H_{26}$), blue beads represent terminal groups (CT) and blue central groups (CM).

PE chains are represented by two different types of coarse-grained beads, each bead contains 3 methylene units. In Figure 2.5 the middle blue beads (CM) represent 3 CH_2 units and the green terminal beads (CT) represent $CH_2-CH_2-CH_3$, in this way the terminal beads are parameterised with slightly different values to those of the central

beads. Each bead is connected to its immediate neighbours via harmonic bond potentials of the form

$$U_{bond} = k_{bond}(l - l_0)^2 \quad (2.34)$$

Where U_{bond} is the difference in potential energy as the bond between beads is stretched, k_{bond} is the usual spring constant, l is the bond length at any given point in time and l_0 is the equilibrium length of the bond. In addition every 3 beads interact via a harmonic potential, U_{angle} which represents the change in potential energy resulting from the change bond angle θ from its equilibrium position θ_0 formed by the arrangement of the beads. This can be written as

$$U_{angle} = k_{angle}(\theta - \theta_0)^2 \quad (2.35)$$

where k_{angle} is the angular spring constant. Beads which are not immediate neighbours on the same chain and those from other chains interact via a LJ 9-6 potential of the following form

$$U_{LJ(9-6)} = \frac{27}{4}\tau \left(\left(\frac{\sigma}{r} \right)^9 - \left(\frac{\sigma}{r} \right)^6 \right) \quad r < r_c \quad (2.36)$$

where r is the separation between pairs of beads and τ and σ are parameters which depend on the bead types in any given pair interaction. Values of all parameters for PE can be found in [41, 42] and depend on the mixture of bead types in any given interaction i.e. CM or CT. The potentials used in Chapter 6 are shown in Figure 2.6 for reference.

To make the most efficient use of computation time the short-ranged LJ potential is usually truncated such that interactions with atoms that fall outside a certain cut-off distance r_c are considered negligible. In LAMMPS this is dealt with by using neighbour lists which keep track of nearby particles, reducing the number of atoms when calculating the total potential energy. In [42] the cut-off distance for bulk PE is given to be 15 Å in

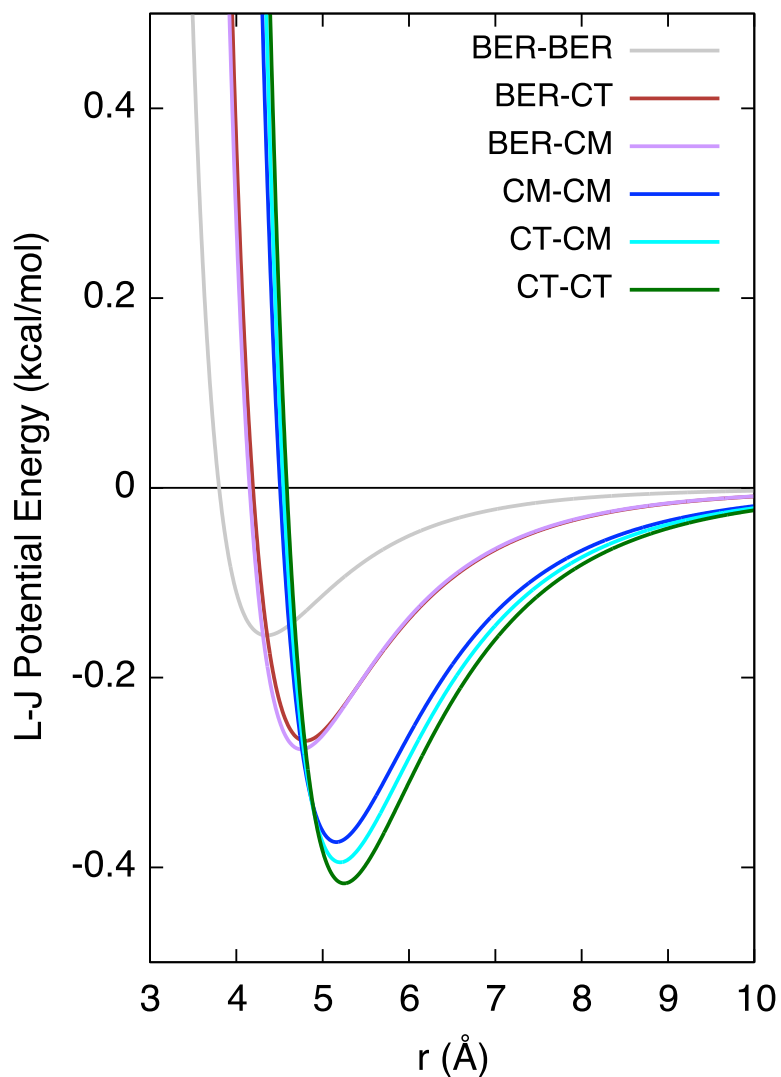


Figure 2.6: Lennard-Jones potential functions for the interactions between all possible bead types. Note CT and CM denote terminal and central coarse-grained beads, BER denotes the coarse-grained graphene beads. The coarse-grained model of graphene was studied previously in [43] and the parameterisation graphene-alkane interactions is taken from [44] for C60 fullerenes in a hydrocarbon (tridecane) melt. The CG-SDK model parameters for polyethylene can be found in [42].

line with the original SDK model [41].

2.3.3.3 Local Order Parameter

The local P_2 order parameter is a measure of the local alignment between atoms (or polymer chains in the case of Figure 2.7) within a given cut-off distance r_c . For an arbitrary bead i , its local P_2 ordering is given by

$$P_2(i) = \frac{1}{N} \sum_{j=1}^N \frac{3 \cos^2 \theta_j - 1}{2}, \quad r \leq r_c \quad (2.37)$$

Where θ_j is the angle between the backbone of bead i with the j th bead inside the cut-off distance and N is the number of neighbouring beads within the cut-off. In the case of Figure 2.7, the angle between bead A and bead B is given by

$$\cos \theta = \frac{\vec{A} \cdot \vec{B}}{|\vec{A}| \cdot |\vec{B}|} \quad (2.38)$$

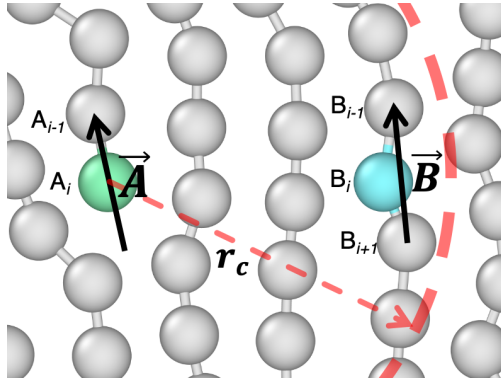


Figure 2.7: Assigning the local crystallinity, P_2 order parameter, of a single coarse-grained bead A_i (green), at the end of chain A with a neighbouring bead B_i (blue) in chain B . For terminal bead A_i its local director is taken as $\vec{A} = A_i - A_{i-1}$ and for the central bead as $\vec{B} = B_{i+1} - B_{i-1}$. The cut-off distance for neighbouring beads r_c is indicated.

In MD simulations of polymers, such as those in Chapter 6 it is useful to identify local crystalline clusters and assign crystallinity to individual atoms.

2.3.3.4 Tensor Order Parameter

In a computer simulation the order parameter may be computed in the following way

$$S = \frac{1}{N} \left\langle \sum_i^N \left(\frac{3}{2} \cos^2 \theta_i \right) - \frac{1}{2} \right\rangle \quad (2.39)$$

where θ_i is the angle of the i th bond vector with the nematic director. The orientation of the nematic director is however already known from theory [45] hence it is more useful to compute instead

$$S' = \frac{1}{N} \left\langle \sum_i^N \left(\frac{3}{2} (\mathbf{n} \cdot \mathbf{u}_i)^2 - \frac{1}{2} \right) \right\rangle \quad (2.40)$$

$$= \frac{1}{N} \sum_i^N \langle \mathbf{n} \cdot \left(\frac{3}{2} \mathbf{u}_i \mathbf{u}_i - \frac{1}{2} \mathbf{I} \right) \cdot \mathbf{n} \rangle \quad (2.41)$$

$$= \frac{1}{N} \sum_i^N \langle \mathbf{n} \cdot \mathbf{Q} \cdot \mathbf{n} \rangle \quad (2.42)$$

where \mathbf{n} is an arbitrary unit vector and $\mathbf{Q}_i = \frac{3}{2} \mathbf{u}_i \mathbf{u}_i - \frac{1}{2} \mathbf{I}$. The tensor order parameter is given by

$$\langle \mathbf{Q} \rangle = \frac{1}{N} \sum_i^N \langle \mathbf{Q}_i \rangle \quad (2.43)$$

and is a traceless symmetric 2nd-rank tensor with three eigenvalues λ_+ , λ_0 and λ_- . The nematic order parameter is defined as the largest positive eigenvalue of $\langle \mathbf{Q} \rangle$ and the true nematic director is its corresponding eigenvector [46, 47].

2.3.3.5 Finite Size Scaling

Section 2.2.5 describes some important scaling relations which are a prerequisite for the understanding of finite size scaling in MC simulations. In the same way we can write the singular part of the free energy in terms of the finite lattice size in a given simulation as [48–50].

$$F(L, T) = L^{-\frac{(2-\alpha)}{\nu}} \mathcal{F}(\tau L^{\frac{1}{\nu}}) \quad (2.44)$$

In this case the exponents assume their infinite values and the argument is given that the correlation length, which diverges as $\tau^{-\nu}$ as the transition is approached, is limited by the finite lattice size. Following the same procedure as before, the scaling relationships can be obtained by appropriate differentiation, this time in terms of the lattice size L instead of the field H .

$$M = L^{-\frac{\beta}{\nu}} M^0(\tau L^{\frac{1}{\nu}}) \quad (2.45)$$

$$\chi = L^{\frac{\gamma}{\nu}} \chi^0(\tau L^{\frac{1}{\nu}}) \quad (2.46)$$

$$C = L^{\frac{\alpha}{\nu}} C^0(\tau L^{\frac{1}{\nu}}) \quad (2.47)$$

Here M^0 , χ^0 and C^0 are scaling functions which reduce to proportionality constants in the vicinity of the phase transition, see [18, 19].

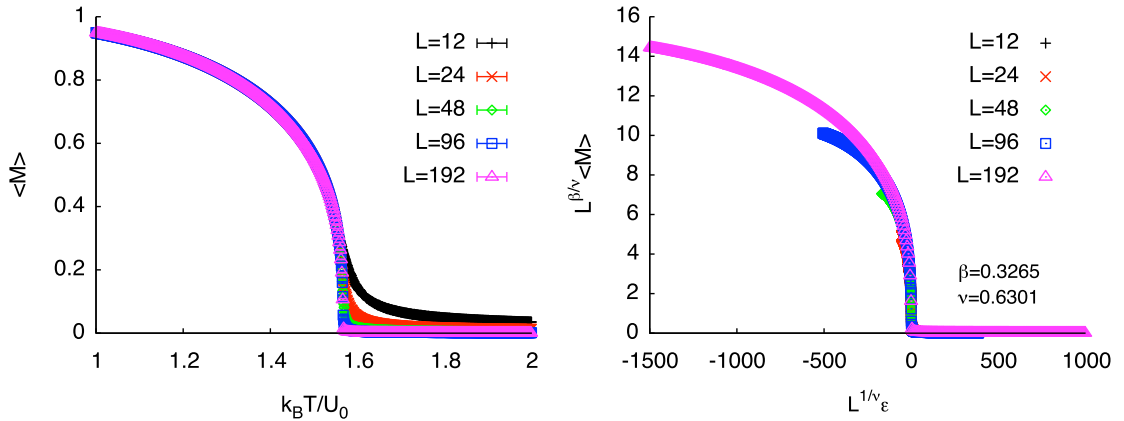


Figure 2.8: Example order parameter (left) and associated scaling plot for a 3d Ising like liquid crystal model system reproduced from [7].

2.3.3.6 Rotational Isomeric State Model

The potential energy of rotating two monomers ($\text{CH}_3\text{-CH}_3$) about their central bond can be approximated by the following, as outlined in [51].

$$E(\theta) = \frac{E^\circ}{2}(1 - \cos 3\theta) \quad (2.48)$$

Where E° is the rotational barrier height and θ is the angle as measured from the staggered form depicted in Figure 2.9 (b). Note however for n-alkanes or other long chain molecules i.e. $\text{CH}_3\text{-CH}_2\text{-CH}_2\text{-CH}_3$, rotation about the central bond presents a different picture, than that of Equation 2.48 since the substitution of a larger group allows for a reduced energy minimum or (trans) state to be favoured at 180° as well as the two minima (gauche \pm) at $\pm 60^\circ$ respectively. A representative picture of the potential energy as a function of rotation angle about the central C-C bond is shown in Figure 2.9 (a), note the Newman projection indicating the position of the C or H atoms as viewed along the central bond. Interestingly these potential energy minima correspond to the torsional angles allowed on a diamond lattice of carbon atoms.

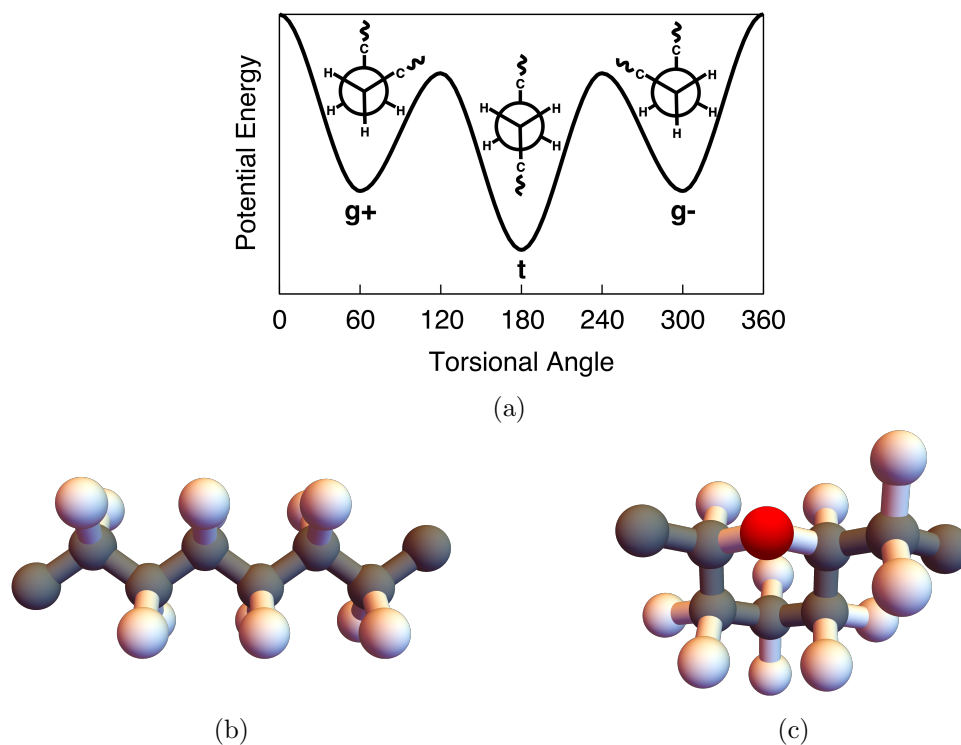


Figure 2.9: (a) Torsional potential energy of C-C bond in n-Alkane chain along with Newman projections illustrating the position of atoms as viewed along the central carbon bond at their respective minima, the curve is representative of the shape only. (b) Minimum energy *tttt* conformation of an isolated Alkane on a diamond lattice. (c) High energy conformation *tg⁻g⁺tg⁻* both disfavoured in reality and forbidden on a diamond lattice, C atoms (black), H atoms (white), H-H conflict (red).

The RIS model is a statistical model which assumes chains may have fixed bond angles in the t, g^+ and g^- states as if the C-C backbone of the chains fit perfectly on a diamond lattice. Note that in this model successive g, g' bonds are disallowed since this results in a H-H conflict between neighbouring monomers along the chain, see Figure 2.9 (c). This configuration is highly disfavoured in real n-alkanes, only occurring at very high temperatures and is forbidden in the coarse-grained model for alkanes on diamond. A number of important statistics can be groomed from this model since it is exactly solvable, via the transfer matrix method which is analogous to the Ising system presented in Section 2.2.4. A detailed account of the RIS model is given in [51] but for our purposes we simply use the coarse-grained representation in Chapter 3 taking into account additional interactions between neighbouring chains.

2.4 Experimental Techniques

In this section we cover the basics of the common experimental techniques used to identify LC phases and determine their structure.

2.4.1 Polarising Optical Microscopy

POM uses polarised light to identify LC phases under the microscope and was first used to study LC's by Lehmann [2]. The basic setup is shown in Figure 2.10 (a) where two crossed polarisers are placed above and below a birefringent sample oriented at 90° to one another. Light passing through the first polariser produces a plane wave which, if uninterrupted when passing through the sample, appears dark through the second polariser. The anisotropy of an LC sample results in birefringent properties which means that the plane polarised light beam passing through the sample is split

into two components polarised perpendicularly to each other. These components are termed the ordinary and extraordinary wavefronts and propagate differently depending on their respective interactions with the sample and are out of phase on their exit. They are recombined with constructive and destructive interference as they move through the second polariser at which point information about the sample may be extracted. Under POM LC's are known for producing beautiful images one of which is shown in Figure 2.10 (b) for a newly synthesised double-tapered ionic Minidendron [52] similar to that studied in Chapter 3.

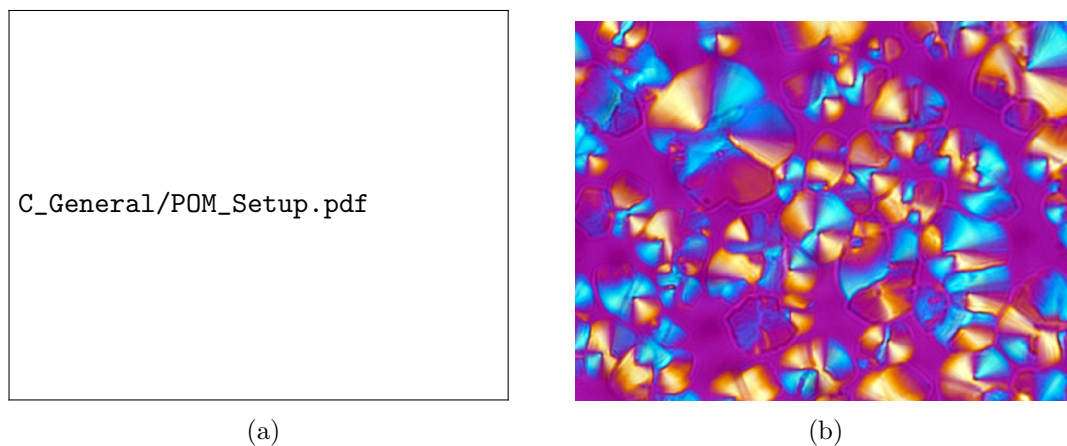


Figure 2.10: (a) Polarising optical microscopy setup reproduced with permission from [53] (b) POM texture of Na of 3,4,5-tris-dodecyloxybenzoic acid, at 93°C, reproduced with permission from [52].

2.4.2 X-ray Diffraction

Bragg's law underpins all modern scattering methods and it can be derived by considering a model system in which an incident wave is scattered by a series of parallel partially reflecting planes. In Figure 2.11 the incident beam \vec{k} is diffracted by the set of parallel planes and its intensity is subsequently controlled by constructive or destructive interference. For a theoretically infinite set of planes, with very small

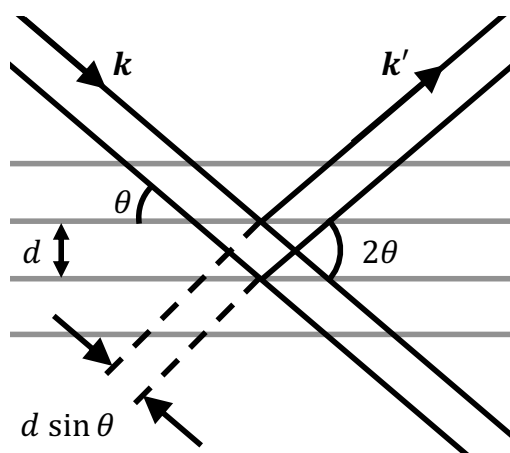
reflective coefficients, the only surviving reflection is one that constructively interferes perfectly with the other waves reflected by each set of neighbouring parallel planes. The different path lengths of the different waves reflected by neighbouring planes, with separation distance d , must be an integral multiple of the wavelength λ , this is neatly summarised by Bragg's law, given by

$$2d \sin \theta = n\lambda \quad (2.49)$$

where n is an integer and θ is as defined in Figure 2.11. Here modern examples of X-ray scattering techniques used to probe the structure of LC samples will be briefly described to aid the reader, for an introduction to scattering methods focused around liquid crystals see [54].

- **SAXS:** A typical SAXS setup uses a monochromatic beam of X-rays incident on a sample with typical wavelengths in the region of 0.07-0.2nm. Sometimes these beams can be delivered from a laboratory source or from a synchrotron, which subsequently provides a much higher flux than laboratory sources. Lab sources produce divergent beams which make separating the weak scattered beam, which contains structural information about the sample, from the strong main beam even more difficult. In labs this problem is moderated by line or point collimation and the primary purpose of using a synchrotron is to provide a more focused beam, to overcome this problem. Crucially with this method a small scattering angle is used such that larger object dimensions can be probed.
- **WAXS:** In WAXS the setup is much the same as that in SAXS except the detector is placed much closer to the sample such that a larger scattering angle can be probed. Both SAXS and WAXS are often performed at the same time.
- **GISAXS/GIWAXS:** In this method the incident beam grazes the sample surface

at such a small angle that the beam mostly undergoes total external reflection. Typically the angle is slightly above the critical angle in order to probe into a thin film sample. Grazing incidence is used to improve the signal of thin films as it decreases the volume contributing to the overall diffraction and in LC thin films the surface alignment is useful in determining the lattice structure and symmetry. This allows the properties of the surface of the sample to be probed and the method was particularly useful in determining the surface activity of LC's in Chapter 4.



(a)



(b)

Figure 2.11: (a) Scattering from parallel planes where d is the plane separation distance and \vec{k} and \vec{k}' are incident and scattered wave vectors respectively. The magnitude of \vec{k} and \vec{k}' is $\frac{2\pi}{\lambda}$ with the path difference waves partially reflected from successive planes given by $2d \sin \theta$. (b) Dr Liliana Cseh stood next to the Xenocs Genix 3d Instrument at Zhejiang Sci-Tech University used to study some of the compounds discussed in Chapter 3.

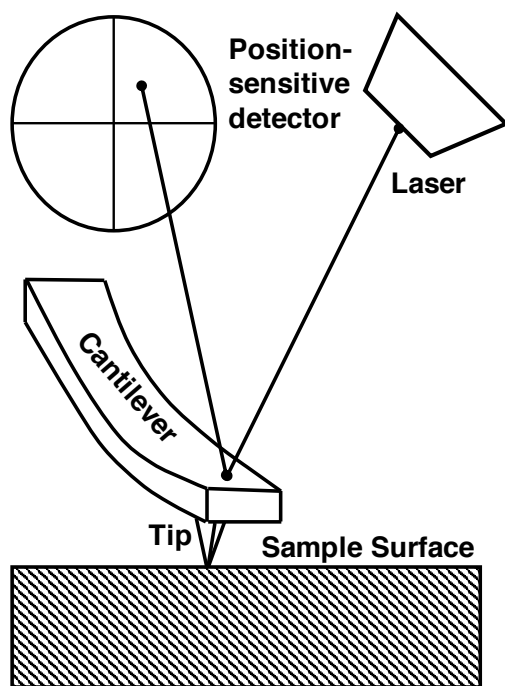
2.4.3 Atomic Force Microscopy

An AFM consists of a sharp cantilever with an atomically sharp probe attached. The probe is brought close to the sample surface, such that forces between the probe and sample can be felt, i.e. VdW, capillary and electrostatic forces. It moves over the surface in an x-y raster format using a feedback loop to keep the separation of the sample and

the tip constant. The changing motion of the cantilever and subsequent output from the feedback loop contains information on the surface topography and is later used to form the surface image corresponding to surface height or cantilever deflection for example. An AFM typically operates on one of 3 different modes:

- **Contact Mode:** The tip is kept in constant contact with the surface, such that forces between the tip and the sample are always repulsive typically of the order of 10^{-9} N. It is then dragged across the surface to build up a picture of the surface by analysing the cantilever deflection in a DC feedback amplifier. This method is usually used where frictional or adhesive-forces are dominant and is not suitable for deformable soft systems.
- **Tapping Mode:** The tip is placed into contact with the surface and then lifted off several times a second to avoid dragging the tip to the next position and potentially damaging the sample. This is implemented by oscillating the cantilever using a piezoelectric crystal near its resonant frequency, usually with an amplitude in the region of 2nm cycling around 50,000 times each second. A feedback loop is used in much the same way as contact mode except the oscillation is now kept constant and the changing oscillation of the cantilever is used to build up a picture of the surface topography. The amplitude can be related to the height of the surface contours and the phase to the softness or viscosity. This is the chosen imaging mode demonstrated in Chapter 6 and is most suitable for imaging polymers adsorbed on surfaces.
- **Non-Contact Mode:** In this mode the tip does not touch the surface, instead it hovers, typically 50-100nm above the surface where attractive VdW forces between the tip and the sample can still be felt. The forces in this mode are much weaker than contact or tapping modes. The tip is given a small AC oscillation and the

change in this oscillation is used to build up a surface picture. It is typically low resolution, for high resolution imaging the tip needs to measure forces which may only extend as far as 1nm above the surface. Often the contaminant liquid layer obstructs this process and the tip becomes lost in the liquid or hovers above it, out of range of the VdW forces of the true surface.



(a)



(b)

Figure 2.12: (a) Basic operation of an AFM (b) AFM used by Dr Ruibin Zhang in the Dept of Materials Science and Engineering at the University of Sheffield, to produce the images of adsorbed alkane monolayers in Chapter 6. Image courtesy of Dr Nic Mullin from the Dept of Physics and Astronomy at the University of Sheffield.

2.5 Computer Simulations of Liquid Crystals and Polymers

The simulation of soft matter simulation is a vast field encompassing many different systems including, liquids, polymers, gels, liquid crystals, biological systems and many more. In this thesis two of these systems, liquid crystals and polymers, are studied. Computational studies of phase transitions in liquid crystals (LC's) and crystallisation in polymers are generally regarded as separate fields. These systems differ crucially in one important aspect in that the former retains some form of order in the liquid/melt state and the latter generally does not. A liquid crystalline system for example may undergo several phase transitions between its crystalline form and isotropic melt whereas polymers do not exhibit this behaviour. Not unless they are used as flexible spacers to join to mesogenic groups. Pure polymers exhibit a phenomenon known as chain folding, due to their long nature, which is unique only to polymers. This allows them to exhibit numerous crystalline phases when subject to differing degrees of undercooling. In Chapters 3 and 4 the focus is understanding phase transitions in thermotropic liquid crystals formed from highly complex mesogens with novel shapes, taper-shaped minidendrons and bolamphiphiles respectively, as opposed to more traditional LCs with rod-like or disc-like shapes which have been well studied computationally. Whereas Chapters 5 and 6 shift the focus onto polymers, specifically crystal growth models and polymers adsorbed on surfaces, which have been less well studied than bulk polymer systems.

Regardless of the chosen system, the most important part of the modelling process is the construction of a model which captures the essential physics. Often each type of model has its own benefits and drawbacks, for example Monte Carlo (MC) simulations either on and off lattice are more suited for studying equilibrium properties as opposed

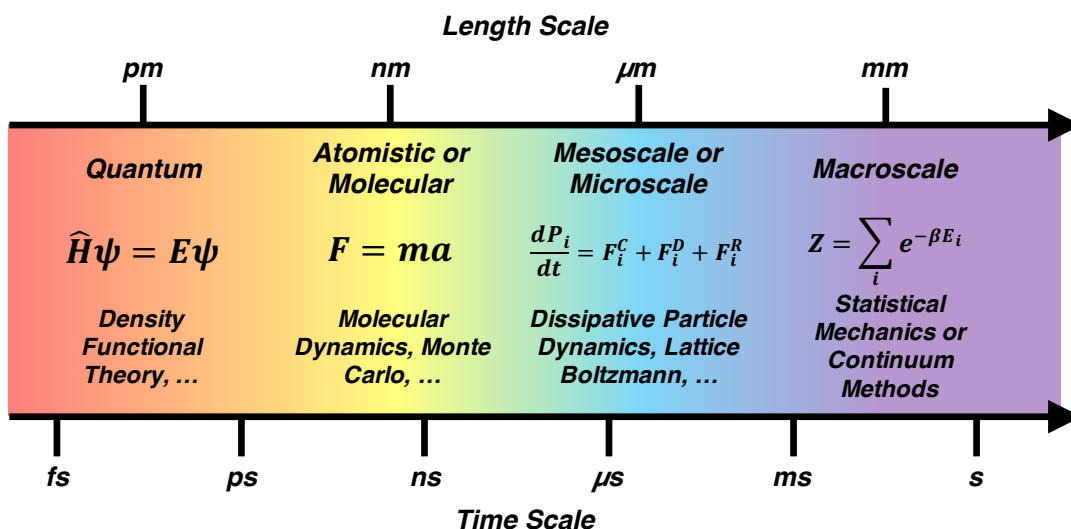


Figure 2.13: Appropriate techniques across different length and timescales.

to dynamics. All atom Molecular Dynamics (MD) simulations may be better suited for studying dynamical properties but are hampered by small system sizes and short timescales due to the number of atoms required. Coarse-grained (CG) models may be used to speed up calculation times but this often comes at the additional cost of losing some of the interesting physics. When choosing a model it is important first to establish what it is that should be calculated, for example equilibrium properties or dynamical ones and which technique is best suited to the time and length scales one wishes to study, see Figure 2.13 for some examples. Quite often many studies will adopt a multi-scaled modelling approach using different techniques on smaller length scales to inform models on large ones and vice versa.

In this section the existing literature in the two areas aforementioned is briefly reviewed. Due to obvious space constraints it is not possible to review both of these exciting areas in their entirety, as such the reader is pointed to several highly cited reviews in the corresponding Sections 2.5.1 and 2.5.2.

2.5.1 Highly Complex Liquid Crystals

Traditional liquid crystals have been well studied computationally and several high-quality review articles already exist including general reviews of LC simulation; most recently by Allen (2019) [55], Zannoni (2018) [56], Maitai (2012) [57], Wilson (2008-2005) [58–60] and Care and Cleaver (2005) [61]. Other more detailed model specific reviews such as those focused on lattice models in particular [46, 62], generic off-lattice models [63, 64] and all atomistic simulations [65, 66] may also be consulted. The topic of LC simulation, particularly for traditional thermotropic calamitic and discotic mesogens, has been well reviewed. Within the last 10-15 years however, perhaps pushed by new model developments and an increase in efficiency and availability of computational resources, compounds with novel shapes have begun to feature more prominently. Note in this thesis lyotropic liquid crystals are not touched upon but some key computational studies of solvated LC's will be mentioned where applicable since modelling solvated systems can inform the coarse-graining methods used in bulk systems.

Beginning with Dendrimers, a very limited number of simulations have been performed. Likely due to the long timescales required to simulate their phase behaviour which, until now, had rendered these problems intractable. This is no more apparent than in some of the earliest MD studies, which although impressive at the time, were limited to production runs of the order of hundreds of picoseconds at fixed temperature in order to study hexagonal columnar phases of discotic mesogens [67, 68] or simply the role of side chains in a single column [69]. Accessing behaviour on nanosecond timescales was simply not feasible, even now coarse-grained simulations prove difficult. Other methods have been employed including, MC lattice models [70, 71], off lattice MC simulations [72], coarse-grained/generic MD simulations [73–76] and mean field models [77] which until now have been limited to studying behaviour in thermodynamic equilibrium such as structural conformational properties, and dynamical behaviour in small systems

over very short timescales. It is only very recently that studying the dynamics of phase transitions in these systems has become accessible for two reasons, firstly rapid developments in coarse-grained modelling, opening up much larger system sizes for study and secondly an increase in computational power and the general availability of HPC resources, since the cost of these systems is much lower than 20 years ago.

To our knowledge there are only two prior studies of the dynamics of phase transitions in thermotropic dendritic systems. In the first [78, 79] coarse-grained MD simulations were employed to model generation 3 dendrimers in bulk and the relation between molecular shape and the symmetry of macroscopic phases. One recalls an earlier much smaller all atomistic study of this type [80], illustrating perfectly how computational advances are allowing this sort of problem to be revisited. In that study the shape of the molecules were modified a priori and equilibrated over short timescales in specific lattices such as BCC, FCC and A15 to find the most efficient packing. In order to modify the shape of the CG dendrimer molecules in this more recent study, an external symmetry breaking potential field was applied, either uniaxially or in a planar fashion. The result is that for a uniaxial field after equilibration the system adopts a Smectic-A or lamella type phase at low temperatures ($T < 500\text{K}$) which transforms into a cubic phase on heating, in the planar case an hexagonal columnar phase is formed and transitions to an isotropic phase at around 500K. What is interesting is that depending on the applied field both phases are stable in the specified temperature range. Assessing which one is thermodynamically stable requires free energy calculations which are not possible computationally at present, although some success has been had in other areas [81]. It will be interesting to see developments in the near future on how this work evolves and it is worth noting that a number of earlier works in lyotropic systems contributed towards these studies [82, 83].

In the second study [84], that is perhaps closest to the work carried out in Chapter 3,

taper-shaped minidendrons were studied using a CG generic representation and with 3 atom types for the attractive H groups (alkali metals), more weakly attracting π - π interactions and mutually repulsive terminal chains. Interactions between unlike bead groups were all taken to be repulsive. This is to date the closest example to the work carried out in Chapter 3. In this case the system was prepared in an isotropic phase and quenched to different temperatures at different pressures in order to map out the phase diagram. The hexagonal columnar phase is formed first, which moves onto a BCC phase, to an unseen supramolecular sphere fluid and then finally to an isotropic melt. It is known from experiment that the phase diagram for these molecules is far richer than that. Slight changes in the attractive head groups as well as increasing the chain length drastically alter the phase behaviour in these molecules. It would be interesting to see how this work progresses, for example how changing the size of the attractive group at the apex and the length of the terminal chains influences the phase diagram. No further studies have since been reported. What is obvious from these cutting edge pieces of work is that we are still some way off studying first-order transitions between columnar phases in MD simulations of minidendrons. Hence in Chapter 3 we choose to model this unusual transition using a lattice model theory which is solved self-consistently using parameters informed by both coarse-grained simulations and experiment.

Whereas dendrimers may seem like old hat to some, bolamphiphiles are a new branch of compounds which have only recently been synthesised and computational studies of them have therefore been limited to the last 10 years. In fact there are no computational studies of these systems prior to 2008. Thus far, lattice models, coarse-grained MD and dissipative particle dynamics simulations (DPD) have been employed to study both the equilibrium and dynamical behaviour of these systems. Specifically T-shaped and X-shaped examples of these compounds have been studied. One of the earliest studies [85] reports a coarse-grained (CG) MD simulation using a generic model and

without considering specific chemical details, were able to quantitatively reproduce the experimental behaviour. This demonstrated that retaining specific details such as a rigid rod with attractive sticky ends and a chain attached laterally with repulsive interactions was sufficient to induce the ordering observed in experiment. However tuning the model to a specific chemistry of real bolamphiphiles was not performed. Shortly after DPD was employed to study X-shaped compounds with a similar generic CG model [86] but crucially with miscible and immiscible side chains. It was found that molecules with compatible side chains formed square or hexagonal phases but when incompatible phase separate into multi-color tilings. This is particularly interesting for hexagonal phases since the side chains can never fully phase segregate and are frustrated. It is interesting to note that the 3-colour hexagonal tiling was only stable for a very small range of parameters, specifically when interactions of both arms are symmetric, this has still not been observed experimentally. This equilibrium ordering phenomena of this frustrated system has also been studied using lattice model MC and also predicted the existence of a 3-colour phase [87].

The effects of changing the length of the side chains had not been studied until a recent DPD study of T-shaped compounds with variable chain lengths [88]. Which demonstrated that extending the length of the side chains leads to the formation of a pentagonal phase preceding the hexagonal phase but crucially with non-uniform pentagons, i.e. pentagons with 2 distinct vertex angles. The effect of tuning the backbone length in T-shaped molecules was then studied using a generic model in [89], where it was found that changing the backbone length “on the fly” allowed for the bilayer sheets, square, hexagonal and pentagonal phases to reversibly transform to one another. This essentially has the same effect as fixing the backbone lengths and varying the length of the side chains. Bates published an early review on this topic [90]. Further DPD studies [91] then investigated the effect of replacing the “sticky” terminal beads with alkane

chains which are crucially incompatible with the laterally attached oligo(oxyethylene) spacer and polar group in reality. Here the effect of varying the length of the laterally attached chain leads to novel LC phases, including polygonal phases aforementioned and cubic gyroid phase. The effect of branching the side chains into a “swallow-tail” has also recently been studied by computer simulation [92] and under confinement in a cylindrical carbon nanotube [93]. Simulations of X-shaped molecules with incompatible side chains as well as different lengths however remain unstudied by computer simulations, recent experiments have reported the discovery of snub-square tilings for example [94] and even quasi-periodic tilings [95]. This ordering phenomena of X-shaped molecules with incompatible side chains is studied in Chapter 4.

It is worth mentioning other studies of complex LC phases that have also appeared including bent-core mesogens [96, 97] and chiral compounds [98] however they are not relevant to the work carried out in this thesis.

2.5.2 Polymers

Polymeric systems remain an important topic to study since their use is abundant throughout our everyday lives and would look quite different without them. Simulations of polymers are vital in order to understand the complexity of the vast number of synthetic and naturally occurring polymers and improve the formulation of manufactured products. Several general reviews of polymer simulations already exist [99–101], covering techniques such as MC methods [102, 103], MD simulations, DPD [104] and multi-scale modelling in general [105]. There are several other reviews focused on simulations of specific topics such as polymer crystallisation [106], gels [107], amorphous polymers [108], polymers for use in drug delivery [109], elastomers [110], nano-composites [107] and many more besides [111, 112]. However very few reviews exist covering simulations

of polymers adsorbed on surfaces or near interfaces [113, 114], a useful text by Jones (1999) is also recommended which covers this topic extensively [115]. It is clear that this rich area of soft matter simulation is immense and so to avoid getting lost let us focus on the two key areas touched upon in this thesis, simulations of polymer crystallisation in general and of n-alkanes (model polymers) and their special relationship when adsorbed on graphite. It is important to note, polymer crystallisation has been extensively studied and the reader is pointed to several reviews on this important topic [106, 116, 117], only some select and very recent works will be covered in what follows.

Beginning with polymer crystallisation, this field may be subdivided into 4 key mechanisms which induce crystallisation. Firstly how polymers solidify from the melt phase, which may include the nucleation process itself or the growth following after the initial nucleation barrier has been overcome. This thesis is primarily focused in this area, specifically on polypropylene or polyethylene. It is probably the most saturated part of the field and a huge variety of computational techniques have been used to study this, including MD/MC simulations using all atom representations [118–125] as well as coarse-grained ones [42, 126–129], MC lattice models [130, 131] and continuum approaches [129, 132, 133]. Crystallisation may be induced through other means such as deforming or shearing [134–138] i.e. in injection moulding or extrusion processes, from solution via evaporation or precipitation [139, 140] and finally under confinement, which encompasses surface effects [141] often drastically altering crystalline properties.

In general, computational studies of n-alkanes adsorbed on graphite substrates have been restricted to small alkanes with lengths less than 60 carbon atoms, with a few exceptions all using united atom (all atomistic) models. The reason for this is because of the special relationship between the graphite substrate and the similar bond length in alkanes. On that note it is worth thinking about the chosen method in Chapter 6 which uses coarse-grained representation as opposed to an all atom representation. This

method is chosen because it is easier to simulate larger system (i.e. multiple lamellae) over longer timescales with such a model and because this study is focused on the large scale melting behaviour of ultra-long n-alkanes when adsorbed on graphite. As will become clear modelling a few hundred alkanes that are 120 carbons long using an all atomistic representation is already pushing the limits of what is reliable. For example in one of the earliest studies [142] a monolayer of $C_{32}H_{66}$ alkanes were studied by all atomistic MD simulation on graphite using a united atom approach. The system size in this case was limited to a few molecules. It was shown that simultaneous intermolecular and intramolecular disordering was occurring at the melting point indicating the presence of a phase transition in the monolayer.

A number of years later simulations of larger alkanes up to ($C_{400}H_{802}$) were performed in a two-part study [143, 144], where a graphite substrate interacts with a strictly mono-disperse polyethylene melt. It is worth noting that in this study although it is claimed $C_{400}H_{802}$ is studied the results are not shown and the system size is incredibly small (40 molecules). In this case not only is the region in which the monolayer exists examined but also 4 further distinct regions above it. For example the mass density and nematic (P2) ordering as a function of distance from the substrate were also studied and even though they claim that the P2 results should be treated with “extreme caution” there are clear distinct layers in which the order drops successively towards that of the melt. This is apparent not just in alkanes adsorbed on surfaces but for polymers adsorbed on surfaces in general. The local conformations of the chains in the distinct layers were also studied (trains, loop and tail) and it was seen that the shortest alkanes have a tendency to adsorb fully onto the substrate with train and tail conformations fully dominating in the adsorbed layers. Those longer chains with number of carbons greater than 78 did not exhibit this behaviour with the probability of all train conformations being negligible. Dynamical properties were also studied including

mobility and long-time diffusive properties. It is seen that the mobility of atoms in the first adsorbed layer is considerably slower than the bulk whereas the opposite is true at the vacuum interface where the mobility attains higher values than that of the bulk. It is worth noting that mobility is faster in the x-y plane than in the z-direction. Similar phenomena have been observed in Chapter 6.

The effect of substrate interaction strength on the adsorption of undecane $C_{11}H_{24}$ was then studied using all atomistic MD simulations, using a united atom approach [145]. It was found that the weaker substrates facilitated a perpendicular alignment of chains (standing up) as opposed to parallel alignment with a more strongly attractive substrate. The effect of film thickness was also probed and it was found that in thicker layers the perpendicular morphology was preferred with parallel alignments being preferred in the thinner layers. This study was however limited by system size and timescales considered. Another studies $C_{24}H_{50}$ (tetracosane) monolayers on graphite [146], using a united atom model and highlights the importance of tuning the non-bonded interactions with great care and that when chosen correctly, the smectic phase appears in good agreement with the experimentally observed behaviour. This was then extended in [147] whereby the molecular length was increased to $C_{32}H_{66}$ with similar results forming smectic phases in both cases. Height profiles generally showed that the atoms are confined to within the first layer as is known from earlier simulations. One of the first MD simulations to successfully reproduce the experimentally observed melting behaviour was that of [148] in which 104 C_6H_{14} (hexane) molecules adsorbed as monolayers adsorbed on graphite. Crucially a strong reliance between the structure factor of the molecules and the melting temperature was demonstrated. This motivated a further study [149] where an interesting observation was made in that the scaling factor of the non-bonded electrostatic interactions, often assumed without justification, plays a sensitive role in the molecular stiffness and ability of the molecules to deform. Since melting of alkanes is

primarily driven by internal deformation of the molecules and an increasing number of gauche defects it is crucial that this be tuned correctly. It was discovered that scaling factor must decrease as chain length increases, approaching zero for chain lengths greater than 50 carbons. Still all atomistic models at this point have been either able to provide statistics on large system sizes on short timescales or small system sizes on large timescales but not both.

More recent studies have been able to simulate much larger systems over much larger timescales. For example in [150] large scale simulations of 336 $C_{50}H_{102}$ adsorbed as a monolayer on graphite were performed using a united atom approach for a few hundred nanoseconds. In this study the monolayers appeared to form multiple layers and did not fully wet the graphene surface as observed experimentally, this is likely due to a weaker graphene-alkane interaction than in reality. Furthermore the effect of chain length on the preferred orientation of n-alkanes on graphite was studied in [151] in that shorter alkanes prefer a perpendicular alignment and vice versa for longer alkanes. Unfortunately studies of ultra-long n-alkanes are non-existent. In Chapter 6 an extensively developed coarse-grained model of bulk polyethylene [42, 126, 128] is employed to study the melting behaviour of 1800 $C_{390}H_{782}$ alkanes adsorbed on graphene, taking parameterisations from previous studies as a guide [41, 43, 44]. This would correspond to well over 2 million individual atoms in an all atom representation.

In this section, simulations of LCs and polymers have been introduced. Computational studies of LCs therein of dendrimers, bolamphiphiles and other dense highly-structured phases and polymers including polymer crystallisation and model polymers adsorbed in graphite/graphene have been discussed. It is hoped that this overview will provide future graduate students with a useful beginners resource when embarking on studying liquid crystalline and polymeric systems. It will be exciting to see how in the future computational advances will render problems, in the modelling of soft matter systems

in general, more tractable.

Bibliography

- [1] F. Reinitzer. *Monatshefte für Chemie/Chemical Monthly*, 9(1):421–441, 1888.
- [2] O. Lehmann. *Zeitschrift für Physikalische Chemie*, 4:462, 1889.
- [3] M. G. Friedel. *The mesomorphic states of matter*. US Army Engineer Research and Development Laboratories, 1967.
- [4] P.-G. De Gennes and J. Prost. *The physics of liquid crystals*, volume 83. Oxford university press, 1993.
- [5] W. S. Fall, M.-H. Yen, X. Zeng, L. Cseh, Y. Liu, G. A. Gehring, and G. Ungar. *Soft Matter*, 15(1):22–29, 2019.
- [6] S. Chandrasekhar, B. Sadashiva, and K. Suresh. *pramana*, 9(5):471–480, 1977.
- [7] W. S. Fall, C. Nürnberger, X. Zeng, F. Liu, S. J. Kearney, G. A. Gehring, C. Tschierske, and G. Ungar. *Molecular Systems Design & Engineering*, 4(2):396–406, 2019.
- [8] S. P. Sreenilayam, V. P. Panov, J. K. Vij, and G. Shanker. *Liquid Crystals*, 44(1):244–253, 2017.
- [9] K. Huang. *Introduction to statistical physics*. Chapman and Hall/CRC, 2009.
- [10] E. Ising. *Z. Phys.*, 31:253–258, 1925.
- [11] R. Peierls. On ising’s model of ferromagnetism. In *Mathematical Proceedings of the*

Cambridge Philosophical Society, volume 32, pages 477–481. Cambridge University Press, 1936.

- [12] H. A. Kramers and G. H. Wannier. *Physical Review*, 60(3):252, 1941.
- [13] L. Onsager. *Physical Review*, 65(3-4):117, 1944.
- [14] H. E. Stanley. *Phase transitions and critical phenomena*. Clarendon Press, Oxford, 1971.
- [15] M. E. Fisher. *Reviews of Modern Physics*, 46(4):597, 1974.
- [16] M. Hasenbusch. *Physical Review B*, 82(17):174433, 2010.
- [17] J. M. Yeomans. *Statistical mechanics of phase transitions*. Clarendon Press, 1992.
- [18] M. Newman and G. Barkema. *Monte Carlo methods in statistical physics chapter 1-4*. Oxford University Press: New York, USA, 1999.
- [19] K. Binder, D. M. Ceperley, J.-P. Hansen, M. Kalos, D. Landau, D. Levesque, H. Mueller-Krumbhaar, D. Stauffer, and J.-J. Weis. *Monte Carlo methods in statistical physics*, volume 7. Springer Science & Business Media, 2012.
- [20] H. B. Callen and T. A. Welton. *Physical Review*, 83(1):34, 1951.
- [21] R. Kubo. *Journal of the Physical Society of Japan*, 12(6):570–586, 1957.
- [22] R. Kubo. *Reports on progress in physics*, 29(1):255, 1966.
- [23] M. M. Waldrop. *Nature News*, 530(7589):144, 2016.
- [24] H. Markram. *Scientific American*, 306(6):50–55, 2012.

- [25] C. H. Museum. Los alamos scientists Paul Stern (left) and Nick Metropolis playing chess with the maniac computer, 1951.
- [26] A. Herbert. *Los Alamos Science, Fall*, 1986.
- [27] N. Metropolis, A. W. Rosenbluth, M. N. Rosenbluth, A. H. Teller, and E. Teller. *The Journal of Chemical Physics*, 21(6):1087–1092, 1953.
- [28] R. J. Glauber. *Journal of Mathematical Physics*, 4(2):294–307, 1963.
- [29] K. Kawasaki. *Physical Review*, 145(1):224, 1966.
- [30] U. Wolff. *Nuclear Physics B-Proceedings Supplements*, 17:93–102, 1990.
- [31] C. M. Fortuin and P. W. Kasteleyn. *Physica*, 57(4):536–564, 1972.
- [32] R. H. Swendsen and J.-S. Wang. *Physical review letters*, 58(2):86, 1987.
- [33] U. Wolff. *Physical Review Letters*, 62(4):361, 1989.
- [34] K. Langfeld, B. Lucini, R. Pellegrini, and A. Rago. *The European Physical Journal C*, 76(6):306, 2016.
- [35] J. E. Lennard-Jones. *Proc. Roy. Soc. A*, 106:463–477, 1924.
- [36] W. C. Swope, H. C. Andersen, P. H. Berens, and K. R. Wilson. *The Journal of Chemical Physics*, 76(1):637–649, 1982.
- [37] D. Frenkel and B. Smit. *Understanding molecular simulation: from algorithms to applications*, volume 1. Elsevier, 2001.
- [38] M. P. Allen and D. J. Tildesley. *Computer simulation of liquids*. Oxford university press, 2017.

- [39] S. Plimpton. *Journal of Computational Physics*, 117(1):1–19, 1995.
- [40] L. Verlet. *Physical review*, 159(1):98, 1967.
- [41] W. Shinoda, R. DeVane, and M. L. Klein. *Molecular Simulation*, 33(1-2):27–36, 2007.
- [42] K. W. Hall, T. W. Sirk, M. L. Klein, and W. Shinoda. *The Journal of Chemical Physics*, 150(24):244901, 2019.
- [43] R. DeVane, M. L. Klein, C.-c. Chiu, S. O. Nielsen, W. Shinoda, and P. B. Moore. *The Journal of Physical Chemistry B*, 114(19):6386–6393, 2010.
- [44] C.-c. Chiu, R. DeVane, M. L. Klein, W. Shinoda, P. B. Moore, and S. O. Nielsen. *The Journal of Physical Chemistry B*, 114(19):6394–6400, 2010.
- [45] R. Eppenga and D. Frenkel. *Molecular Physics*, 52(6):1303–1334, 1984.
- [46] G. Luckhurst and G. W. Gray. *The molecular physics of liquid crystals*. Academic press, 1979.
- [47] R. D. Mountain and T. W. Ruijgrok. *Physica A: Statistical Mechanics and its Applications*, 89(3):522–538, 1977.
- [48] V. Privman. *Finite size scaling and numerical simulation of statistical systems*. World Scientific Singapore, 1990.
- [49] K. Binder. Finite size effects at phase transitions. In *Computational methods in field theory*, pages 59–125. Springer, 1992.
- [50] M. Fisher. *Lecture Notes in Physics*, 186(1), 1971.

- [51] P. J. Flory and M. Volkenstein. *Biopolymers: Original Research on Biomolecules*, 8(5):699–700, 1969.
- [52] Y.-X. Li, F.-F. Fan, J. Wang, L. Cseh, M. Xue, X.-B. Zeng, and G. Ungar. *Chemistry—A European Journal*, 25(60):13739–13747, 2019.
- [53] N. I. I. MicroscopyU. Polarized light microscopy, 2020.
- [54] P. M. Chaikin, T. C. Lubensky, and T. A. Witten. *Principles of condensed matter physics*, volume 10. Cambridge university press Cambridge, 1995.
- [55] M. P. Allen. *Molecular Physics*, 117(18):2391–2417, 2019.
- [56] C. Zannoni. *Liquid Crystals*, 45(13-15):1880–1893, 2018.
- [57] P. K. Maiti, V. A. Kumar, and K. Ayappa. *Journal of the Indian Institute of Science*, 89(2):229–241, 2012.
- [58] M. R. Wilson. *International Reviews in Physical Chemistry*, 24(3-4):421–455, 2005.
- [59] M. R. Wilson. *Chemical Society Reviews*, 36(12):1881–1888, 2007.
- [60] M. R. Wilson. Computer simulations of soft self-organising molecular materials. In *AIP Conference Proceedings*, volume 979, pages 166–177. American Institute of Physics, 2008.
- [61] C. Care and D. Cleaver. *Reports on progress in physics*, 68(11):2665, 2005.
- [62] P. Pasini, C. Chiccoli, and C. Zannoni. Liquid crystal lattice models i. bulk systems. In *Advances in the Computer Simulations of Liquid Crystals*, pages 99–119. Springer, 2000.
- [63] D. Frenkel. *Computer Physics Communications*, 44(3):243–253, 1987.

- [64] M. P. Allen. *Philosophical Transactions of the Royal Society of London. Series A: Physical and Engineering Sciences*, 344(1672):323–337, 1993.
- [65] C. M. M. R. W. Judith and A. HOWARD. *Molecular Physics*, 93(6):955–964, 1998.
- [66] M. R. Wilson. Atomistic simulations of liquid crystals. In *Liquid Crystals I*, pages 41–64. Springer, 1999.
- [67] I. Ono and S. Kondo. *Bulletin of the Chemical Society of Japan*, 65(4):1057–1061, 1992.
- [68] A. Maliniak. *The Journal of Chemical Physics*, 96(3):2306–2317, 1992.
- [69] F. M. Mulder, J. Stride, S. J. Picken, P. H. Kouwer, M. P. de Haas, L. D. Siebbeles, and G. J. Kearley. *Journal of the American Chemical Society*, 125(13):3860–3866, 2003.
- [70] M. L. Mansfield and L. I. Klushin. *Macromolecules*, 26(16):4262–4268, 1993.
- [71] M. L. Mansfield. *Polymer*, 35(9):1827–1830, 1994.
- [72] Z. Y. Chen and S.-M. Cui. *Macromolecules*, 29(24):7943–7952, 1996.
- [73] M. Murat and G. S. Grest. *Macromolecules*, 29(4):1278–1285, 1996.
- [74] K. Karatasos, D. Adolf, and G. Davies. *The Journal of Chemical Physics*, 115(11):5310–5318, 2001.
- [75] P. K. Maiti, T. Çam, S.-T. Lin, and W. A. Goddard. *Macromolecules*, 38(3):979–991, 2005.
- [76] C. N. Likos. *Soft Matter*, 2(6):478–498, 2006.

- [77] D. Boris and M. Rubinstein. *Macromolecules*, 29(22):7251–7260, 1996.
- [78] J. Ilnytskyi, J. Lintuvuori, and M. R. Wilson. *Condensed Matter Physics*, 2010.
- [79] J. Ilnytskyi. Self-assembly of nanoparticles decorated by liquid crystalline groups: Computer simulations. In *Self-Assembly of Nanostructures*. IntechOpen, 2020.
- [80] Y. Li, S.-T. Lin, and W. A. Goddard. *Journal of the American Chemical Society*, 126(6):1872–1885, 2004.
- [81] F. J. Martínez-Veracoechea and F. A. Escobedo. *The Journal of Chemical Physics*, 125(10):104907, 2006.
- [82] M. R. Wilson, J. M. Ilnytskyi, and L. M. Stimson. *The Journal of Chemical Physics*, 119(6):3509–3515, 2003.
- [83] V. Percec, D. A. Wilson, P. Leowanawat, C. J. Wilson, A. D. Hughes, M. S. Kaucher, D. A. Hammer, D. H. Levine, A. J. Kim, F. S. Bates, et al. *Science*, 328(5981):1009–1014, 2010.
- [84] A. J. Crane and E. A. Müller. *Soft Matter*, 7(16):7465–7476, 2011.
- [85] A. J. Crane, F. J. Martínez-Veracoechea, F. A. Escobedo, and E. A. Müller. *Soft Matter*, 4(9):1820–1829, 2008.
- [86] M. Bates and M. Walker. *Soft Matter*, 5(2):346–353, 2009.
- [87] S. George, C. Bentham, X. Zeng, G. Ungar, and G. A. Gehring. *Physical Review E*, 95(6):062126, 2017.
- [88] M. A. Bates and M. Walker. *Molecular Crystals and Liquid Crystals*, 525(1):204–211, 2010.

- [89] T. D. Nguyen and S. C. Glotzer. *ACS nano*, 4(5):2585–2594, 2010.
- [90] M. A. Bates and M. Walker. *Liquid Crystals*, 38(11-12):1749–1757, 2011.
- [91] X. Liu, K. Yang, and H. Guo. *The Journal of Physical Chemistry B*, 117(30):9106–9120, 2013.
- [92] Y. Sun, P. Padmanabhan, M. Misra, and F. A. Escobedo. *Soft Matter*, 13(45):8542–8555, 2017.
- [93] Q.-Y. Wu, W.-d. Tian, and Y.-q. Ma. *The Journal of Physical Chemistry B*, 121(38):8984–8990, 2017.
- [94] C. Nürnberger, H. Lu, X. Zeng, F. Liu, G. Ungar, H. Hahn, H. Lang, M. Prehm, and C. Tschierske. *Chemical Communications*, 55(29):4154–4157, 2019.
- [95] M. Poppe, C. Chen, S. Poppe, F. Liu, and C. Tschierske. *Communications Chemistry*, 3(1):1–8, 2020.
- [96] P. J. Camp, M. P. Allen, and A. J. Masters. *The Journal of Chemical Physics*, 111(21):9871–9881, 1999.
- [97] S. M. Shamid, S. Dhakal, and J. V. Selinger. *Physical Review E*, 87(5):052503, 2013.
- [98] R. Memmer. *Liquid Crystals*, 27(4):533–546, 2000.
- [99] T. E. Gartner III and A. Jayaraman. *Macromolecules*, 52(3):755–786, 2019.
- [100] S. C. Glotzer and W. Paul. *Annual Review of Materials Research*, 32(1):401–436, 2002.
- [101] D. N. Theodorou. *Chemical Engineering Science*, 62(21):5697–5714, 2007.

- [102] K. Binder and M. Müller. *Current opinion in colloid & interface science*, 5(5-6):314–322, 2000.
- [103] A. Panagiotopoulos. *Fluid Phase Equilibria*, 76:97–112, 1992.
- [104] R. D. Groot and P. B. Warren. *The Journal of Chemical Physics*, 107(11):4423–4435, 1997.
- [105] K. Kremer and F. Müller-Plathe. *Molecular Simulation*, 28(8-9):729–750, 2002.
- [106] T. Yamamoto. *Polymer*, 50(9):1975–1985, 2009.
- [107] A. Karatrantos, N. Clarke, and M. Kröger. *Polymer reviews*, 56(3):385–428, 2016.
- [108] M. Kotelyanskii. *Trends in Polymer Science*, 5(6):192–197, 1997.
- [109] S. M. Loverde. *Molecular Simulation*, 40(10-11):794–801, 2014.
- [110] K. C. Jha and M. Tsigie. *Rubber Chemistry and Technology*, 86(3):401–422, 2013.
- [111] C. Li and A. Strachan. *Journal of Polymer Science Part B: Polymer Physics*, 53(2):103–122, 2015.
- [112] L. Levi, V. Raim, and S. Srebnik. *Journal of Molecular Recognition*, 24(6):883–891, 2011.
- [113] J. Baschnagel, H. Meyer, F. Varnik, S. Metzger, M. Aichele, M. Müller, and K. Binder. *Interface Science*, 11(2):159–173, 2003.
- [114] I. Szleifer. *Current Opinion in Colloid & Interface Science*, 1(3):416–423, 1996.
- [115] R. A. L. Jones. *Polymers at surfaces and interfaces*. Cambridge University Press, 1999.

- [116] N. Waheed, M. J. Ko, and G. C. Rutledge. Atomistic simulation of polymer melt crystallization by molecular dynamics. In *Progress in Understanding of Polymer Crystallization*, pages 457–480. Springer, 2007.
- [117] M. Hütter, G. C. Rutledge, et al. Monte carlo simulations of semicrystalline polyethylene: Interlamellar domain and crystal-melt interface. In *Progress in Understanding of Polymer Crystallization*, pages 261–284. Springer, 2007.
- [118] P. Yi, C. R. Locker, and G. C. Rutledge. *Macromolecules*, 46(11):4723–4733, 2013.
- [119] T. Yamamoto. *The Journal of Chemical Physics*, 107(7):2653–2663, 1997.
- [120] N. Wentzel and S. T. Milner. *The Journal of Chemical Physics*, 132(4):044901, 2010.
- [121] M. Hütter, P. J. in't Veld, and G. C. Rutledge. *Polymer*, 47(15):5494–5504, 2006.
- [122] N. Waheed, M. Lavine, and G. Rutledge. *The Journal of Chemical Physics*, 116(5):2301–2309, 2002.
- [123] K. Esselink, P. Hilbers, and B. Van Beest. *The Journal of Chemical Physics*, 101(10):9033–9041, 1994.
- [124] C. Luo and J.-U. Sommer. *Macromolecules*, 44(6):1523–1529, 2011.
- [125] J. J. de Pablo, M. Laso, and U. W. Suter. *The Journal of Chemical Physics*, 96(3):2395–2403, 1992.
- [126] K. W. Hall, T. W. Sirk, S. Percec, M. L. Klein, and W. Shinoda. *The Journal of Chemical Physics*, 151(14):144901, 2019.

- [127] K. W. Hall, T. W. Sirk, S. Percec, M. L. Klein, and W. Shinoda. *Polymers*, 12(2):447, 2020.
- [128] K. W. Hall, S. Percec, and M. L. Klein. *The Journal of Chemical Physics*, 150(11):114901, 2019.
- [129] S. Whitlam, Y. R. Dahal, and J. D. Schmit. *The Journal of Chemical Physics*, 144(6):064903, 2016.
- [130] W. Hu, D. Frenkel, and V. B. Mathot. *Macromolecules*, 36(21):8178–8183, 2003.
- [131] P. G. Higgs and G. Ungar. *The Journal of Chemical Physics*, 100(1):640–648, 1994.
- [132] M. Muthukumar. *Philosophical Transactions of the Royal Society of London. Series A: Mathematical, Physical and Engineering Sciences*, 361(1804):539–556, 2003.
- [133] S. T. Milner. *Soft Matter*, 7(6):2909–2917, 2011.
- [134] S. T. Milner and J. D. Newhall. *Physical review letters*, 105(20):208302, 2010.
- [135] M. J. Ko, N. Waheed, M. S. Lavine, and G. C. Rutledge. *The Journal of Chemical Physics*, 121(6):2823–2832, 2004.
- [136] M. S. Lavine, N. Waheed, and G. C. Rutledge. *Polymer*, 44(5):1771–1779, 2003.
- [137] R. S. Graham and P. D. Olmsted. *Physical review letters*, 103(11):115702, 2009.
- [138] D. A. Nicholson and G. C. Rutledge. *Polymer*, page 122605, 2020.
- [139] P. Welch and M. Muthukumar. *Physical review letters*, 87(21):218302, 2001.

- [140] C.-M. Chen and P. G. Higgs. *The Journal of Chemical Physics*, 108(10):4305–4314, 1998.
- [141] W. Zhang, E. D. Gomez, and S. T. Milner. *Macromolecules*, 49(3):963–971, 2016.
- [142] F. Y. Hansen, K. Herwig, B. Matthies, and H. Taub. *Physical review letters*, 83(12):2362, 1999.
- [143] V. A. Harmandaris, K. C. Daoulas, and V. G. Mavrantzas. *Macromolecules*, 38(13):5796–5809, 2005.
- [144] K. C. Daoulas, V. A. Harmandaris, and V. G. Mavrantzas. *Macromolecules*, 38(13):5780–5795, 2005.
- [145] T. Yamamoto, K. Nozaki, A. Yamaguchi, and N. Urakami. *The Journal of Chemical Physics*, 127(15):154704, 2007.
- [146] L. Firlej, B. Kuchta, M.-W. Roth, M. Connolly, and C. Wexler. *Langmuir*, 24(21):12392–12397, 2008.
- [147] A. Diama, B. Matthies, K. Herwig, F. Y. Hansen, L. Criswell, H. Mo, M. Bai, and H. Taub. *The Journal of Chemical Physics*, 131(8):084707, 2009.
- [148] C. Wexler, L. Firlej, B. Kuchta, and M.-W. Roth. *Langmuir*, 25(12):6596–6598, 2009.
- [149] L. Firlej, B. Kuchta, M. W. Roth, and C. Wexler. *Journal of Molecular Modeling*, 17(4):811–816, 2011.
- [150] A. J. Bourque and G. C. Rutledge. *European Polymer Journal*, 104:64–71, 2018.

- [151] Y. F. Liu, H. Yang, Z. M. Zhang, and H. Zhang. *Surface Science*, 690:121468, 2019.

Chapter 3

Wedge-Shaped Minidendrons

3.1 Introduction

Since their discovery by Reinitzer in 1888 [1], liquid crystals have attracted the attention of scientists because of their unusual physical properties. Soon after application was realised in the form of a liquid crystal light valve [2] but it was not until 1964 that they were utilised most famously in liquid crystal displays (LCD's), thanks to early pioneering work by Richard Williams. Williams found that nematic LC's exhibit interesting electro-optical properties when generating a series of stripes in a thin LC layer under an applied voltage [3]. Cathode ray TV's were first outsold by LCD's in 2008 and today they can be found in display devices we all use everyday such as smart phones, televisions, laptops and now even in cars and aircraft cockpits. In a typical passive LCD, such as that used in a calculator or digital clock, the ambient light is first plane polarised on entry to the pixel using a film on the top glass surface. The bottom of the glass is coated with indium-tin oxide, to act as a conductor and surfactant is then applied which favours a parallel alignment of the nematic LC component with respect to the polarisation direction of the light and the glass. The same is true for the

bottom glass surface except the outside polarisation film is rotated through 90 degrees and the application of surfactant favours a perpendicular alignment with respect to the polarisation direction of the light. As a consequence the pitch of the nematic LC is rotated through 90 degrees in going from the top to the bottom surface as well as the polarisation direction of the light passing through it. The light therefore passes straight through the cell and onto a mirror reflecting it back through reversing this process and gives the display its typical silvery appearance under ambient light. A crucial property of the nematic LC component is that it has a positive dielectric anisotropy which causes it to orient itself parallel to an applied electric field [4]. Applying voltage across the nematic cell causes the molecules to orient perpendicular to the glass and parallel to the polarisation direction of the light, with the exception of a thin layer close to the glass. Hence the polarisation direction of the light remains mostly unchanged when passing through the cell and the cell appears dark as the light is blocked by the second polariser and never reaches the reflecting mirror. Controlling the applied voltage of each pixel produces an image on the display and extremely efficient consuming minimal power. Traditional LC's, such as nematic or smectic, are most commonly used in LCD's.

Columnar LC's however are less commonly known and primarily find their uses in molecular electronics where their aromatic cores allow for electron transport and the terminal chains act as insulating material [5]. It is no surprise then that nematic and smectic LC's have been the subject of countless theoretical studies [6–8], perhaps motivated by their widespread application but more likely because of their apparent simplicity in comparison to complex 2d columnar or 3d LC's. Theoretical studies of complex 2d columnar and 3d LC's however are very rare [9, 10]. Columnar LC's often undergo continuous phase transitions which involve a change in symmetry i.e. rectangular to hexagonal (Col_r - Col_h) but more recently a first-order transition between two phases of the same hexagonal ($p6mm$) symmetry has been discovered in a series

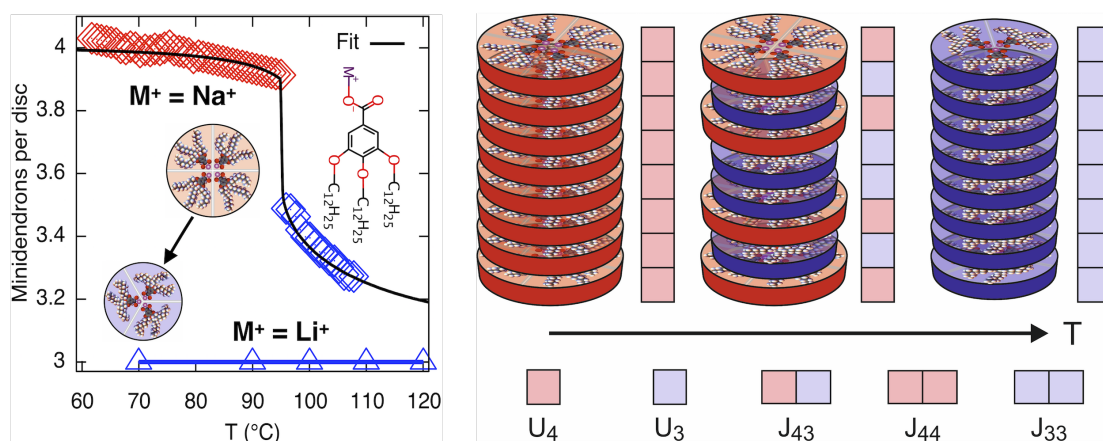
of compounds known as Minidendrons. Minidendrons are fan-shaped molecules with an aromatic head group and flexible terminal chains and often self-assemble to form columns. In this Chapter the first quantitative model of this unusual transition is reported [11] alongside the experimental results in Section 3.2 in the form of a published article. This work draws parallels with the magnetic ordering of a 1d chain of Ising spins in an external field in order to explain the first-order nature of this unusual transition [12, 13]. After which additional experimental results are summarised in Section 3.3 and an extension to the current quantitative model is discussed including the importance of chain length, cation size and mass alongside additional calculations. The Chapter is then concluded and future work is discussed in Section 7 with some discussion of experimental results in newly synthesised compounds with only 2 terminal chains instead of 3.

3.2 Published Article 1

Soft Matter

Molecular Ejection Transition in Liquid Crystal Columns
Self-Assembled from Wedge-Shaped Minidendrons

William S. Fall, Ming-Huei Yen, Xiangbing Zeng, Liliana Cseh,
Yongsong Liu, Gillian A. Gehring and Goran Ungar

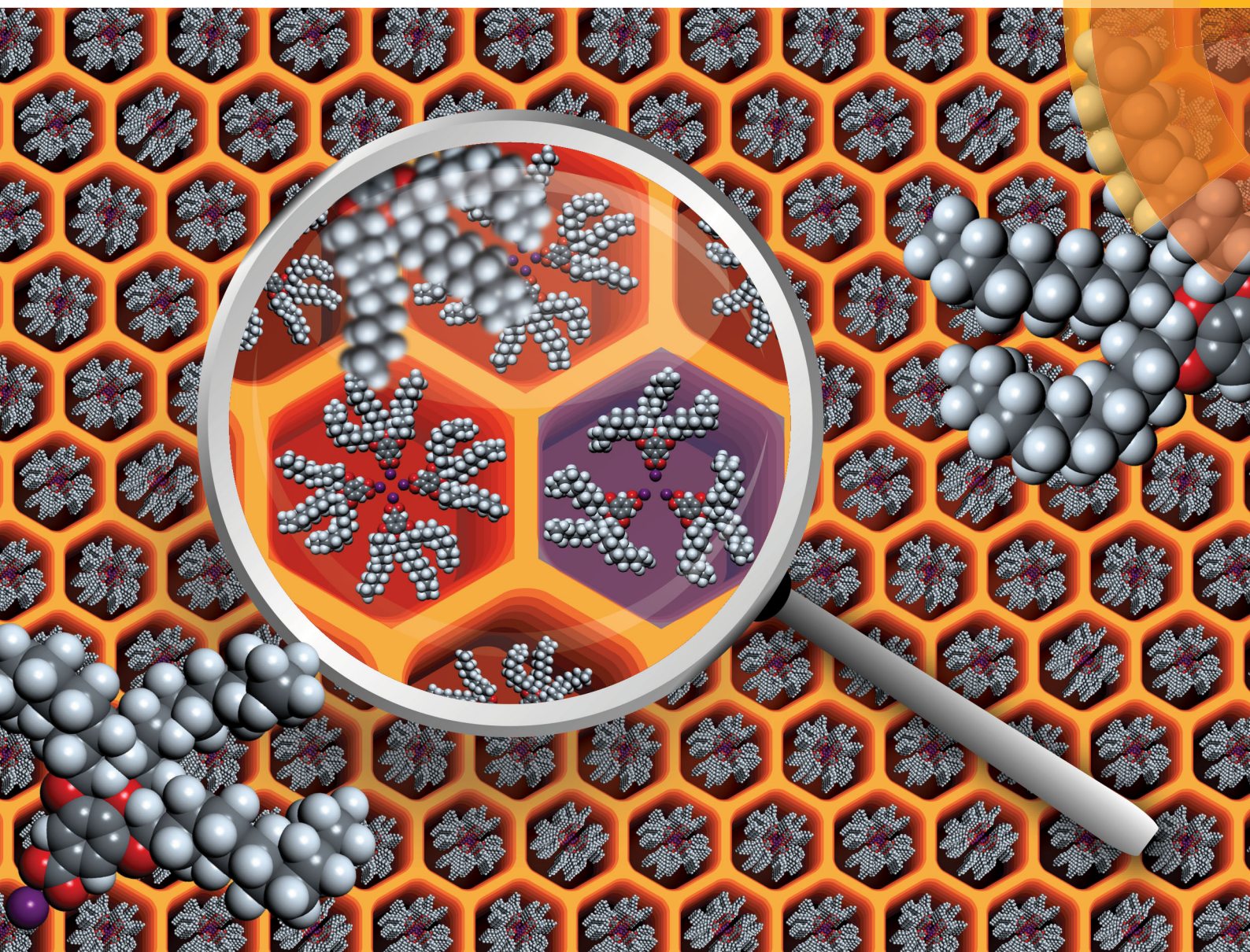


Author Contributions

G.U. conceived and directed all aspects of the project. M.Y. and Y.L., supervised by L.C. and G.U., carried out the experiments. W.S.F., supervised by G.A.G. and X.Z. carried out the simulations. W.S.F. wrote the program. W.S.F. developed the mean field theory with support from G.A.G. and X.Z. All authors contributed to data analysis and production of tables and figures. W.S.F. and G.U. prepared the manuscript with written contributions from all co-authors. W.S.F. produced and designed the front cover. See page **vii** for author declarations.

Soft Matter

rsc.li/soft-matter-journal



ISSN 1744-6848



ROYAL SOCIETY
OF CHEMISTRY

Celebrating
IYPT 2019

PAPER

Gillian A. Gehring, Goran Ungar *et al.*
Molecular ejection transition in liquid crystal columns
self-assembled from wedge-shaped minidendrons



Cite this: *Soft Matter*, 2019, 15, 22

Molecular ejection transition in liquid crystal columns self-assembled from wedge-shaped minidendrons†

William S. Fall,^{ab} Ming-Huei Yen,^c Xiangbing Zeng,^c Liliana Cseh,^d Yongsong Liu,^a Gillian A. Gehring^{id}*^b and Goran Ungar^{id}*^{ac}

Fan-shaped molecules with aromatic head-groups and two or more flexible pendant chains often self-assemble into columns that form columnar liquid crystals by packing on a 2d lattice. Such dendrons or minidendrons are essential building blocks in a large number of synthetic self-assembled systems and organic device materials. Here we report a new type of phase transition that occurs between two hexagonal columnar phases, Col_h1 and Col_h2 , of Na-salt of 3,4,5-tris-dodecyloxy benzoic acid. Interestingly, the transition does not change the symmetry, which is $p6mm$ in both phases, but on heating it involves a quantised drop in the number of molecules $\langle n \rangle$ in the cross-section of a column. The drop is from 4 to 3.5, with a further continuous decrease toward $\langle n \rangle = 3$ as temperature increases further above T_c . The finding is based on evidence from X-ray diffraction. Using a transfer matrix formulation for the interactions within a column, with small additional mean field terms, we describe quantitatively the observed changes in terms of intermolecular forces responsible for the formation of supramolecular columns. The driving force behind temperature-induced molecular ejection from the columns is the increase in conformational disorder and the consequent lateral expansion of the alkyl chains. The asymmetry of the transition is due to the local order between 4-molecule discs giving extra stability to purely $\langle n \rangle = 4$ columns.

Received 10th September 2018,
Accepted 31st October 2018

DOI: 10.1039/c8sm01851k

rsc.li/soft-matter-journal

Introduction

Taper-shaped molecules such as the tree-like “dendrons” have been shown to exhibit rich phase behavior by self-assembly into supramolecular sheets, columns or spheres. Dendrons displaying such liquid crystal (LC) phases usually comprise an aromatic core with flexible chains at the periphery.^{1–4} In many fan-shaped molecules the 2d-ordered columnar phase that appears at lower temperatures transforms on heating to one or a series of 3d spherical micellar phases. These have their counterparts in metals and are either cubic such as $Pm\bar{3}n$ (A15)⁵ and body-centered

cubic (BCC),⁶ or tetragonal (α -phase)⁷ or even quasicrystalline.^{8,9} Interestingly, all phases observed so far in these series of compounds can be seen in the simplest of them, known as ‘minidendrons’^{10–12} (see *e.g.* Fig. 1a). Taper-shaped mesogens, including minidendrons, are some of the most fundamental and widespread building blocks in supramolecular chemistry.¹³ They have been attached to moieties such as organic semi-conductors,^{14,15} ionic conductors,^{16–20} crown ether selective chelators,^{21–23} donor-acceptor complexes and polymers,^{24,25} peptides,²⁶ nanoparticles,^{27,28} quantum dots²⁹ *etc.* In this way, “dendronized” functional materials may be created, useful in a variety of applications.³⁰

Besides displaying an impressive array of complex 2d and 3d nanostructures, wedge-shaped and other “unusual” mesogens undergo numerous phase transitions. However, studies giving a theoretical basis of such phenomena are surprisingly rare in such systems.^{31,32} In more traditional LC’s, *i.e.* nematic and smectic, structures and transitions have been described theoretically in a number of cases by “borrowing” models from other areas of condensed matter and understood in the framework of the same physical principles. Well known examples include the nematic to smectic-A transition,³³ the twist-grain-boundary (TGB) smectic phase³⁴ and the hexatic phases,³⁵ the

^a Department of Physics, Zhejiang Sci-Tech University, Xiasha College Park, Hangzhou 310018, China

^b Department of Physics and Astronomy, University of Sheffield, Sheffield S3 7RH, UK. E-mail: g.gehring@sheffield.ac.uk

^c Department of Materials Science and Engineering, University of Sheffield, Sheffield S1 3JD, UK. E-mail: g.ungar@sheffield.ac.uk

^d Institute of Chemistry Timisoara of Romanian Academy, Timisoara-300223, Romania

† Electronic supplementary information (ESI) available. (1) Spacing and average number of molecules per disc n in the Col_h phase, (2) details of calculation of Coulomb energies, (3) details of chain free energy simulations, including data file of configurations. See DOI: 10.1039/c8sm01851k

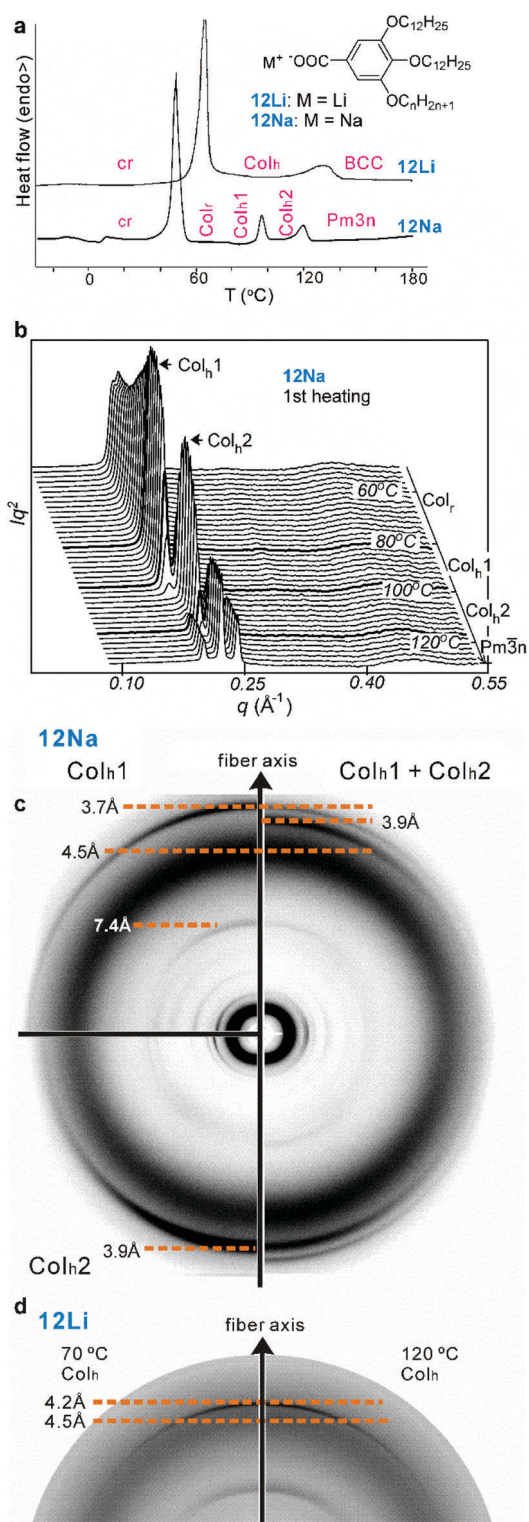


Fig. 1 (a) The compounds and their first DSC heating scans (5 K min⁻¹). Phase abbreviations: cr = crystal; Col_r = rectangular columnar phase (*c2mm* symmetry); Col_h, Col_{h1}, Col_{h2} = hexagonal columnar phases (*p6mm*); BCC and *Pm3n* = body-centered and A15 cubic phases, respectively. (b) Temperature evolution of SAXS curve of 12Na on 1st heating at 5 K min⁻¹. (c) WAXS patterns of an extruded 12Na fiber in the Col_{h1} phase at 85 °C (top left), Col_{h2} phase at 105 °C (bottom left) and the mixture of phases (Col_{h1} + Col_{h2}) at 95 °C (right). (d) Part of WAXS pattern of an extruded fiber of 12Li in the Col_h phase at 70 °C (left) and 120 °C (right).

latter being real-life examples of the Kosterlitz–Thouless theory of 2d melting.³⁶ The present work describes an unusual transition, one that happens within the same *p6mm* hexagonal columnar phase. We show that the ordering of an LC column may be described using the formalism of a magnetic spin chain. Interestingly, an approach linking magnetism and another type of complex soft self-assembly, *i.e.* multicolour tiling in a honeycomb LC,^{37,38} is to our knowledge so far the only other example in complex LC's.

In the hexagonal columnar phase (Col_h) wedge-shaped molecules assemble to form supramolecular discs which in turn stack to form columns.³⁹ With increasing temperature these columns show typically a continuous lateral shrinkage while maintaining positive bulk expansion.^{10,11,40} This has been attributed to continuous shedding of dendrons along the supramolecular column. An optimal average number of molecules per disc, $\langle n \rangle$, exists at a given temperature such that the overall system free energy is minimized. With increasing temperature, the dendrons expand sideways due to the increased entropy of the terminal chains, resulting in a decreasing optimal $\langle n \rangle$, and shedding of surplus dendrons. Similar behavior is observed in the cubic phases where spherical micelles shed their conically shaped dendrons continuously, thus shrinking with increasing temperature,¹⁰ in some cases down to half their size at low temperatures.⁴¹

All cases so far show continuous thermal shrinkage. Herein we report a special case where the lateral shrinkage of the columns is discontinuous, involving a new type of first-order transition between two columnar LC phases of the same hexagonal symmetry but with a quantised change in the average number of molecules in a supramolecular disc. We present experimental evidence and a quantitative statistical model of this unique LC phenomenon.

Experimental results

X-ray diffraction and calorimetry

The compounds used in this study are Na and Li salts of 3,4,5-tris(dodecyl)benzoic acid. They are labeled 12Na and 12Li and are shown in Fig. 1a, together with their calorimetry (DSC) scans. Powder small-angle X-ray scattering (SAXS) curves recorded on heating are shown in Fig. 1b. While 12Li shows only two LC phases, a hexagonal columnar (Col_h) and a body-centered cubic (BCC), 12Na displays a sequence of four LC phases. Crystals melt into a centered rectangular columnar phase (Col_r), symmetry *c2mm*, which gradually transforms into Col_h, plane group *p6mm*, around 82 °C (see Fig. 2a). Above 120–125 °C the columnar transforms into the cubic A15 phase, symmetry *Pm3n*. At the same time crystalline compound 12Li melts directly into the Col_h phase which subsequently transforms into BCC.

Whilst in most other salts the hexagonal lattice parameter, a_h , *i.e.* the distance between column axes, decreases continuously with increasing T ,^{10,11} both 12Li and 12Na are exceptional. In 12Li a_h is virtually independent of temperature⁴² – see Fig. 2.

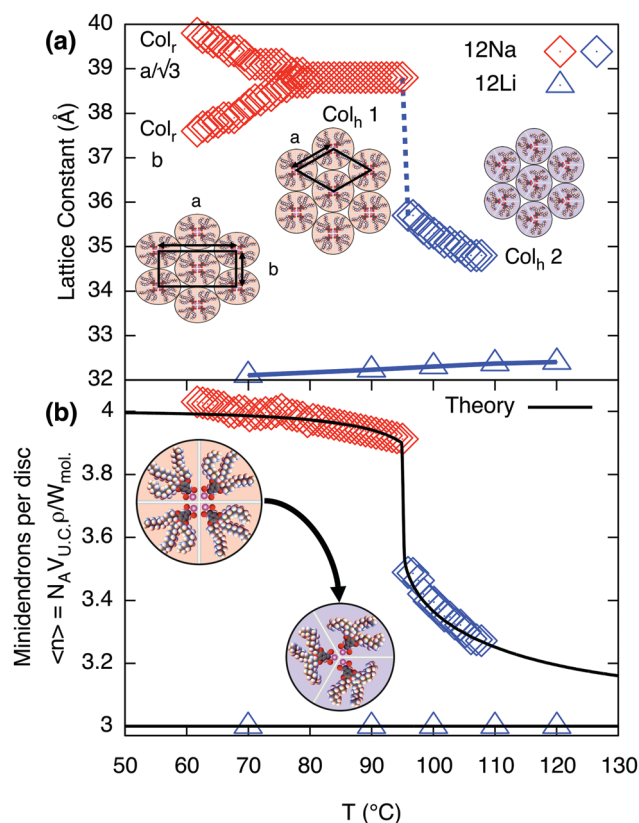


Fig. 2 (a) Inter-columnar distance in compounds 12Na and 12Li on heating, along with schematic drawings of each structure: Col_r, Col_{h1} and Col_{h2}. (b) Calculated number of minidendrons per supramolecular disc, $\langle n \rangle$, for both compounds, along with the best-fit curve from model for 12Na. Fitting parameters are discussed in the subsequent section.

Even more interestingly, in 12Na a clear first order transition is observed between two columnar hexagonal phases, labeled Col_{h1} and Col_{h2}, as shown in Fig. 1 and 2.

Changes in lattice parameters with temperature for 12Na and 12Li are given in Fig. 2a. The first hexagonal phase of 12Na (Col_{h1}) forms at around 82 °C at the convergence of b and $a/\sqrt{3}$ of the Col_r phase. In the Col_{h1} phase the intercolumnar distance a_h remains constant at 39 Å, and at about 95 °C it suddenly decreases by approximately 3 Å to 36 Å, signifying the transition to the Col_{h2} phase. After that in the Col_{h2} phase a_h decreases gradually with increasing temperature. The transition is reversible, albeit with a considerable hysteresis.

Determining the number of minidendrons $\langle n \rangle$

To determine the average number of molecules $\langle n \rangle$ in a supramolecular disc, or stratum of a column we need, besides the cross-section area of the column, also the height of the stratum c and the density ρ . While there is no true 3d long-range order, the wide-angle X-ray scattering (WAXS) pattern of a partially oriented extruded fiber of 12Na shows a relatively sharp meridional arc corresponding to a spacing of 3.7 Å in Col_{h1} and 3.9 Å in Col_{h2} phase (Fig. 1c). These correspond to the π - π stacking distance of benzene rings along the column axis and are taken as c values. The density was measured at

room temperature^{10,11} and then corrected, factoring in thermal expansion (see ESI† and Table S3). $\langle n \rangle$, thus obtained, is plotted against temperature in Fig. 2b. In the Col_{h1} phase of 12Na $\langle n \rangle$ is nearly constant at 4 molecules per stratum, dropping abruptly to 3.5 at the Col_{h1}-Col_{h2} transition and further decreasing continuously toward 3 as T is increased further. In 12Li, on the other hand, $\langle n \rangle$ is constant at 3 within the T -range of stability of the Col_h phase (Fig. 2 and Fig. S1, ESI†).

Theory

Outline

Fig. 3 shows a simplified schematic of the proposed statistical model of a column consisting of interacting supramolecular discs. Each disc may contain either 3 or 4 minidendrons which are held together by an attractive energy U_n (n is the number of minidendrons in each disc), assumed to be dominated by Coulomb interactions at the center of the disc. There are also temperature dependent free energy terms of the end chains $F_n(T)$, mainly entropic due to confinement of the molecule in a slice (1/3 or 1/4) of the disc. Interaction energy J_{mn} between two neighboring discs in a column is also included, and again considered to be dominated by Coulomb interactions. The model Hamiltonian describing a single column, in eqn (1), is constructed in terms of these interaction energies and the projection operators, $P_i^{(3)}$ and $P_i^{(4)}$ which correspond to an arbitrary disc, i , containing 3 or 4 minidendrons respectively ($P_i^{(3)} + P_i^{(4)} = 1$).

$$\begin{aligned} \mathcal{H} = & \sum_i (U_4 + F_4(T)) P_i^{(4)} + \sum_i (U_3 + F_3(T)) P_i^{(3)} \\ & + \sum_i J_{44} P_i^{(4)} P_{i+1}^{(4)} + \sum_i J_{33} P_i^{(3)} P_{i+1}^{(3)} \\ & + \sum_i J_{43} (P_i^{(4)} P_{i+1}^{(3)} + P_i^{(3)} P_{i+1}^{(4)}) \end{aligned} \quad (1)$$

Equilibrium properties of a single column are calculated from eqn (1), assuming that molecules are in a heatbath and a reservoir

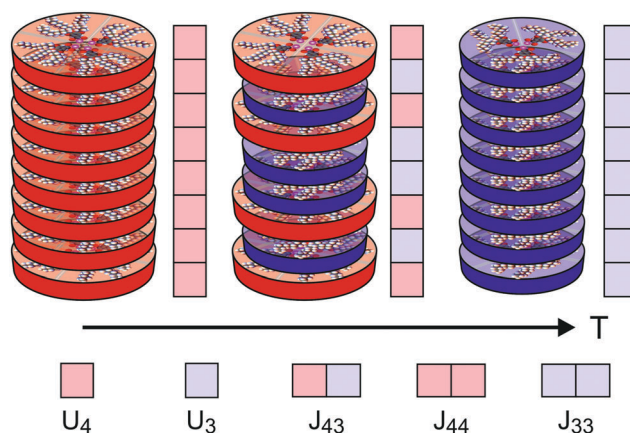


Fig. 3 Model of interacting supramolecular discs of 3 or 4 minidendrons per disc showing the pure (4), mixed (43) and pure (3) phases with increasing temperature. The intra-disc interactions U_n , and inter-disc interactions J_{mn} are also indicated.

of free molecules. Weak inter-columnar interactions are included later to take into account long-ranged interactions both along and across columns.

Calculating the chain free energy $F_n(T)$

Calculating the free energy of the three end chains $F_n(T)$ for a single minidendron presents an interesting problem since there are interactions with other molecules both within and between the supramolecular columns. Two important factors govern the shapes adopted by the chains at a given temperature; these are the number of *gauche* defects n_g and the extent of crystallisation with surrounding monomers. To simulate this effect, the minidendrons were confined within a segment with vertex angle θ and thickness d where the chains are restricted to only those conformations which contain discrete *trans* (t) or *gauche* (g) bonds, according to the Rotational Isomeric State model⁴³ – see Fig. 4(a). The diamond lattice is therefore chosen as a suitable lattice upon which the end chains may arrange themselves. The [111] direction of the lattice is oriented along the axis of the segment, to ensure a symmetric distribution. The core boundary radius, R , is fixed such that volume is kept constant hence $R_{90} = \sqrt{\frac{4}{3}}R_{120}$, where $R_{90} = 10$ Å. For three free chains of length l in unrestricted space, the number of possible conformations N is described by eqn (2).

$$N = (4 \times (3)^{(l-1)})^3 \quad (2)$$

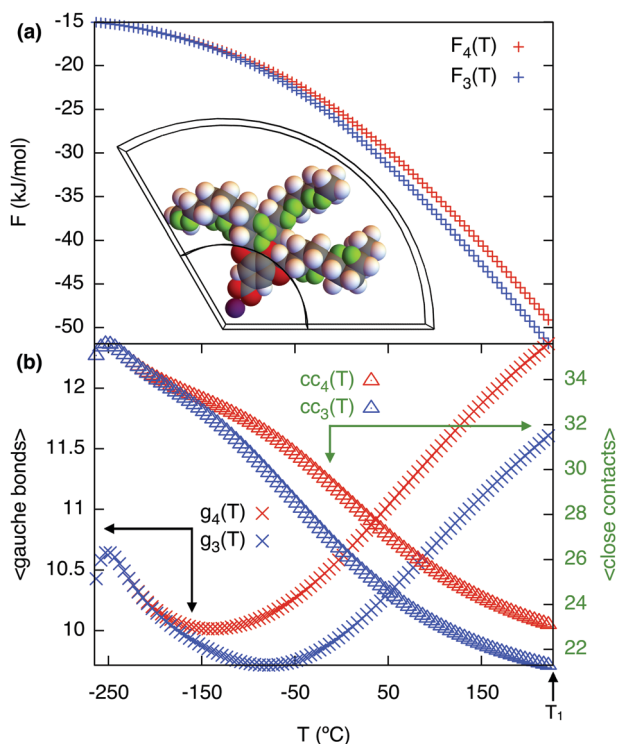


Fig. 4 (a) Chain free energy curves with a confined minidendron in a 120° segment shown in the inset, close contacts are shown in green. (b) *Gauche* bonds g_n and close contacts cc_n vs. temperature in respective geometries. 90° (red) and 120° (blue) from the simulation with $\eta = 4141$ (J mol⁻¹), $\gamma = 0.4$ as defined in eqn (3).

This is of the order 10^{17} for $l = 12$ but for self-avoiding chains in confined space this number falls dramatically, in our case down to 10^7 . The simulations have been run for vertex angles $\theta = 90^\circ$ and 120° , to approximate the confinement of 4 or 3 molecules per disc respectively, at a thickness $d = 3.6$ Å, the closest allowed by the experimental thickness on a diamond lattice. It should be noted that the conformers are self-avoiding such that no two H atoms may come closer than the first nearest neighbor distance. Successive *gg'* bonds are disallowed in the simulation to avoid H–H conflicts from 5th nearest neighbor monomer units, otherwise known as “pentane interference”. All possible conformations are enumerated and the ensemble is then weighted according to eqn (3).

$$E_i = \eta(n_g - \gamma n_{cc}) \quad (3)$$

Here η is the energy cost of introducing a *gauche* defect, n_{cc} is the number of close contacts between first nearest neighboring H atoms and γ represents the energy drop of crystallisation and allows for freezing. In this case, η is taken to be 4141 (J mol⁻¹) with and the expected increase in n_g and decrease in n_{cc} with increasing temperature was found for $\gamma = 0.4$, see Fig. 4(b). The partition function can then be written as eqn (4) and the free energy $F_n(T)$ calculated.

$$\mathcal{Z} = \sum_i e^{-\beta \eta (n_g - \gamma n_{cc})} \quad F_n(T) = -k_B T \log \mathcal{Z} \quad (4)$$

The generated free energy curves are shown in Fig. 4. Both geometries appear identical at low temperature and gradually diverge as temperature is increased. Hence for the chains alone a mixed (43) phase is preferred at low temperature with an increasing preference for (3) at higher temperatures.

Estimating Coulomb interactions U_n and J_{mn}

Coulomb interactions inside the supramolecular core, namely U_n and J_{mn} , are difficult to calculate since the exact arrangement is unknown. However this can be estimated by considering an idealised symmetric ring of alternating cations and anions, see Fig. 5b and Fig. S2 (ESI[†]). This serves as an order of magnitude estimate, the intra-disc interactions U_4 and U_3 , were calculated to be $-479\,289$ (J mol⁻¹) and $-479\,198$ (J mol⁻¹) respectively. Inter-disc interactions were estimated by rotating these rings in plane around an axis perpendicular to their respective centres at the experimentally-determined inter-disc separation of 3.8 Å. The interaction parameter for like rings J_{nn} were always found to have an attractive minimum whereas unlike rings J_{mn} are always repulsive. This can be seen in Fig. 5a, where the minima correspond to $J_{44} = -11241.2$ (J mol⁻¹) and $J_{33} = -10090.2$ (J mol⁻¹) at 45° or 60° respectively.

Solving the 1D column & introducing a mean field

To solve the model we draw analogy with the spin 1/2 Ising model,⁴⁴ by writing the projection operator, $P_i^{(n)}$, in terms of $\sigma_i = \pm 1$.

$$P_i^{(4)} = \frac{1}{2}(1 + \sigma_i) \quad P_i^{(3)} = \frac{1}{2}(1 - \sigma_i) \quad (5)$$

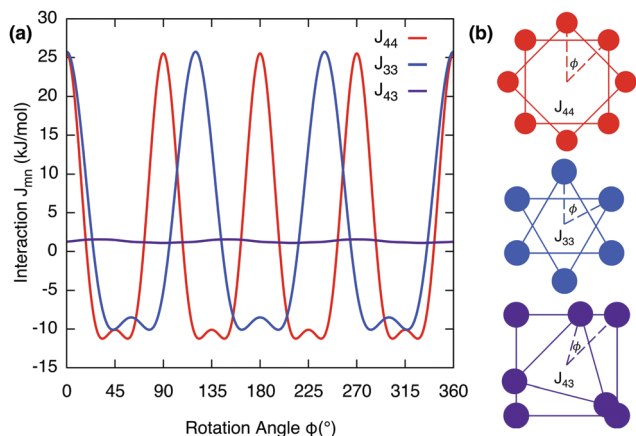


Fig. 5 (a) Inter-disc Coulomb potentials J_{mn} as a function of rotation angle ϕ for rings in plane rotated around an axis perpendicular to their respective centres at the experimentally determined inter-disc separation of 3.8 Å. (b) Simplified rings of cations rotating about their respective centres, for the three separate configurations considered. Anions are not shown but included in the calculations, see Fig. S2 (ESI†).

The Hamiltonian takes a convenient form

$$\mathcal{H} = -K \sum_i \sigma_i \sigma_{i+1} - C(T) \sum_i \sigma_i + \text{const} \quad (6)$$

Here

$$K = \frac{1}{4}(2J_{43} - J_{44} - J_{33}) \quad (7)$$

$$C(T) = \frac{1}{2}((F_3(T) - F_4(T)) + (U_3 - U_4) + (J_{33} - J_{44})) \quad (8)$$

This is then solved *via* the transfer matrix method.⁴⁴ The expectation value of $\langle \sigma \rangle$ can be expressed exactly in terms of the parameters K and $C(T)$, where T_c occurs at $C(T) = 0$.

$$\langle \sigma \rangle = \frac{\sinh \beta C(T)}{\sqrt{\sinh^2 \beta C(T) + e^{-2\beta K}}} \quad \beta = \frac{1}{k_B T} \quad (9)$$

Only nearest neighbor interactions along a single column are considered above, but a mean field interaction, standing for long range (intra- and inter-columnar) interactions, is crucial to achieve long range ordering and a first order transition between phases. Therefore, two additional energy parameters, λ and μ , are introduced; the first disfavours mixing of unlike discs/columns and the second reduces impurities in the region $T < T_c$. This changes eqn (8)–(10) and this means that the solution must be obtained numerically.

$$C'(T) = C(T) - \lambda \langle \sigma \rangle - \mu \langle \sigma \rangle^2 \quad (10)$$

Discussion

The free energy of the chains $F_n(T)$ is evaluated by examining their conformations on a diamond lattice in the confinement of the segment (1/3 or 1/4 of the disc) as described above. The intra-disc Coulomb interactions $U_3 - U_4$ were calculated assuming a near circular arrangement of alternating anions/cations in the core of the disc, see Fig. 5 and Fig. S2 (ESI†). The interactions between neighboring cores that were obtained from the fitting, see Table 1, $J_{33} - J_{44}$ and K , were smaller than those calculated from the Coulomb interactions between the cores. Several important interactions were not included in the calculation: these include the interactions between the benzene rings and between the chains. The mean field interaction terms, $\lambda = 115 \text{ J mol}^{-1}$ and $\mu = 190 \text{ J mol}^{-1}$, which are significantly smaller than the nearest neighbor interaction K , are additional fitting parameters. Note that K is equivalent to the χ parameter in the theory of polymer solutions and blends. The reason that such small additional terms are so important here is because even in their absence, there are very long regions of order along the chains because $K/k_B T_c \sim 1.8$ which is greater than unity. Fig. 6 depicts the effect of each of the above described interactions on the shape of the phase transition. Panel (i) shows how a supramolecular column might behave without interaction between its constituent discs: the free energy of the end chains $F_n(T)$ alone would prefer a mixed (43) phase with increasing preference for (3) at higher temperatures; and introducing the intra-disc interactions U_n stabilizes the (4) phase at lower temperatures. This clearly shows a competition between the entropy-driven end chains and energy-driven core interactions. Panel (ii) describes the behavior of the column with nearest neighbor interactions J_{mn} . In this case, an ordered column in the (4) phase is stable over a considerable T -range and may then continuously transform to the (3) phase *via* the mixed (43) phase. Comparing (i) and (ii), it is clear that core-core interactions are responsible for the stable formation of columns. The effect of long range (intra- and inter-columnar) interactions are shown in (iii) and (iv): λ is responsible for the sharpness of the transition, and μ for the imbalance in tolerance to impurities in (4) and (3) phases. This allows us to produce the characteristic transition shape seen experimentally in Fig. 2b.

Our results demonstrate that the observed transition is driven predominantly by the entropy of the end chains. In our quantitative fitting, the only explicitly temperature dependent term is the free energy of the chains. With increasing temperature the entropy of the end chains of the minidendrons increases due to the growing number of *gauche* defects, see

Table 1 Calculated vs. fitted parameters for the model fit shown in Fig. 2, all values stated are in J mol^{-1} unless otherwise indicated and T_1 is indicated in Fig. 4 at 227 °C

	U_3	U_4	J_{33}	J_{44}	J_{43}	$U_3 - U_4$	$J_{33} - J_{44}$	K	$F_3(T_1) - F_4(T_1)$	λ	μ
Calculated	-479 289	-479 198	-10 090	-11 241	1096	-91	-1151	5881	-2746	—	—
Fitted	-479 289	-479 198	-10 130	-11 985	0	-91	-1855	5529	-2746	115	190

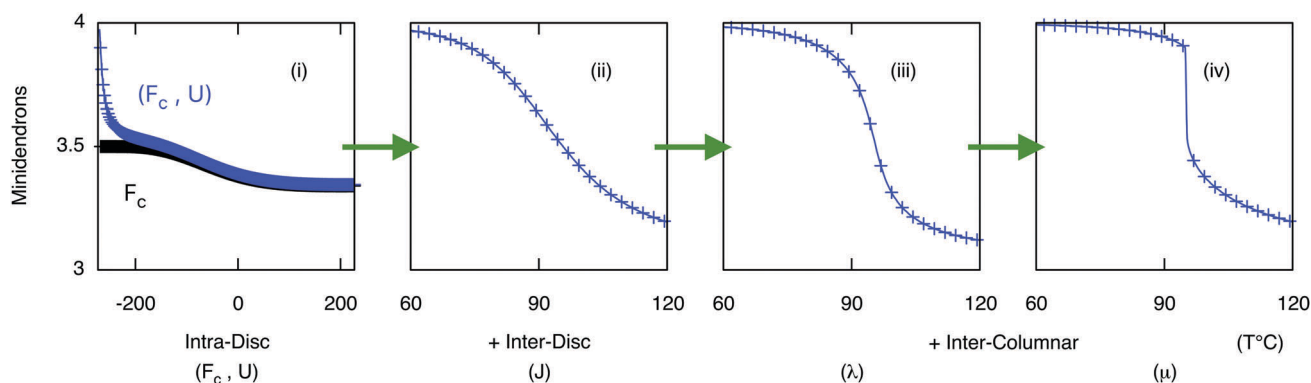


Fig. 6 Average number of molecules per disc as a function of temperature as different interactions are introduced, parameter values can be found in Table 1. (i) using core free energy F_c and intra-disc interactions U_n alone (ii) inter-disc interactions J_{mn} added, and (iii/iv) long range inter-columnar interaction parameters λ and μ included. Note the temperature range in (i) is significantly larger than (ii), (iii) and (iv).

Fig. 4. This leads to the expulsion of minidendrons from the disc, which are now able to overcome the attractive energies holding them together.

The size of the inter-disc $J_{33} - J_{44}$ in comparison to the intra-disc $U_3 - U_4$ would suggest that discs of 4 minidendrons cannot exist without forming a column to stabilise their structure. Once a column is formed the discs are effectively locked into the column by the attraction between their head groups. By increasing temperature, the free energy of the end chains eventually allows for expulsion of a minidendron; when this occurs the entire column is destabilised leading to a sudden runaway expulsion of minidendrons down the column. This is true for an isolated column where K is the only parameter responsible for the continuity/discontinuity of the transition. Further increasing K would lead to a completely symmetric strongly first order transition effectively destroying the characteristic tail seen experimentally. The discontinuity and asymmetry in the transition must result from the attractive energy between the columns themselves. As we approach the critical point from low T , any supramolecular disc which transitions would break the long range order between columns, triggering this energetic transition to occur. The λ and μ terms are then absolutely necessary. Long range interactions are responsible for the discontinuity in the transition, as well as the temperature range over which the (4) phase remains stable.

A clear asymmetry is present in the transition which suggests the supramolecular columns in the (4) phase are able to tolerate the pressure due to the lateral expansion of the end chains with increasing temperature. The characteristic high-temperature tail would suggest that, once shedding has occurred, some (4) discs still exist due to the free space made available by the transition. However, even these remaining discs are then gradually lost at higher temperatures. The resilience of the pure (4)-columns below the transition may be, at least partially, due to additional intra-columnar interactions that develop in (4)-columns, reflected in the appearance of a weak 7.4 Å near-meridional diffraction feature (Fig. 1c). While the main meridional diffraction at 3.7 Å comes from the stacking of individual discs, the weak 7.4 Å arc indicates pairing of adjacent discs. Most likely, the successive discs are

rotated in plane by 45°, minimizing repulsion between alkyl chains and making the column a quadruple 8_1 helix (see Fig. 5 and Coulomb energy calculations in ESI†). It should be noted that neither the 3.7 Å nor the 7.4 Å reflect true long-range order. Upon the Col_h1–Col_h2 transition the 3.7 Å peak shifts to 3.9 Å indicating some tilting of the benzene rings away from the xy plane. At the same time the 7.4 Å feature disappears, meaning that the extra intra-columnar order is lost in the mixed (43) columns.

In contrast to 12Na, 12Li maintains 3-dendron columns in the entire temperature range of the Col_h phase from 70 °C to above 120 °C. The smaller number of dendrons in 12Li discs is attributed to the tight-binding small Li⁺ ions drawing the dendron cores closer to the column centre thereby effectively increasing the molecular taper compared to that of 12Na. We also note that the fiber pattern of the purely (3)-columns of 12Li (Fig. 1d) again contains a clear 7.4 Å arc, suggesting relatively high intra-columnar order, this time possibly of a triple 6_1 helical type (60° rotation between successive discs). Shrinkage of the purely (3)-columns of 12Li appears to be completely prevented, at least up to the temperature at which columns turn into spheres that form the cubic phase (Fig. 2).

This strong resistance to shrinkage and the raising of T_c beyond the range of stability of the columnar phase is primarily due to a weaker intra-disc cohesion U_2 of the (2)-disc. In addition to the lower Coulomb energy of (2)-discs, the ample volume left empty by the removal of the third molecule and the resulting breaking of van der Waals bonds between alkyl chains must contribute significantly to raising the energy of the (2) phase. The extra conformational entropy achieved by turning 120° segments into 180° is clearly insufficient to offset the energy penalty at these moderate temperatures.

However it has been shown recently that addition of free alkane overcomes this obstacle and allows continuous thermal shrinkage of the (3)-columns in 12Li at moderate temperatures.⁴² It was established, using labeled alkane and neutron scattering that, following dendron expulsion, the alkane collects preferentially in the resulting (2)-columns replacing the missing dendrons, effectively increasing U_2 by re-establishing the missing van der Waals bonds. Furthermore we noted the transition in 12Li starts

continuous. Interestingly, the (3)-columns and the (2)-columns were found to occupy defined positions on a 2D superlattice with a three-column hexagonal unit cell. By analogy, it is expected that addition of alkane could turn the shrinkage of (4)-columns in 12Na from discontinuous to continuous.

Experimental methods

The synthesis has been described previously.^{10,11} Powder SAXS experiments were conducted on beamline I22 of the Diamond synchrotron, and the fiber patterns on a Rigaku rotating anode source with multilayer mirrors and a MAR 345 image-plate detector. DSC was recorded on a Perkin-Elmer Pyris instrument at 5 K min⁻¹. Prior to the experiments the samples were vacuum dried for 24 hours and kept in sealed capillaries during the X-ray experiments.

Conclusions

We have reported the first example of a transition between two columnar phases of the same symmetry. To our knowledge, this is also the first case of a transition based entirely on a change in the number of molecules in a self-assembled aggregate. We have described the transition quantitatively. The model is quasi one-dimensional because the largest interactions are along the columns and only small long range interactions are needed to cause the phase transition. The transition is driven by the end chains of the minidendrons that expand as the temperature is raised. This work is another demonstration of the principle of universality, which explains why similar behavior is seen in disparate physical systems with the same dimensionality and number of degrees of freedom. In the original magnetic system the increase in temperature causes disorder along the spin chain; while in the system that is described here it also changes the sign of the ordering field.

Conflicts of interest

There are no conflicts to declare.

Acknowledgements

For help with synchrotron SAXS and fiber WAXS experiments we thank, respectively, Prof. Nick Terrill at I22, Diamond, and Dr Patrick Baker at Sheffield University. Simulations were performed using the Sheffield Advanced Research Computer (ShARC) hosted by the University of Sheffield. Financial support is acknowledged from EPSRC (EP/K034308, EP/P002250), Leverhulme Trust (RPG-2012-804) and NSFC China (21274132).

References

- 1 H. J. Sun, S. Zhang and V. Percec, *Chem. Soc. Rev.*, 2015, **44**, 3900–3923.

- 2 B. Donnio, S. Buathong, I. Bury and D. Guillon, *Chem. Soc. Rev.*, 2007, **36**, 1495–1513.
- 3 C. Tschierske, *Angew. Chem., Int. Ed.*, 2013, **52**, 8828–8878.
- 4 T. Kato, N. Mizoshita and K. Kishimoto, *Angew. Chem., Int. Ed.*, 2006, **45**, 38–68.
- 5 V. Balagurusamy, G. Ungar, V. Percec and G. Johansson, *J. Am. Chem. Soc.*, 1997, **119**, 1539–1555.
- 6 D. J. Yeardley, G. Ungar, V. Percec, M. N. Holerca and G. Johansson, *J. Am. Chem. Soc.*, 2000, **122**, 1684–1689.
- 7 G. Ungar, Y. Liu, X. Zeng, V. Percec and W.-D. Cho, *Science*, 2003, **299**, 1208–1211.
- 8 X. Zeng, G. Ungar, Y. Liu, V. Percec, A. E. Dulcey and J. K. Hobbs, *Nature*, 2004, **428**, 157.
- 9 R. Zhang, X. Zeng and G. Ungar, *J. Phys.: Condens. Matter*, 2017, **29**, 414001.
- 10 G. Ungar, V. Percec, M. N. Holerca, G. Johansson and J. A. Heck, *Chem. – Eur. J.*, 2000, **6**, 1258–1266.
- 11 V. Percec, M. N. Holerca, S. Uchida, W.-D. Cho, G. Ungar, Y. Lee and D. J. Yeardley, *Chem. – Eur. J.*, 2002, **8**, 1106–1117.
- 12 M. A. Shcherbina, A. V. Bakirov, A. N. Yakunin, U. Beginn, L. Yan, M. Möller and S. N. Chvalun, *Soft Matter*, 2014, **10**, 1746–1757.
- 13 S. Hecht and J. M. Fréchet, *Angew. Chem., Int. Ed.*, 2001, **40**, 74–91.
- 14 F. Würthner, C. Thalacker, S. Diele and C. Tschierske, *Chem. – Eur. J.*, 2001, **7**, 2245–2253.
- 15 Z. An, J. Yu, B. Domercq, S. C. Jones, S. Barlow, B. Kippelen and S. R. Marder, *J. Mater. Chem.*, 2009, **19**, 6688–6698.
- 16 G. Ungar, S. Batty, V. Percec, J. Heck and G. Johansson, *Adv. Funct. Mater.*, 1994, **4**, 303–313.
- 17 T. Ichikawa, M. Yoshio, A. Hamasaki, T. Mukai, H. Ohno and T. Kato, *J. Am. Chem. Soc.*, 2007, **129**, 10662–10663.
- 18 M. Peterca, V. Percec, A. E. Dulcey, S. Nummelin, S. Korey, M. Iliés and P. A. Heiney, *J. Am. Chem. Soc.*, 2006, **128**, 6713–6720.
- 19 C. S. Pecinovsky, E. S. Hatakeyama and D. L. Gin, *Adv. Funct. Mater.*, 2008, **20**, 174–178.
- 20 B. Soberats, M. Yoshio, T. Ichikawa, X. Zeng, H. Ohno, G. Ungar and T. Kato, *J. Am. Chem. Soc.*, 2015, **137**, 13212–13215.
- 21 G. Johansson, V. Percec, G. Ungar and D. Abramic, *J. Chem. Soc., Perkin Trans. 1*, 1994, 447–459.
- 22 A. Schulte, S. Laschat, A. Saipa, F. Gießelmann, M. Nimtz, J. L. Schulte, A. Baro and B. Miehlich, *Adv. Funct. Mater.*, 2004, **14**, 163–168.
- 23 Y. Luo, N. Marets and T. Kato, *Chem. Sci.*, 2018, **9**, 608–616.
- 24 V. Percec, M. Glodde, T. Bera, Y. Miura, I. Shiyanovskaya, K. Singer, V. Balagurusamy, P. Heiney, I. Schnell and A. e. a. Rapp, *Nature*, 2002, **419**, 384.
- 25 T. T. Steckler, X. Zhang, J. Hwang, R. Honeyager, S. Ohira, X.-H. Zhang, A. Grant, S. Ellinger, S. A. Odom and D. e. a. Sweat, *J. Am. Chem. Soc.*, 2009, **131**, 2824–2826.
- 26 V. Percec, A. E. Dulcey, M. Peterca, P. Adelman, R. Samant, V. S. Balagurusamy and P. A. Heiney, *J. Am. Chem. Soc.*, 2007, **129**, 5992–6002.
- 27 B. Donnio, P. Garca-Vázquez, J.-L. Gallani, D. Guillon and E. Terazzi, *Adv. Funct. Mater.*, 2007, **19**, 3534–3539.

- 28 K. Kanie, M. Matsubara, X. Zeng, F. Liu, G. Ungar, H. Nakamura and A. Muramatsu, *J. Am. Chem. Soc.*, 2011, **134**, 808–811.
- 29 M. Matsubara, W. Stevenson, J. Yabuki, X. Zeng, H. Dong, K. Kojima, S. F. Chichibu, K. Tamada, A. Muramatsu and G. e. a. Ungar, *Chem*, 2017, **2**, 860–876.
- 30 X. Feng, M. E. Tousley, M. G. Cowan, B. R. Wiesenauer, S. Nejati, Y. Choo, R. D. Noble, M. Elimelech, D. L. Gin and C. O. Osuji, *ACS Nano*, 2014, **8**, 11977–11986.
- 31 Y. Li, S.-T. Lin and W. A. Goddard, *J. Am. Chem. Soc.*, 2004, **126**, 1872–1885.
- 32 P. Zihlerl and R. D. Kamien, *J. Phys. Chem. B*, 2001, **105**, 10147–10158.
- 33 P. G. de Gennes and J. Prost, *The physics of liquid crystals*, Oxford University Press, 1995, vol. 83, pp. 507–527.
- 34 S. John and T. Lubensky, *Phys. Rev. B: Condens. Matter Mater. Phys.*, 1986, **34**, 4815.
- 35 D. R. Nelson and B. Halperin, *Phys. Rev. B: Condens. Matter Mater. Phys.*, 1980, **21**, 5312.
- 36 J. Kosterlitz, *J. Phys. C: Solid State Phys.*, 1973, **6**, 1181.
- 37 X. Zeng, R. Kieffer, B. Glettner, C. Nürnberger, F. Liu, K. Pelz, M. Prehm, U. Baumeister, H. Hahn and H. Lang, *et al.*, *Science*, 2011, **331**, 1302–1306.
- 38 S. George, C. Bentham, X. Zeng, G. Ungar and G. A. Gehring, *Phys. Rev. E*, 2017, **95**, 062126.
- 39 B. Mu, X. Hao, J. Chen, Q. Li, C. Zhang and D. Chen, *Polym. Chem.*, 2017, **8**, 3286–3293.
- 40 Y. K. Kwon, S. N. Chvalun, J. Blackwell, V. Percec and J. A. Heck, *Macromolecules*, 1995, **28**, 1552–1558.
- 41 X. Yao, L. Cseh, X. Zeng, M. Xue, Y. Liu and G. Ungar, *Nanoscale Horiz.*, 2017, **2**, 43–49.
- 42 M.-H. Yen, J. Chaiprapa, X. Zeng, Y. Liu, L. Cseh, G. H. Mehl and G. Ungar, *J. Am. Chem. Soc.*, 2016, **138**, 5757–5760.
- 43 P. J. Flory and M. Volkenstein, *Statistical mechanics of chain molecules*, 1969.
- 44 H. A. Kramers and G. H. Wannier, *Phys. Rev.*, 1941, **60**, 252.

Supporting Information for:

Quantised Molecular Ejection Transition in

Liquid Crystal Columns Self-Assembled from

Wedge-Shaped Minidendrons

William S. Fall,^{†,‡} Ming-Huei Yen,[¶] Xiangbing Zeng,[¶] Liliana Cseh,[§]
Yongsong Liu,[†] Gillian A. Gehring,^{*,‡} and Goran Ungar^{*,†,¶}

[†]*Department of Physics, Zhejiang Sci-Tech University, Xiasha College Park, Hangzhou 310018,
China*

[‡]*Department of Physics and Astronomy, University of Sheffield, Sheffield S3 7RH, U.K.*

[¶]*Department of Materials Science and Engineering, University of Sheffield, Sheffield S1 3JD,
U.K.*

[§]*Institute of Chemistry Timisoara of Romanian Academy, Timisoara - 300223, Romania*

E-mail: g.gehring@sheffield.ac.uk; g.ungar@sheffield.ac.uk

Contents

1	Spacings and average number of molecules per disc n in the Col_h phase	S3
2	Calculation of Coulomb Interactions (U_n, J_{mn})	S4
3	Chain Free Energy Simulation $F_n(T)$	S6
	References	S8

1 Spacings and average number of molecules per disc n in the Col_h phase

Table S1: Calculation of average number of molecules $\langle n \rangle$ in a unit cell (disc) of Col_h phase of 12Li at 70°C

$a(\text{Å})$	32.1 ^a
$c(\text{Å})$	4.2 ^b
Volume of unit cell (10^3 Å^3)	3.74
Volume of 12Li ($10^3 \text{ Å}^3/\text{molecule}$)	1.24 ^c
$\langle n \rangle$	3.0

a: From Fig. 2a. **b:** from Fig. 1d. **c:** Experimental density of 1.02 g/cm^3 for 12Li measured in crystalline state at room temperature¹ was increased by 7% for expansion on melting and extrapolated to 70 °C using thermal expansivity $9.49 \times 10^{-4} + 1.35 \times 10^{-6} T - 0.53 \times 10^{-8} T^2 + 6.28 \times 10^{-11} T^3 \text{ K}^{-1}$, where T is temperature, reported for alkane $n\text{-C}_{12}\text{H}_{26}$.³

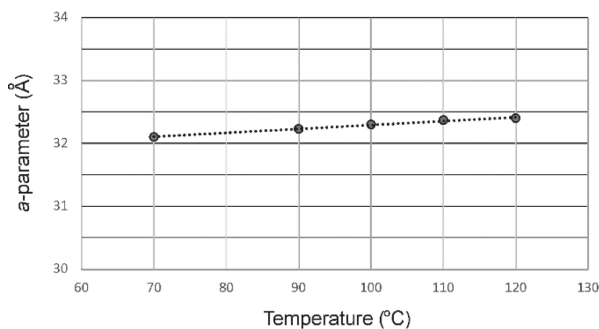


Figure S1: Experimental lattice parameter vs. temperature for the Col_h phase of 12Li.

Table S2: Lattice parameter and number of molecules of 12Li per disc as a function of temperature.

$T(^{\circ}\text{C})$	$a(\text{\AA})$	$\langle n \rangle$
70	32.1	3.0
90	32.23	3.0
100	32.3	3.0
110	32.37	3.0
120	32.4	3.0

Table S3: Lattice parameters and number of molecules of 12Na per disc as a function of temperature.

Phase	T ($^{\circ}\text{C}$)	a (\AA)	b (\AA)	c (\AA) ^a	V_{disc} (10^3\AA^3) ^b	V_{mol} (10^3\AA^3)	$\langle n \rangle$
Col _r	65	39.6 ^c	37.8	3.7	4.80	1.19	4.02
	70	39.2 ^c	38.2	3.7	4.80	1.20	3.99
	75	39.1 ^c	38.6	3.7	4.83	1.21	4.00
Col _{h1}	80	38.8		3.7	4.82	1.22	3.97
	85	38.8		3.7	4.81	1.22	3.93
	90	38.8		3.7	4.81	1.23	3.91
	95	38.8		3.7	4.82	1.24	3.90
Col _{h2}	100	35.2		3.9	4.19	1.25	3.36
	105	34.9		3.9	4.11	1.26	3.28

a: measured from fibre X-ray diffraction (Figure S1c). **b:** In calculation of the volume of the 12Na molecule, an experimental density of 1.01 g/cm³ measured in crystalline state at room temperature is used, corrected by thermal expansion using the formula for alkane n-C₁₂H₂₆.³ **c:** $a/\sqrt{3}$.

2 Calculation of Coulomb Interactions (U_n, J_{mn})

Calculated intra-disk U_n Coulomb interactions (Equation S1), all atoms separated by radii given in Table S4. Radius of O atoms is estimated (Equation S2). O-M-O bond angle minima are 173.456 $^{\circ}$ and 189.356 $^{\circ}$ for configurations of $n=4$ or $n=3$ minidendrons per supramolecular disc respectively. O=C-O angle fixed at 120 $^{\circ}$, see Figure S2(a). Final values (J/mol): $U_4 = -479289$, $U_3 = -479198$.

$$U_n = \frac{N_A q^2}{4\pi\epsilon_0 n} \left(\frac{1}{2} \sum_{i=1}^n \sum_{j=1}^{n(i \neq j)} \frac{1}{|r_{M_i-M_j}|} - \frac{1}{2} \sum_{i=1}^n \sum_{j=1}^{2n} \frac{1}{|r_{M_i-O_j}|} + \frac{1}{8} \sum_{i=1}^{2n} \sum_{j=1}^{2n(i \neq j)} \frac{1}{|r_{O_i-O_j}|} \right) \quad (\text{S1})$$

$$R_{O^{\frac{1}{2}}} = \frac{1}{2} \left(R_{O^0} + \frac{1}{3} (2R_{O^0} + R_{O^{-2}}) \right) \quad (\text{S2})$$

Table S4: Atomic radii used in Coulomb calculations.²

Element	Radius(Å)	Vdw/Ionic
Na	1.02	Ionic
C	1.70	Vdw
O ⁰	1.52	Vdw
O ⁻²	1.35	Vdw
O ^{1/2}	1.49	(Equation S2)

Calculated inter-disk J_{mn} Coulomb interactions (Equation S4), using atomic radii in Table S4 and inter-disk spacing of 3.8 Å. Figure S2(b) depicts 3 different configurations used to produce Figure 5 in the main manuscript, where cations and anions are rotated around an axis perpendicular to their respective centres, see Equation S4. Final calculated minima (J/mol): $J_{44} = -11241.2$, $J_{43} = 1096.3$, $J_{33} = -10090.2$.

$$n' = n_1 + n_2 \quad (\text{S3})$$

$$J_{n_1 n_2} = \frac{N_A q^2}{4\pi\epsilon_0 n'} \left(\frac{1}{2} \sum_{i=1}^{n'} \sum_{j=1}^{n'(i \neq j)} \frac{1}{|r_{M_i-M_j}|} - \frac{1}{2} \sum_{i=1}^{n'} \sum_{j=1}^{2n'} \frac{1}{|r_{M_i-O_j}|} + \frac{1}{8} \sum_{i=1}^{2n'} \sum_{j=1}^{2n'(i \neq j)} \frac{1}{|r_{O_i-O_j}|} - n_1 U_{n_1} - n_2 U_{n_2} \right) \quad (\text{S4})$$

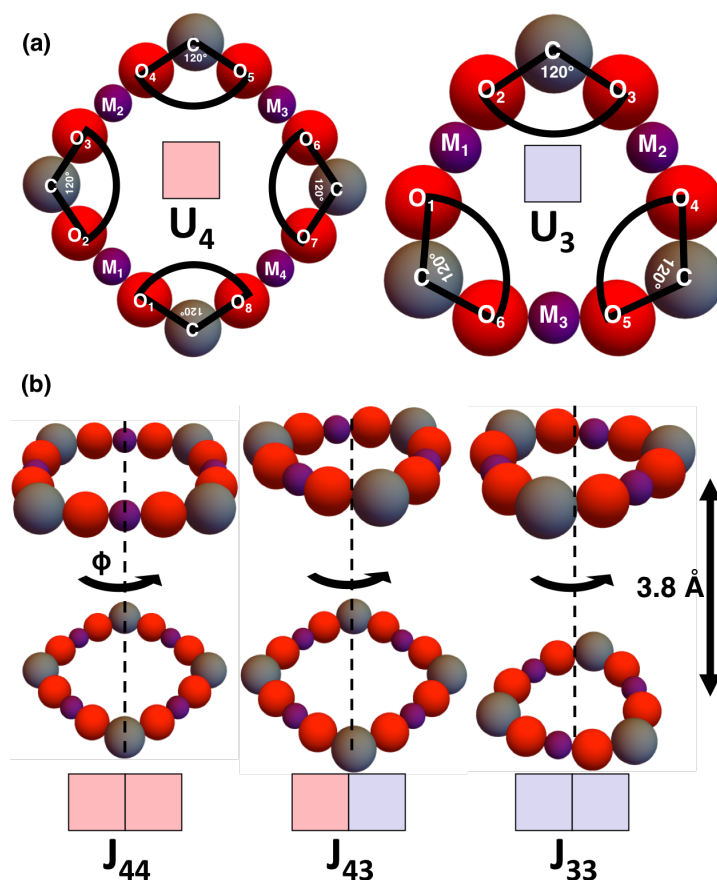


Figure S2: (a) Idealised ring of alternating cations/anions, Carbon-C (gray), Oxygen-O (red), Sodium-Na (purple), O=C-O bond angle drawn explicitly. (b) Schematic of rotating disks with exaggerated inter-disk spacing.

3 Chain Free Energy Simulation $F_n(T)$

All atoms lie on the diamond lattice where the first neighbor distance $a = 1.54 \text{ \AA}$ is equal to the C-C bond length in alkanes. The basis vectors are given in Table S5. Starting points of oxygen atoms are $(2,-2,0)$, $(1,1,1)$, $(-2,2,0)$, which sit approximately 2.95 \AA from each other. C atoms are confined to a segment thickness of 3.6 \AA the closest match available to experimentally determined thickness when restricted to the diamond lattice. H atoms may cross this boundary. Each alkane conformer is formed using alternating sets of basis vectors in Table S5 where immediate back steps are forbidden i.e. a cannot be followed by a' . Conformers are self-avoiding and successive

gg' ($\pm 60^\circ$) torsional angles are disallowed ("pentane interference"). Chains attached at positions 3 and 5 on the benzene ring start at points of a different parity to the central chain attached at 4, hence they can be considered shorter since the position of the first C atom is effectively fixed. Total number of conformers found is 41,376,644 and 69,386,880 for the 90° and 120° geometries, respectively.

Table S5: Diamond lattice vectors

<i>a</i>	(1,1,1)	<i>a'</i>	(-1,-1,-1)
<i>b</i>	(-1,-1,1)	<i>b'</i>	(1,1,-1)
<i>c</i>	(-1,1,-1)	<i>c'</i>	(1,-1,1)
<i>d</i>	(1,-1,-1)	<i>d'</i>	(-1,1,1)

Note: conformers.tar.bz2 containing .dat files are arranged in 3 tab separated columns. Rows correspond to a unique configuration with 3 entries (3 chains) each with a unique identifier, i.e. 174617474527 corresponds to ac'db'ac'dc'da'bd' as defined in Table S5.

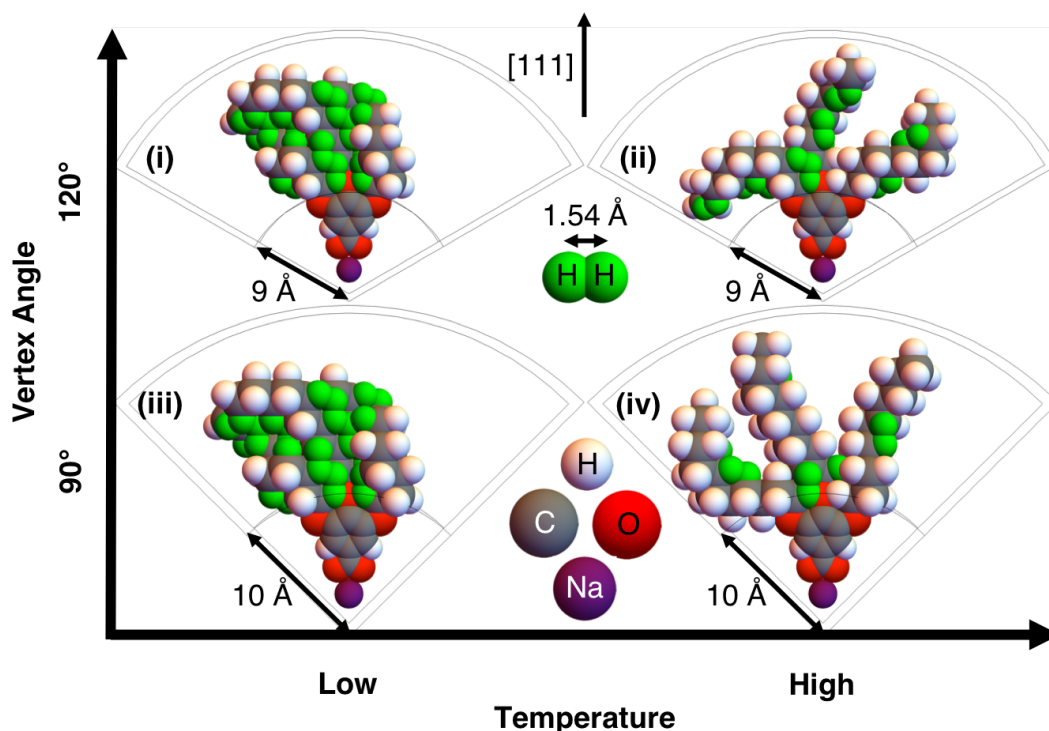


Figure S3: Minidendrons with alkyl chains in confined geometry depicting the effect of vertex angle and temperature on chain conformations. Close contacts (green) show chain crystallization. [111] direction is indicated.

References

- (1) V. Percec, M. N. Holerca, S. Uchida, W.-D. Cho, G. Ungar, Y. Lee and D. J. Yeardley, *Chem. Eur. J.*, 2002, 8, 1106-1117.
- (2) R. D. Shannon, *Acta Crystall. A-Cryst.*, 1976, 32, 751-767.
- (3) R. A. Orwoll and P. J. Flory, *J. Am. Chem. Soc.*, 1967, 89, 6814-6822.

3.3 Additional Experimental Work & Model Predictions

In the previous work [11] the first-order nature of the unusual transition between two hexagonal phases of the same hexagonal symmetry was reported in one of a series of salts of 3,4,5-tris docecyl benzoic acid namely 12Na. The quantitative model provided a remarkably accurate description of the energetics of the transition when fitted to the experimental data. Further experimental work has now revealed similar transitions in other compounds with heavier ions and longer chains, namely 14Na and 12K [14, 15]. Experimental data is limited and consequently the transition temperatures have not yet been accurately determined. Nevertheless, important characteristics have already been seen which point to a transitional smoothing at longer chain lengths and heavier ions accompanied by a shift in transition temperature. In this short additional section the model in [11] is extended to provide a qualitative prediction of the behaviour in 14Na and 12K.

The calculations of both intra and inter-disc Coulomb interactions (U_n and J_{mn}) were repeated using the same procedure outlined in [11] only with a slightly larger radius of 1.38 Å for the K^+ ions, parameters are given in Table 3.1 alongside those for Na reported in [11] for comparison. With a larger cation both (U_n and J_{mn}) are more strongly attractive and subsequently $U_3 - U_4$ is increased from 91 J/mol to 143 J/mol whereas $J_{33} - J_{44}$ decreases from 1151 J/mol to 1097 J/mol. Remarkably the increase in $U_3 - U_4$ is almost completely offset by the decrease in $J_{33} - J_{44}$ such that the transition temperature in potassium K^+ is raised by less than 1 Kelvin in comparison to Na. The value of the model parameter $K = J_{33} + J_{44} - 2J_{43}$, which disfavors mixing of unlike discs, is much larger which will sharpen the transition dramatically.

Increasing the chain length from 12 to 14 carbons required running further simulations



Figure 3.1: Unprocessed synchrotron XRD data for compounds 12Na, 14Na and 12K showing how the lattice parameter varies with temperature. The compounds shown here all show similar first-order transitions between hexagonal columnar phases. Note Col_r and Col_h denote rectangular and hexagonal phases respectively. Reproduced with permission from [14].

of the end chains, following exactly the same procedure outlined in [11], using a coarse-grained representation of the terminal chains, see Section 2.3.3.6 or [11] SI. It is worth noting that the change in core size, when moving from Na to K, was too small to be felt by the end chains in the current model when re-evaluating their free energy. For larger cations however i.e. Rb or Cs this should be taken into consideration since this may alleviate the geometrical frustration felt by the terminal chains close to the column core. At longer chain lengths both $F_3^{(l)}(T)$ and $F_4^{(l)}(T)$ are more strongly negative with increasing temperature and in addition $F_3(T) - F_4(T)$ is more weakly negative. This is due to the restricted geometry being less strongly felt for longer chain lengths until very high temperatures resulting in a transitional smoothing in 14Na in comparison to 12Na.

It was then quickly realised that with the current set of calculated parameters the transition temperature in 12K would be nearly identical to that of 12Na in stark contrast with experiment, see Figure 3.1. Previously the model had not considered the mass of the metal cations and the subsequent free energy contribution resulting from phonon vibrations in the core of cations. Therefore, the theory was extended to include phonon vibrations to see if this may be responsible for the decreased transition temperature seen in 12K experimentally.

When calculating the Coulomb interactions inside the core of cations as outlined in [11], it was necessary to minimise the idealised configuration of alternating cations and anions by varying the angle subtended by the metal cation and the static oxygen anions. This amounts to displacing the metal cations in both the $x - y$ and z directions by bringing the static oxygen anions closer to one another. In Figure 3.2 the potential functions are plotted for all the possible modes in 12Na, where the cation configurations at both the minimum and the extremes have been drawn in for clarity. Upon doing so it was noticed that the potentials for all cations had surprisingly flat minimums, hence their oscillations around the potential may make a significant contribution to the free energy.

In order to extend the model we consider that there are n modes per n molecules and write the partition function of the phonon vibrations as the following

$$\mathcal{Z}_n = \mathcal{Z}_n^{(y)} + \mathcal{Z}_n^{(z)} \quad \mathcal{Z}_n = \frac{1}{n} \frac{n}{\beta \hbar \omega_n} \quad \omega_n = \sqrt{\frac{k_n}{m}} \quad (3.1)$$

where $\mathcal{Z}_n^{(y)}$ and $\mathcal{Z}_n^{(z)}$ are the contributions from displacing the M^+ cations in the x - y and z directions respectively, n is the number of modes equivalent to the number of molecules, ω_n is the angular frequency of the vibration, m is the mass of the constituent

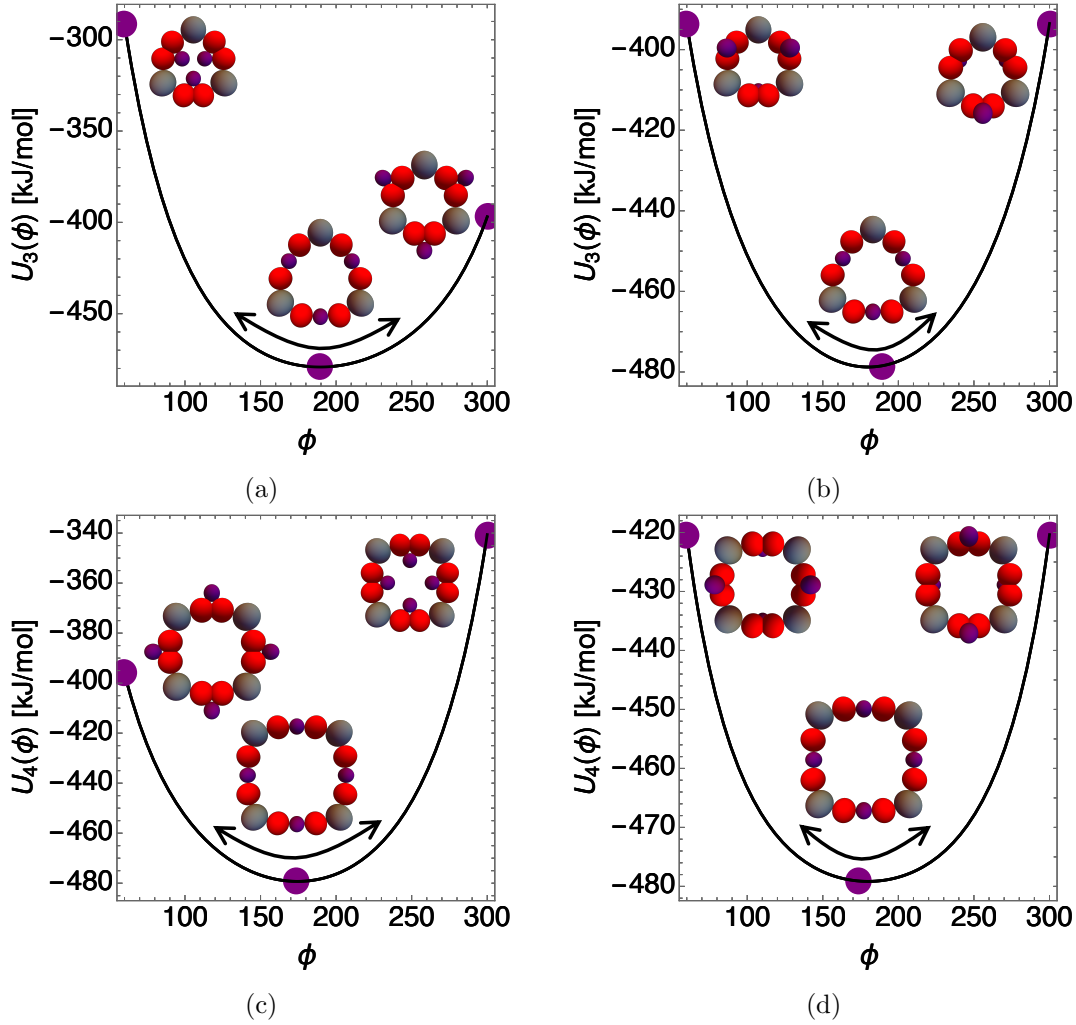


Figure 3.2: All possible modes for 12Na, other cations are not shown. The purple atoms denote the metal cations and their respective position in the potential function. (a) $U_3(\theta_{xy}, \theta_{zmin})$, (b) $U_3(\theta_{xymin}, \theta_z)$, (c) $U_4(\theta_{xy}, \theta_{zmin})$, (d) $U_4(\theta_{xymin}, \theta_z)$

molecules and k_n is the spring constant. Which may be written as the following

$$\mathcal{Z}_n = \frac{1}{\beta \hbar} \left(\frac{1}{\omega_n^{(y)}} + \frac{1}{\omega_n^{(z)}} \right) = \frac{1}{\beta \hbar} \frac{\omega_n^{(y)} + \omega_n^{(z)}}{\omega_n^{(y)} \omega_n^{(z)}} \quad (3.2)$$

The free energy of n molecules may then be written as the following using the usual

definition as outlined in Section 2.2.3.

$$F_n^{(v)}(T) = -k_B T \log[\mathcal{Z}_n] = -k_B T \log \left[\frac{1}{\beta \hbar} \frac{\omega_n^{(y)} + \omega_n^{(z)}}{\omega_n^{(y)} \omega_n^{(z)}} \right] \quad (3.3)$$

The masses in this case are unknown but for our model they are not required. Recall that the quantity of interest is in fact $F_3^{(v)}(T) - F_4^{(v)}(T)$ and by performing this simple subtraction, the unknown masses cancel. Using equation 3.1 the contribution to the free energy of vibrational motion is given by.

$$F_3^{(v)}(T) - F_4^{(v)}(T) = k_B T \log \left[\frac{\sqrt{k_y^{(3)}} + \sqrt{k_z^{(3)}}}{\sqrt{k_y^{(4)}} + \sqrt{k_z^{(4)}}} \sqrt{\frac{k_y^{(4)} k_z^{(4)}}{k_y^{(3)} k_z^{(3)}}} \right] = QT \quad (3.4)$$

The spring constants may then be calculated by performing a simple kx^2 fitting of the curves shown in Figure 3.2, the exact parameters for the spring constants are given in Table 3.1. The contribution to the free energy was found to be of the order of $k_B T$ in the temperature region of interest, the effect of vibrations on the free energy curves can be seen in Figure 3.3(a).

Since the transition temperature in 12K had not yet been accurately determined new parameters acquired from fitting the experimental data could not be relied upon. Instead however a prediction could be made by making some sensible assumptions. Firstly since the core size and lattice parameters are almost identical in 12Na and 12K, see Figure 3.1, the mean field parameters must be similar if not identical since $E \propto e^{-\frac{r}{\lambda}}$. The inter-disc interaction parameters J_{33} and J_{44} for Na were increased by 0.3% and 6.6% without vibrations and 0.3% and 8.7% respectively with vibrations to fit the experimental data and so we assume the values are reduced by the same amount for the K^+ ions as well. The fitted intra-disc interaction values in Na were identical to the calculated values and were not changed hence the same is assumed to be true for K. The free energy of the end chains was also assumed to be identical in both 12Na and 12K. This yields the parameter

set in Table 3.1 which may be used to provide a model prediction for 12K and 14Na with or without phonon vibrations included in the model.

lM^+	U_3 (J/mol)	U_4 (J/mol)	J_{33} (J/mol)	J_{44} (J/mol)	J_{43} (J/mol)	λ (J/mol)	μ (J/mol)	Q (J/mol/K)
As Calculated								
12Na	-479198	-479289	-10090	-11241	1096	0	0	-0.638300
12K	-417546	-417689	-14637	-15734	1412	0	0	-1.18987
Without Vibrations								
12Na	-479198	-479289	-10030	-11985	0	115	190	0
14Na	-479198	-479289	-10030	-11985	0	115	190	0
12K	-417546	-417689	-14694	-16775	0	115	190	0
With Vibrations								
12Na	-479198	-479289	-10030	-12220	0	130	190	-0.638300
14Na	-479198	-479289	-10030	-12220	0	130	190	-0.638300
12K	-417546	-417689	-14694	-17104	0	130	190	-1.18987

Table 3.1: Parameters as calculated for 12Na (green) and 12K (blue), mean field terms were not calculated. Fitted parameters with and without vibrations included for 12Na (fitted), 12K (estimated) and 14Na. Calculations were performed as described in Publication 3.2, see SI.

In Figure 3.3 beginning with the increase in chain length from 12 to 14 in Na. The new curves show a clear transitional smoothing and an increase in transition temperature with increasing chain length. Most notably the transition in 14Na is still first-order but this time with a smaller discontinuity than in 12Na. This is consistent with the experimental curves in Figure 3.1 for 14Na (red), note the smaller jump in comparison to 12Na (green). The raised transition temperature however is not consistent and early experimental results suggest that the transition temperature is somewhere below 14Na, see Figure 3.1. This is likely to be due to the increased distance between neighbouring columns resulting from the enlarged chain length consistent with the increased lattice parameter seen in Figure 3.1. It is likely that reducing the mean field terms would bring the transition in 14Na below that of 12Na and into line with experiment.

Including vibrations in Na has the effect of smoothing the transition and lowering the

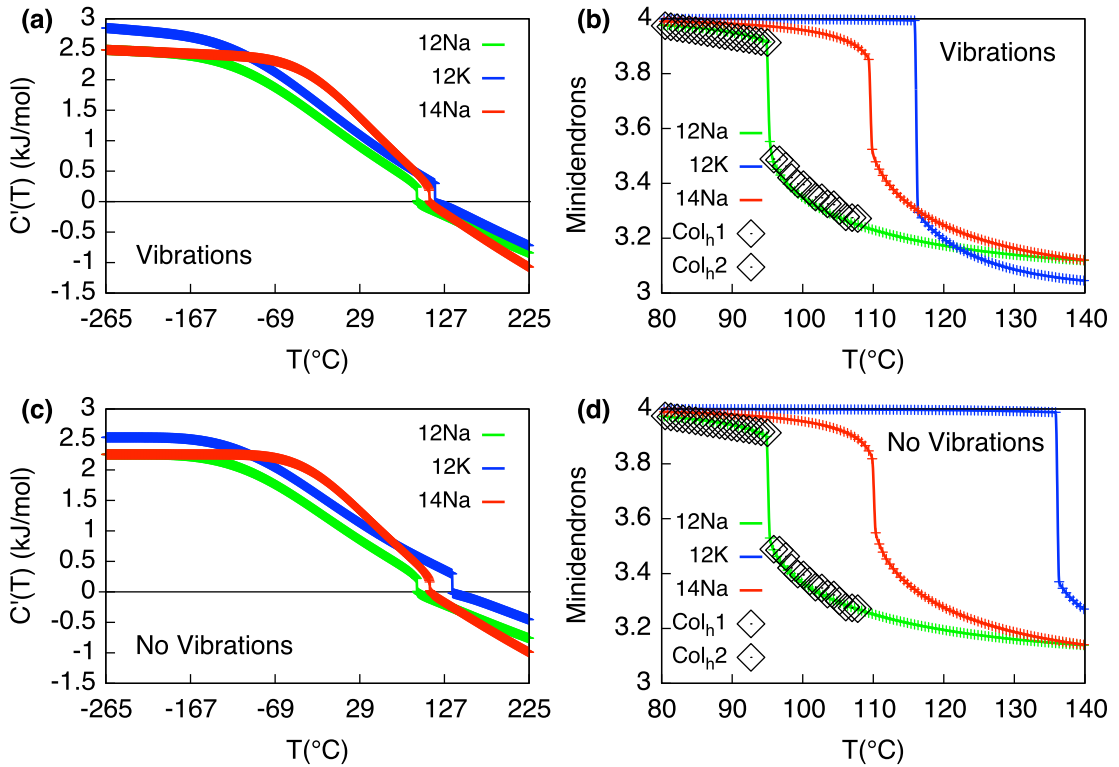


Figure 3.3: Model predictions with and without vibrations included: (a) $C'(T)$ vs temperature with vibrations. (b) model fit for 12Na (green) and predicted curves for 12K (blue) and 14Na (red) shown alongside the calculated number of minidendrons per discs from experiment for 12Na as given in [11]. (c) $C'(T)$ vs temperature without vibrations (b) model fit for 12Na (green) and predicted curves for 12K (blue) and 14Na (red) shown alongside the calculated number of minidendrons per discs from experiment for 12Na (green) as given in [11]. The full set of parameters can be found in Table 3.1.

transition temperature by a small fraction. The J_{44} parameter was increased by around 0.2 kJ/mol, from its fitted value without vibrations included, in order to raise the transition temperature to refit the experimental data. The mean field term λ was also raised by around 5 J/mol to compensate for the transitional smoothing brought on by vibrations. The predicted parameters for 12K show an increase in transition temperature and a stronger first-order jump, both characteristics appear inconsistent with Figure 3.1 with and without vibrations. The transition temperature is closest to the experimental trend with vibrations included however and clearly illustrate how vibrations have a

much larger effect on heavier ions, reducing the transition temperature. This Chapter, the shortcomings of the model extension and suggested improvements will be discussed in Section 7.1.

Bibliography

- [1] F. Reinitzer. *Monatshefte für Chemie/Chemical Monthly*, 9(1):421–441, 1888.
- [2] G. W. Gray and S. M. Kelly. *Journal of Materials Chemistry*, 9(9):2037–2050, 1999.
- [3] R. Williams. *The Journal of Chemical Physics*, 39(2):384–388, 1963.
- [4] P. J. Collings. *Liquid crystals: nature’s delicate phase of matter*. Princeton University Press, 2002.
- [5] X. Feng, M. E. Tousley, M. G. Cowan, B. R. Wiesenauer, S. Nejati, Y. Choo, R. D. Noble, M. Elimelech, D. L. Gin, and C. O. Osuji. *ACS Nano*, 8(12):11977–11986, 2014.
- [6] P.-G. De Gennes and J. Prost. *The physics of liquid crystals*, volume 83. Oxford university press, 1993.
- [7] S. John and T. Lubensky. *Physical Review B*, 34(7):4815, 1986.
- [8] D. R. Nelson and B. Halperin. *Physical Review B*, 21(11):5312, 1980.
- [9] Y. Li, S.-T. Lin, and W. A. Goddard. *J. Am. Chem. Soc.*, 126(6):1872–1885, 2004.
- [10] P. Zihlerl and R. D. Kamien. *J. Phys. Chem. B*, 105(42):10147–10158, 2001.
- [11] W. S. Fall, M.-H. Yen, X. Zeng, L. Cseh, Y. Liu, G. A. Gehring, and G. Ungar. *Soft Matter*, 15(1):22–29, 2019.

- [12] X. Zeng, R. Kieffer, B. Glettner, C. Nürnberger, F. Liu, K. Pelz, M. Prehm, U. Baumeister, H. Hahn, H. Lang, et al. *Science*, 331(6022):1302–1306, 2011.
- [13] S. George, C. Bentham, X. Zeng, G. Ungar, and G. A. Gehring. *Physical Review E*, 95(6):062126, 2017.
- [14] Y. Liu. *Two-and three-dimensional liquid crystalline structures in self-assembled supramolecular dendrimers*. PhD thesis, University of Sheffield, 2004.
- [15] M.-H. Yen. *Self-Assembly of Minidendrons in 2D and 3D Liquid Crystal Lattices and Superlattices*. PhD thesis, University of Sheffield, 2015.

Chapter 4

X-Shaped Bolapolyphiles

4.1 Introduction

X-Shaped molecules comprising of a rigid backbone with polar groups at either end with different, sometimes incompatible side arms have been demonstrated to form complex compartmentalised 2d nano-scale structures or tilings. In these tiling patterns the walls are formed by the rigid backbone and the flexible side chains fill the centres of their respective nano-compartments. Such structures can be simple trigonal or hexagonal tilings [1, 2], more complicated networks of small and large honeycombs [3] to highly complex multicolour tilings [2] and more recently even quasi-periodic tilings [4], see Figure 4.1. These different packings generally arise from tiny variations in chain length between the side chains and the rigid backbone, the chemical composition of the side chains themselves, their compatibility and even the swapping of polar groups. The compatibility between side chains often leads to micro-phase separation of chains into their respective compartments, such that compartments have different chemical compositions or colours.

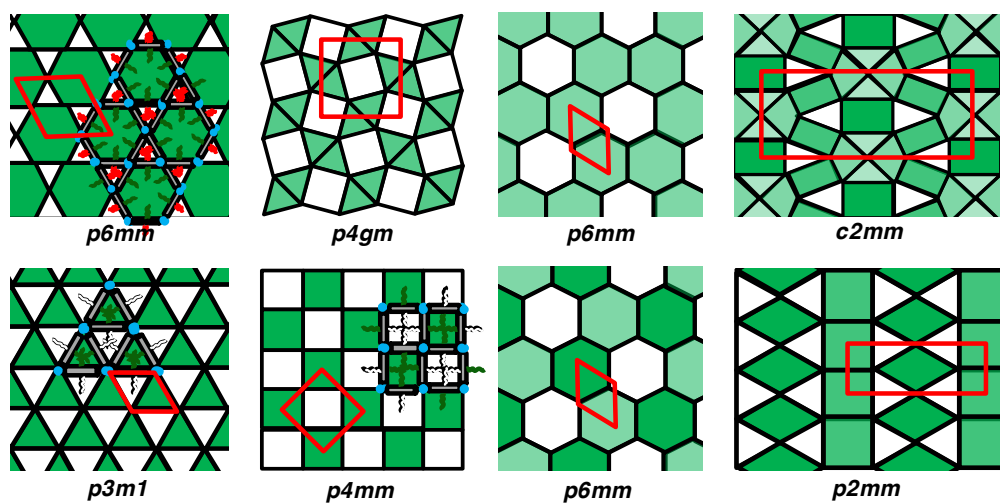


Figure 4.1: Example tilings found in X-shaped compounds.

The ordering phenomena in these systems have been likened to that of magnetic systems in condensed matter physics, in particular the ordering of Ising or Potts models on various periodic lattices such as trigonal or hexagonal. In the original magnetic system spin flips are replaced by 180° rotations of the molecules around the molecular backbone. Only two such comparisons have been drawn before. In the first a mean field theory of a strongly frustrated hexagonal tiling was devised [2], considering only pairwise interactions between side chains inside the nano-compartments which predicted the formation of a semi-ordered intermediate phase. In the second, the existence of an intermediate phase prompted a further MC study into this strongly frustrated liquid crystal in which two-phase transitions were reported [5]. First a single-colour disordered phase moves into a strongly frustrated two-colour intermediate tiling on cooling and onto a final three-colour ordered tiling at low temperatures, the latter phase although predicted remains undiscovered in LC tilings.

Until now one of the simplest structures had eluded discovery in X-shaped compounds with incompatible side chains, one which is notoriously difficult to stabilise [6], the ordered square honeycomb tiling. This pattern has previously only been found in

block-copolymers with a relatively large nano-compartments [7]. In this work the first sub 5nm square honeycomb tiling is reported in a LC formed from X-shaped bolamphiphiles with two mutually incompatible perfluoroalkyl and carbosilane side chains [8, 9]. The LC exhibits an unusual order-disorder transition between a two-colour chessboard tiling at low temperatures, where the side chains segregate into their respective cells, to a single-colour mixed disordered phase at high temperatures. Interestingly this system is exactly analogous to the 3d Ising model under Kawasaki spin flips dynamics moreover since the dimensionality and number of degrees of freedom are identical it is certain to have the same critical exponents as the 3d Ising universality class.

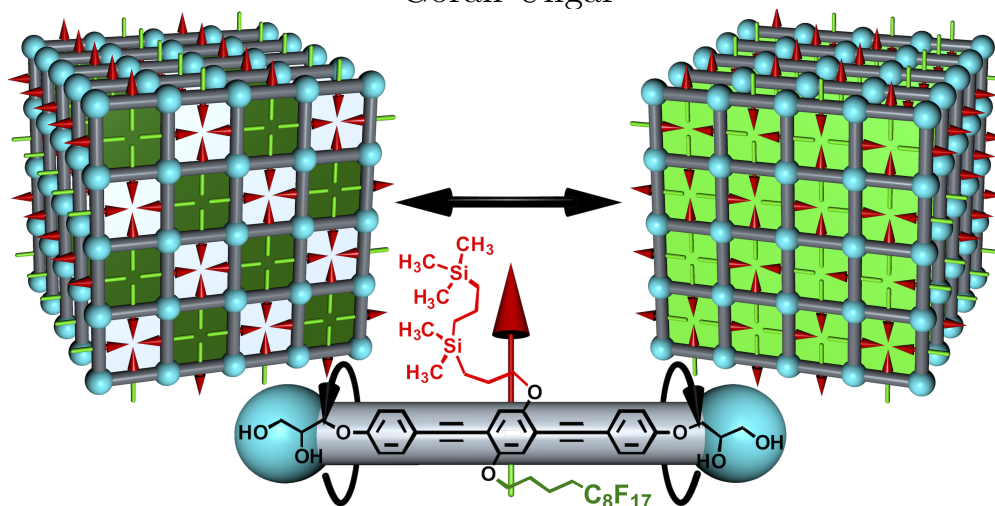
This motivated a six week undergraduate research experience project to study the simple ordering phenomena in this model system in 2d. It was decided that I would co-supervise the project a write C++ code for the student and provide the computational expertise as part of the doctoral development programme. It was later realised that the problem was more complex in two important ways, firstly that ordering was occurring in 3d and that kinematic effects were also important. I continued working on the problem after the project had finished and the results are published in [8].

4.2 Published Article 2

Molecular Systems Design & Engineering

An Ising Transition of Chessboard Tilings in a Honeycomb Liquid Crystal

William S. Fall, Constance Nürnberger, Xiangbing Zeng, Feng Liu,
Stephen J. Kearney, Gillian A. Gehring, Carsten Tschierske and
Goran Ungar



Author Contributions

G.U. and C.T. conceived and directed all aspects of the project. C.N., supervised by C.T. and X.Z carried out the experiments. W.S.F. and S.J.K, supervised by G.A.G., X.Z and G.U. carried out the MC simulations. W.S.F wrote the program. F.L. performed MD simulations in materials studio. All authors contributed to data analysis and production of tables and figures. W.S.F and G.U. prepared the manuscript with written contributions from all co-authors. See page **vii** for author declarations.



Cite this: DOI: 10.1039/c8me00111a

An Ising transition of chessboard tilings in a honeycomb liquid crystal†

William S. Fall,^{a,c} Constance Nürnberger,^b Xiangbing Zeng,^b Feng Liu,^a Stephen J. Kearney,^c Gillian A. Gehring,^{b,c} Carsten Tschierske^b and Goran Ungar^b

We have designed a compound that forms square liquid crystal honeycomb patterns with a cell size of only 3 nm and with zero in-plane thermal expansion. The compound is a bolaamphiphile with a π -conjugated rod-like core and two mutually poorly compatible side-chains attached on each side of the rod at its centre. The system exhibits a unique phase transition between a “single colour” tiling pattern at high temperatures, where the perfluoroalkyl and the carbosilane chains are mixed in the square cells, to a “two-colour” or “chessboard” tiling where the two chain types segregate in their respective cells. Small-angle transmission and grazing incidence X-ray studies (SAXS and GISAXS) indicate critical behaviour both below and above the transition. Both phase types are of considerable interest for sub-5 nm nanopatterning. The temperature dependence of ordering of the side chains has been investigated using Monte Carlo (MC) simulation with Kawasaki dynamics. For a 3-dimensional system with 2 degrees of freedom, universality predicts that the transition falls into the 3d Ising class; MC was therefore used to calculate observables and determine the critical exponents accessible in experiment. Theoretical values of ν , γ and, perhaps most importantly, of the order parameter β have been calculated and then compared with those determined experimentally. β found experimentally is close to the theoretical value, but ν and γ values are significantly smaller than predicted. To explain the latter, the measured susceptibility above T_c is compared with those from simulations of different lattice sizes. The results suggest that the discrepancies result from a reduced effective domain size, possibly due to kinetic suppression of large scale fluctuations.

Received 14th December 2018,
Accepted 28th January 2019

DOI: 10.1039/c8me00111a

rsc.li/molecular-engineering

Design, System, Application

For surface patterning on a sub-10 nm scale, self-assembling columnar liquid crystals with 2d long-range periodicity, are the natural choice. For application in nano-electronics, the pattern should ideally be square and have zero in-plane thermal expansivity. Moreover, it may be desirable to add a degree of complexity in the pattern, such as producing a “chessboard” pattern with alternative squares chemically different thus, *e.g.* combining alternating p- and n-semiconducting pathways, or electronically and ionically conducting channels, or similar. This report shows how such a system can be achieved in principle, based on an inverse columnar phase where a bistolane rod-like core provides a fixed-sized square honeycomb framework held together by H-bonding glycerol end-groups. The prismatic cells are filled alternately by a semiperfluorinated (F) and a carbosilane (Si) chain, respectively attached to either side of the linear core. The chessboard structure with 3 nm alternating square cells is achieved through an appropriate choice of the core length, side-chain area to core length ratio, and the level of incompatibility between the side-chains, as detailed in the Introduction.

Introduction

Among numerous well established or developing applications of liquid crystals (LC) is nanoscale patterning on the sub-10 nm length scale.^{1,2} Such patterning may be used in organic electronics and photovoltaics,^{3–8} in selective membranes,^{9–11} for ion conducting arrays,^{12,13} cubosomes¹⁴ and hexosomes¹⁵ for drug delivery *etc.* For use in soft nanolithography highly ordered arrays are required, preferably with a square or rectangular lattice and high dimensional stability, ideally with zero thermal expansion. Self-assembled square arrays with high order have been achieved using block copolymers, but

^a State Key Laboratory for Mechanical Behaviour of Materials, School of Materials Science & Engineering, Xi'an Jiaotong University, Xian 710049, China

^b Department of Chemistry, Martin Luther University Halle-Wittenberg, Kurt-Mothes-Str. 2, 06120 Halle, Germany.

E-mail: carsten.tschierske@chemie.uni-halle.de

^c Department of Physics and Astronomy, University of Sheffield, Sheffield S3 7RH, UK. E-mail: g.gehring@sheffield.ac.uk

^d Department of Materials Science and Engineering, University of Sheffield, Sheffield S1 3JD, UK. E-mail: x.zeng@sheffield.ac.uk, g.ungar@sheffield.ac.uk

† Electronic supplementary information (ESI) available: Optical micrographs, DSC traces, X-ray diffraction data, volume fractions and electron densities of constituent moieties, details of synthesis and chemical characterization, energies used in MC simulation. See DOI: 10.1039/c8me00111a

not on a sub-10 nm scale.¹⁶ Columnar LC phases are an obvious choice for sub-10 nm and even sub-5 nm arrays. But the conventional columnar phases, with an aromatic column core and a peripheral corona of flexible, most often aliphatic chains, usually have hexagonal symmetry.^{17,18} Rectangular columnar phases are not rare, but typically they are centred (plane group $c2mm$), meaning that they are again just distorted hexagonal arrays. Square columnar phases are exceptions.^{19,20} Even compounds with a square molecular shape mainly form hexagonal lattices, because the soft aliphatic corona allows rotational averaging around the column axis.

Promising and already extensively studied bolaamphiphiles consisting of a polyaromatic rod-like core, H-bonding end-groups and laterally attached flexible chains, have shown great versatility in forming a range of “inverted” columnar LC phases, *i.e.* honeycombs with aromatic walls (the “wax”) and the side-chains as cell fillers (the “honey”).^{21–24} These honeycomb networks prevent rotational averaging. The number of sides in the polygonal cross-section of a prismatic cell (the “tile”) is determined by the ratio between the area of the filler side-chains to the length of the rod-like core. Normally the side length of the polygon equals the length of the molecule, although in some cases double-length sides were found containing two end-linked rods.^{25,26} A range of tiling patterns have been obtained in this way, from simple triangular to highly complex nanopatterns containing up to five different coexisting tile types.²⁷ Square patterns were, however, only found under special circumstances in a small temperature range.^{21,28} *E.g.*, Recently, several members of a series of terphenyl-based bolaamphiphiles were found to exhibit non-centred ($p2mm$) rectangular lattices; however the cell aspect ratio was highly temperature sensitive, reaching 1 : 1 (square lattice) only close to isotropization temperature.²⁹

Beside their application potential, LCs are of considerable scientific interest, providing soft matter and low-dimensional equivalents to phenomena such as phase transitions, extensively studied in more traditional areas of condensed matter physics. Well known examples include the nematic to smectic-A transition³⁰ and the twist-grain-boundary (TGB) smectic phase,³¹ both having their analogue in superconductivity, as well as the hexatic smectics being easily accessible examples of 2D melting phenomena.³² Ferro-, ferri- and anti-ferroelectric chiral smectics³³ and the currently topical twist-bend nematic phase^{34,35} are further examples of new states of condensed matter. In contrast to numerous studies of phase transitions in nematics and smectics, transitions in thermotropic LCs with two-dimensional order have been investigated in only a few cases experimentally^{36–38} or by theory and simulation.^{27,39–44}

In the LC square patterns previously reported all squares were uniform. In order to increase functionality, the combinations of different squares, filled with different materials would be required. For this purpose a change in molecular design was required, whereby the single lateral alkyl chain of the above-mentioned terphenyls is replaced by two different and incompatible chains at the two opposite sides of the

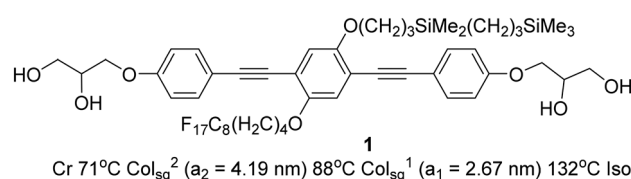
rod-like unit. The incompatibility between perfluorinated alkyl chains and hydrocarbon chains⁴⁵ is a successfully employed approach to obtaining multicolour tiling patterns.^{24,25} However, in order to achieve adequate incompatibility the number of CH₂ and CF₂ units must be sufficiently large for the demixing energy to overcome the entropy penalty. However, these longer chains require more space in the prismatic cells. In order to retain square cells, the terphenyl cores forming the honeycomb were extended by the incorporation of additional ethynyl units between the benzene rings. Furthermore, in order to lower the crystal melting point, a highly branched carbosilane unit was used instead of a linear alkyl chain. The introduction of silicon as branching points into a hydrocarbon chain allows a synthesis in fewer steps than would be required for similarly branched hydrocarbons.

Here we report the self-assembly of a new LC system, formed by a bolapolyphile with a 1,4-bis(phenylethynyl) benzene (“bistolane”) core⁴⁵ with two disparate chains attached laterally to the 2 and 5 positions (compound 1, Scheme 1).

As will be shown in the following sections, this compound is found to form a square honeycomb with exceptional dimensional stability. Moreover it displays a disorder–order transition from a uniform square tiling to a two-colour chessboard-type tiling where the two side-chains segregate in separate square cells. The transition is thought to be a close real life example of the well-known and widely studied Ising model of magnetic spins.⁴⁶ Monte Carlo simulations show the critical behaviour (*e.g.* development of short range fluctuations and long range order around the phase transition temperature), observed by X-ray diffraction, to closely match the 3D Ising model on both sides of the transition, provided the finite domain size is taken into account.

Experimental results

The synthesis of compound 1 was performed by Sonogashira coupling as the key steps⁴⁵ as described in the ESI.† Polarized optical microscopy (POM) images (Fig. 1 and S1†) show birefringent textures with frequent fan shapes. In fact large areas of the images remain black (Fig. 1a and c) indicating that the mesophase is optically uniaxial with the optic axis perpendicular to the glass surface (homeotropic alignment). The birefringence persists up to 132 °C. Differential scanning calorimetry (DSC) shows a weak melting endotherm on second heating around 70 °C, and a sharp isotropization peak at 132



Scheme 1 Compound 1 and its transition temperatures (Cr = crystal, Col_{sq}² = two-colour square columnar phase, Col_{sq}¹ = single-colour square columnar phase, Iso = isotropic liquid).

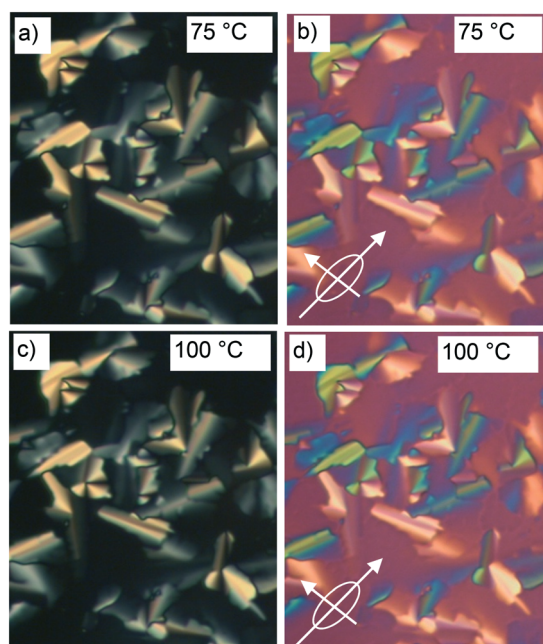


Fig. 1 Optical micrographs of compound **1** between crossed polarizers recorded at (a and b) 75 °C and (c and d) 100 °C. Images b and d were recorded with an additional λ retarder plate, whose indicatrix orientation is depicted in the images. The field-of-view width is 0.1 mm.

°C, transition enthalpy 5.6 J g^{-1} (Fig. S2†). The latter transition shows very little hysteresis on cooling, while crystallisation is completely suppressed at the cooling rate used (10 K min^{-1}).

Powder small-angle X-ray scattering (SAXS) curves of compound **1** recorded during continuous heating at 0.5 K min^{-1} are shown in Fig. 2a. The bold trace at $T_c = 88 \text{ °C}$ marks the phase transition between two square columnar phases. In both phases reflections indexed as (10), (11), (20) etc. are seen, their q^2 ratio being 1:2:4:5.... This defines the plane group as $p4mm$ in both cases. Most notable is the decay and eventual disappearance of the strong (10) reflection of the low- T phase at T_c , along with the disappearance of (21) and (30) peaks. On heating above T_c the intensity of the remaining Bragg peaks stays almost unchanged: the (11), (20) and (22) diffraction peaks transit smoothly into the (10), (11) and (20) peaks of the high- T square phase. Remarkably also, the remaining peaks do not shift in the entire range from room temperature to the isotropization temperature T_i .

The above indexing of the diffraction pattern was also confirmed by grazing incidence SAXS (GISAXS) experiments on a surface-oriented thin film of **1** on silicon substrate, as shown in Fig. 3. Although most of the sample is homeotropic, giving diffraction peaks on the horizon line, off-equatorial reflections are also seen from areas where the columns lie parallel to the surface, rotationally averaged in the film plane. The most notable feature in Fig. 3 is the existence of strong diffuse scattering above T_c in place of the (10) Bragg reflections of the low- T phase – the relationship is highlighted by the

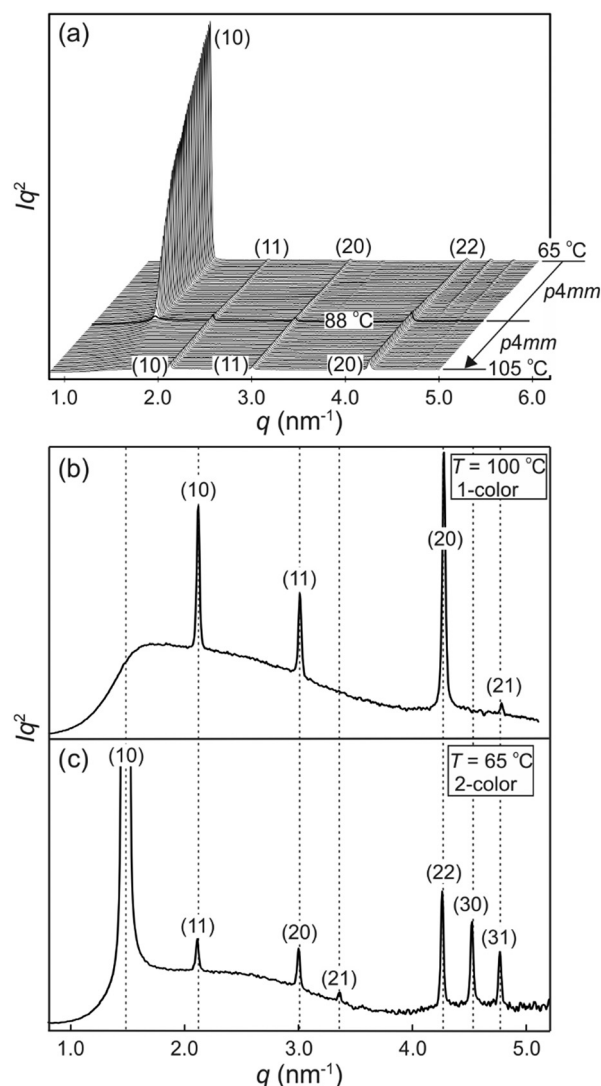


Fig. 2 Powder SAXS traces of compound **1**. (a) Stacked traces recorded during heating at 0.5 K intervals . The bold curve is recorded at T_c (b and c) SAXS trace of the high-temperature 1-colour square honeycomb phase at 100 °C (b), and of the low-temperature 2-colour chessboard phase recorded at 65 °C . Miller indices (hk) apply to the respective lattices.

light blue lines in Fig. 3. This indicates the persistence of short-range critical electron density fluctuations above T_c , which will be analysed quantitatively further below.

The lattice parameters a_1 and a_2 of the high- and low- T phases are 2.96 nm and 4.19 nm , respectively. As the ratio is exactly $\sqrt{2}$, the area of the unit cell of the low- T phase is twice that of the high- T phase. Electron density maps, calculated on the basis of relative diffraction intensities and the selected structure factor phases given in Table S1,† are shown in Fig. 4a and c.

Considering the molecular model, we note that $a_1 = 2.96 \text{ nm}$ is very close to the $2.80\text{--}3.05 \text{ nm}$ length of the molecule, as measured between the ends of the glycerol groups, depending on the glycerol conformation. This, combined

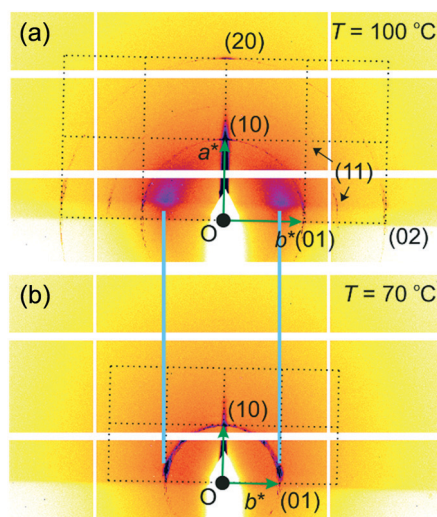


Fig. 3 GISAXS pattern of the (a) 1-colour phase and (b) 2-colour phase. Dotted lines indicate the reciprocal lattice applicable to areas with planar columns. The majority of the sample is homeotropic, giving rise to all-equatorial reflections; these are visible in the top pattern (note the (11) arc near the horizon), but not in the bottom one, as these reflections are beyond the horizon because of the slightly higher tilt of the substrate plane relative to the incident beam.

with the fact that the high birefringence axis (*i.e.* the long axis of the π -conjugated molecular core) is perpendicular to the columns (see POM images with a λ retarder plate in Fig. 1b and d and S1c†), strongly suggests the model in Fig. 4b for the high- T phase. Such a model is consistent with the general self-assembly mode of bolapolyphile LC honeycombs, except that a square honeycomb is rather rare. In this structure the cell walls consist of molecular cores lying normal to column axis with each of the two side chains located in the two neighbouring cells. In the high- T phase the cells are filled on average with a 1:1 mixture of F and Si chains. The model in Fig. 4b has been subjected to 30 cycles of molecular dynamics annealing between room T and 700 K lasting 30 ps in total. It shows a reasonable packing density, indicating that the model is feasible. It is also consistent with the electron density map, where the light blue squares reflect the fact that the average electron density of the combined F and Si chain (572 e nm^{-3}) is somewhat higher than that of the bistolane/glycerol core (518 e nm^{-3}) – for details see Table S2.†

The doubling of the unit cell below T_c , the high intensity of the (10) reflection of the low- T lattice, and the reconstructed electron density map in Fig. 4c all suggest that a disorder–order transition takes place at T_c , with the F and Si chains preferentially occupying alternative cells, creating a chessboard tiling as in Fig. 4c and d. In a structure with perfectly segregated Si and F chains, we calculate that the contrast between Si and F cells would be $714 - 430 = 284 \text{ e nm}^{-3}$, which is >5 times higher than the contrast between the mixed cell interior and the bistolane/glycerol wall. Hence the very much stronger (10) Bragg reflection of the chessboard

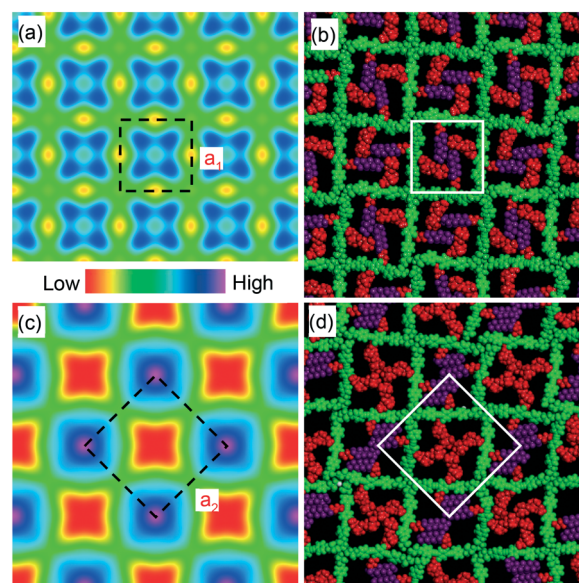


Fig. 4 (a and c) Electron density maps of the (a) high- T and (b) low- T phase in the xy plane perpendicular to the columns. The medium-high density squares in (a) (blue) contain a mixture of perfluorinated (F) and carbosilane (S) chains, the blue/purple squares in (c) contain predominantly F chains, while the red squares in (c) contain mainly Si chains. The four dark maxima in each blue square in (a) are believed to be artifacts (“ripples”) due to early truncation of the Fourier series, *i.e.* due to the small number of measured reflections. (b and d) Snapshots of molecular models after annealing dynamics runs in the (b) high- T and (d) low- T chessboard phase. Colour code: green = π -conjugated core including glycerol end groups (medium electron density), red = alkyl and carbosilane groups (lowest density), purple = perfluoroalkyl groups (highest density). For details of molecular dynamics annealing see Methods. The white squares delineate a unit cell.

phase compared to that of its (11) reflection or of the (10) reflection of the high- T phase (note that the intensity scales roughly as square of the electron density contrast).

Theory

The change of symmetry between cells, containing a disordered mix of chains, to a state where there is long range chessboard order is analogous to that of interacting Ising spins. In the model adopted here (Fig. 5) the orientation of the side chains can only take one of two values, allowing only 180° rotational jumps of the molecules around their terphenyl axes. These are equivalent to spin flips in the original magnetic model. Intermediate states are disallowed, and the energy of each cell of the system depends only on the types of side chain therein. A molecular flip alters the balance between the numbers of perfluoroalkyl and carbosilane chains in the two adjoining cells. Dynamics in which this spin or molecular ‘flipping’ impacts both neighbouring configurations is known as Kawasaki Dynamics. While the symmetry of the system changes abruptly at the transition temperature or critical temperature (T_c), a particular physical property (*e.g.* order parameter) of the system changes continuously above or below the transition,

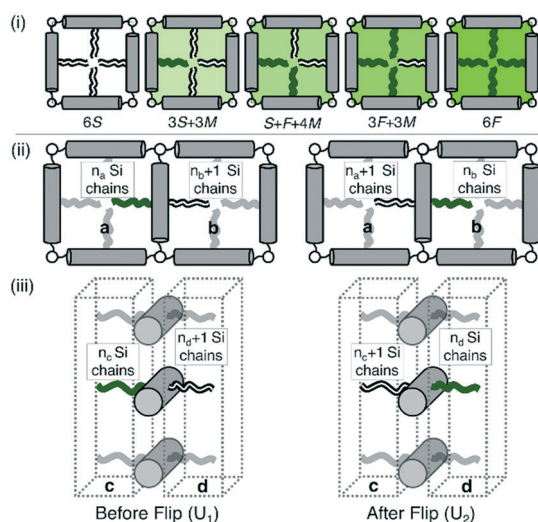


Fig. 5 (i) Allowed configurations of the square tiles and their associated energies in terms of pair interactions S, F and M (see Table 1) (ii) in plane interactions: the configurations 1 and 2 of a chain in the fully ordered state that is flipped between squares a and b. Square a contains n_a Si chains and $3 - n_a$ F chains, similarly for b. (iii) Out of plane interactions: the configurations 1 and 2 of a chain in the fully ordered state that is flipped between columnar interaction regions c and d. Region c contains n_c Si chains and $2 - n_c$ F chains, similarly for d.

and depends on some power of the magnitude of the temperature difference to the transition temperature; this power is known as a critical exponent.

Since both the dimensionality and degrees of freedom are the same, by universality, it is sensible to conclude that the model should have the critical exponents of the 3d Ising universality class. A simple lattice model has been devised and MC simulation is used to test this conjecture. The theoretical values for the critical exponents are determined and compared with experimental values in the sections that follow. It is interesting to note that due to the introduction of pairwise interactions, we conclude that there is only one significant energy in this problem; that is the energy difference between like attractive and unlike mutually repulsive chains. The ordered states are therefore found to be exactly symmetric. Any one molecule contains one chain of each type hence flipping a molecule changes the energy state of both neighbouring tiles; this is analogous to the 3d Ising model of magnetic spins under Kawasaki spin flip dynamics.

Each LC molecule is comprised of two different side chains one silicone (S) and one fluorine (F) which may pairwise interact. Like interactions are more strongly attractive than unlike interactions which results in an order-disorder transition. Within each supramolecular square the side chains can interact equally through 3 different pair interactions; these are S: Si-Si, F: F-F and M: Si-F. Crucially, chain-chain interactions within a square carry equal weight and the positioning inside the supramolecular square is neglected. The total possible number of interactions which exist in any

given square describes the squares energy, that is for n Si chains and $(4 - n)$ F chains the total energy can be expressed as the number of distinct interactions; Si-Si: $n(n - 1)/2$, F-F: $((4 - n)(3 - n))/2$ and Si-F: $n(4 - n)$.

The 5 possible configuration energies for an arbitrary square containing n Si chains and $(4 - n)$ F chains and their multiplicities are given in Table 1. The multiplicities add to $2^4 = 16$ with the largest contribution coming from configuration with an equal number of Si and F chains; indicating the importance of entropy in driving this order-disorder transition.

In Fig. 5(i) the configurations before and after a molecule has been flipped on the border between two squares is shown; this is an example of Kawasaki dynamics where the flipping of a single molecule directly changes the energy of both neighbouring squares involved. Interactions between neighbouring molecules out of plane are also included, depicted in Fig. 5(ii); these are taken to be half those in plane. The initial and final configuration energy of the 2 states, U_1 and U_2 respectively, can be expressed in terms of the pair interactions and number of Si chains in and out of plane

$$U_1 = \left(n_a + \frac{n_c}{2}\right)M + \left(4 - n_a - \frac{n_c}{2}\right)F + \left(n_b + \frac{n_d}{2}\right)S + \left(4 - n_b - \frac{n_d}{2}\right)M \quad (1)$$

$$U_2 = \left(n_a + \frac{n_c}{2}\right)S + \left(4 - n_a - \frac{n_c}{2}\right)M + \left(n_b + \frac{n_d}{2}\right)M + \left(4 - n_b - \frac{n_d}{2}\right)F \quad (2)$$

Here n_a and n_b are the number of Si chains in square a and b respectively; n_c and n_d are the number of Si chains in the respective columnar interaction regions (Fig. 5(ii) and (iii)). Hence, the energy change of flipping a molecule $\Delta U = U_1 - U_2$ can be written as

$$\Delta U = (n_a - n_b)U_0 + (n_c - n_d)\frac{U_0}{2} \quad (3)$$

The constant $U_0 = [S + F - 2M]$ is therefore the only significant energy involved in the model since any chain flip affects the chain number in both the neighbouring squares. In our case U_0 is always negative because like chains attract more strongly; a chessboard ordering can occur only for negative U_0 .

Table 1 Energy of a square with n Si chains and $(4 - n)$ F chains with pair interactions and multiplicities for each n

No. Si	No. F	Energy	Multiplicity
4	0	6S	1
3	1	3S + 3M	4
2	2	S + F + 4M	6
1	3	3F + 3M	4
0	4	6F	1

Monte-Carlo simulation and critical phenomena

Monte Carlo simulations have been performed on a 3d periodic square lattice for 5 different lattice volumes, 12^3 , 24^3 , 48^3 , 96^3 and 192^3 , in order to test the scaling properties and calculate the critical exponents. There are $V = 2L^3$ molecules involved in the simulation for each of the respective lattice volumes. The system employs the Metropolis method,⁴⁷ in which sample configurations are generated from previous states according to a transition probability. This transition probability is directly proportional to the energy difference, ΔU , between the initial and final states, given by eqn (3). Thus, by calculating the energy ΔU involved for a given molecular 'flip' between two neighbouring squares, the Boltzmann weighting can be evaluated at a specified temperature. It is therefore possible to evolve the system and subsequently sample its phase space by accepting or rejecting many flips using random sampling. This is known as the Metropolis algorithm; a molecular 'flip' is depicted in Fig. 5 which illustrates the molecular equivalent of Kawasaki dynamics for our system. It is well known that the thermodynamic exponents do not depend on the chosen dynamics *i.e.* Glauber or Kawasaki.

The 3d lattice is broken down into columns of L 2d chessboards each containing two identical sublattices A and B, this is depicted in Fig. 6. A fully ordered 2-colour tiling, (Fig. 6a) consists of alternating columns of supramolecular squares comprising of 4 Si or 4F chains such that the number of Si or F chains in either sublattice is maximised, see Fig. 6b. For a single colour tiling the columns comprise of a mixture of Si or F chains where, on average, the number of Si or F chains in any cell are equal, Fig. 6c and d. The order parameter, σ_i , for one sample configuration is defined as

$$\sigma_i = \frac{\left| \sum_{\{A\}} n_{Si} - \sum_{\{B\}} n_{Si} \right|}{V} \quad (4)$$

such that the thermal average $\langle \sigma \rangle$ approaches unity in the fully ordered state. A plot of $\langle \sigma \rangle$ is shown as a function of temperature for five lattice sizes in Fig. 7a, which shows the smoothing that occurs for small lattice sizes. Here each summation runs over square sites in lattice {A} or lattice {B} and n_{Si} represents the number of Si chains in each unit

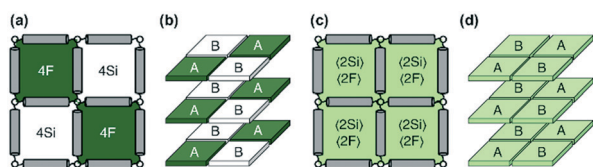


Fig. 6 (a) The fully ordered state in terms of 2d squares, (b) fully ordered state in 3d, where the sublattices A and B are indicated, (c) the fully disordered state, (d) the fully disordered state in 3d, where the sublattices A and B are indicated.

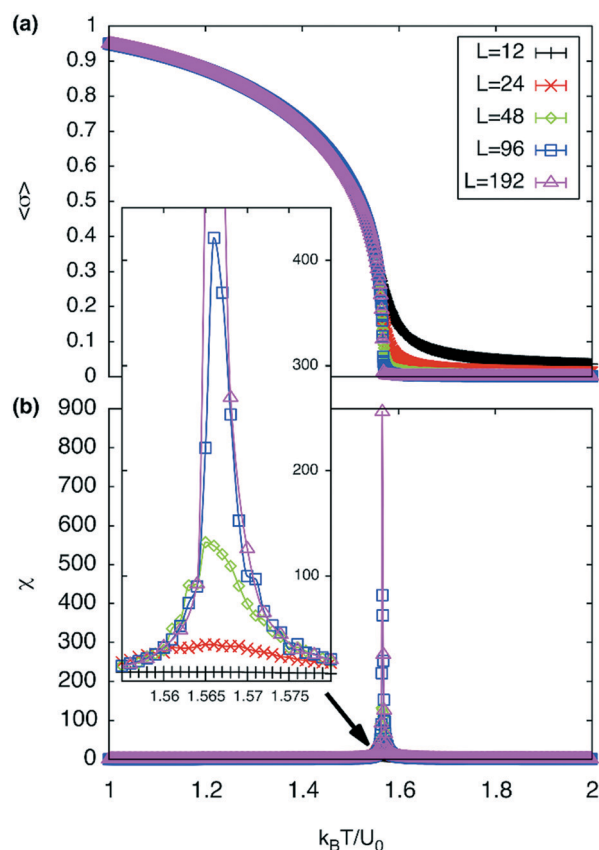


Fig. 7 (a) Order parameter per square, $\langle \sigma \rangle$, as a function of temperature and (b) susceptibility, χ , as a function of temperature. The inset contains a magnified plot of the susceptibility around T_c showing the effect of finite domain sizes.

square. The long range correlations, related to the diffuse scattering in our system, are given by the susceptibility

$$\chi = \frac{\langle \sigma^2 \rangle - \langle \sigma \rangle^2}{TV} \quad (5)$$

A plot of χ as a function of temperature is shown in Fig. 7b for 5 different lattice sizes. An initial thermalisation of 10^4 MC steps is performed and 10^5 measurements were taken at each temperature. The ensemble averages for the order parameter $\langle \sigma \rangle$ and susceptibility χ are calculated in order to construct the phase diagram. According to universality, the transition should fall into the 3d Ising universality class. By considering the scaling functions for the order parameter, and susceptibility we can confirm this by fitting to the Ising exponents, the scaling functions are given by⁴⁸

$$\begin{aligned} \tilde{X}(L^{\nu} \tau) &= L^{-\frac{\gamma}{\nu}} \chi_L(\tau) \\ \tilde{\sigma}(L^{\nu} \tau) &= L^{\frac{\beta}{\nu}} \sigma_L(\tau) \end{aligned} \quad (6)$$

here τ is reduced temperature, L is the size of the respective lattice and ν , γ and β are the critical exponents.

Measurements have been taken in the critical region in which the scaling function holds thus we consider a relatively small temperature window $1 < k_B T/U_0 < 2$. Fig. 8 shows the resulting data collapse which shows excellent agreement with the 3d Ising exponents⁴⁹ $\nu = 0.6301$, $\gamma = 1.2372$ and $\beta = 0.3265$. This not only confirms the validity of the proposed statistical model but also the universality class in which it resides.

Experimental determination of the critical exponents

The critical exponent β is related to the order parameter (sublattice magnetization) σ , below the transition temperature T_c , by the following relationship

$$\sigma = [(T_c - T)/T_c]^\beta \quad (7)$$

We make the assumption that the sublattice magnetization σ is proportional to the amplitude of diffraction, *i.e.* that the flip of direction of side groups at a side of a square cell (equivalent to a flip of spin), results in a constant increase (or decrease) to the overall structure factor $F_{(10)}$ of the (10)

diffraction peak of the two coloured square phase. As the diffraction intensity $I_{(10)}$ is proportional to $|F_{(10)}|^2$, it varies as

$$I_{(10)} \propto (T_c - T)^{2\beta} \quad (8)$$

The critical exponent β can be found by fitting the diffraction intensity $I_{(10)}$ as a function of temperature to the above equation.

The best-fit to the experimentally determined intensities suggests that $2\beta = 0.766$ and $\beta = 0.383$ (Fig. 2a and 9a). This is slightly larger than the value of $\beta = 0.326$ expected for a 3d-Ising model and also derived by our Monte Carlo simulation. For comparison, the theoretically predicted curve from the 3d Ising model is shown also in Fig. 9a (broken curve). It is evident that the observed experimental data follows the theoretical curve closely, even though the experimentally observed transition is less sharp than predicted by theory. This slight discrepancy could be attributed possibly to the system not residing in thermal equilibrium, despite the relatively slow heating rate used ($0.5 \text{ }^\circ\text{C min}^{-1}$).

While the change of order parameter below critical temperature carries information of β , two other critical exponents, γ and ν , are related to the local fluctuation-correlation of the order parameter above the critical point, *i.e.* $\langle \sigma_i \sigma_j \rangle$. Similarly to what has been discussed before, such fluctuations will be reflected in the local fluctuation of structure factor (F_i at lattice point i and F_i proportional to σ_i) and leads to diffuse scattering, with an intensity proportional to $\langle F_i F_j^* \rangle$, around $q_{(10)}$. The experimental diffuse scattering peaks just below and above the critical point are shown in Fig. 9b.

For a 3d Ising model, the correlation function $G(r)$ takes the form

$$G(r) = \frac{1}{r^{1+\eta}} \exp\left(-\frac{r}{\xi}\right) \quad (9)$$

here ξ is the correlation length. For the 3d Ising model it can thus be deduced that the diffuse scattering peak is a slightly modified Lorentzian

$$I(\Delta q) = A \left[\frac{1}{\left(\frac{1}{\xi}\right)^2 + \Delta q^2} \right]^{1-\eta/2} = \frac{A \xi^{2-\eta}}{[1 + \Delta q^2 \xi^2]^{1-\eta/2}} \quad (10)$$

Since for the 3D Ising model critical exponent η is extremely small (0.036), the diffuse peak can be treated as Lorentzian. Therefore, we have fitted the diffuse peaks as shown Fig. 9c and d to a Lorentzian function and retrieved the peak height h_D in addition the full width at half maximum (FWHM) values as a function of temperature (Fig. 9, data shown by empty circles). Above the critical point the correlation length ξ is proportional to $(T - T_c)^{-\nu}$. The peak height h_D is proportional to the susceptibility χ , and $(T - T_c)^{-\gamma}$ where $\gamma =$

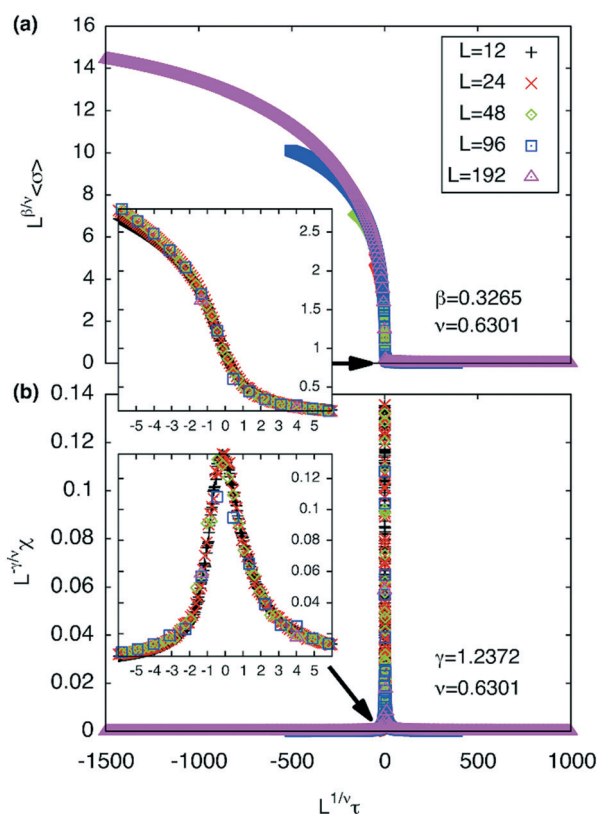


Fig. 8 (a) Scaling plot of the order parameter and (b) of the susceptibility. The fit assumes 3d Ising exponents $\nu = 0.6301$, $\gamma = 1.2372$ and $\beta = 0.3265$ where T_c is taken to be $\sim 1.5665 k_B T/U_0$. $\tau(T) = (T - T_c)/T_c$. Magnified scaling plots are shown in the inset depicting the data collapse around $\tau(T_c)$.

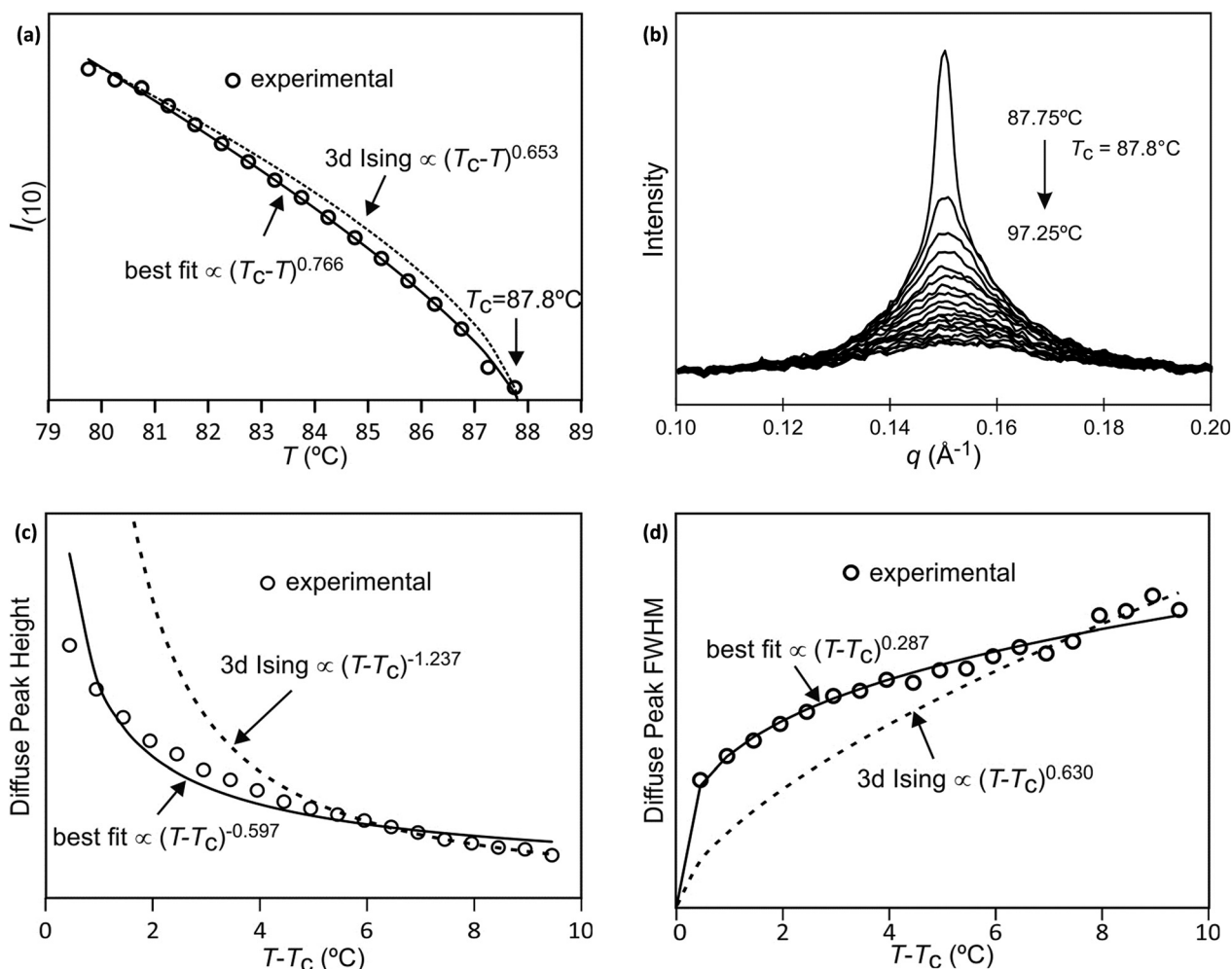


Fig. 9 (a) Fitting of $I(10)$ intensity as a function of temperature, (b) Diffuse scattering due to local fluctuation of order parameter, just below and above the critical temperature of Si2F8. Comparison of experimental data, best-fit and theoretical curves of (c) diffuse peak height and (d) FWHM above T_c .

$(2 - \eta)v$; and the FWHM $= 2/\xi$ is inversely proportional to the correlation length, therefore⁵⁰

$$\begin{aligned} h_d \propto \chi &\propto (T - T_c)^{-\gamma} \\ \text{FWHM} &= 2/\xi \propto (T - T_c)^{\nu} \end{aligned} \quad (11)$$

The best-fit and theoretical curves from fitting of peak height and FWHM of the diffuse scattering are compared in Fig. 9.

Discussion

Both best-fit values of γ (0.597) and ν (0.287) are much smaller than the theoretical values: γ should be 1.2372 and ν should be 0.6301. The most evident differences of the experimental diffuse peak to that predicted by theory are found close to the critical temperature: the diffuse peak height is expected to be much higher, while the FWHM is expected to

be much smaller *i.e.* correlation length should be much larger than observed.

Such reduction of diffuse peak height or measured susceptibility close to the critical temperature can in fact be seen in our Monte Carlo simulation with different sample sizes (number of cells). Fig. 10a shows the simulated susceptibility for four different domain sizes (12^3 , 24^3 , 48^3 , 96^3 and 192^3 cells respectively), and a significant reduction in the susceptibility close to the critical temperature can be clearly seen for domain sizes of 12^3 and 24^3 cells. In fact the trend in the 24^3 cells is very close to that experimentally observed (Fig. 10a), suggesting a domain size of only ~ 70 nm. On the other hand, the width of the (10) Bragg diffraction peak of the two-colour square phase below T_c , and of the (10) peak of the single-colour square phase above T_c , suggest a much larger domain size of ~ 250 nm. We speculate that large scale fluctuations of local two-coloured patches are likely to be restricted kinetically, as they involve converting mixed cells at the boundaries of such local patches by exchanging the directions of the two side groups of molecules (Fig. 10b). While in a spin model an

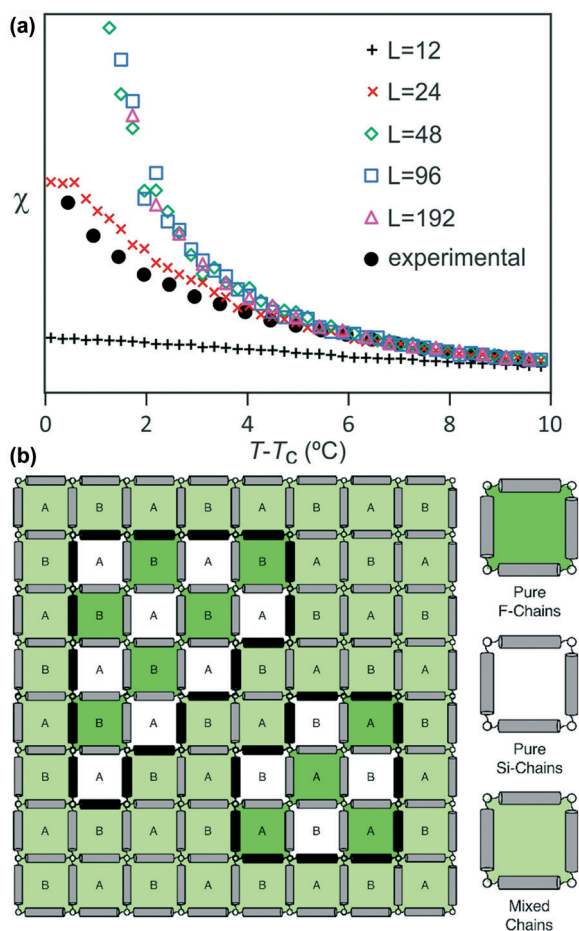


Fig. 10 (a) Comparison of experimental and simulated susceptibility, for four different sample sizes with 12^3 , 24^3 , 48^3 , 96^3 and 192^3 cells respectively, above the critical temperature. (b) Local two-coloured fluctuations in the single colour phase above the critical temperature, where A and B label the sublattices. Black molecules mark the domain walls separating the ordered and disordered patches.

inversion of spin has no energy barrier, in our system the corresponding change molecular orientation always has one. Therefore, the chance of large scale fluctuations will be significantly reduced when compared to the situation when no such energy barrier is present. This would result in a smaller effective domain size for the two-colour fluctuations.

Conclusions

We have successfully created a system that self-assembles forming square 2d patterns with a sub-5 nm period. The compound displays two types of square patterns, one simple and another of the chessboard type. The size of the square cells does not change over a 100 K temperature interval, making this type of template eminently suitable for stable nanopatterning. The order-disorder critical transition between the chessboard and simple square phases has been further investigated by Monte Carlo simulation and, as expected, it belongs to the universality class of a 3d Ising model. Good agreement between the experimental and theo-

retical values of the critical exponent β have been found. While there are apparent discrepancies for critical exponents γ and ν , Monte Carlo simulations suggest that this may result from the reduced effective domain size, as large scale fluctuations above critical temperature are suppressed for kinetic reasons.

Having learned the basic nano-architectonic principles of creating 1- and 2-colour square patterns from the above results, in a follow-up study we undertook to increase the cell size. Thus a series of related bolapolyphiles were synthesised, having a longer oligo(*p*-phenyleneethynylene) core involving five benzene rings instead of only three in the bistolane core and suitably extended side-chains.⁵¹ Both, the mixed-chain and the chessboard phases were observed for compounds with appropriate chain lengths, showing that the principles of architectural design learned from the present work are applicable to a wider class of materials and are generic.

Experimental methods

Materials

The syntheses of compound 1 and its intermediates are described in the ESI† together with the analytical data. NMR spectra were recorded with a Varian VXR spectrometer (400 MHz); HR-MS spectra were recorded on Bruker micrOTOF-Q II APPI spectrometer.

Polarizing microscopy and DSC

Phase transitions were determined by DSC (DSC-7, Perkin Elmer in 30 μ l Al pans) with heating and cooling rates of 10 K min^{-1} and by polarizing optical microscopy using a Optiphot 2 polarizing microscope (Nikon) in combination with a Mettler FP-82 Hot stage.

Synchrotron X-ray diffraction and electron density reconstruction

High-resolution small-angle powder diffraction (SAXS) experiments were recorded on Beamline I22 at Diamond Light Source. Samples were held in evacuated 1 mm capillaries. A modified Linkam hot stage was used with a hole for the capillary drilled through the silver heating block and mica windows attached to it on each side. Thermal stability was within 0.2 °C. q calibration and linearization were verified using several orders of layer reflections from silver behenate and a series of *n*-alkanes. GISAXS experiments were carried out on Beamline I16 at Diamond Light Source. Thin films were prepared from the melt on a silicon wafer. The thin film coated $5 \times 5 \text{ mm}^2$ Si plates were placed on top of a custom built heater, which was then mounted on a six-circle goniometer. The sample enclosure and the beam pipe were flushed with helium. The Pilatus detectors were used for both SAXS and GISAXS. The diffraction peaks were indexed on the basis of their d -spacing ratio and the position in the GISAXS pattern. Once the diffraction intensities were

measured and the corresponding plane group determined, 2-D electron density maps could be reconstructed, on the basis of the general formula

$$E(xy) = \sum_{hk} \sqrt{I(hk)} \exp(i2\pi(hx + ky) + \phi_{hk}) \quad (12)$$

As the observed diffraction intensity $I(hk)$ is only related to the amplitude of the structure factor $|F(hk)|$, the information about the phase of $F(hk)$, ϕ_{hk} , cannot be determined directly from experiment. However, since the plane group $p4mm$ is centrosymmetric, the structure factor $F(hk)$ is always real and ϕ_{hk} is either 0 or π . This makes it possible for a trial-and-error approach, where candidate electron density maps are reconstructed for all possible phase combinations, and the “correct” phase combination is then selected on the merit of the maps, helped by prior physical and chemical knowledge of the system.

Molecular dynamics simulation

Annealing dynamics runs were carried out using the Forcite module of Material Studio, Accelrys, with the Universal Force Field. The structure in Fig. 4 was obtained with either two or four molecules in a square box with the side equal to the experimentally determined unit cell length and a height of 0.40 nm, with 3d periodic boundary conditions. The size of the box was 5×5 honeycomb cells for the single-colour phase and 8×8 honeycomb cells (32 unit cells) for the 2-colour phase. 30 temperature cycles of NVT dynamics were run between 300 and 700 K, with a total annealing time of 30 ps.

Conflicts of interest

There are no conflicts to declare.

Acknowledgements

The authors acknowledge fundings for this work from EPSRC (EP-K034308, EP-P002250), DFG (392435074) and the National Natural Science Foundation of China (No. 21761132033, 21374086). We are grateful to Dr. N. Terill and O. Shebanova at I22, and Dr. G. Nisbet and S. Collins at I16, Diamond Light source for help with SAXS and GISAXS experiments respectively. Simulations were performed using the Sheffield Advanced Research Computer (ShARC) hosted by the University of Sheffield.

Notes and references

- C. Sinturel, F. S. Bates and M. A. Hillmyer, High χ -Low-N Block Polymers: How Far Can We Go?, *ACS Macro Lett.*, 2015, 4, 1044–1050.
- K. Nickmans and A. P. Schenning, *Adv. Mater.*, 2018, 30, 1703713.
- S. Sergeev, W. Pisula and Y. H. Geerts, *Chem. Soc. Rev.*, 2007, 36, 1902–1929.
- M. O'Neill and S. M. Kelly, *Adv. Mater.*, 2011, 23, 566–584.
- W. Pisula, M. Zorn, J. Y. Chang, K. Müllen and R. Zentel, *Macromol. Rapid Commun.*, 2009, 30, 1179–1202.
- M. Kumar and S. Kumar, *Polym. J.*, 2017, 49, 85–111.
- Q. Li, *Nanoscience with liquid crystals*, Springer, Cham, 2014.
- M. Prehm, G. Götz, P. Bäuerle, F. Liu, X. Zeng, G. Ungar and C. Tschierske, *Angew. Chem.*, 2007, 119, 8002–8005.
- X. Feng, M. E. Tousley, M. G. Cowan, B. R. Wiesener, S. Nejati, Y. Choo, R. D. Noble, M. Elimelech, D. L. Gin and C. O. Osuji, *ACS Nano*, 2014, 8, 11977–11986.
- S. Bhattacharjee, J. A. M. Lugger and R. P. Sijbesma, *Macromolecules*, 2017, 50, 2777–2783.
- C. Li, J. Cho, K. Yamada, D. Hashizume, F. Araoka, H. Takezoe, T. Aida and Y. Ishida, *Nat. Commun.*, 2015, 6, 8418.
- T. Kato, M. Yoshio, T. Ichikawa, B. Soberats, H. Ohno and M. Funahashi, *Nat. Rev. Mater.*, 2017, 2, 17001.
- C. Tschierske, *Top. Curr. Chem.*, 2012, 318, 1–108.
- A. Angelova, B. Angelov, B. Papahadjopoulos-Sternberg, C. Bourgaux and P. Couvreur, *J. Phys. Chem. B*, 2005, 109, 3089–3093.
- H. Q. Wang, P. B. Zetterlund, C. Boyer, B. J. Boyd, T. J. Atherton and P. T. Spicer, *Langmuir*, 2018, 34, 13662–13671.
- C. Tang, E. M. Lennon, G. H. Fredrickson, E. J. Kramer and C. J. Hawker, *Science*, 2008, 322, 429–432.
- T. Wöhrle, I. Wurzbach, J. Kirres, A. Kostidou, N. Kapernaum, J. Litterscheidt, J. C. Haenle, P. Staffeld, A. Baro, F. Giesselmann and S. Laschat, *Chem. Rev.*, 2016, 116, 1139–1241.
- M. A. Shcherbina, X. Zeng, T. Tadjiev, G. Ungar, S. H. Eichhorn, K. E. S. Phillips and T. J. Katz, *Angew. Chem., Int. Ed.*, 2009, 48, 7837–7840.
- H. Mukai, M. Yokokawa, M. Ichihara, K. Hatsusaka and K. Ohta, *J. Porphyrins Phthalocyanines*, 2010, 14, 188–197.
- Y. Chino, K. Ohta, M. Kimurab and M. Yasutake, *J. Porphyrins Phthalocyanines*, 2017, 21, 159–178.
- X. H. Cheng, M. Prehm, M. K. Das, J. Kain, U. Baumeister, S. Diele, D. Leine, A. Blume and C. Tschierske, *J. Am. Chem. Soc.*, 2003, 125, 10977–10996.
- C. Tschierske, *Chem. Soc. Rev.*, 2007, 36, 1930–1970.
- G. Ungar, C. Tschierske, V. Abetz, R. Holyst, M. A. Bates, F. Liu, M. Prehm, R. Kieffer, X. B. Zeng, M. Walker, B. Glettner and A. Zywockinski, *Adv. Funct. Mater.*, 2011, 21, 1296–1323.
- C. Tschierske, C. Nürnberger, H. Ebert, B. Glettner, M. Prehm, F. Liu, X. B. Zeng and G. Ungar, *Interface Focus*, 2012, 2, 669–680.
- M. Prehm, F. Liu, U. Baumeister, X. Zeng, G. Ungar and C. Tschierske, *Angew. Chem., Int. Ed.*, 2007, 46, 7972–7975.
- F. Liu, R. Kieffer, X. B. Zeng, G. Ungar, K. Pelz, M. Prehm and C. Tschierske, *Nat. Commun.*, 2012, 3, 1104.
- X. Zeng, R. Kieffer, B. Glettner, C. Nürnberger, F. Liu, K. Pelz, M. Prehm, U. Baumeister, H. Hahn, H. Lang, G. A. Gehring, C. H. M. Weber, J. K. Hobbs, C. Tschierske and G. Ungar, *Science*, 2011, 331, 1302–1306.
- X. Cheng, F. Liu, X. Zeng, G. Ungar, J. Kain, S. Diele, M. Prehm and C. Tschierske, *J. Am. Chem. Soc.*, 2011, 133, 7872–7881.

- 29 A. Lehmann, A. Scholte, M. Prehm, F. Liu, X. B. Zeng, G. Ungar and C. Tschierske, *Adv. Funct. Mater.*, 2018, **28**, 1804162.
- 30 P. G. de Gennes and J. Prost, *The physics of liquid crystals*, Oxford university press, 1995, vol. 83, pp. 507–527.
- 31 S. John and T. Lubensky, *Phys. Rev. B: Condens. Matter Mater. Phys.*, 1986, **34**, 4815.
- 32 D. R. Nelson and B. Halperin, *Phys. Rev. B: Condens. Matter Mater. Phys.*, 1980, **21**, 5312.
- 33 M. Conradi, M. Cepic, M. Copic and L. Musevic, *Phys. Rev. Lett.*, 2004, **93**, 227802.
- 34 D. Chen, J. H. Porada, J. B. Hooper, A. Klittnick, Y. Shen, M. R. Tuchband, E. Korblova, D. Bedrov, D. M. Walba and M. A. Glaser, *et al.*, *Proc. Natl. Acad. Sci. U. S. A.*, 2013, **110**, 15931–15936.
- 35 W. D. Stevenson, H.-X. Zou, Z. Ahmed, X.-B. Zeng, C. Welch, G. Ungar and G. H. Mehl, *Phys. Chem. Chem. Phys.*, 2018, **20**, 25268–25274.
- 36 C. R. Safinya, K. S. Liang and W. A. Varady, *Phys. Rev. Lett.*, 1984, **53**, 1172–1175.
- 37 M.-H. Yen, J. Chaiprapa, X. B. Zeng, Y. Liu, L. Cseh, G. H. Mehl and G. Ungar, *J. Am. Chem. Soc.*, 2016, **138**, 5757–5760.
- 38 W. S. Fall, M.-H. Yen, X.-B. Zeng, L. Cseh, Y.-S. Liu, G. A. Gehring and G. Ungar, *Soft Matter*, 2019, **15**, 22–29.
- 39 A. J. Crane, F. J. Martinez-Veracoechea, F. A. Escobedo and E. A. Muller, *Soft Matter*, 2008, **4**, 1820–1829.
- 40 M. A. Bates and M. Walker, *Soft Matter*, 2009, **5**, 346–353.
- 41 T. D. Nguyen and S. C. Glotzer, *ACS Nano*, 2010, **4**, 2585–2594.
- 42 X. Liu, K. Yang and H. Guo, *J. Phys. Chem. B*, 2013, **117**, 9106–9120.
- 43 Y. Sun, P. Padmanabhan, M. Misra and F. A. Escobedo, *Soft Matter*, 2017, **13**, 8542–8555.
- 44 S. George, C. Bentham, X. B. Zeng, G. Ungar and G. A. Gehring, *Phys. Rev. E*, 2017, **95**, 062126.
- 45 B. Glettner, F. Liu, X. Zeng, M. Prehm, U. Baumeister, M. Walker, M. A. Bates, P. Boesecke, G. Ungar and C. Tschierske, *Angew. Chem., Int. Ed.*, 2008, **47**, 9063–9066.
- 46 E. Ising, *Z. Phys.*, 1925, **31**, 253–258.
- 47 N. Metropolis, A. W. Rosenbluth, N. M. Rosenbluth and A. H. Teller, *J. Chem. Phys.*, 1953, **21**, 1087–1092.
- 48 M. Newman and G. Barkema, *Monte Carlo methods in statistical physics*, Oxford University Press, New York, USA, 1999, pp. 229–236.
- 49 A. Pelissetto and E. Vicari, *Phys. Rep.*, 2002, **368**, 549–727.
- 50 L. P. Kadanoff, W. Götze, D. Hamblen, R. Hecht, E. Lewis, V. V. Palciauskas, M. Rayl, J. Swift, D. Aspnes and J. Kane, *Rev. Mod. Phys.*, 1967, **39**, 395.
- 51 C. Nürnberger, H. Lu, X. Zeng, F. Liu, G. Ungar, H. Hahn, H. Lang, M. Prehm and C. Tschierske, *Chem. Commun.*, submitted.

Supporting Information

An Ising Transition of Chessboard Tilings in a Honeycomb Liquid Crystal

William S. Fall,^{a,c} Constance Nürnberger,^b Xiangbing Zeng,^{d,*} Feng Liu,^a Stephen J. Kearney,^c Gillian A. Gehring^{c,*} Carsten Tschierske^{b,*} and Goran Ungar^{a,d,*}

Contents

1. Additional Data	2
1.1 Polarizing microscopy and DSC	2
1.2 Additional XRD data.....	3
2. Synthesis.....	5
2.1 General	5
2.2. Intermediates	6
2.3. Compound 1	8
3. Theoretical Model and MC	8
4. References	8

1. Additional Data

1.1 Polarizing microscopy and DSC

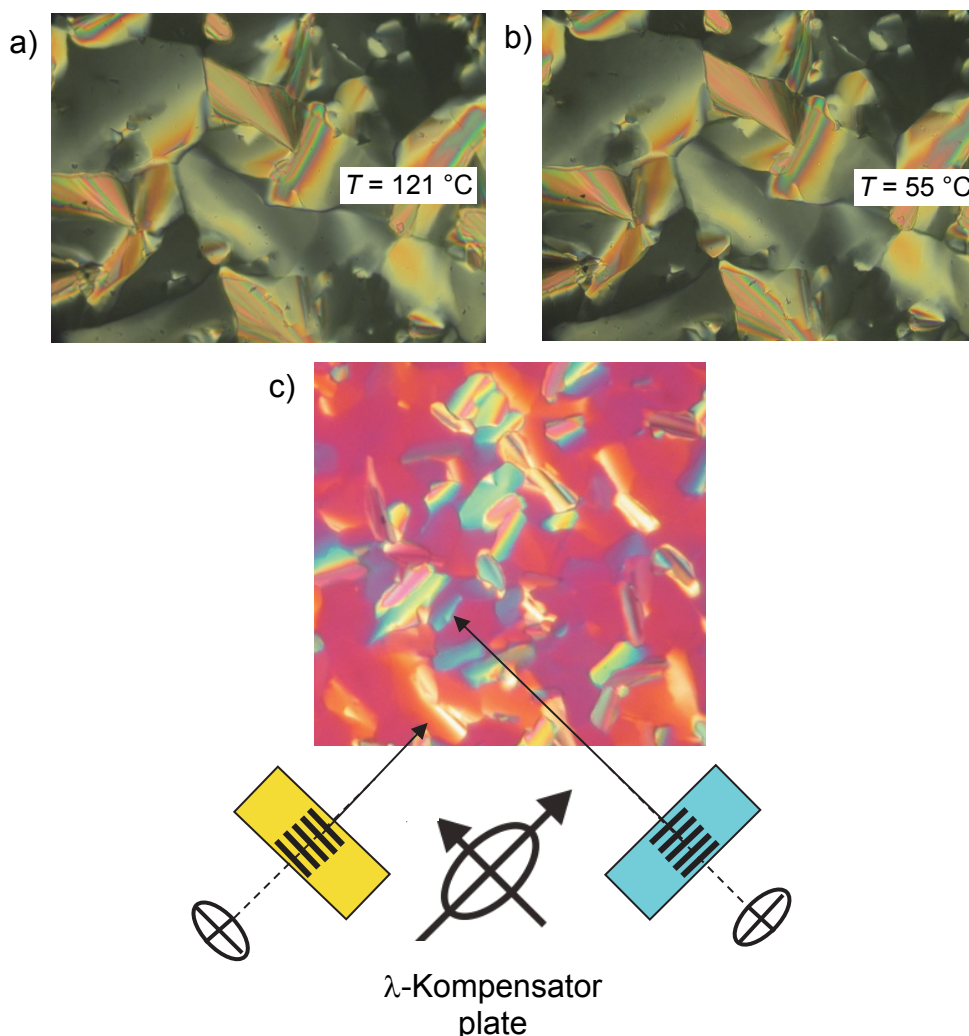


Figure S1 Textures of the Col_{squ} phases of compound 1 as observed between crossed polarizers a) in the Col_{squ} phase at $T = 121\text{ }^{\circ}\text{C}$ and b) in the chessboard $\text{Col}_{\text{squ}}^2$ phase at $T = 55\text{ }^{\circ}\text{C}$; the optically isotropic dark areas represent homeotropically aligned regions (columns almost perpendicular to the surfaces) which indicate the uniaxiality of both phases; c) shows the texture with additional λ -retarder plate, which is identical in both phases; the black lines indicate the direction of the π -conjugation pathway of the rod-like cores in the yellow and blue areas, confirming that these rods are aligned perpendicular to the column long axis as typical for honeycomb type LC phases.

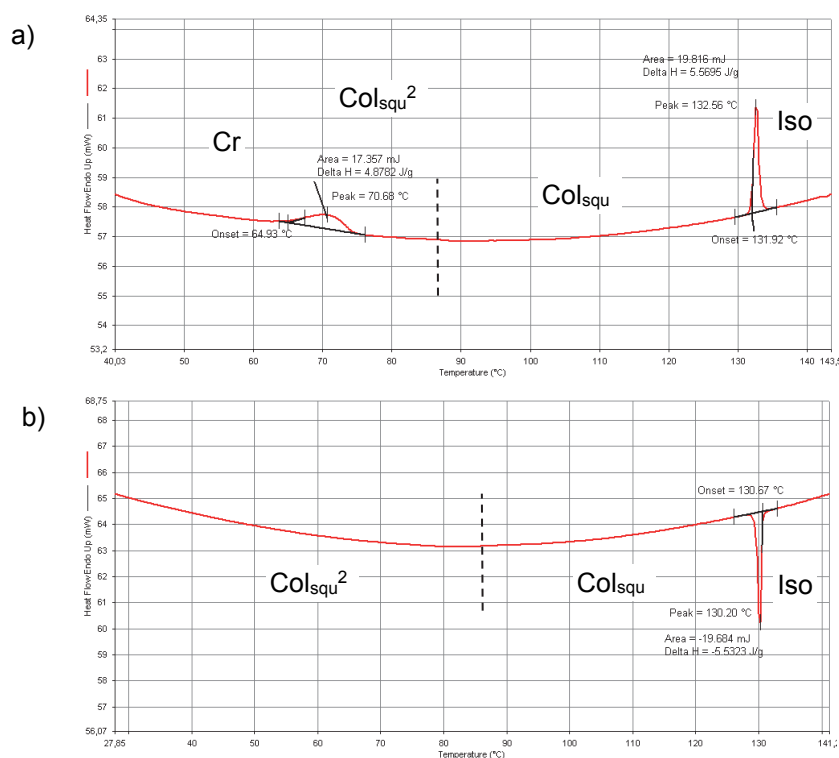


Figure S2. Second DSC heating and cooling scans of compound **1**, recorded at rate 10 K min⁻¹ a) on heating and b) on cooling.

1.2 Additional XRD data

Table S1. Experimental and calculated d -spacings and intensities of the observed SAXS Bragg peaks of compound **1** in the (a) high- T one-color $p4mm$ phase at 100 °C, and (b) low- T chessboard $p4mm$ phase at 65 °C. All intensities are Lorentz and multiplicity corrected. Structure factor phase angles used in electron density calculations are also given.

a) High- T phase at 100°C

(hk)	$d_{\text{obs.}}$ -spacing (nm)	$d_{\text{calc.}}$ -spacing (nm)	<i>intensity</i>	<i>phase</i>
(10)	2.96	2.96	48.2	0
(11)	2.09	2.09	29.7	0
(20)	1.48	1.48	100.0	π
(21)	1.32	1.32	1.4	π
$a_1 = 2.96$ nm				

b) Low- T phase at 65°C

(hk)	$d_{\text{obs.}}$ –spacing (nm)	$d_{\text{cal.}}$ –spacing (nm)	<i>intensity</i>	<i>phase</i>
(10)	4.19	4.19	100.0	0
(11)	2.96	2.96	0.4	π
(20)	2.10	2.10	0.5	π
(21)	1.87	1.87	0.1	π
(22)	1.48	1.48	1.4	0
(30)	1.40	1.40	1.0	0
(31)	1.32	1.32	0.3	0
$a_2 = 4.19$ nm				

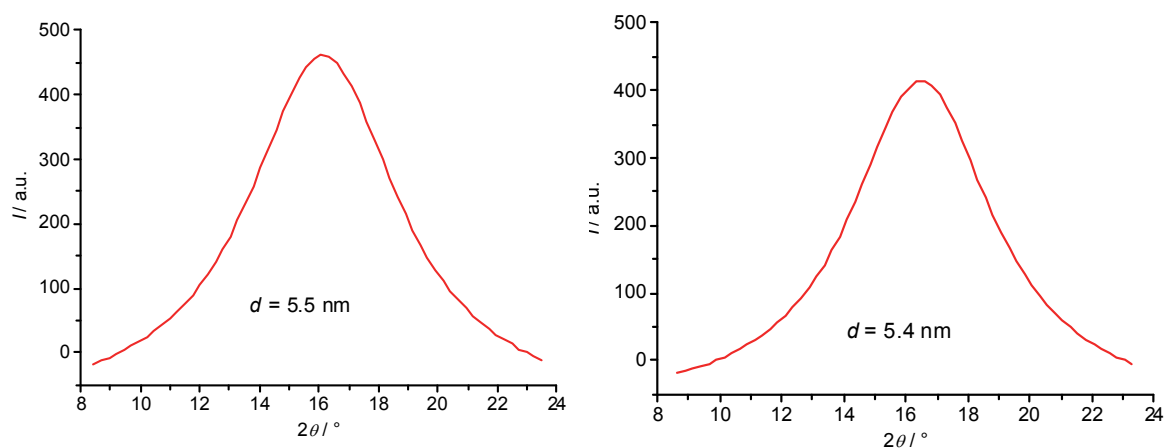


Figure S3. WAXS patterns of compound **1** at a) 115 °C and b) 60 °C.

Table S2. Relative volumes and electron densities for different parts of molecule ^{a)}

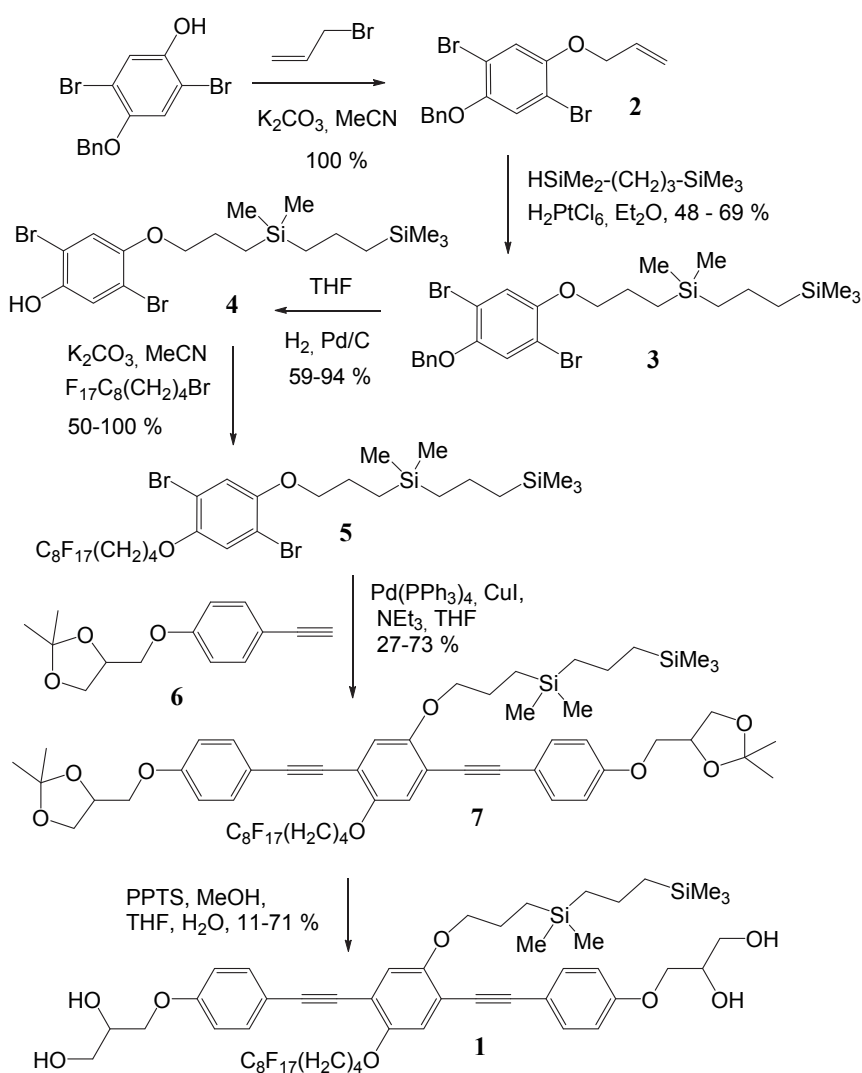
	V%	Electron density (electrons/nm ³)
Rod-like core (arom. + glyc.)	44.8	518
F-chain	29.6	714
Si-chain	25.6	430
Mixed Si- and F-chains	55.2	572

^{a)} Measured from molecular model using the Connolly surface method.

2. Synthesis

2.1 General

Unless otherwise noted, all starting materials are purchased from commercial sources and are used without further purification. Column chromatography is performed with silica gel 60 (63-200 μm , Fluka). Determination of structures and purity of intermediates and products is obtained by NMR spectroscopy (VARIAN Gemini 2000 and Unity Inova 500, all spectra are recorded at 27 $^{\circ}\text{C}$). The purity of all products is checked with thin layer chromatography (silicagel 60 F₂₅₄, Merck). CHCl_3 and $\text{CHCl}_3/\text{MeOH}$ mixtures are used as eluents and the spots are detected by UV radiation. All compounds represent racemic mixtures of diastereomers due to the stereogenic centers in the glycerol units; no attempts are made to separate these mixtures. The synthesis is performed as outlined in Scheme S1.



Scheme S1. Synthesis of compound **1**.

2.2. Intermediates

4-Benzyloxy-2,5-dibromophenol is prepared as reported in ref.^{S1} 5,5,6,6,7,7,8,8,9,9,10,10,11,11,12,12,12-heptafluorododecylbromide is synthesized according to the procedures given in ref. ^{S2,S3} and 4-(4-ethynylphenoxy)methyl)-2,2-dimethyl-1,3-dioxolane (6) is prepared as described in refs. ^{S1,S4}

2-Chloro-2,6,6-trimethyl-2,6-disilaheptane ^{S5,S6}

Allytrimethylsilane (26.2 g; 0.2 mol), chlorodimethylsilane (26.1 g; 0.3 mol) and a solution of H₂PtCl₆ (10 mg) in isopropanol (0.5 ml) are dissolved in diethyl ether (25 ml) under an Ar-atmosphere and stirred at 25 °C for 48 hrs. The product is fractionated by distillation. Yield 40.9 g (85 %), colourless liquid, b.p. 108 °C at 8×10⁻² bar (ref. S5: b.p.: 192 °C at ambient pressure). ¹H-NMR (CDCl₃, 400 MHz) δ = 1.47-1.43 (m, 2H, -CH₂-CH₂-CH₂-), 0.90-0.87 (m, 2H, -CH₂-), 0.61-0.57 (m, 2H, -CH₂-), 0.04 (s, 6H, -Si(CH₃)₂-), -0.02 (s, 9H, -Si(CH₃)₃).

2,6,6-Trimethyl-2,6-disilaheptane ^{S5}

Under an argon atmosphere 2-chloro-2,6,6-trimethyl-2,6-disilaheptane (20.0 g, 0.1 mol) is dissolved in dry diethyl ether (150 ml) and LiAlH₄ (2.2 g, 0.07 mol) is added at 25 °C. The mixture is stirred for 72 hrs and then filtered through a glass drip under Ar-atmosphere. The solvent is distilled off under normal pressure and the residue is distilled under vacuo. Yield: 11.0 g (66 %); colourless liquid, b.p.: 80 °C at 8×10⁻² bar. (ref. S5: b.p.: 85 °C at 25 mbar). ¹H-NMR (CDCl₃, 400 MHz) δ = 3.88 (m, 1H, Si-H), 1.41-1.33 (m, 2H, -CH₂-CH₂-CH₂-), 0.65-0.61 (m, 2H, -CH₂-), 0.57-0.53 (m, 2H, -CH₂-), 0.05 (d, 6H, ³J(H-H) = 3.6 Hz, -Si(CH₃)₂-), -0.04 (s, 9H, -Si(CH₃)₃).

1-Allyloxy-4-benzyloxy-2,5-dibromobenzene (2)

4-Benzyloxy-2,5-dibromophenol (4.3 g, 12.1 mmol), allyl bromide (1.1 ml, 3.0 mmol) and K₂CO₃ (3.6 g, 25.9 mmol) are dissolved in MeCN (100 ml) and refluxed with stirring for 8 hrs. After cooling to 25 °C water (100 ml) is added. The aqueous solution is extracted with diethyl ether (3 x 50 ml) and the organic layers are unified, washed with water (100 ml) and dried over Na₂SO₄. The solvent is removed at a rotary evaporator and the residue is crystallized from petroleum ether. Yield: 3.9 g (98 %); colorless solid, m.p.: 92-83 °C. ¹H-NMR (CDCl₃, 400 MHz) δ = 7.45-7.30 (m, 5H, -O-CH₂-(C₆H₅)), 7.15 (s, 1H, Ar-H), 7.11 (s, 1H, Ar-H), 6.07-5.98 (m, 1H, -CH=CH₂), 5.47-5.42 (m, 1H, -CH=CH₂), 5.31-5.28 (m, 1H, -CH=CH₂), 5.06 (s, 2H, -O-CH₂-(C₆H₅)), 4.54-5.52 (m, 2H, -O-CH₂-CH=CH₂).

1-Benzyloxy-2,5-dibromo-4-(4,4,8,8-tetramethyl-4,8-disilanonyloxy)benzene (3)

Under an Ar-atmosphere **2** (3.0 g, 9.4 mmol), 2,2,6-trimethyl-2,6-disilaheptane (1.70 g, 9.7 mmol) and H₂PtCl₆ (13 mg in 1 ml isopropanol) are dissolved in dry diethyl ether (40 ml) and stirred for 48 hrs at 25 °C. The solvent is removed at a rotary evaporator and the residue is purified by column chromatography on silica gel (eluent: CHCl₃/n-hexane). Yield: 3.7 g (69 %); colorless oil; ¹H-NMR (CDCl₃, 400 MHz) δ = 7.45-7.29 (m, 5H, -O-CH₂-(C₆H₅)), 7.14 (s, 1H, Ar-H), 7.08 (s, 1H, Ar-H), 5.05 (s, 2H, -O-CH₂-(C₆H₅)), 3.91-3.88 (m, 2H, -O-CH₂-), 1.82-1.74 (m, 2H, -O-CH₂-CH₂-), 1.36-1.25 (m, 2H, -CH₂-CH₂-CH₂-), 0.63-0.51 (m, 6H, -CH₂-Si), -0.01 (s, 6H, Si-(CH₃)₂), -0.04 (s, 9H, Si-(CH₃)₃).

2,5-Dibromo-4-(4,4,8,8-tetramethyl-4,8-disilanonyloxy)phenol (4)

In a pressure resistant vessel **3** (5.2 g, 9.1 mmol) is dissolved in dry THF (30 ml). Under an Ar-atmosphere Pd/C (10% Pd, 0.3g) is added. After flushing with H₂ (3x) the vessel is shaken for 24 hrs under a H₂ atmosphere (2.8 bar) at 40 °C. Afterwards the vessel is flushed with Ar, the catalyst is filtered off and the solvent is removed at a rotary evaporator under reduced pressure. The residue is purified by column chromatography on silica gel (eluent: CHCl₃). Yield: 2.8 g (63 %); colorless oil; ¹H-NMR (CDCl₃, 400 MHz) δ = 7.22 (s, 1H, Ar-H), 6.95 (s, 1H, Ar-H), 5.09 (s, 1H, -OH), 3.89-3.85 (m, 2H, -O-CH₂-), 1.81-1.74 (m, 2H, -O-CH₂-CH₂-), 1.37-1.29 (m, 2H, -CH₂-CH₂-CH₂-), 0.62-0.52 (m, 6H, -CH₂-Si-), -0.02 (s, 6H, -Si-(CH₃)₂), -0.05 (s, 9H, -Si-(CH₃)₃).

1,4-Dibromo-2-(4,4,8,8-tetramethyl-4,8-disilanonyloxy)-5-(5,5,-6,6,7,7,8,8,9,9,-10,10,11,11,12,12,12-heptafluorododecyloxy)-benzene (5)

A mixture of **4** (0.5 g, 1.7 mmol), 1-bromo-5,5,6,6,7,7,8,8,9,9,10,10,11,11,12,12,-12-heptafluorododecane (0.6 g, 1.1 mmol) and K₂CO₃ (1.0 g, 7.2 mmol) and dry CH₃CN (40 ml) is stirred under reflux for 16 hours. After cooling water (150 ml) is added and the reaction mixture is extracted with CHCl₃ (3x50 ml). The combined organic layers are dried over Na₂SO₄ and evaporated under reduced pressure at a rotary evaporator. The crude product is purified by column chromatography on silica gel (eluent: CHCl₃/n-hexane 1:4 V/V). Yield: 0.8 g (83 %); colorless solid, m.p.: 53-54 °C; ¹H-NMR (CDCl₃, 400 MHz) δ = 7.07 (s, 1H, Ar-H), 7.06 (s, 1H, Ar-H), 3.99-3.96 (m, 2H, -O-CH₂-), 3.91-3.87 (m, 2H, -O-CH₂-), 2.25-2.12 (m, 2H, -CH₂-CF₂-), 1.91-1.84 (m, 4H, -O-CH₂-CH₂-CH₂-CF₂-), 1.83-1.74 (m, 2H, -O-CH₂-CH₂-), 1.37-1.29 (m, 2H, -CH₂-CH₂-CH₂-), 0.62-0.50 (m, 6H, -CH₂-Si-), -0.02 (s, 6H, -Si-(CH₃)₂), -0.05 (s, 9H, -Si-(CH₃)₃).

1-(4,4,8,8-Tetramethyl-4,8-disilanonyloxy)-2,5-bis(4-(2,2-dimethyl-1,3-dioxolane-4-yl)-methoxy)phenylethynyl)-4-(5,5,6,6,7,7,8,-8,9,9,10,10,-11,11,12,12,12-heptafluorododecyloxy)benzene (7)

Under an argon atmosphere a mixture of **5** (0.4 g, 0.4 mmol), **6** (0.2 g, 1.0 mmol), Pd[PPh₃]₄ (20 mg) and CuI (2 mg) in dry triethylamine (30 ml) is stirred under reflux for 16 hrs. After cooling the solvents are distilled off at an rotatory evaporator. Water (100 ml) is added and the reaction mixture is extracted with diethyl ether (3x50 ml). The combined organic layers are washed with water (50 ml), brine (50 ml), dried over Na₂SO₄ and evaporated under reduced pressure using a rotary evaporator. The crude product is purified by column chromatography on silica gel (eluent: CH₂Cl₂ with 2 % (V/V) diethyl ether). Yield: 0.29 g (56 %); pale yellow solid, m.p. 114 °C; ¹H-NMR (CDCl₃, 400 MHz) δ = 7.43-7.41 (m, 4H, Ar-H), 6.99 (s, 1H, Ar-H), 6.96 (s, 1H, Ar-H), 6.88-6.84 (m, 4H, Ar-H), 4.48-4.45 (m, 2H, -O-CH₂-), 4.18-4.13 (m, 2H, -O-CH₂-), 4.08-4.03 (m, 4H, -O-CH₂-), 3.98-3.93 (m, 4H, -O-CH₂-), 3.92-3.87 (m, 2H, -O-CH₂-), 2.15 (m, 2H, -CH₂-CF₂-), 1.92-1.91 (m, 4H, - (CH₂)₂-CH₂-CF₂-), 1.86-1.82 (m, 2H, -O-CH₂-CH₂-), 1.45 (s, 6H, -CH₃), 1.39 (s, 6H, -CH₃), 1.36-1.30 (m, 2H, -CH₂-CH₂-CH₂-), 0.69-0.65 (m, 2H, -Si-CH₂-), 0.59-0.51 (m, 4H, -Si-CH₂-), -0.02 (s, 6H, -Si-(CH₃)₂), -0.06 (s, 9H, -Si(CH₃)₃).

2.3. Compound 1

1-(4,4,8,8-Tetramethyl-4,8-disilanonoxo)-2,5-bis(4-(2,3-dihydroxypropoxy)phenylethynyl)-4-(5,5,6,6,7,7,8,8,9,9,10,10,11,11,12,12-hexadecafluorododecyloxy)benzene (1)

A solution of **7** (0.4 g, 0.2 mmol) and pyridinium 4-toluensulphonate (0.05 g) in a mixture of MeOH (30 ml) water (1 ml) and THF (30 ml) is stirred at 60 °C under a reflux condenser for 48 hrs. The progress of the reaction is recorded with TLC. After all **7** is used up the mixture is evaporated under reduced pressure at a rotary evaporator and the residue is taken up in diethyl ether and water (100 ml each). The organic layer is separated and the aqueous phase is extracted twice with diethyl ether. The combined organic phases are washed with water (50 ml) brine (50 ml), dried over Na₂SO₄ and evaporated under reduced pressure at a rotary evaporator. The crude product is purified by column chromatography on silica gel (eluent: EtOAc) and crystallized from MeOH/CHCl₃. Yield: 50 mg (17 %); pale yellow solid, Cr 72 Col_{squ}²/p4mm 88 Col_{squ}/p4mm 133 Iso (°C); ¹H-NMR (CDCl₃, 400 MHz) δ = 7.44 (t, *J*^{H,H}=8.5Hz, 4H, Ar-H), 6.97 (s, 1H, Ar-H), 6.97 (s, 1H, Ar-H), 6.88-6.85 (m, 4H, Ar-H), 4.11-4.01 (m, 8H, -O-CH-, -O-CH₂-), 3.97 (t, *J*^{H,H}=6.6Hz, 2H, -O-CH₂-), 3.85-3.82 (m, 2H, -O-CH₂-), 3.76-3.73 (m, 2H, O-CH₂-), 2.52-2.51 (m, 2H, -OH), 2.17-2.12 (m, 2H, -CH₂-CF₂-), 1.92 (m, 4H, -(CH₂)₂-CH₂-CF₂-), 1.86-1.78 (m, 2H, -O-CH₂-CH₂), 1.37-1.30 (m, 2H, -CH₂-CH₂-CH₂-), 0.70-0.65 (m, 2H, -Si-CH₂-), 0.60-0.51 (m, 4H, -Si-CH₂-), -0.02 (s, 6H, -Si-(CH₃)₂), -0.06 (s, 9H, -Si-(CH₃)₃). ¹⁹F-NMR (CDCl₃, 200 MHz): δ = -81.14 (m, 3F, -CF₃), -114.74 (m, 2F, -CH₂-CF₂-), -122.23 (s, 6F, -CF₂-), -123.10 (s, 2F, -CF₂-), -123.79 (s, 2F, -CF₂-), -126.48 (m, 2F, -CF₂-CF₃). HR-ESI-MS: m/z [M+Cl]⁻ 1213.3224 (calc. 1213.3160).

3. Theoretical Model and MC

Table S3 Energy of a square with *n* Si chains and (4-*n*) F chains with pair interactions and multiplicities for each *n*.

No. Si	No. F	Energy	Multiplicity
4	0	6 <i>S</i>	1
3	1	3 <i>S</i> + 3 <i>M</i>	4
2	2	<i>S</i> + <i>F</i> + 4 <i>M</i>	6
1	3	3 <i>F</i> + 3 <i>M</i>	4
0	4	6 <i>F</i>	1

4. References

-
- S1 B. Glettner, F. Liu, X. Zeng, M. Prehm, U. Baumeister, M. Walker, M. A. Bates, P. Boesecke, G. Ungar, C. Tschierske, *Angew. Chem. Int. Ed.* 2008, **47**, 9063–9066.
S2 G. Johansson, V. Percec, G. Ungar, J. P. Zhou, *Macromolecules*, 1996, **29**, 646-660.

-
- S3 F. Liu, R. Kieffer, X. Zeng, K. Pelz, M. Prehm, G. Ungar, C. Tschierske, *Nat. Commun.* 2012, **3**, 1104.
- S4 W. B. Austin, N. Bilow, W. J. Kelleghan, K. S. Y. Lau, *J. Org. Chem.* 1981, **46**, 2280.
- S5 H. Hahn, *Synthese und Charakterisierung SiH-funktionalisierter Carbosilane als Bausteine in Bent-Core Mesogenen*, PhD Thesis Technical University Chemnitz, 2005.
- S6 H. Jancke, G. Engelhardt, H. Kriegsmann, L. M. Volkova, N. V. Delazari, K. A. Andrianov, *Z. Anorg. Allg. Chem.* 1973, **402**, 97.

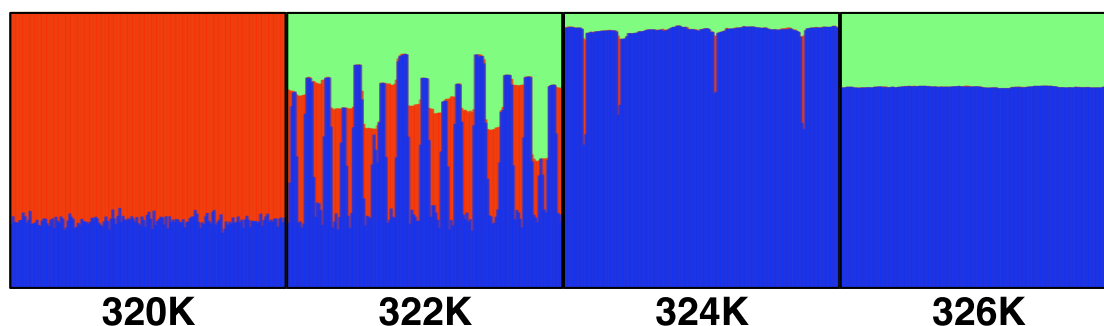
Bibliography

- [1] C. Tschierske, C. Nürnberger, H. Ebert, B. Glettner, M. Prehm, F. Liu, X.-B. Zeng, and G. Ungar. *Interface Focus*, 2(5):669–680, 2012.
- [2] X. Zeng, R. Kieffer, B. Glettner, C. Nürnberger, F. Liu, K. Pelz, M. Prehm, U. Baumeister, H. Hahn, H. Lang, et al. *Science*, 331(6022):1302–1306, 2011.
- [3] B. Glettner, F. Liu, X. Zeng, M. Prehm, U. Baumeister, M. Walker, M. A. Bates, P. Boesecke, G. Ungar, and C. Tschierske. *Angewandte Chemie International Edition*, 47(47):9063–9066, 2008.
- [4] X. Zeng and G. Ungar. personal communication.
- [5] S. George, C. Bentham, X. Zeng, G. Ungar, and G. A. Gehring. *Physical Review E*, 95(6):062126, 2017.
- [6] M. Poppe, C. Chen, F. Liu, M. Prehm, S. Poppe, and C. Tschierske. *Soft Matter*, 13(27):4676–4680, 2017.
- [7] C. Tang, E. M. Lennon, G. H. Fredrickson, E. J. Kramer, and C. J. Hawker. *Science*, 322(5900):429–432, 2008.
- [8] W. S. Fall, C. Nürnberger, X. Zeng, F. Liu, S. J. Kearney, G. A. Gehring, C. Tschierske, and G. Ungar. *Molecular Systems Design & Engineering*, 4(2):396–406, 2019.
- [9] C. Nürnberger, H. Lu, X. Zeng, F. Liu, G. Ungar, H. Hahn, H. Lang, M. Prehm, and C. Tschierske. *Chemical Communications*, 55(29):4154–4157, 2019.

Chapter 5

Self-Poisoning in Isotactic Polypropylene

William S. Fall, Tom H. Sexton, Gillian A. Gehring, Goran Ungar
and Xiangbing Zeng



Author Contributions

G.U. conceived and directed all aspects of the project. W.S.F., supervised by G.A.G. and X.Z extended the model, wrote and carried out the simulations. W.S.F wrote the program. X.Z and T.H.S developed the 1d-model with support from G.A.G. See page **vii** for author declarations.

5.1 Introduction

When polymers crystallise, a small crystal nucleus must first be present out from which a larger crystal may grow. This occurs in one of two ways, either thermal motion brings elongated chains together to form a nucleus or growth proceeds from interfaces or impurities, such as remnants of the catalysts used during synthesis still present in the polymer. This process is known as primary nucleation, secondary nucleation on the other hand occurs when crystals of the new phase are already present. Primary nucleation then can occur heterogeneously or homogeneously, whereas secondary nucleation occurs only heterogeneously.

In homogenous primary nucleation a critical nucleus size exists which allows for continuous growth, this size occurs when the bulk free energy overcomes that of the surface energy. This barrier was neatly summarised by Gibbs as the difference in free energy between the initial liquid and final crystalline phases, ΔG .

$$\Delta G = -V\Delta g_f + A\gamma + B\gamma_e \quad (5.1)$$

The negative term $-V\Delta g_f$ represents the free energy of a crystal with volume V and stabilises the crystal whereas the positive surface term $A\gamma + B\gamma_e$ destabilises it. In this case $A\gamma$ and $B\gamma_e$ are the fold and end surface energies respectively where A and B denote the areas associated with each. Homogenous nucleation is very rare due to the high energy barrier that must be overcome whereas heterogenous nucleation occurs more easily due to the reduced surface energy required when nucleating on an already crystalline surface. In industrial applications nucleating agents are often added to speed up the crystallisation process.

Molten polymers are entangled and irregularly coiled and contrary to materials

comprised of simple molecular units, often retain this structure when rapidly quenched as an amorphous solid. Some polymers do form regions with a degree of ordering on cooling by folding and aligning, as illustrated in the spherulitic structure depicted in Figure 5.1 (b) and are called semi-crystalline polymers. Common examples include polyethylene and polypropylene [1]. In the same way liquid crystals form complex phases, the rapid cooling of polymers often leads to interesting structures with some degree of ordering present. When a system is moved away from thermodynamic equilibrium quickly, the time available to kinetic processes, such as the conformational rearrangement of a single polymer chain, is significantly reduced. In this situation a large energy barrier is present which blocks the path to the equilibrium state, this results in metastable states being formed. Thermodynamics is not enough on its own to describe these systems because kinematic processes are dominating.

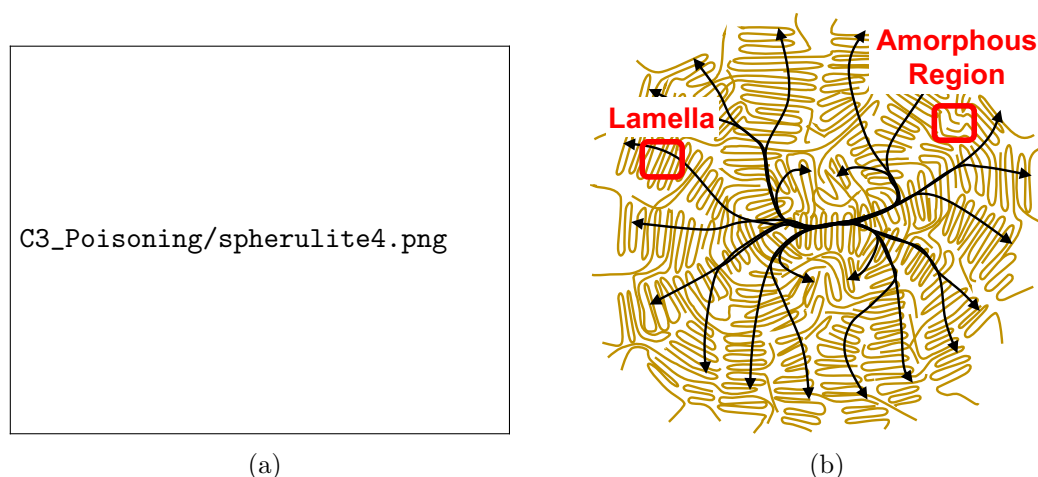


Figure 5.1: (a) Optical micrograph showing spherulites in i-PP reproduced with permission from [2]. (b) Schematic model of a spherulite where black arrows indicate direction of molecular alignment. Lamella and amorphous regions are indicated.

Isotactic polypropylene freezes below 130°C which is some 40°C below the melting point at 170° and requires large undercooling to crystallise. It is argued by some that this may be due to the strict conformational requirements for a chain to join the growing

crystal as well as the presence of a competing mesophase. This is true particularly at high cooling rates and the structure of the mesophase remains controversial, due to the experimental difficulties encountered when studying it. i-PP is known to exhibit 3 well understood phases, with varying degrees of undercooling, called α , β and γ [3, 4] which are depicted in Figure 5.2. The α -phase form consists of monoclinic unit cells of alternating left and right-handed helices (2-white and 2-gold respectively) in the b-axis direction parallel to the a-c plane. It is the most stable form of crystalline i-PP and has the lowest free energy. With larger temperature gradients the β -phase can also be found, with a trigonal unit cell and it is metastable relative to the α -phase. The γ -phase forms often in low molecular weight degraded i-PP with an orthorhombic unit cell composed of sheets of parallel chains inclined at 80° to each another. In this thesis we are concerned only with the α -phase.

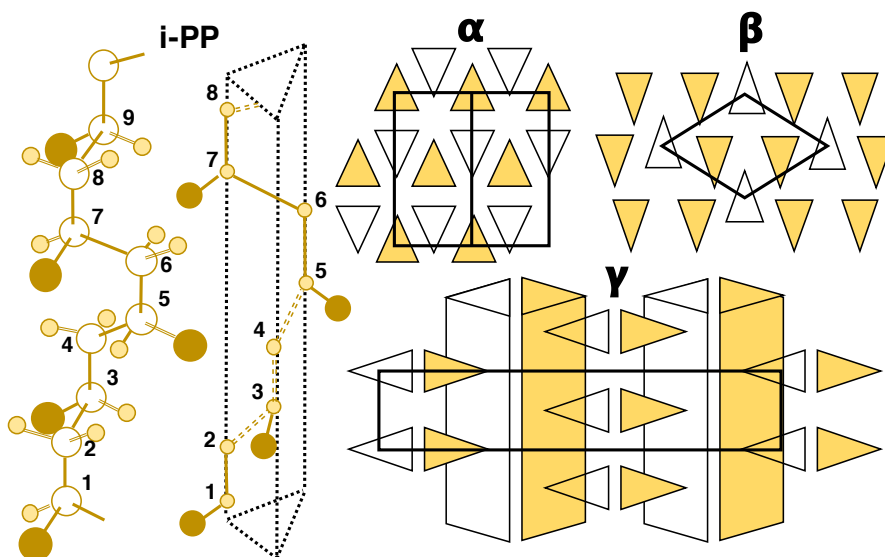


Figure 5.2: The left-handed helix of i-PP with the down position of the methyl groups drawn in gold, with its representation drawn as a triangular prism. Different phases of i-PP: α -phase as viewed perpendicular to the a-b plane, c-axis is out of plane, β -phase with c-axis out of plane and the γ phase. For the α -phase $a=2.096$ nm and $b=0.665$ nm.

At very high undercoolings however, i-PP exhibits an additional phase that is not

completely amorphous but instead partially ordered, sometimes known as smectic or paracrystalline phase, in this work it is referred to as the mesophase throughout [5, 6]. The structure of this mesophase is highly ordered in comparison to the melt but its presence in i-PP has important implications. It has been found recently to accompany the formation of the α -phase at very large undercoolings [7–9] and forms rapidly in comparison. Even though the crystalline phase has a lower free energy the rapid formation of a metastable mesophase may seriously impede the rate of crystallisation [10], this is believed to be an example of self-poisoning [11, 12]. The purpose of this work is to simulate the growth of the crystal in the region where the ordered crystal is stable and the mesophase is unstable and use it to demonstrate that the growth of the α -phase diminishes as the temperature of the metastable phase is reached.

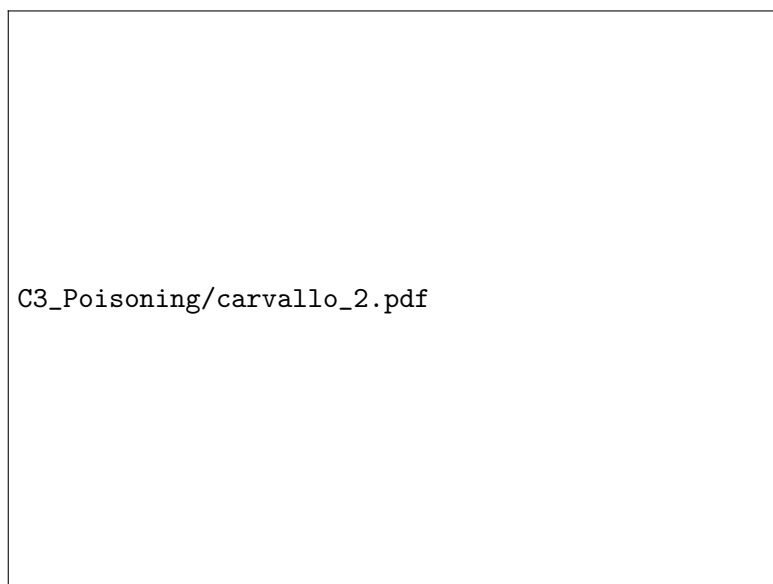


Figure 5.3: Inverse time-to-peak as a function of temperature for i-PP, lines are drawn for clarity, reproduced with permission from [7].

Using a 1d theory, the growth of a single crystalline stem is modelled and solved exactly. This has been modelled previously for n-alkanes in [13] where the rate of crystallisation was shown to be suppressed by metastable folded chains which block the growth of

the extended chain crystal [14, 15]. Self-poisoning has also been seen in simulations of polyethylene [16] and simulations of crystal nuclei in a hard-rod liquid [17]. A recent study has also provided a more general description of self-poisoning in any materials demonstrating it is ubiquitous [18]. The phenomena that occurs when the existence of an unstable disordered phase inhibits the growth of the ordered phase has been termed self-poisoning [12]. Neighbouring interactions are then investigated by simulating a 2d line of L interacting growth stems using random sampling. Nearest-neighbour interactions are included in order to capture self-poisoning in action and find better correspondence with the unusual behaviour observed in i-PP.

5.2 Theory and Model Description

The self-poisoning model of isotactic polypropylene describes the competition between a metastable mesophase, where random polymer chains can attach to the growth surface directly from the melt and a stable α -phase, where chains may convert to the correct helicity at the growing α -phase surface buried beneath. A single chain, n monomers long, in the mesophase may attach to a growth stem at rate A and detach at rate B as depicted in Figure 5.4(a) where the red blocks represent chains in the mesophase. It is unrealistic to assume α -phase chains can attach directly from the melt and consequently the α -phase (blue) is only able to grow by conversion of a mesophase chain at the α -meso interface. This process occurs at a different rate depending on the number of mesophase blocks m , in a given stem. For an uncovered stem ($m \leq 1$) meso- α conversion occurs at rate C whereas for a covered stem ($m > 1$) a slower rate C^* is chosen. It is also possible for an α -phase block to backwards convert to a mesophase block at rates D or D^* for uncovered or covered blocks respectively. Conversion always takes place at the interface and it is impossible in this model for an α -phase block to be found above a mesophase

block.

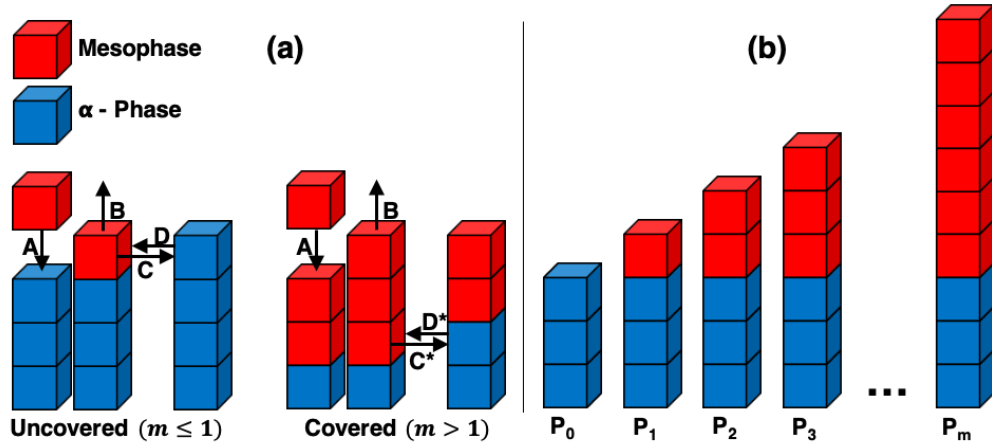


Figure 5.4: (a) Allowed processes in the self-poisoning model for i-PP for uncovered ($m \leq 1$) and covered ($m > 1$) stems. Attachment A and detachment B may occur at the same rate in both situations. Conversion of a mesophase block to an α -phase block and vice versa may occur at rates C and D respectively when $m \leq 1$ and C^* and D^* when $m > 1$. (b) Possible stem states in the 1d model, where m denotes the number of mesophase blocks (red) above the alpha phase stem (blue). P_m is the probability of a given state, containing m mesophase blocks occurring above the α -phase.

The growth rate can be established by considering each of the allowed different processes that can occur for a given α -phase stem with m mesophase blocks attached to it. This is depicted in Figure 5.4, where P_m indicates the probability of each state occurring. Recall that conversion takes place at two different rates for $m \leq 1$ and $m > 1$, the rate equations can simply be written as follows

$$\begin{aligned}
 \frac{dP_0}{dt} &= -(A + D)P_0 + (B + C)P_1 \\
 \frac{dP_1}{dt} &= (A + D)P_0 - (B + C)P_1 - (A + D^*)P_1 + (B + C^*)P_2 \\
 \frac{dP_m}{dt} &= (A + D^*)P_{m-1} - (B + C^*)P_m - (A + D^*)P_m + (B + C^*)P_{m+1}
 \end{aligned} \tag{5.2}$$

Since we are only interested in the growth rate R , of the α -phase, which must proceed through conversion of the mesophase, we can assume a steady state where mesophase blocks are continually adsorbing, desorbing and converting at the growth front. Using

that $\frac{dP_m}{dt} = 0$ and $\sum_{m=0}^{\infty} P_m = 1$ with a little algebra the growth rate R , of the α -phase may be written as

$$\begin{aligned} R &= -DP_0 + (C - D^*)P_1 + (C^* - D^*) \sum_{i=2}^{\infty} P_i \\ &= \frac{(B + C^* - A - D^*)(AC - BD) + (A + D)(AC^* - BD^*)}{(B + C)(B + C^* - A - D^*) + (B + C^*)(A + D)} \end{aligned} \quad (5.3)$$

The crystals growth is a two-step process whereby a mesophase chain must first attach to the surface of the ordered α -phase stem and then a long dwell time is required such that the probability of meso- α conversion is sufficiently large. The rate equations are given as follows starting with the rate of attachment of incoming mesophase chains.

$$A(T) = \begin{cases} \exp\left(-\frac{T\Delta S_{meso}^M + 2\sigma_{meso}^e}{k_B T}\right) & T < T_{meso}^M \\ \exp\left(-\frac{T\Delta S_{meso}^M + 2\sigma_{meso}^e + (n-1)(T-T_{meso}^M)\Delta S_{meso}^M}{k_B T}\right) & T \geq T_{meso}^M \end{cases} \quad (5.4)$$

The mesophase attachment rate $A(T)$, for $T < T_{meso}^M$ includes a temperature-independent term ΔS_{meso}^M , accounting for the extra entropy cost of attaching a mesophase chain and a temperature-dependent term for the surface free energy required (σ_{meso}^e) which raises the rate with increasing temperature. For $T \geq T_{meso}^M$ an additional term is required which depends on the chain length n , which accounts for the larger entropic cost associated with attaching larger chain to the surface. Here the surface term σ_{meso}^e is considered to account for the barrier present due to the creation of a surface for which there must be a free energy penalty. The rate of detachment $B(T)$, is similarly given as follows

$$B(T) = \begin{cases} \exp\left(\frac{(n-1)(T-T_{meso}^M)\Delta S_{meso}^M - T\Delta S_{meso}^M}{k_B T}\right) & T < T_{meso}^M \\ \exp\left(-\frac{T_{meso}^M \Delta S_{meso}^M}{k_B T}\right) & T \geq T_{meso}^M \end{cases} \quad (5.5)$$

where the detachment of a mesophase for $T < T_{meso}^M$ has a similar entropic

term penalising the removal of longer chain from the growth front. The temperature-dependent term $T_{meso}^M \Delta S_{meso}^M$ accounts for the extra entropic cost associated with detaching a mesophase chain below T_{meso}^M . For $T \geq T_{meso}^M$ the entropic cost of detaching a mesophase chain is smallest at T_{meso}^M and the rate increases exponentially with increasing temperature. In this case the surface term σ_{meso}^e is ignored because the surface free energy is not initially lost on removal but instead when returning to the melt which is not considered. Converting a mesophase chain to an α -phase chain via process $C(T)$, must factor in both the entropic gain of converting between the two phases $\Delta S_{\alpha}^M - \Delta S_{meso}^M$ and the end surface free energy lost when doing so $2(\sigma_{\alpha}^e - \sigma_{meso}^e)$.

$$C(T) = \exp\left(-\frac{T(\Delta S_{\alpha}^M - \Delta S_{meso}^M) + 2(\sigma_{\alpha}^e - \sigma_{meso}^e)}{k_B T}\right) \quad (5.6)$$

The entropic cost is temperature-independent and the end surface free energy contribution is reduced with increasing temperature, subsequently raising the rate of conversion. The conversion rate is different for a covered stem and for simplicity this is chosen such that $\frac{C^*(T)}{C(T)}$ is constant. Here we again consider the barrier present in converting a mesophase chain to an alpha-phase chain since it required the creation of the surface for which there must be a free energy penalty. Similarly an α -phase chain may backwards convert via process $D(T)$ to a mesophase chain. In this case the chain length must be taken into account since a longer chain is more stable and takes a longer time to convert as well as the entropic cost of converting between the two phases.

$$D(T) = \exp\left(\frac{(n-1)(\Delta T_{\alpha} \Delta S_{\alpha}^M - \Delta T_{meso} \Delta S_{meso}^M) - (T_{\alpha}^M \Delta S_{\alpha}^M - T_{meso}^M \Delta S_{meso}^M)}{k_B T}\right) \quad (5.7)$$

where $\Delta T_{\alpha} = T - T_{\alpha}^M$ and $\Delta T_{meso} = T - T_{meso}^M$. The first term in the exponent factors in the additional entropic cost of converting between the two phases at a given temperature and decreases the rate of conversion for the smallest chains. The second term is the usual entropic cost of converting between both phases and the conversion rate for a covered

stem is similarly chosen such that $\frac{D^*(T)}{D(T)}$ is constant for convenience. In this case the surface term σ_{meso}^e is ignored because the creation of a high energy surface is not required when converting from the more ordered α -phase to the less ordered mesophase.

Two further processes must be taken into account, firstly the overall viscosity of the polymer with decreasing temperature. This is included to factor in the slowed rate of attachment of stems as the polymer melt forms a glass. In this case the time-temperature superposition principle can be used, which states that a change in temperature of a polymer results in a change in timescale. The Williams-Landel-Ferry equation [19] is therefore used to define a shift factor a_f for the growth rate.

$$a_f = \exp\left(\frac{17.44(T - T_g)}{T - T_g + 51.6}\right) \quad (5.8)$$

where T_g is the glass transition temperature of polypropylene (250K). Secondly the dependence of the rate on the chain length is considered, this is well described using Hoffman nucleation theory [20]. As the number of monomers n increases the rate should also slow, except where n is small where there are a higher proportion of end chains with higher end surface energy. Thus the rate of nucleation is constructed using the free energy of primary nuclei, consisting of a bundle of b chains, each with n repeating units in much the same way as Gibb's barrier described earlier. We estimate this by summing the surface energy (side and end surfaces) and bulk. That is

$$G_N = n\sqrt{b}(4\sigma_s + \Delta T \Delta S_\alpha^M) + 2b\sigma_e - nb\Delta T \Delta S_\alpha^M \quad (5.9)$$

The minimum thickness for nucleation consequently defines the minimum number of chain segments required to nucleate on the growth front, after which the rest of the chain follows as it automatically lowers the free energy. This is also why the mesophase attachment rate $A(T)$, depends on n when the mesophase is unstable ($T > T_m$) and not

when it is stable, whilst the opposite is true for the detachment rate $B(T)$. For a given T and n , G_N is maximised when $\frac{\partial G_N}{\partial b} = 0$

$$b = \left(\frac{n(4\sigma_s + \Delta T \Delta S_\alpha^M)}{2(n\Delta T \Delta S_\alpha^M - 2\sigma_e)} \right)^2 \quad (5.10)$$

This therefore defines the critical size of nuclei and its free energy.

$$G_N^{max} = \frac{n^2 Z k_B T}{n - n_{min}}, \quad Z = \frac{(4\sigma_s + \Delta T \Delta S_\alpha^M)^2}{4k_B T \Delta T \Delta S_\alpha^M}, \quad n_{min} = \frac{2\sigma_e}{\Delta T \Delta S_\alpha^M} \quad (5.11)$$

The nucleation rate can then be written as

$$N = N_0 \exp\left(\frac{-G_N^{max}}{k_B T}\right) = N_0 \exp\left(\frac{-n^2 Z}{n - n_{min}}\right) \quad (5.12)$$

The optimum chain length n for a given ΔT is taken to be the length at which the nucleation rate is maximal, for our purposes we simply assume $n \sim 2n_{min}$. This yields the final growth rate for the self-poisoning model of i-PP including nucleation and temperature correction.

$$R' = N a_f^2 R \quad (5.13)$$

The parameter selection for i-PP is given in Table 5.1 and the resulting curve is shown in Figure 5.5 alongside the results for i-PP from [7]. The heat of fusion of the α -phase is given in [7] as $H_\alpha^M = 210$ J/g and the molar mass of polypropylene is 42 g/mol which yields $H_\alpha^M = 8840$ J/mol equivalent to $H_\alpha^M = 1.47 \times 10^{-20}$ J/monomer. Taking the melt temperature of the α -phase to be $T_\alpha^M = 460$ K [21] the entropy $\Delta S_\alpha^M = \frac{H_\alpha^M}{T_\alpha^M}$, is estimated to be 3.19×10^{-23} J/K. Despite several experimental attempts to calculate the enthalpy of fusion for the mesophase it is still difficult to estimate [22, 23]. Instead since $\Delta S_{meso} < \Delta S_\alpha^M$ as it is more disordered, ΔS_{meso} is taken to be 3.00×10^{-23} J/K corresponding to a heat of fusion for the mesophase $H_{meso}^M \approx 140$ J/g. The side surface energy, $\sigma_\alpha^s = E_\alpha^s \times \frac{a}{4} \times \frac{b}{3}$ and end surface energy $\sigma_\alpha^e = E_\alpha^e \times \frac{a \times b}{4}$ surface were calculated

using that $E_{\alpha}^s = 1 \times 10^{-20}$ J/nm² and $E_{\alpha}^e = 1 \times 10^{-19}$ J/nm² estimated from [24]. For the unit cell parameters a and b see Figure 5.2, σ_{meso}^e was taken to be $\approx 1/3 \sigma_{\alpha}^e$.

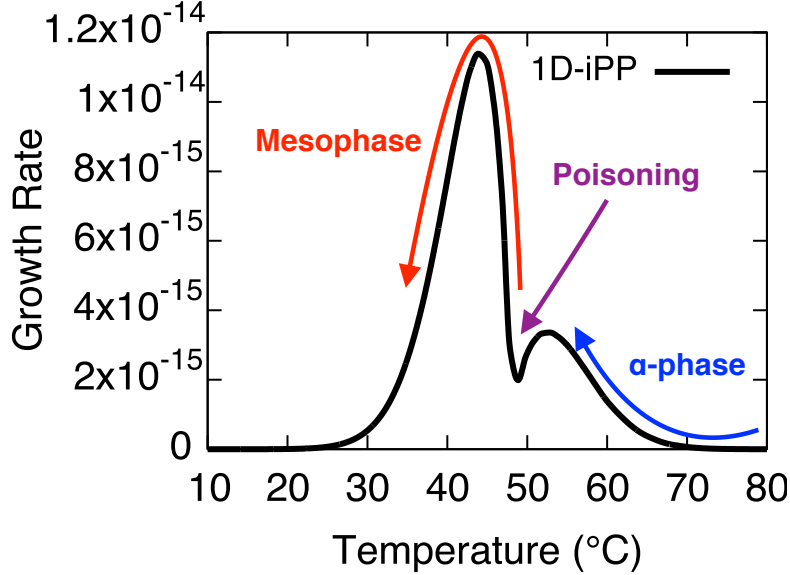


Figure 5.5: The growth rate, in arbitrary units for the 1d model using the estimated parameters for i-PP. Blue and red regions indicate the α -phase and mesophase dominated regions respectively, the poisoning temperature is indicated at 322K (purple).

T_{α}^M (K)	$\Delta S_{\alpha}^M = \frac{H_{\alpha}^M}{T_{\alpha}^M}$ (J/K)*10 ⁻²³	σ_{α}^e (J)*10 ⁻²³	σ_{α}^s (J)*10 ⁻²³	$\frac{C^*}{C}$	T_{meso}^M (K)	$\Delta S_{meso}^M = \frac{H_{meso}^M}{T_{meso}^M}$ (J/K)*10 ⁻²³	σ_{meso}^e (J)*10 ⁻²³	$\frac{D^*}{D}$
460	3.19	3485	113.5	0.001	350	3.00	1350	0.001

Table 5.1: Parameters used in the 1d model for i-PP. Entropy is given per monomer, side and end surface energies are per end.

The 1d model provides a semi-quantitative description of the poisoning phenomenon in i-PP and a stringent test of the model assumptions. In Figure 5.5 both above and below the poisoning temperature the rate of crystallisation shows the experimentally observed peaks dominated by the rapid formation of the mesophase and α -phase at low and high temperature respectively. Both peaks are narrower in experiment, see Figure 5.3 and in particular above the poisoning temperature the peak should be both broader and flatter. The sharpness of both peaks is primarily due to the 1d nature of the solid-on-solid model

and the fixed crystal thickness. Carefully introducing interactions between neighbouring stems, in a pseudo-2d fashion, should stabilise the crystals growth and allow for the entrapment of crystal defects. Moreover allowing the thickness of the incoming crystals to change at different temperatures would further stabilise the growth allowing for the crystals with the optimum thickness to form at the optimum temperature. In Sections 5.3 and 5.4 neighbouring interactions are introduced for a line of 1d interacting growth stems in order to test this assumption.

5.3 Simulation

In order to probe the importance of neighbouring interactions in the model a 2d square lattice of α , meso or liquid sites are considered, analogous to the 3-state Potts Model of a ferromagnet where sites can be in one of 3 equally probable states. The crystal growth is modelled as a 1d line of L growth stems in the x-direction, which interact via nearest-neighbour interactions. Crucially in this model the α -phase is always present and only its growth is considered, not its initial nucleation. Periodic boundary conditions are used to simulate a near infinite crystal width and growth progresses upwards in the y-direction. In contrast to the Potts Model changing the state of each site corresponds to removing to, adding to or converting sites at an already existing interface of a growing crystal. Magnetic systems in general do not have this restriction.

The simulation progresses, at a given stem i , by considering the allowed processes that may take place which depends on both the height of the stem h_i and the number of α -phase chains held by it, $n_i^{(\alpha)}$. The methods are described in detail in [13, 25, 26]. For an α -phase stem, $h_i = n_i^{(\alpha)}$, processes A and C can take place. For a stem containing one or more mesophase blocks $h_i > n_i^{(\alpha)}$, two different process sets may occur. If $h_i - n_i^{(\alpha)} = 1$ processes A , B , C and D can take place otherwise $h_i - n_i^{(\alpha)} > 1$ and processes A , B , C^*

and D^* can take place such that blocks convert more slowly when the interface is buried. See Figure 5.6 or 5.4 for a depiction of these processes in the quasi-1d simulation and 1d model respectively. In the simulation the key values recorded for each stem are the total stem height, h_i and the number of alpha phase stems it contains $n_i^{(\alpha)}$ such that there is only ever a single α -meso interface. This ensures that for covered and uncovered stems alike it is impossible for an α -phase block to be found above a mesophase block. A maximum rate $R_{Max}(T) = A(T) + B(T) + C(T) + D(T) + C^*(T) + D^*(T)$ is then defined as the sum of all the model processes and a random number is drawn between 0 and $R_{max}(T)$ to decide which process will take place. Crucially it is important to note that the sum of all the allowed processes $R_i(T)$, at a given stem i may be less than the maximum rate $R_{Max}(T)$ such that $R_i(T) < R_{Max}(T)$. In this situation it is possible that the stem remains unchanged during this MC step, thus the probability of a process taking place is $\frac{R_i(T)}{R_{Max}(T)}$. A single MC step is then equivalent to a physical time of $\frac{1}{R_{Max}(T)}$. The growth rate in the simulation $\langle R_{sim}(T) \rangle$, is measured using Equation 5.14.

$$\langle R_{sim}(T) \rangle = a_f(T)^2 N(T) R_{Max}(T) \frac{1}{M} \sum_{i=1}^L h_i \quad (5.14)$$

Where $a_f^2(T)$ and $N(T)$ are as defined in Section 5.2, L is the number of growth stems, h_i is the stem height and M is the number of MC steps. In this case detailed balance is ensured for the growth parameters because P_m is in steady state. The overall equilibrium state however is the α -phase hence the growth regime is already out of equilibrium and detailed balance does not apply.

The probability of the allowed processes at each site must be adjusted by factoring in nearest-neighbour interactions at any given stem i as shown in Figure 5.6, where the clear empty boxes indicate the neighbours considered for each of the given processes. The adjusted rates are now introduced, where n_α , n_m and n_l indicate the number of

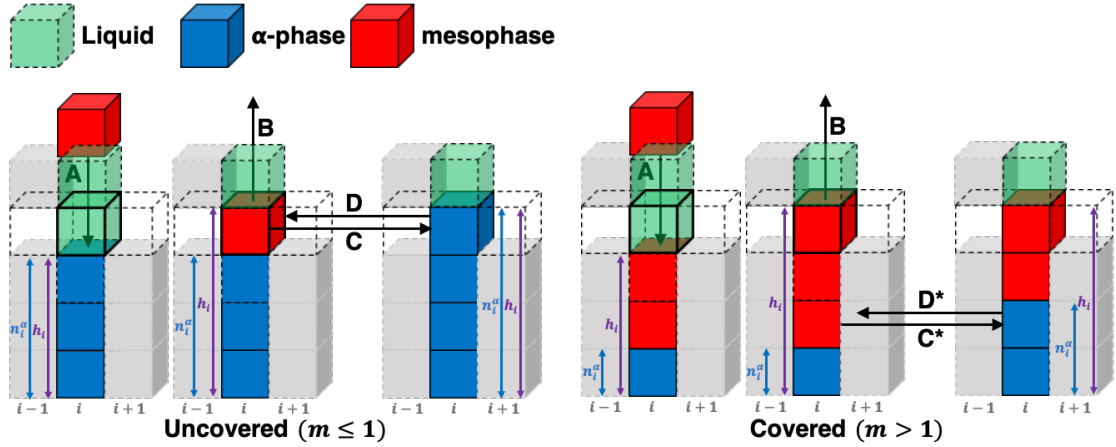


Figure 5.6: Illustration of the allowed processes in the 2d self-poisoning model for i-PP for uncovered and covered stems. Liquid, meso and α -phase neighbours are shown in green, red and blue respectively. Attachment A and detachment B may occur at the same rate in both situations. Conversion of a mesophase block to an α -phase block and vice versa may occur at rates C and D respectively when $m \leq 1$ and C^* and D^* when $m > 1$, dashed boxes indicate nearest-neighbour interactions with neighbouring stems. The height of the alpha phase $n_i^{(\alpha)}$ (blue arrow) and total height of the stem h_i (purple arrow) as used in the simulation have been drawn in for clarity.

neighbouring blocks in the, α -phase, mesophase and liquid phase respectively.

$$A(T) = A_0 \exp(-\gamma(n_l - n_m - n_\alpha)) \quad (5.15)$$

$$B(T) = B_0 \exp(\gamma(n_l - n_m - n_\alpha)) \quad (5.16)$$

$$C(T) = C_0 \exp(\delta(n_\alpha - n_m - n_l)) \quad (5.17)$$

$$D(T) = D_0 \exp(-\epsilon(n_\alpha - n_m - n_l)) \quad (5.18)$$

Parameters γ , δ and ϵ correspond to the mesophase attachment or detachment coupling $A(T)$ or $B(T)$, the mesophase conversion coupling $C(T)$ and the α -phase conversion coupling $D(T)$ respectively. Prefactors A_0 , B_0 , C_0 and D_0 represent the rates of the 1d model which may be raised or lowered according to the neighbouring configurations. The model assumes that in process $A(T)$ both mesophase and α -phase neighbours are

equivalent and that only liquid neighbours lower the rate of attachment, whilst the opposite is true for $B(T)$. For the conversion process $C(T)$, mesophase and liquid neighbours are treated as equivalent and decrease the conversion rate while α -phase neighbours increase the rate, the opposite is true for $D(T)$. Whilst in reality the situation is more complex, poisoning should still be observed with even the simplest sensible neighbouring interactions in the model. Refinement of nearest-neighbour interactions will be discussed in Chapter 7 as future work.

5.4 Results and Discussion

The simulations were run for 1.5×10^7 iterations at each temperature between 260K and 380K at 1K intervals. Snapshots of the α -phase crystal growth front were recorded for each temperature at 4 different intervals during runtime and are plotted in Figure 5.7(b) alongside the final growth fronts recorded at the end of each simulation run at 320K, 322K, 324K and 326K. The parameters for the 1d rates in Section 5.2 were kept the same and the rates were raised or lowered using the interaction scheme outlined in Section 5.3. The parameters γ , δ and ϵ were all set at 0.5 such that, regardless of the neighbouring configuration, the maximum attainable rate is that of the 1d model.

The growth rate at all temperatures with neighbouring interactions switched off and on is shown in Figure 5.7 (a) in black and red respectively. It is immediately obvious that including interactions between the neighbouring stems has not had the desired effect of broadening and flattening the α -phase peak, the reason for this is that as $T \rightarrow T_{meso}^M$ the ratio of the mesophase detachment rate to that of meso- α conversion $\frac{C(T)}{B(T)}$ falls rapidly to zero and the growth of the α -phase is arrested. In order to overcome this problem it has been suggested that the model should incorporate a new process whereby α -phase chains with the correct helical conformation may attach directly from the melt. This

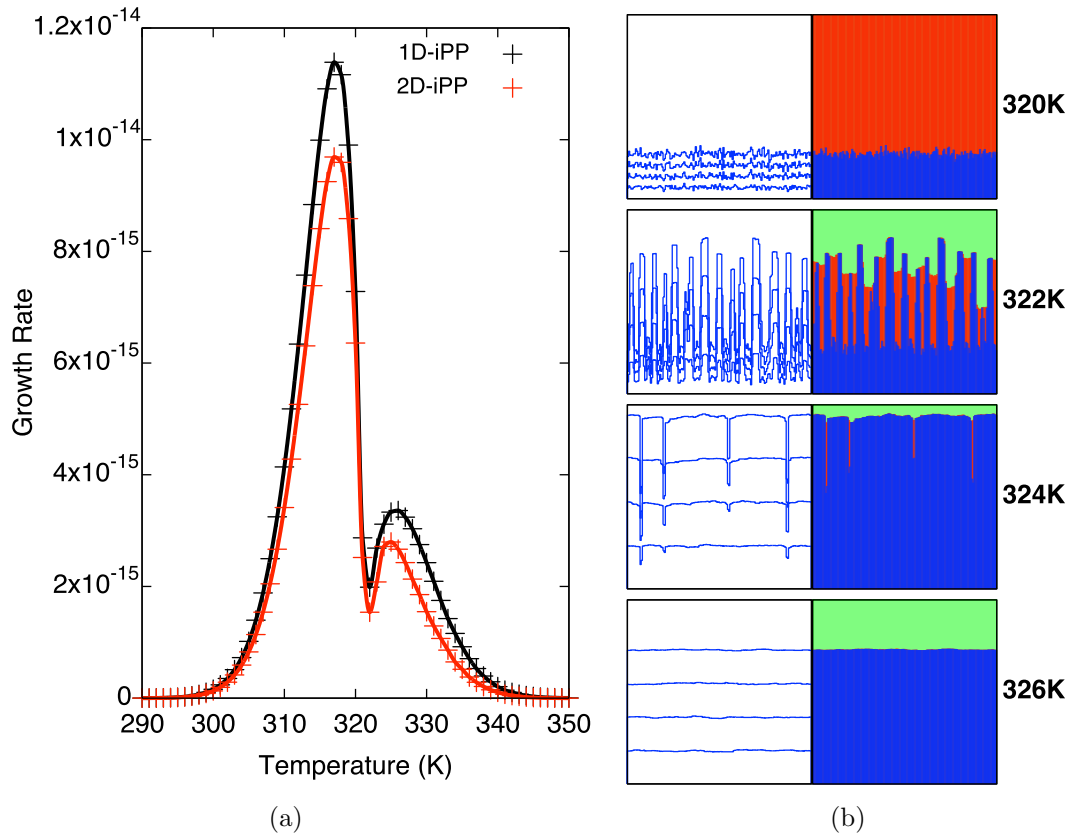


Figure 5.7: (a) Growth rate as a function of temperature measured from 2d simulation with neighbouring interactions switched on (red) and off (black), $\gamma = \delta = \epsilon = \frac{1}{2}$. (b) Adsorption of chains in the mesophase (red) onto a growing α -phase chain crystal (blue) where the liquid-phase is shown in green. The left-hand side shows the progression of the α -phase chain crystal at 4 different increments during runtime. The right-hand side shows both the α -phase and mesophase chains at one moment in time. In each case $\gamma = \delta = \epsilon = \frac{1}{2}$, parameters for the 1d rates are kept the same. The minimum growth occurs close to 322K, below this temperature mesophase chains completely block the growth of the α -phase chain crystal.

would allow the α -phase to continue to grow when $T > T_{meso}^M$.

Snapshots of the growth front have been taken at 4 different temperatures around the poisoning point and are shown in Figure 5.7 (b), the α -phase, mesophase and surrounding liquid are shown in blue, red and green respectively. The left-hand side of the diagram shows the height of the α -phase growth front $n_i^{(\alpha)}$, at 4 different intervals during runtime

and the right-hand side shows the height of both the mesophase and α -phase chains h_i , at one point in time. At 326K the α -phase crystal grows continuously with the growth rate gradually decreasing as T approaches $T \rightarrow T_{meso}^M$, at this temperature the mesophase is highly unstable and will either quickly convert into the α -phase form or rapidly desorb. Only a few mesophase blocks are observable on the surface of the α -phase crystal at this temperature. At 324K the α -phase is growing rapidly and an increasing number of mesophase chains are building up on the surface, with some mesophase stems grouping together to block the growth of the α -phase beneath resulting in deep valleys in the α -phase crystal. The full effect of poisoning can be seen at 322K where the mesophase chains are partially stable, large portions of mesophase crystal have built up causing the surface of the α -phase crystal to become very rough and mesophase chains saturate the surface of the growing crystal beneath. Growth is only possible at this point by rapid conversion of mesophase chains but once the interface becomes buried the system will drop to a slower rate of conversion. This results in the growth front seen at 320K where the growth of the α -phase crystal is completely blocked by the formation of the mesophase and the interface between the two phases is buried. Some α -phase crystal growth will occur via conversion but this rapidly decreases as the temperature is lowered even further. At this temperature the mesophase crystal is self-supporting and does not require the presence of α -phase chains to seed its growth, the growth front of the α -phase is also notably rough.

It is also worth mentioning that the crystal morphology, even in this pseudo-2d model, can be compared with the AFM images of the growth of i-PP in [7]. Figure 5.8 shows the AFM images for i-PP at 60°C. A significant number of lamellae appear to grow in a sea of highly dense irregular objects which is likely to be the mesophase in question, the cross-hatched patterns are typical of the α -phase. This is consistent with the poisoning model whereby mesophase domains block the growth of the α -phase crystal and the

surface morphology is very rough, see Figure 5.7 (b) 322K.

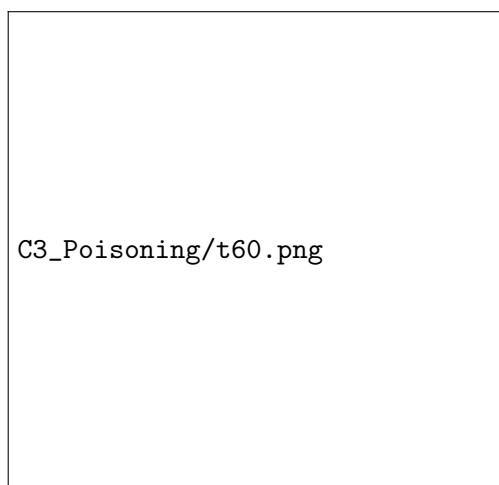


Figure 5.8: AFM image of i-PP at 60°C reproduced with permission from [7].

Our 1d model and pseudo-2d simulations provide a clear proof of concept for the existence of self-poisoning in i-PP. In spite of the model's simplicity, semi-quantitative agreement has been found with the experimentally observed growth rate at large undercooling. Specifically the two-step process involved in building the α -phase crystal captures the competition between chains finding the correct helicity to attach to the growth front of the α -phase crystal and their desorption. The overgrowth of the mesophase and its detachment from the surface limits the α -phase growth.

In future work it would be interesting to extend this model to other cleaner systems where the proximity of the glass transition does not have a significant influence on crystal growth. In recent work, long chain polyethylenes with bromines substituted periodically along the backbone have been seen to crystallise in two different forms [27]. In form I chains grow by attaching to the growth front in an elongated all-trans crystal form, in form II a sawtooth zig-zag crystal is formed where bromine atoms sit at the apex of the zig-zag. Chains may attach to the growing crystal in either of these two forms and it has been seen that the same minimum in the growth rate appears and is more pronounced

than in i-PP. This is thought to be due to competition between the different forms where the growing zig-zag form blocks the all-trans crystal form. It would be interesting to re-parameterise the 1d and 2d models to capture this behaviour, to see if self-poisoning can again explain the growth rate minimum seen in semi-crystalline polymers.

Bibliography

- [1] G. W. Ehrenstein. *Polymeric materials: structure, properties, applications*. Carl Hanser Verlag GmbH Co KG, 2012.
- [2] S.-G. Yang, H.-J. Xie, H. Saba, L. Cseh, and G. Ungar. *Polymer*, 191:122246, 2020.
- [3] P. Corradini, C. De Rosa, G. Guerra, and V. Petraccone. *Polymer communications (Guildford)*, 30(9):281–285, 1989.
- [4] D.-W. Van der Meer. *University of Twente*, 2003.
- [5] S. Brückner, S. V. Meille, V. Petraccone, and B. Pirozzi. *Progress in Polymer Science*, 16(2-3):361–404, 1991.
- [6] L. Hanna, P. Hendra, W. Maddams, H. Willis, V. Zichy, and M. Cudby. *Polymer*, 29(10):1843–1847, 1988.
- [7] D. Cavallo, L. Zhang, G. Portale, G. Alfonso, H. Janani, and R. Alamo. *Polymer*, 55(15):3234–3241, 2014.
- [8] D. Mileva, J. Wang, M. Gahleitner, P. Doshev, and R. Androsch. *Polymer*, 102:214–220, 2016.
- [9] D. Mileva, M. Gahleitner, P. Shutov, T. Vestberg, J. Wang, and R. Androsch. *Thermochimica Acta*, 677:194–197, 2019.

- [10] C. Schick and R. Androsch. *Polymer Crystallization*, 1(4):e10036, 2018.
- [11] G. Ungar, E. G. R. Putra, D. De Silva, M. Shcherbina, and A. Waddon. The effect of self-poisoning on crystal morphology and growth rates. In *Interphases and Mesophases in Polymer Crystallization I*, pages 45–87. Springer, 2005.
- [12] M. Dosière. *Crystallization of polymers*, volume 405. Springer Science & Business Media, 2012.
- [13] P. G. Higgs and G. Ungar. *The Journal of Chemical Physics*, 100(1):640–648, 1994.
- [14] G. Ungar and A. Keller. *Polymer*, 28(11):1899–1907, 1987.
- [15] G. Ungar and X.-b. Zeng. *Chemical reviews*, 101(12):4157–4188, 2001.
- [16] J. Ramos, J. F. Vega, and J. Martínez-Salazar. *Macromolecules*, 48(14):5016–5027, 2015.
- [17] T. Schilling and D. Frenkel. *Journal of Physics: Condensed Matter*, 16(19):S2029, 2004.
- [18] S. Whitelam, Y. R. Dahal, and J. D. Schmit. *The Journal of Chemical Physics*, 144(6):064903, 2016.
- [19] M. L. Williams, R. F. Landel, and J. D. Ferry. *Journal of the American Chemical Society*, 77(14):3701–3707, 1955.
- [20] J. Armistead and J. D. Hoffman. *Macromolecules*, 35(10):3895–3913, 2002.
- [21] K. Mezghani and P. J. Phillips. *Polymer*, 39(16):3735–3744, 1998.
- [22] F. De Santis, S. Adamovsky, G. Titomanlio, and C. Schick. *Macromolecules*, 39(7):2562–2567, 2006.

- [23] F. De Santis, S. Adamovsky, G. Titomanlio, and C. Schick. *Macromolecules*, 40(25):9026–9031, 2007.
- [24] Y. F. Wang and D. R. Lloyd. *Polymer*, 34(22):4740–4746, 1993.
- [25] G. Gilmer and P. Bennema. *Journal of Applied Physics*, 43(4):1347–1360, 1972.
- [26] D. M. Sadler. *The Journal of Chemical Physics*, 87(3):1771–1784, 1987.
- [27] X. Zhang, W. Zhang, K. B. Wagener, E. Boz, and R. G. Alamo. *Macromolecules*, 51(4):1386–1397, 2018.

Chapter 6

Ultralong n-Alkanes Adsorbed on Graphite

6.1 Introduction

Polyethylene (PE) is the most abundant plastic on earth and it is used in products such as plastic bags, artificial hips and even bullet-proof vests; last year production was in excess of 110 million tonnes. Improving the processing of PE, in particular understanding its behaviour on cooling and the crystallisation process has important implications in polymer processing. The processing techniques of PE are in constant development and as they evolve new experimental and theoretical studies are required which can provide important insights at a molecular level into PE. Motivated by the significant interest in PE globally our collaborators (Ungar and co-workers) have had a long-standing interest in the phenomenon of polymer melting and crystallisation [1–6]. Recent advancements in chemical synthesis of polymers has allowed mono-disperse n-alkanes with fixed length to be synthesised for the first time. These model polymers provide ideal systems where open questions about polymer melting and crystallisation can be tackled with precision. Coupled with the improved availability of atomic force microscopes, it is now feasible to visualise these systems at high resolution. This is the foundation of the experimental

work showcased in this chapter and it has created the ideal opening for a theoretical study.

A high resolution AFM study of mono-disperse ultra-long n-alkanes ($C_{60}H_{122}$, $C_{122}H_{246}$, $C_{194}H_{390}$, $C_{246}H_{494}$ and $C_{390}H_{782}$) adsorbed on a graphite surface as monolayers has been performed to better understand the polymer crystallisation process. The melting of polymers in bulk is well known to be a strongly first-order transition but when adsorbed on graphite it was soon realised that they may melt gradually from their ends inwards, until over half the chain is disordered before finally melting. Moreover the monolayer can be found to melt up to 80K above the bulk melting temperature. In the 1960s it was predicted that this behaviour could be observed [7] in bulk but it has never been captured in action until now.

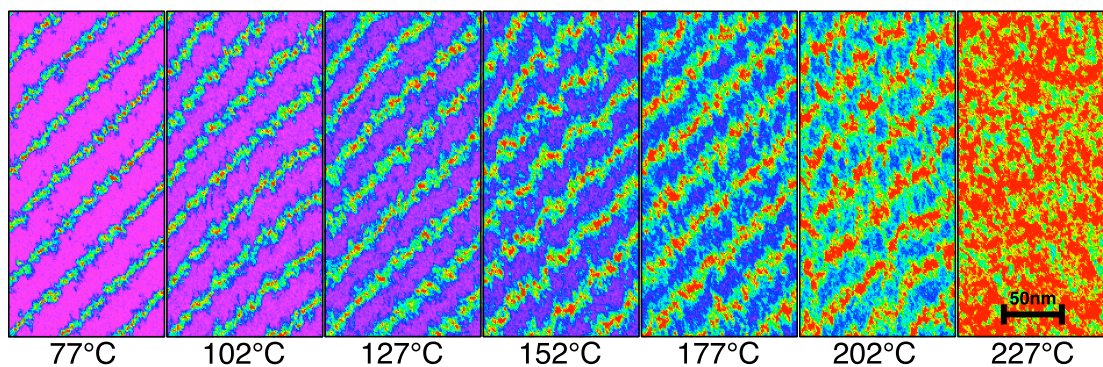
In order to study these monolayers and understand why pre-melting may occur in an essentially 2d melt and not in 3d on such a large scale required a coarse-grained MD model. That same year I had been introduced to Dr Kyle Hall after being invited to give a talk at the ARL's strategic materials meeting at the Temple Materials Institute in 2019. Being familiar with his work developing coarse-grained models of PE we began discussing the problem and it was quickly decided that we would work together simulating these monolayers. The coarse-grained model in question is the SDK (Shinoda-DeVane-Klein) [8] model which has been shown to be a viable CG model for simulating PE [9]. In this work coarse-grained MD simulations of ultra-long $C_{390}H_{782}$ alkanes adsorbed as monolayers on graphite are performed which successfully reproduce the experimentally observed pre-melting phenomenon at all temperatures below the melt with important implications for the melting of polymers in general. Together with the experimental results and a simple mean field theory the results provide a complete explanation of the why ultra-long n-alkanes adsorbed on graphite may melt nearly continuously. This work has been submitted as a two part publication.

6.2 Published Article 3

Submitted

1. Reinterpreting Bulk Polymer Melting: Insights from Quasi-Continuous Melting in Model Polymer Monolayers

Ruibin Zhang, William S. Fall, Kyle Wm. Hall, Gillian A. Gehring,
Xiangbing Zeng and Goran Ungar



Author Contributions

G.U. conceived and directed all aspects of the project. R.B.Z., supervised by G.U., carried out the AFM experiments. W.S.F., supervised by G.A.G. and K.Wm.H., carried out the molecular dynamics simulations together with K.Wm.H. X.B.Z. developed the mean field theory with support from G.A.G. All authors contributed to data analysis and production of tables and figures. X.B.Z. and G.U. prepared the manuscript with written contributions from all co-authors. See page **viii** for author declarations.

Reinterpreting Bulk Polymer Melting: Insights from Quasi-Continuous Melting in Model Polymer Monolayers

Ruibin Zhang^{1,2,3}, William S. Fall^{1,4}, Kyle Wm. Hall⁵, Gillian A. Gehring⁴, Xiangbing Zeng^{2,*}, Goran Ungar^{1,3,*}

1. State Key Laboratory for Mechanical Behavior of Materials, Shaanxi International Research Centre for Soft Materials, Xi'an Jiaotong University, Xi'an, 710049, China.
2. Department of Materials Science and Engineering, University of Sheffield, Sheffield S1 3JD, UK.
3. Department of Physics, Zhejiang Sci-Tech University, Hangzhou, 310018, China.
4. Department of Physics and Astronomy, University of Sheffield, Sheffield S3 7RH, UK.
5. Department of Chemistry, Temple University, Philadelphia, Pennsylvania 19122, USA.

*Correspondence to: x.zeng@sheffield.ac.uk, g.ungar@sheffield.ac.uk.

Receipt Date:

Abstract: Polymers, like other pure substances, normally melt abruptly. However, we report nearly continuous melting of lamellar crystals in monolayers of ultralong n-alkane C₃₉₀H₇₈₂ on graphite. This was observed by AFM and described using mean-field theory and MD simulation. Remarkably, the final melting point is 80°C above that of the bulk alkane, and the crystalline fraction in lamellae decreases continuously from nearly 100% to only 40% before the monolayer finally melts. We show that the absence of such continuous melting in bulk alkanes or polymers is due to steric overcrowding at the crystal-melt interface, not present in the monolayer because molecular segments can escape into the third dimension.

KEYWORDS. long-chain alkanes, atomic force microscopy, molecular dynamics simulation, polymer crystallization, chain tilt.

Crystal melting is normally a strongly first-order transition. At the melting point (T_m), a pure substance faces a stark choice between being a low-energy, low entropy crystal and a high-energy, high-entropy liquid (Fig. 1a). However, 3D long-range positional and orientational order of a crystal can disappear in two or more separate steps through intermediate liquid-crystalline states (Fig. 1b).¹ Most crystalline long-chain molecules and polymers do not form liquid crystals, but it had been suggested that their crystal-melt transition may not be sharp either: lamellar crystals may melt from the surface inward nearly continuously (Fig. 1c).^{2,3,4,5} However, only a very limited amount of “premelting” has been seen,⁶ involving disordering of a surface layer only a few atoms deep. Polymers usually melt over a range of temperatures but mainly due to the diversity in thickness of their lamellar crystals. When the thickness is uniform and thickening during heating is suppressed, melting occurs within 2°C,⁷ and in long-chain monodisperse n-alkanes within a 1°C interval.⁸ However, here we report that nearly continuous equilibrium melting from surface inward can indeed occur in monolayers of long-chain compounds.

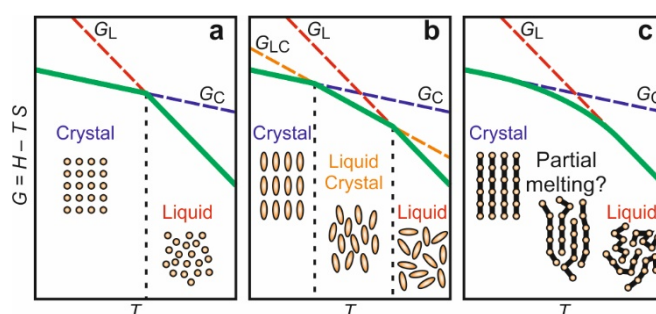


FIG. 1. Schematic free energy-temperature profiles for crystal-liquid phase transition. (a) A normal crystal. (b) A liquid crystalline compound. (c) Hypothetic scenario for long-chain molecules/polymer. C, LC, L are the three phases.

Our investigation centers on the melting behavior of ultra-long linear alkanes. Here we focus on the longest exactly monodisperse alkane ever synthesized, $n\text{-C}_{390}\text{H}_{782}$.⁹ while the behaviour of a whole series of six such compounds, from $\text{C}_{60}\text{H}_{122}$ to $\text{C}_{390}\text{H}_{782}$, is described in the accompanying paper in *Phys. Rev. B*.¹⁰ Monodisperse linear paraffins with chain length $n > 100$ have been synthesized through a series of protection-coupling-deprotection steps,^{8,9,11,12} and have provide unique model polymers allowing stringent tests of theories of polymer crystallization and morphology, unblurred by polydispersity.^{8,13,14,15} Herein the melting behavior of graphite-supported monomolecular layers of $n\text{-C}_{390}\text{H}_{782}$ is investigated using atomic

force microscopy (AFM). Large scale molecular dynamics (MD) simulations are also performed, and a semi-quantitative analytical model is constructed. Together these studies provide experimental evidence as well as an explanation of the extraordinary nearly continuous melting, ending 80°C above the bulk melting point, of this model polymer. The findings help the general understanding of the relatively underexplored phenomenon of polymer melting. The accompanying paper,¹⁰ in addition to involving other long alkanes, also reports on a new surface roughening transition manifesting itself as a change from tilted to perpendicular chain stacking in the lamellar crystals as the temperature is raised.

n-Alkanes C_nH_{2n+2} and polyethylene (PE) molecules adhere particularly strongly to the graphite (001) surface, due to a close epitaxial match between hydrogens on alternative CH_2 groups of an all-trans alkane chain (0.254nm) and the centers of the six-membered rings of graphite (0.246nm) (Fig. 2a). Previous studies on adsorbed short alkanes, mainly in the length range $20 < n < 40$ ^{16,17,18,19,20,21,22} have found that monolayers on graphite melt at temperatures somewhat above bulk melting point T_m^{bulk} , with additional phase transitions in the ordered state.²³ A “pre-freezing” effect several degrees above T_m^{bulk} was also found in polyethylene thin layers.²⁴ Most notably, melting of monolayers 45°C above T_m^{bulk} has been reported for $C_{60}H_{122}$.²⁵ However, there have been only three reported AFM studies of ultra-long alkanes.^{18,26,27}

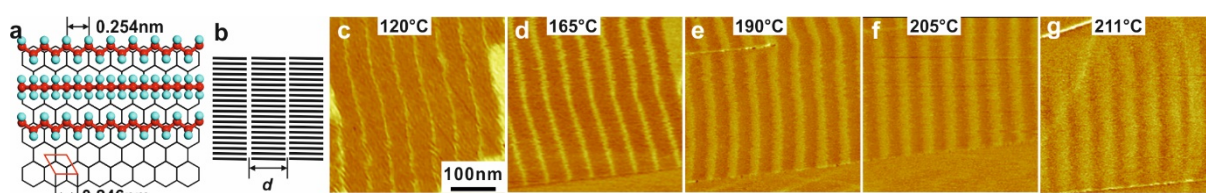


FIG. 2. (a) Epitaxial arrangement of n-alkane chains on graphite (001) surface. (b) 3 lamellae of 20 chains (schematic). (c-g) AFM phase images of a monolayer of $n-C_{390}H_{782}$ at increasing temperatures. $d = 50.0$ nm, calculated chain length 49.8nm. Details of AFM experiments see Appendix.

Figs. 2c-g show AFM phase images of monolayer (~ 0.4 nm thick¹⁰) melt-crystallized films of $n-C_{390}H_{782}$, recorded at increasing temperatures. The bright lines are soft amorphous regions around chain ends with increased phase lag ϕ in response to AFM tip tapping. The dark bands are stiffer ordered regions containing parallel

chains (Fig. 2b) which are known to align epitaxially along one of the three [100] directions of the graphite lattice.^{23,26} Error! Bookmark not defined. According to previous studies, the orientation of the C-C-C zigzag plane alternates from chain to chain between parallel and perpendicular to the graphite surface (Fig. 2a).²¹

By analogy with the structures seen in bulk alkanes and polymers we will refer to the monolayer ribbons of parallel chains as lamellae, to the regions around chain ends as lamellar surfaces, and to periodicity d as lamellar thickness.

Two extraordinary phenomena are observed on heating. Firstly, the lamellae were found to persist to above 211°C, 80°C above T_m^{bulk} of n-C₃₉₀H₇₈₂, which is 132°C⁸ (Fig. 2g). Secondly, the soft stripes gradually widen with increasing temperature at the expense of the darker crystalline layers. Close to the final melting point T_m their thickness even exceeds that of the remaining crystalline layers, with d remaining constant. The same behavior is also seen on cooling, hence the observed surface melting is an equilibrium phenomenon. We also calculated the averaged phase profiles $-\Delta\phi$ at different temperatures - see Fig. 3e; the originally narrow soft layers (minima) broaden to become eventually wider than the rigid middle before all periodicity disappears at T_m .

MD simulations of a C₃₉₀H₇₈₂ monolayer on graphite were performed as described in Appendix and ¹⁰. The experimental $\Delta\phi$ is proportional to the irreversible movement of chains by the AFM tip, which is impeded if the chains are straight and parallel as in the crystalline portion, but becomes allowed as chains are misaligned. Hence we calculate the local alignment order parameter $P_2 = \frac{1}{2}\langle 3\cos^2\theta - 1 \rangle$ for all chain segments. Higher (lower) P_2 indicates higher (lower) segment order.¹⁰

Maps of simulated lamellar structures are provided in Fig. 3a based on the P_2 order parameter where the darker color is for a larger value of P_2 . The light areas reveal differing degrees of melting near the chain ends below T_m . Above T_m all periodicity is lost. This is an interesting case of almost 2D liquid as it remains in contact with the graphite, however entropy allows some chains to cross.

The P_2 maps indeed show a remarkable likeness to the AFM images. At $T > 102^\circ\text{C}$ the order-disorder interfaces are evidently rough, with molecular centers displaced at random. Even in the bulk chain sliding is facilitated by moving g^+tg^- kinks,²⁸ so it must

occur readily in a monolayer where out-of-plane displacement by kinks is allowed. At 77°C the low- P_2 regions are rather localized, whereas at 202°C they are dispersed more widely (Figs. 3b,c). Bent chains predominate in the melt (Fig. 3d for 327°C).

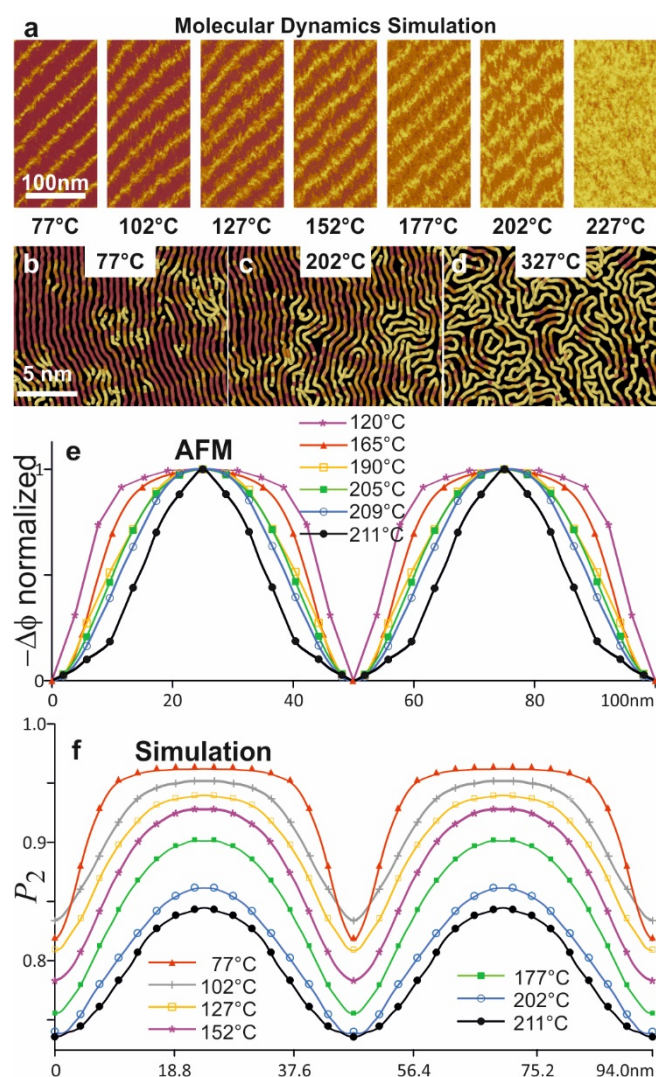


FIG. 3. (a) Crystallinity (P_2) maps from MD simulations for temperatures between 77°C and 227°C (see Appendix for details). Each map was calculated by partitioning the simulated surface into a 1 nm x 1 nm grid, and then locally averaging P_2 values across 50 instantaneous configurations (at 20ps intervals). (b-d) Zoomed-in snapshots of the simulations at 77°C, 202°C and 327°C produced using OVITO.²⁹ The tubes correspond to individual alkane chains, and are colored according to their P_2 values. (e) Averaged and normalized AFM phase shift ($-\Delta\phi$) profiles of $C_{390}H_{782}$ at temperatures from 120°C to 211°C, with maximum phase shift at the surface (as 0) and minimum (as 1) at the center of the lamellae. (f) P_2 profiles calculated from the respective simulated P_2 maps. In our MD simulations the abscissa values are

measured along the molecular direction which was actually inclined to the observed stripes.

The match between the simulated P_2 order parameter maps and AFM phase images is best shown in Figs. 3e,f, where averaged P_2 profiles of the $C_{390}H_{782}$ lamellae at different temperatures are plotted together with the experimental phase profiles. In both cases the thickness of the ordered (crystalline) regions decreases with increasing temperature. At 211°C more than half of the lamellar thickness is disordered, matching the experimental results. The ordering of the molecular segments in MD simulations is also examined by calculating the average z-displacement away from the graphite substrate, as well as the chain mobility parameter.¹⁰ Both observables show trends similar to that of P_2 as a function of temperature. It is remarkable that aspects of molecular simulation, such as T_m , order parameters and average profiles are in such close agreement with experiment.

A mean-field model of a lamella of extended chains is constructed in order to explain the continuous thinning of the lamellae leading to their final melting. The model of an alkane chain with n CH_2 (methylene) groups is shown in Fig. 4a where x methylenes are molten; x can be distributed freely between the two ends of the chain. However, a clean-cut switch between crystalline and molten states of the methylenes at the crystal-melt boundary is unrealistic. Conformations of chain segments emerging from the crystalline layer will be highly restricted due to the lack of lateral space, referred to as “overcrowding” at the crystal-melt interface (Fig. 4a).^{30,31} For mathematical expediency, in our model this is taken into account by assuming that the first $t/2$ groups of the melted ends have the energy of the melt but the entropy of the ordered chain. Therefore we can write the free energy of the partially melted chain as

$$F_P(x) = \begin{cases} xT_m^0 S_m - k_B T \ln(x + 1) & 0 < x < t \\ x(T_m^0 - T)S_m + tTS_m - k_B T \ln(x + 1) + 2\sigma_e & t < x < n - 1 \end{cases} \quad (\text{Equation 1})$$

Here T_m^0 is the ultimate melting point of the polymer of infinite length, S_m is the melt entropy per CH_2 , and $\sigma_e = H_e - TS_e$ is the free energy contribution from the two ends of each chain. The chain sliding entropy equals $k_B \ln(x + 1)$, as for the x end methylenes there are $x + 1$ choices in selecting the position at which to separate the two ends by the $n - x$ ordered units. When the surface is rough, i.e. when $x > t$,

there is an additional increase in the system free energy $2\sigma_e$ due to the disappearance of the smooth end surface (the factor 2 is used as each molecule has two ends).

The minimum free energy of a partially melted chain is therefore found at

$$x = x_0 = \begin{cases} \frac{k_B}{S_m} \frac{T}{T_m^0} - 1 & 0 < x_0 < t \\ \frac{k_B}{S_m} \frac{T}{T_m^0 - T} - 1 & t < x_0 < n - 1 \end{cases}$$

(Equation 2)

This results in a high-free-energy transition layer of thickness $t/2$ between crystal and melt. Thus the more severe the overcrowding the larger the t . In our model partial melting of the chain, however, does not in itself reduce the system free energy below T_m , as the entropy increase on melting the end segments comes with an increase in enthalpy due to loss of crystallinity. Stabilization of partially melted chains should come from the extra translational entropy $k_B \ln(x + 1)$ of the molecules free to slide through the crystalline layer.

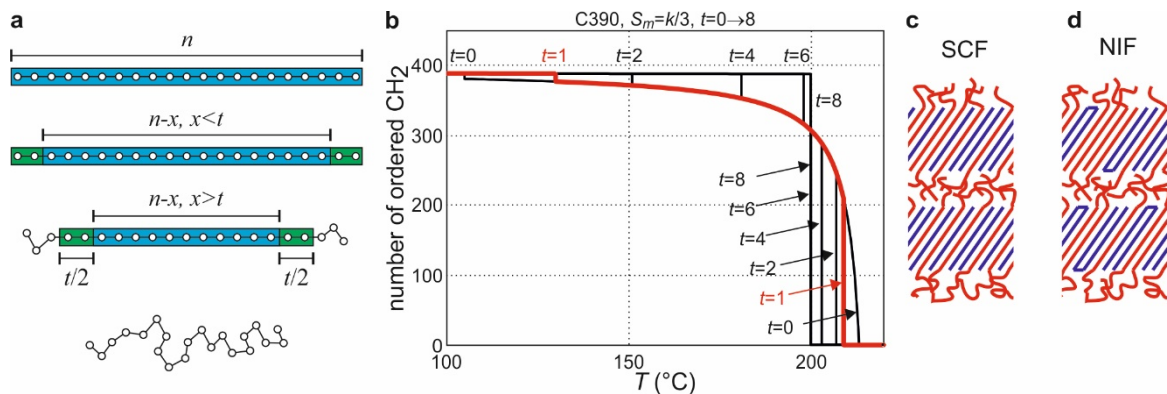


FIG. 4. (a) Schematic models of chains in different states. Top to bottom: fully crystalline, no surface disorder; smooth surface with small premelting/surface disorder, $x < t$; rough surface with significant premelting, $x > t$; and melt. (b) Number of CH₂ groups remaining in the ordered middle of the lamellae (proportional to crystallinity), calculated for transition layer thickness t from 0 to 8. (c) Semicrystalline form (SCF) can be thermodynamically stable in binary mixtures of ultra-long n-alkanes with only the chain ends of the longer alkane melted (shorter alkane molecules are colored blue and longer alkane red).³² (d) Tight chain folding and tilting are needed to alleviate overcrowding and allow growth of metastable

semicrystalline NIF lamellae in pure ultra-long alkanes (folded chain colored blue and non-folded red).³³

The equations, developed in ref 10, allow us to evaluate the free energies of perfectly ordered chains, partially melted chains with $x < t$, with $x > t$, and of full melt. By equating pairs of free energies, we were able to reproduce the surface roughening transition (the small abrupt drops in crystallinity, not discussed here), the continuous partial melting and the final melting, all shown in Fig. 4b for n-C₃₉₀H₇₈₂, for different values of t (for more details see ref 10). At low temperatures the crystallinity is nearly 100%, decreasing continuously with increasing temperature, reaching around 50% before final melting, with the best-fit value of the “overcrowding” parameter t of only 1 (red curve). For $t = 0$ (no overcrowding) melting becomes completely continuous. However, an increase in t decreases T_m , and continuous melting disappears when $t \geq 8$.

In the following we compare melting in 2D and 3D systems of chain molecules and examine why no significant premelting occurs in the bulk. For perfectly aligned chains exiting a 3D crystal to instantly adopt random segment orientation, their effective cross-section must increase by a factor g of 2-3 according to theory^{30,31} and 2.3 according to experiment.³² Therefore, in order for a polymer lamella to grow large laterally, a fraction $(1-g^{-1})$ of all chains must either end at the interface, or re-enter the crystal through a sharp fold to make room for the escaping chains. Regarding melting, there would be no thermodynamic advantage in a bulk lamella melting gradually by crystal thinning and thereby having to increase the number of energy-costly chain folds.

Interestingly, while not continuous, a two-step melting does actually occur in the bulk, in co-crystallizing binary mixtures of ultra-long alkanes.³² An semicrystalline form (SCF, Fig. 4c) is stable within $\sim 20^\circ\text{C}$ below the final T_m . Its lamellae contain fully crystalline shorter, and only partially crystalline longer chains, whose dangling ends form a liquid layer. Translational entropy of the longer chains was also thought to stabilize the phase. Another example of a nearly stable semicrystalline phase is the “non-integer form” (NIF) of pure long alkanes, which crystallizes from melt below T_m of the once-folded-chain form (Fig. 4d).^{33,34} NIF lamellae can only grow when enough chains are folded. Generally, surface overcrowding has been accepted as

causing chain-folded crystallization of polymers, but its role in preventing continuous melting has not been recognized until now.

A key question to answer is why near-continuous melting is possible in a thin film but not in the bulk. Our results point to the following two reasons: Firstly and most importantly, the surface overcrowding problem is solved in thin film by “escape in the third dimension”, with chain segments able to detach from the substrate and cross at the crystal-liquid interface, as evidenced by the simulation.¹⁰ This means a greatly reduced t in 2D. An additional advantage of 3D escape is to facilitate g^+tg^- kink formation and hence chain sliding, which stabilizes the semicrystalline state. The second factor deciding if melting could be continuous is the value of melt entropy S_m . For alkanes on graphite the best-fit has $S_m=k_B/3$. This low S_m value is expected as molten chains are pinned to the substrate, making the melt nearly two-dimensional. When S_m is lower, the number of disordered chain ends x for the same undercooling ΔT is higher according to Equation 2, as the entropy of chain sliding (proportional to $k_B \ln(x+1)$) becomes relatively more effective in stabilizing the partially melted state. The higher the S_m , the less effective the sliding and the narrower the premelting range. However, if the overcrowding effect is small as in 2D ($t=1$), taking the experimental value $S_m=1.2k_B$ ($k_B/S_m=0.83$) for bulk PE, the premelting range is narrower but still significant (Fig. 9d in ref. 10). This points to the presence of steric overcrowding at the crystal-amorphous interface being the dominant factor preventing continuous melting in the bulk.

In conclusion, as predicted long ago for polymers but never witnessed, continuous melting has now been observed on a long-chain n-alkane absorbed on graphite. Our experimental observations, molecular dynamics simulation, and theoretical analysis show that such behavior is a result of the much reduced overcrowding effect at the crystal-melt interface, and the much reduced entropy of an essentially 2D melt. The reversal of such conditions, particularly the presence of severe surface overcrowding, is the reason why premelting is almost negligible in bulk polymers and other chain systems.

We are grateful to Professor Michael L. Klein at Temple University for providing the resources and support for the Molecular Dynamics Simulation work, and helpful discussions in manuscript preparation. We are most obliged to Drs. Gerald Brooke

and Shahid Mohammed of University of Durham for providing the long alkane compound. This work used the ARCHER UK National Supercomputing Service (<http://www.archer.ac.uk>). The authors acknowledge funding from EPSRC (EP-P002250, EP-T003294), the 111 Project 2.0 of China (BP2018008), and from NSFC (grant 21674099).

APPENDIX: EXPERIMENTAL METHODS

$C_{60}H_{122}$ was purchased from Sigma Aldrich, and long chain *n*-alkanes $C_{122}H_{246}$, $C_{194}H_{390}$, $C_{246}H_{494}$ and $C_{390}H_{782}$ were kindly provided by Dr. G. M. Brooke of Durham University.

Highly ordered pyrolytic graphite (HOPG) wafers were obtained from Mikromasch, Germany. Ultrathin alkane films on HOPG were prepared by spin-coating, in which one droplet of alkane in toluene (1-10mg/ml) was deposited on a freshly cleaved surface of HOPG at 2000 rpm with an Ossila spin coater. All sample films were subsequently dried in a vacuum oven for 2 hours. The AFM experiment was performed in tapping mode using a Cypher ES AFM instrument, which was equipped with a heating stage allowing heating of sample in air from ambient to 250°C in a sealed environment. AFM scanings were carried out typically at 10°C intervals on heating to detect changes in morphology. Precise phase transition temperatures were determined by imaging at 1°C intervals. Scanning was carried out in repulsive force regime by keeping the phase shift below 90°, and a 90% set point ratio was used. The drive amplitude was gently increased for scanning at higher temperatures in order to prevent the tip from sticking to the sample surface.

Molecular Dynamics (MD) simulations were performed of a periodic 6-lamella monolayer structure composed of 1800 $C_{390}H_{782}$ molecules adsorbed on a graphite surface (141nm x 281nm). The system was modelled using the coarse-grain (CG) SDK model^{35,36,37} without any alterations to the model. This CG model is appropriate for aliphatic and aromatic species,^{35,36,37} and has been previously verified to capture the important features of long-chain alkane systems and associated processes (e.g., crystallization).^{38,39,40} The CG SDK model represents 3 methylene units along an alkane backbone using a single coarse-grain segment (bead). All simulations were performed using the Large-scale Atomic/Molecular Massively Parallel Simulator (LAMMPS)⁴¹ using common methodological strategies (for details see section S2,

SI). The prepared system was annealed from 77°C to 327°C in 25°C intervals (for details see section S2, SI) The tilt-perpendicular transition was not probed in this study since the T-P transition relies on fine details not present in the current representation; the SDK CG beads of the alkane chains (3 CH₂ groups) are larger than the longitudinal shear associated with the tilted phase (1-2 CH₂ groups), and the SDK model approximates graphene using a cubic representation. In keeping with previous studies on alkanes and polymers,^{38,39,40,42,43,44} the ordering of polymer chain segments (i.e., their crystallinity) was probed using the P₂ order parameter (for details see section III, Ref. 10).

-
- ¹ P. G. de Gennes and J. Prost, *The Physics of Liquid Crystals*, 2nd Ed. (Clarendon Press, Oxford, 1993).
- ² P. J. Flory and A. Vrij, *J. Am. Chem. Soc.* **85**, 3548 (1963).
- ³ H. G. Zachmann, *Z. Naturforschg.* **19a**, 1397 (1964).
- ⁴ H. Baur, *Colloid & Polymer Sci.* **256**, 833 (1978).
- ⁵ B. Wunderlich, *Macromolecular Physics* (Academic Press, New York, 1976-1980).
- ⁶ Y. Tanabe, G. R. Strobl, and E. W. Fisher, *Polymer* **27**, 1147 (1986).
- ⁷ H. E. Bair, R. Salovey, and T. W. Huseby, *Polymer* **8**, 9 (1967).
- ⁸ G. Ungar, J. Stejny, A. Keller, I. Bidd, and M. C. Whiting, *Science* **229**, 386 (1985).
- ⁹ I. Bidd and M. C. Whiting, *Chem Commun.* **1985**, 543.
- ¹⁰ R. B. Zhang, W. S. Fall, K. Wm. Hall, G. A. Gehring, X. B. Zeng and G. Ungar, *Phys. Rev. B* (accompanying full paper)
- ¹¹ G. M. Brooke, S. Burnett, S. Mohammed, D. Proctor, and M. C. Whiting, *J. Chem. Soc. - Perkin Trans.* **1**, 1635 (1996).
- ¹² K. S. Lee and G. Wegner, *Makromol. Chem.-Rapid Comm.* **6**, 203 (1985).
- ¹³ S. J. Organ, G. Ungar, and A. Keller, *Macromolecules* **22**, 1995 (1989).
- ¹⁴ G. Ungar and X. B. Zeng, *Chemical Reviews* **101**, 4157 (2002).
- ¹⁵ G. Ungar, E. G. R. Putra, D. S. M. de Silva, M. A. Shcherbina, A. J. Waddon, *Adv. Polym. Sci.* **180**, 45 (2005).
- ¹⁶ J. P. Rabe and S. Buchholz, *Phys. Rev. Lett.* **66**, 2096 (1991).
- ¹⁷ J. P. Rabe and S. Buchholz, *Science* **253**, 424 (1991).
- ¹⁸ L. Askadskaya and J. P. Rabe, *Phys. Rev. Lett.* **69**, 1395 (1992).
- ¹⁹ K. Morishige, Y. Takami, and Y. Yokota, *Phys. Rev. B* **48**, 8277 (1993).
- ²⁰ K. W. Herwig, B. Matthies, and H. Taub, *Phys. Rev. Lett.* **75**, 3154 (1995).
- ²¹ F. Y. Hansen, K. W. Herwig, B. Matthies, and H. Taub, *Phys. Rev. Lett.* **83**, 2362 (1999).
- ²² A. J. Bourque and G. C. Rutledge, *Eur. Polym. J.* **104**, 64 (2018).
- ²³ A. Diama, B. Matthies, K. W. Herwig, F. Y. Hansen, L. Criswell, H. Mo, M. Bai, and H. Taub, *J. Chem. Phys.* **131**, 084707 (2009).
- ²⁴ A. -K. Löhmann, T. Henze, and T. Thurn-Albrecht, *PNAS* **111**, 17368 (2014).
- ²⁵ S. N. Magonov and N. A. Yerina, *Langmuir* **19**, 500 (2003).
- ²⁶ S. N. Magonov, N.A. Yerina, G. Ungar, D. H. Reneker and D. A. Ivanov, *Macromolecules* **36**, 5637 (2003).
- ²⁷ A. Tracz and G. Ungar, *Macromolecules*, **38**, 4962 (2005).
- ²⁸ G. Ungar, *Macromolecules* **19**, 1317 (1986).

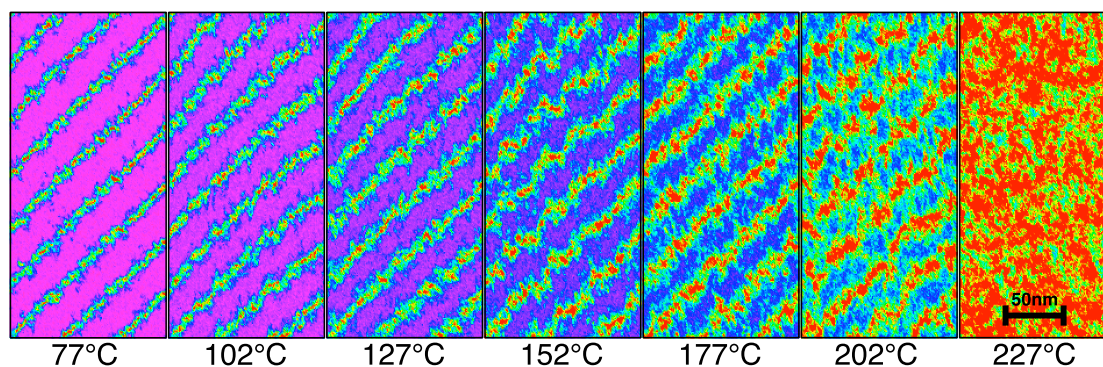
-
- ²⁹ A. Stukowski, *Modelling and Simulation in Materials Science and Engineering* **18**, 015012 (2009).
- ³⁰ C. M. Guttman and E. A. DiMarzio, *Macromolecules* **15**, 525 (1982).
- ³¹ S. Balijepalli and G. C. Rutledge, *Macromol. Symp.* **133**, 71 (1998).
- ³² X. B. Zeng and G. Ungar, *Macromolecules* **34**, 6945 (2001).
- ³³ X. B. Zeng and G. Ungar, *Polymer* **39**, 4523 (1998).
- ³⁴ G. Ungar, X. B. Zeng, G. M. Brooke, and S. Mohammed, *Macromolecules* **31**, 1875 (1998).
- ³⁵ W. Shinoda, R. DeVane, and M. L. Klein, *Mol. Simul.* **33**, 27 (2007).
- ³⁶ R. DeVane, M. L. Klein, C. -c. Chiu, S. O. Nielsen, W. Shinoda, and P. B. Moore, *J. Phys. Chem.* **B114**, 6386 (2010).
- ³⁷ C. -c. Chiu, R. DeVane, M. L. Klein, W. Shinoda, P. B. Moore, and S. O. Nielsen, *J. Phys. Chem.* **B114**, 6394 (2010).
- ³⁸ K. Wm. Hall, T. W. Sirk, M. L. Klein, W. Shinoda, *J. Chem. Phys.* **150**, 244901 (2019).
- ³⁹ K. Wm. Hall, T. W. Sirk, S. Percec, M. L. Klein, and W. Shinoda, *J. Chem. Phys.* **151**, 144901 (2019).
- ⁴⁰ K. Wm. Hall, S. Percec, and M. L. Klein, *J. Chem. Phys.* **150**, 114901 (2019).
- ⁴¹ S. Plimpton, *J. Comp. Phys.* **117**, 1 (1995).
- ⁴² P. Yi, C. R. Locker, and G. C. Rutledge, *Macromolecules* **46**, 4723 (2013).
- ⁴³ T. Yamamoto, *J. Chem. Phys.* **115**, 8675 (2001).
- ⁴⁴ C. Liu and M. Muthukumar, *J. Chem. Phys.* **109**, 2536 (1998).

6.3 Published Article 4

Submitted

2. Quasi-Continuous Melting and a Roughening Transition in Monolayers of Ultra-Long Alkanes: New Insights into Polymer Melting

Ruibin Zhang, William S. Fall, Kyle Wm. Hall, Gillian A. Gehring,
Xiangbing Zeng and Goran Ungar



Author Contributions

G.U. conceived and directed all aspects of the project. R.B.Z., supervised by G.U., carried out the AFM experiments. W.S.F., supervised by G.A.G. and K.Wm.H., carried out the molecular dynamics simulations together with K.Wm.H. X.B.Z. developed the mean field theory with support from G.A.G. All authors contributed to data analysis and production of tables and figures. X.B.Z. and G.U. prepared the manuscript with written contributions from all co-authors. See page **viii** for author declarations.

Quasi-continuous melting and a roughening transition in monolayers of ultra-long alkanes: new insights into polymer melting

Ruibin Zhang^{1,2,3}, William S. Fall^{1,4}, Kyle Wm. Hall⁵, Gillian A. Gehring⁴, Xiangbing Zeng^{2,*}, Goran Ungar^{1,3,*}

1. State Key Laboratory for Mechanical Behavior of Materials, Shaanxi International Research Centre for Soft Materials, Xi'an Jiaotong University, Xi'an, 710049, China.
2. Department of Materials Science and Engineering, University of Sheffield, Sheffield S1 3JD, UK.
3. Department of Physics, Zhejiang Sci-Tech University, Hangzhou, 310018, China.
4. Department of Physics and Astronomy, University of Sheffield, Sheffield S3 7RH, UK.
5. Department of Chemistry, Temple University, Philadelphia, Pennsylvania 19122, USA.

*Correspondence to: x.zeng@sheffield.ac.uk, g.ungar@sheffield.ac.uk.

Receipt Date:

Abstract: It is taken for granted that semicrystalline polymers melt in a sharp first-order transition because this is what other pure substances do. In the 1960s, however, it was predicted that the lamellar polymer crystals could melt gradually from the surface inward, but this has never been observed. Here we report just such unprecedented nearly continuous melting, in monolayers of several extended-chain ultra-long n-alkanes up to $C_{390}H_{782}$ adsorbed on graphite. Experimental evidence is obtained by atomic force microscopy, and is supported by mean-field theory and molecular dynamics simulations. Remarkably, the final temperature of melting to an attached liquid phase is up to 80°C above the bulk melting point. Moreover, with increasing temperature, the ordered lamellar fraction decreases continuously and reversibly down to as low as 40% before final melting. This occurs by the two crystal-liquid interfaces moving steadily closer. The absence of such continuing melting in the bulk is attributed to severe steric overcrowding preventing the interface movement without the introduction of energy-costly chain folds. In monolayer films the lateral expansion of parallel chains exiting the crystal at the interface is

accommodated by escape in the third dimension. An additional novel feature, not observed in the bulk, is a reversible phase transition from tilted to perpendicular chain lamellae on heating, attributed to roughening of the interface.

KEYWORDS. long-chain alkanes, atomic force microscopy, molecular dynamics simulation, polymer crystallization, chain tilt.

I. INTRODUCTION

Crystal melting is normally a strongly first-order transition. At the melting point (T_m), a pure substance faces a stark choice between being a low-energy, low entropy crystal and a high-energy high-entropy liquid (Fig. 1a). However, 3D long-range positional and orientational order of a crystal can disappear in two or more separate steps, through intermediate liquid-crystalline states (Fig. 1b).¹ Even though most crystalline long-chain molecules and polymers do not form liquid crystals, it had been suggested, primarily by Zachmann in the 1960s that their crystal-melt transition may still not be sharp: lamellar crystals may melt from the surface inward nearly continuously (Fig. 1c).^{2,3,4,5} However, only very limited “premelting” has been seen,⁶ involving disordering of a surface layer only a few atoms deep. Polymers usually melt over a range of temperatures but mainly due to the often wide distribution in thickness of their lamellar crystals. Since lamellar thickness is strongly dependent on crystallization temperature, that distribution may result from non-isothermal crystallization. When lamellar thickness is uniform and thickening during heating is suppressed, melting in polymers occurs within 2°C,⁷ and in long-chain monodisperse n-alkanes within a 1°C interval.⁸ However, here we report that indeed more than half the crystalline fraction can be lost through continuous equilibrium melting from crystal surface inward in very thin layers of long-chain compounds.

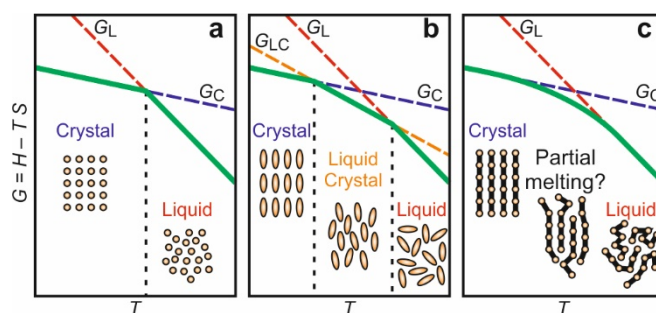


FIG. 1. Schematic free energy-temperature profiles for crystal-liquid phase transition. (a) A normal crystal. (b) A liquid crystalline compound. (c) A hypothetical scenario in long-chain molecules/polymers. C, LC and L stands for the three phases.

Our investigation focuses on the melting behavior of ultra-long normal alkanes, i.e. monodisperse linear paraffins C_nH_{2n+2} with chain length $n > 100$.^{8,9,10} Such compounds provide unique model polymers allowing stringent tests of theories of polymer crystallization and morphology, without the obfuscations that arise from

polydispersity.^{8,11,12,13} These are prototype chain molecules, oligomers of polyethylene (PE), itself a prototype polymer with the simplest chemical structure. In this work we study the temperature dependence of lamellar morphology and melting in monomolecular films of five ultra-long n-alkanes from C₁₂₂H₂₄₆ to C₃₉₀H₇₈₂, as well as C₆₀H₁₂₂, on highly ordered pyrolytic graphite (HOPG) by high-temperature atomic force microscopy (AFM). Large scale molecular dynamics simulations were also performed, and a semi-quantitative analytical model is constructed. Together they provide the experimental observation as well as an explanation of the extraordinary nearly continuous melting of these model polymers, helping the general understanding of the somewhat neglected but important phenomenon of polymer melting. A short report of this work, focusing only on the longest alkane C₃₉₀H₇₈₂, is presented in ref. 14.

n-Alkanes C_nH_{2n+2} and polyethylene molecules adhere particularly strongly to the graphite (001) surface due to the close epitaxial match between a hydrogen on every other CH₂ group of an all-trans alkane chain, 0.254nm apart, and the electron-rich center of a six-membered rings of graphite 0.246nm apart (Fig. 2a). Previous studies on adsorbed short alkanes, mainly in the length range 20<n<40^{15,16,17,18,19,20,21} have found that monolayers on graphite melt at temperatures somewhat above bulk melting point T_m^{bulk} , with additional phase transitions in the ordered state.²² A “pre-freezing” effect a few degrees above T_m^{bulk} was also found in PE thin layers.²³ Most notably, melting of monolayers of C₆₀H₁₂₂ 45 °C above T_m^{bulk} has been reported.²⁴ Only three studies have been reported on thin films of alkanes with n>60.^{17,25,26}

II. AFM RESULTS

II.A. Morphology of the monolayer

Fig. 2d shows AFM phase images of melt-crystallized monolayer films of a series of n-alkanes, C₆₀H₁₂₂, C₁₂₂H₂₄₆, C₁₉₄H₃₉₀, C₂₄₆H₄₉₄ and C₃₉₀H₇₈₂, recorded at selected temperatures. All images show nearly parallel periodic lines corresponding to the lamellar structure formed by side-by-side packing of extended alkane chains. The contrast comes from the different mechanical response, i.e. phase lag ϕ , to tip tapping between the more disordered hence softer molecular chain ends (yellow/white) and the more ordered crystal-like and thus harder interior of the lamellae (dark brown).

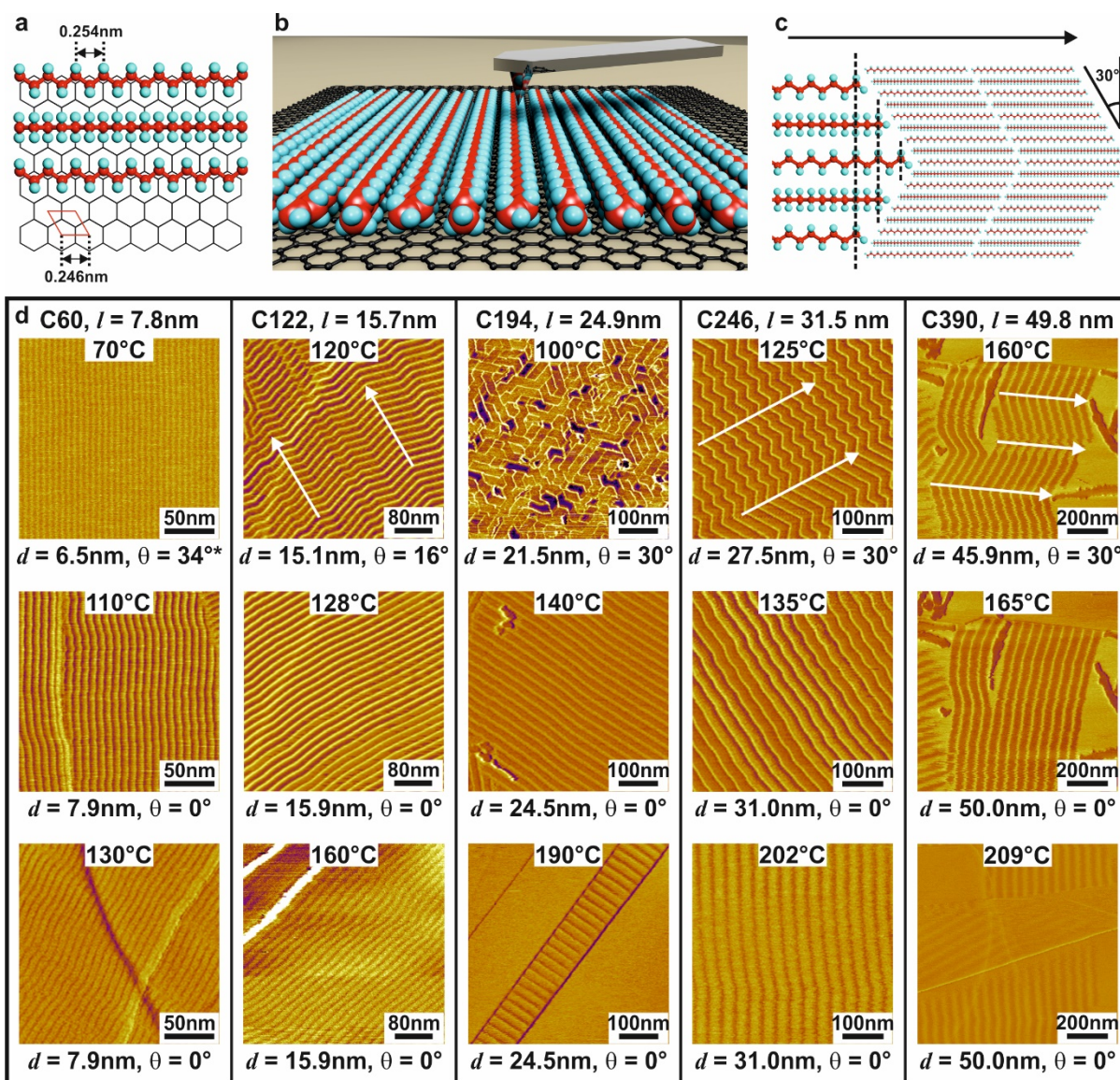


FIG. 2. Temperature-dependent morphology of ultra-long alkane monolayers on graphite. (a) Epitaxial arrangement of n-alkane molecules on graphite (001) surface. Red are carbons and light-blue are hydrogens. (b) An artist's impression of the alkane monolayer on graphite surface studied by AFM. (c) Schematic depiction of two monolayer lamellae with lamellar normals tilted at 30° to the chains direction; a detail of lamellar surface is shown on the left (see also Fig. 4b). (d) AFM phase images of n-alkanes $\text{C}_{60}\text{H}_{122}$, $\text{C}_{122}\text{H}_{246}$, $\text{C}_{194}\text{H}_{390}$, $\text{C}_{246}\text{H}_{494}$ and $\text{C}_{390}\text{H}_{782}$ at three different temperatures. Yellow/white = soft amorphous regions. Top row: tilted-chain, lamellae with flush chain-end surface; arrows indicate chain direction. Middle row: perpendicular-chain lamellae immediately above T_{T-P} . Bottom row: perpendicular form close to melting, showing widening of the amorphous layers to more than half the lamellar spacing d . The extended chain length l for each compound is shown,

along with d and the tilt angle θ , which is the angle between the molecular direction and the lamellar normal. *For $C_{60}H_{122}$ at $70^\circ C$, the molecular direction cannot be measured directly from the AFM image as there are no zigzags, so θ is estimated using $\cos\theta = d/l$.

The monolayer nature of the ultrathin films under study, is confirmed by height images taken at places where the HOPG substrate is not fully covered by the alkane (Fig. 3). The thickness of such films is only ~ 0.4 nm, i.e. the thickness of a single alkane molecule lying parallel to the graphite surface. According to previous studies, the orientation of the C-C-C zig-zag plane alternates from chain to chain between parallel and perpendicular to the graphite surface (Fig. 2a), in an arrangement similar to that of the (110) plane in orthorhombic crystals of alkanes and PE.²² The monolayer on top of the HOPG surface is schematically shown in Fig. 2b. The stripes in the AFM images are in fact thin ribbons of in-plane transverse-lying chains (Fig. 2c), but even so we shall refer to them as lamellae, in analogy with crystalline lamellae in bulk alkanes and polymers; in the same vein we refer to the edges of the ribbons as lamellar surfaces or, if wider, amorphous layers, and to the ordered portion of the ribbons as crystalline. By the same analogy we will refer to the periodicity along lamellar normal as lamellar thickness d .

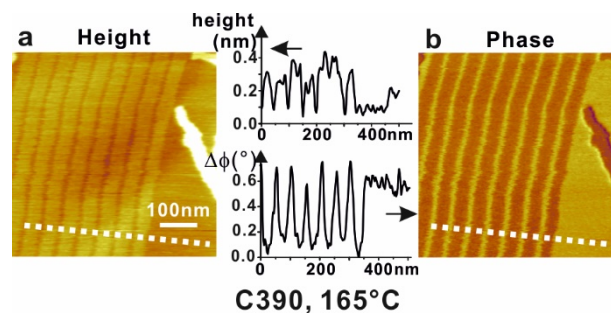


FIG. 3. Comparison between (a) height and (b) phase images of a monolayer of extended-chain $C_{390}H_{782}$. The height scan (top middle) and phase scan (bottom middle) are recorded along the white dashed line. The height difference between the top of the monolayer and the graphite surface is measured as ~ 0.4 nm.

Comparison between the height and phase images is shown in Fig. 3 for $C_{390}H_{782}$ at $165^\circ C$ as an example. In most cases, the phase images provide a better contrast between the ordered and disordered parts of the lamellae, shown in the scanned profiles in the middle of Fig. 3. More importantly, the physical meaning of the height

values obtained for such monolayers with thickness of only ~ 0.4 nm is ambiguous as the measured height is also affected by the local stiffness of the film. In fact the apparent height of the amorphous (molten) layers is in all images somewhat less than that of the crystalline layers. It stays so even as the melt area increases with temperature (see below) while the total area occupied by the alkane remains constant; the expected increase in melt thickness due to volume expansion is not detected in the height profiles. Consequently through the rest of the paper we will focus on the phase images as they generally provide better contrast and their signal can be linked directly to the ordering in the lamellar structure.

At lower temperatures (top row in Fig. 2d) sharp chain-end-containing yellow/white lines separating the lamellae (lamellar surface lines) are observed in phase images of all alkanes. The lamellae are often zigzagging and consistently appear correlated throughout the whole imaged area along a symmetry axis, which can be identified as the molecular direction (white arrows, Fig. 2d). There are frequent reversals in tilt direction, with the molecular direction remaining the same. The tilt angle θ between molecular chain axis and the lamellar normal for all our compounds is $\sim 30^\circ$, with the exception of $C_{122}H_{246}$ where it is $\sim 16^\circ$. $\theta \approx 30^\circ$ and $\theta \approx 16^\circ$ translate into a longitudinal shear by two and one CH_2 group between neighbouring chains, respectively.^{27,28}

The observed morphologies in Figs. 2 and 3 agree with previous studies of melt-crystallized n-alkanes on graphite, in that molecules in the ordered phase always lie in the plane of the graphite surface and parallel to one of the three [100] directions of the graphite lattice.^{22,25,26} The latter is most clearly seen in the image of $C_{194}H_{390}$ at $100^\circ C$ (Fig. 2d), where there are perfectly tessellating chevron-like molecular blocks with three distinct molecular orientations, rotated in plane by $\sim 120^\circ$, while the chevron angle is $2 \times 30 = 60^\circ$.

The integer shift of molecular positions, by 1 or 2 CH_2 groups, suggests that the epitaxial relationship between the alkane and the graphite lattice is kept for all molecules in the ordered (crystalline) layers. The measured lamellar thicknesses, tilt angles and molecular lengths are listed in Table 1, and correspond well with the calculated extended lengths of the molecules.

Table 1. Measured lamellar thicknesses (d), tilt angles (θ) and molecular lengths (l). Molecular length of n-alkanes in nm is calculated using the relation $n \times 0.1272 + 0.2$, where 0.1272 is half the c lattice parameter of polyethylene.⁸

Compound	Temperature (°C)	Lamellar thickness d (nm)	Tilt angle θ (°)	Apparent molecular length $d/\cos\theta$ (nm)	Theoretical molecular length l (nm)
C ₆₀ H ₁₂₂	70	6.5	30*	7.5	7.83
	110	7.9	0	7.9	
	140	7.9	0	7.9	
C ₁₂₂ H ₂₄₆	120	15.1	16	15.7	15.72
	128	15.9	0	15.9	
	160	15.9	0	15.9	
C ₁₉₄ H ₃₉₀	100	21.5	30	24.8	24.88
	140	24.5	0	24.5	
	190	24.5	0	24.5	
C ₂₄₆ H ₄₉₄	125	27.5	30	31.8	31.49
	135	31.0	0	31.0	
	202	31.0	0	31.0	
C ₃₉₀ H ₇₈₂	160	45.9	30	53.0	49.81
	165-211	50.0	0	50.0	

*Assumed to be 30°, as no zig-zag was found in the AFM picture so tilt angle could not be measured directly.

Upon further heating, a tilted-to-perpendicular (T-P) transition can be observed in all compounds, where the lamellae lose their zig-zag morphology – compare the first and second rows of Fig. 2d. They become largely straight but slightly wavy, lying perpendicular rather than tilted to the molecular direction. The lamellar thickness d now equals the extended chain length (Table 1). It should be noted that the T-P transition occurs at temperatures above the respective bulk melting point of the alkanes⁸ – see Fig. 4a. The T-P transition is discussed further in Sections II.C and IV.

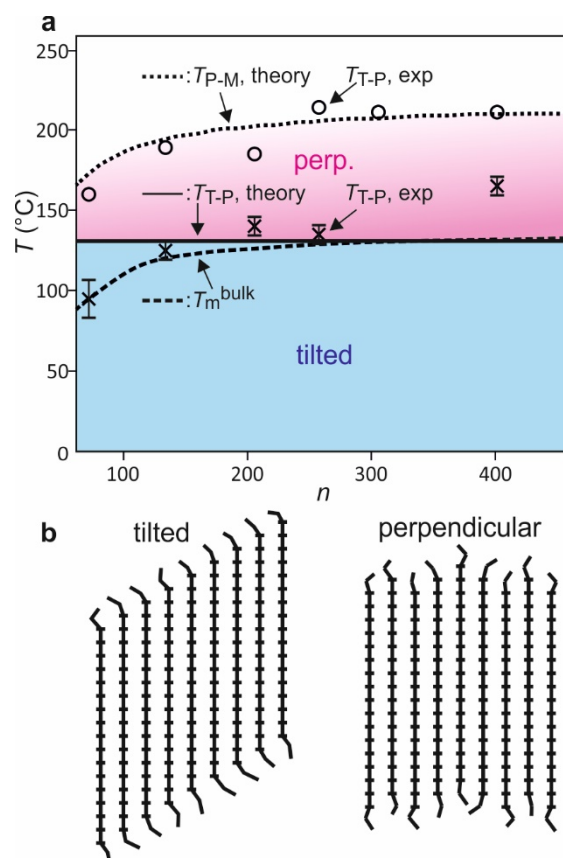


FIG. 4. (a) Experimental and theoretical phase transition temperatures for alkanes of different length n . Crosses: transition temperature between tilted and perpendicular forms, T_{T-P} ; circles: perpendicular to melt transition temperature, T_{P-M} . Dotted (T_{T-P}) and full lines (T_{P-M}) are derived from theory in Section IV. The bulk melting point T_m^{bulk} (broken line) is plotted for comparison. (b) Schematic drawings of tilted and perpendicular forms showing the higher entropy of the perpendicular form, due to random shift of positions of neighbouring molecules and more conformational choices for the disordered chain ends.

II.B. Monolayer melting - Experimental

Two extraordinary phenomena are observed on heating the alkanes above the T-P transition. Firstly, the monolayer lamellae are found to persist in the perpendicular form to temperatures up to 80°C above the bulk melting point T_m^{bulk} (Fig. 4a). Secondly, for all n-alkanes examined melting is seen to proceed gradually, from the lamellar surface inwards; with increasing temperature the bright amorphous layers progressively broaden at the expense of the darker crystalline layers. Close to the melting point of the perpendicular form T_{P-M} , the apparent amorphous layer thickness

becomes even larger than that of the remaining crystalline layer, with d remaining almost constant (Fig. 2d, bottom row).

This behavior of the perpendicular form is clearest in the longest n-alkane, $C_{390}H_{782}$. Progress in its protracted surface melting is shown in the AFM phase images in Figs. 5a-e. The perpendicular form of the monolayer persists until 212°C , 80°C above its T_m^{bulk} of 132°C .⁸ In order to show better the broadening of the amorphous layers with increasing temperature, we have calculated the averaged profiles $\Delta\phi$ for each compound in the perpendicular form at different temperatures. These were subsequently inverted ($-\Delta\phi$) and normalized so that 0 corresponds to maximum phase shift and the softest/most disordered parts of the lamellae, and 1 to minimum phase shift and the stiffest/most ordered parts. Normalized profiles for different alkanes are shown in Figs. 5f-j. The normalization was done for easier comparison of results at different temperatures, as the absolute values of the phase angle depend on experimental conditions such as the property of the probes, driving frequency, driving amplitude and temperature, etc. In all alkanes long enough to be scanned with sufficient resolution, i.e. in $C_{194}H_{390}$, $C_{246}H_{494}$ and $C_{390}H_{782}$ (Figs. 5h-j), the trend is the same, the original narrow soft surface layer (minima in Figs. 5f-j) broadens to eventually become wider than the rigid middle just before the lamellae finally melt. In $C_{60}H_{122}$ and $C_{122}H_{246}$ the observed effect is limited, partly due to the finite instrumental resolution at elevated temperatures.

It is interesting that the lamellar period d remains temperature-independent throughout the continuous melting process of the P form. Taking the specific volume of molten PE at 200°C to be approximately 20% larger than that of the crystal, as a first approximation we can assume that the specific area of a 2D melt would be $1.20^{2/3}-1 = 1.16$, i.e. 16% larger than that of the 2D crystal. Since the ordered monolayer lamellae do not expand laterally, if the amorphous chains were completely pinned to the graphite surface the amorphous domains would be expected to widen by 16% at melting, meaning that for a 50% crystalline alkane at the melting point d would have increased by 8% compared to the nearly fully crystalline system at T_{T-P} . For $C_{390}H_{782}$ this would amount to a Δd of 4 nm. The fact that no such expansion is observed must mean that there is significant “escape in the 3rd dimension” of the molten parts of the chains, with some chain cross-overs likely.

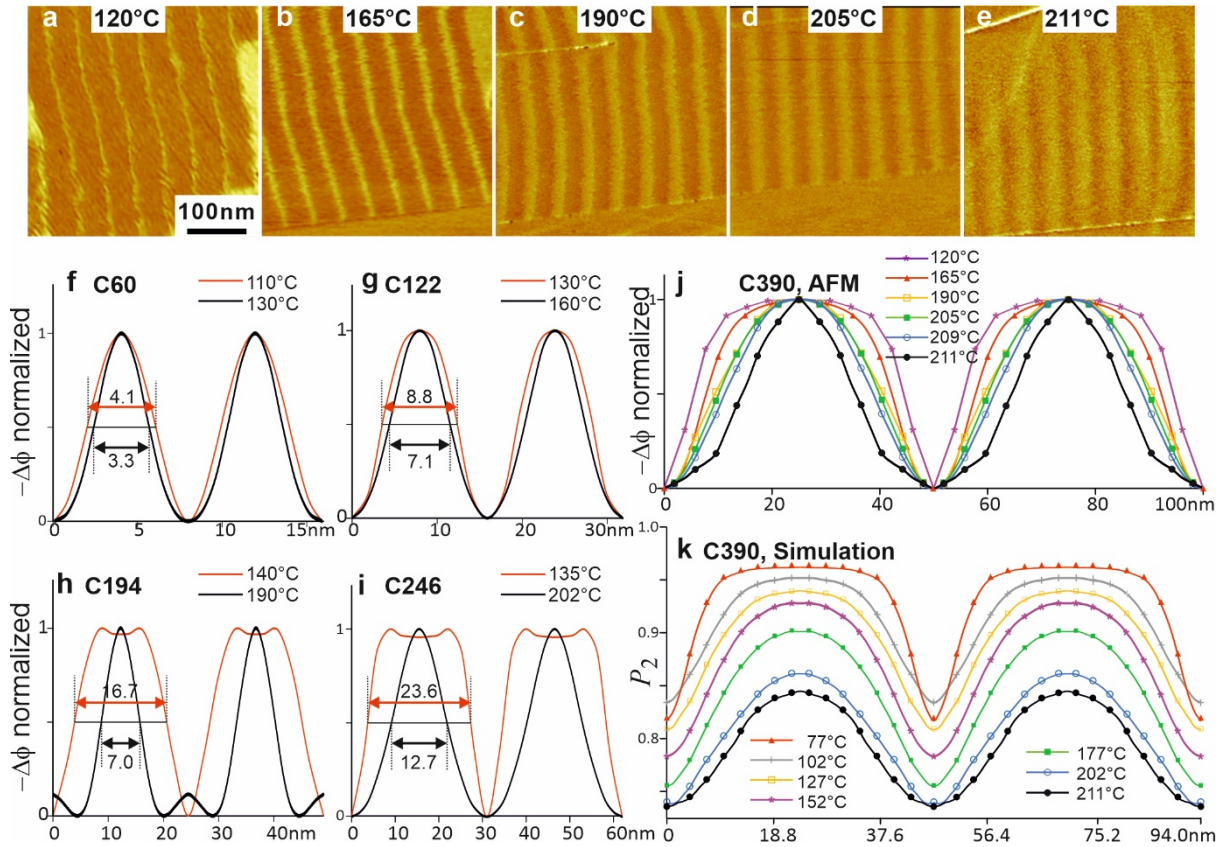


FIG. 5. Continuous melting of monolayers on graphite. (a-e) AFM phase images of C₃₉₀H₇₈₂ at different temperatures in the perpendicular phase. Note the progressive broadening of the amorphous (bright) layers with increasing temperature. For consistency, image (a) is recorded from a supercooled P form, as the equilibrium form at 120°C is the tilted (T) form. (f-j) Normalized AFM phase ($-\Delta\phi$) profiles of the perpendicular form. The double maxima at low temperatures for C₁₉₄H₃₉₀ and C₂₄₆H₄₉₄ are artefacts due to asymmetry caused by AFM scanning direction. (k) P₂ profiles calculated from the respective simulated P₂ maps. In our MD simulations we were not able to reproduce the experimentally observed change in molecular tilt on heating (T-P transition), and molecules remain inclined to the lamellar surface. For better comparison with AFM profiles, the abscissa values are measured along the molecular direction rather than along lamellar normal.

It is important to stress that the continuous surface melting is an *equilibrium phenomenon*. Within the temperature range of the P form the molten streaks narrow down, i.e. crystallize, when temperature is lowered with no noticeable hysteresis.

II. C. On tilted-perpendicular transition

While Fig. 2d shows straightening of the zigzag lamellae on heating through the T-P transition, Fig. 6 shows, on the examples of $C_{122}H_{246}$, $C_{194}H_{390}$ and $C_{390}H_{782}$, that on cooling of the melt the perpendicular form returns. Similar to melting, the T-P transition is reversible, albeit the reverse P-T transition takes place with some delay. Note that the image of $C_{390}H_{782}$ at 120°C in Fig. 5a, still in the P form, was recorded immediately after cooling, before the P-T transition had a chance to occur.

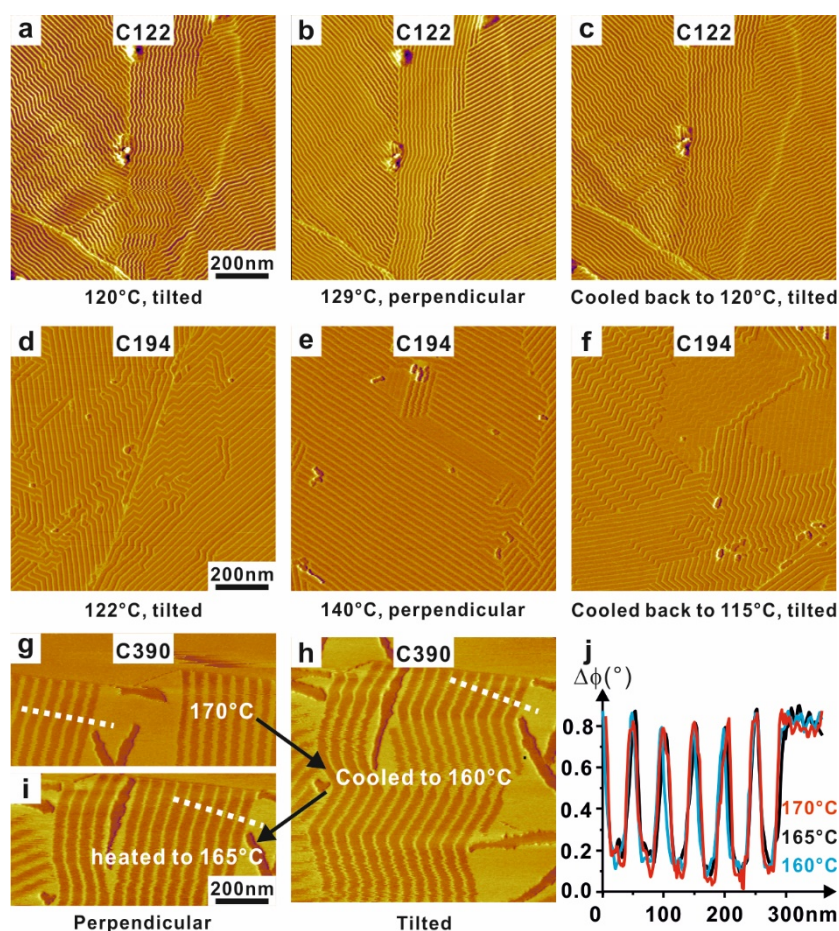


FIG. 6. Reversibility of the tilted-perpendicular phase transition on heating and cooling as observed in $C_{122}H_{246}$, $C_{194}H_{390}$ and $C_{390}H_{782}$. Note that the sample had moved east by ca 400 nm between (g) and (h). (j) Scanned phase profiles of $C_{390}H_{782}$ at temperatures show very little change above and below the T-P transition. The lines of scan are shown as dotted white lines in (g)-(i).

We attribute the T-P transition to roughening of the crystal-amorphous interface, based on the following known behavior of bulk linear alkanes and PE. The reverse, i.e. a P-T transition, occurs on heating shorter bulk crystalline alkanes with $n \geq 30$ ($n = \text{odd}$);²⁹ here the low-temperature P-form has crystallographically ordered end groups whose increasing mobility at higher temperatures requires larger surface area,

driving the P-T transition.^{30,31,32} Meanwhile, in longer alkanes, starting already at around $n=40$, as well as in PE, it is possible to obtain samples through either solution or melt crystallization at relatively low temperatures, where the chains are perpendicular, i.e. aligned with the lamellar normal. However, such structures are metastable. Surface regularization on heating converts these metastable P-forms to stable forms with smooth but tilted surfaces.^{27,31,32} Notably, this P-T transition is irreversible, and on cooling the lamellae remain tilted. Moreover, work on labelled ultra-long alkanes has shown that the metastable perpendicular lamellar surfaces in such quenched compounds is anything but ordered, having frozen-in roughness with protruding or buried chain ends or folds.^{33,34,35,36} Thus even though the average shear between neighbouring chains is larger than one or two CH_2 groups, it is irregular and the average lamellar tilt is zero. It is important to reiterate that the aforementioned phenomenology is distinct from what is observed in the current study, where the T-P transition on heating alkane monolayers is reversible, as both the T and P forms are thermodynamically stable.

Thus there are three types of perpendicular lamellar phases: the equilibrium high-order low- T form in shorter odd alkanes, the kinetically rough nonequilibrium low- T form in bulk long alkanes and PE, and now, as suggested here, the *high- T equilibrium rough interface* form in monolayers of long alkanes (Fig. 4b). Note that the equilibrium-roughness P phase in monolayers is stable only above the bulk melting point (see Fig. 4a), therefore it is perhaps not surprising that this perpendicular form and the T-P transition on heating have not been observed in the bulk.

III. MOLECULAR DYNAMICS SIMULATION

In order to better understand the nearly-continuous melting of n-alkane monolayers observed by AFM, Molecular Dynamics (MD) simulations were performed of a periodic 6-lamella monolayer structure composed of 1800 $\text{C}_{390}\text{H}_{782}$ molecules adsorbed on a graphite surface. Note that the system at full atomistic resolution would correspond to well over two million particles. Therefore, to enhance the computational tractability of our molecular dynamics simulations, the $\text{C}_{390}\text{H}_{782}$ chains and underlying graphene were represented using the coarse-grain (CG) SDK model^{37,38,39} without any alterations. This CG model represents 3 methylene units along an alkane backbone using a single coarse-grain segment (bead), and is

appropriate for aliphatic and aromatic species,^{37,38,39} and has been previously verified to capture the important features of long-chain alkane systems and associated processes such as crystallization.^{40,41,42}

The SDK model represents graphene using a CG cubic lattice, so the system was constructed such that the lamellar interfaces were at a 45° with respect to the chain direction, which was parallel to underlying graphene lattice (specifically, the y direction of the simulation cell). The system was periodic in all three directions, but the monolayer and graphene were only continuous along x and y. Along x and y, the system was 141 nm and 282 nm, respectively. The simulation cell was 20 nm along z ensuring that the periodic images of the monolayer did not interact; the SDK model uses a 1.5 nm cut-off for non-bonded intramolecular and intermolecular interactions. In order to improve the computational efficiency of the simulations, only the positions of CG beads of the alkane chains were evolved during the molecular dynamics simulations, i.e. the graphene substrate was treated as rigid.

In keeping with previous studies on alkanes and polymers,^{40,41,42,43,44,45} the ordering of polymer chain segments was probed using the local P_2 order parameter, which assesses the local alignment between individual polymer chains, and has been used extensively to distinguish crystalline and non-crystalline polymer chain segments in polyethylene systems.^{40-42, Error! Bookmark not defined.-Error! Bookmark not defined.} Details of how the P_2 values are calculated are provided in Section VII.C.

In agreement with our AFM results, our MD simulations of a $C_{390}H_{782}$ monolayer on a graphite substrate similarly reveal differing degrees of surface melting at temperatures both at and below 211°C. At higher temperatures, the monolayer is molten. Maps of the simulated lamellar structures are provided in Fig. 7a based on the P_2 order parameter, which as described above measures local alignment of polymer chain segments and can be used to measure polymer crystallinity. Each P_2 map is averaged from 50 instantaneous configurations taken at 20ps intervals during the simulation, calculated by partitioning the simulated surface into 1 nm x 1 nm grids. Higher and lower P_2 values indicate that an alkane chain segment is more or less ordered, respectively. As the more disordered parts (yellow/white) of the molecules are softer, resulting in a larger phase shift on the AFM working in the tapping mode, it is expected that the P_2 maps should provide a good indication of their corresponding AFM phase images. The P_2 maps indeed show a remarkable

likeness to the real AFM images. The simulations also show that the P_2 order parameter of the molecular segments is lower when they are closer to the lamellar end surfaces and that the thickness of the more disordered (amorphous) layers increases with increasing temperature. The order-disorder interfaces at temperatures higher than 102°C are evidently rough. The observed interface roughening is in agreement with our interpretation of the nature of the T-P transition – see below.

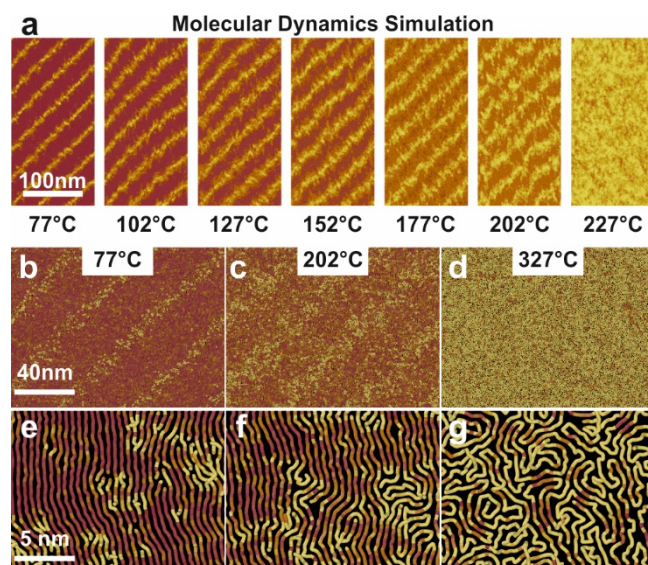


FIG. 7. (a) Reconstructed crystallinity (P_2) maps from MD simulations for temperatures between 77°C and 227°C . Darker and lighter regions correspond to higher and lower P_2 values (i.e., more ordered and less ordered regions). (b-g) Zoomed-in snapshots of the simulations at 77°C , 202°C and 327°C produced using OVITO.⁴⁶ The tubes correspond to individual alkane chains, and are colored according to their P_2 values.

The match between the simulated P_2 order parameter maps and AFM phase images is best shown in Fig. 5, where averaged P_2 profiles of the $\text{C}_{390}\text{H}_{782}$ lamellae at different temperatures (Fig. 5k) are plotted together with the experimental phase profiles (Fig. 5j). In both cases, the thickness of the more ordered (crystalline) regions decreases with increasing temperature. At the highest temperature simulated below melt, 211°C , more than half of the lamellar thickness is disordered, which closely matches the experimental results. It is remarkable that certain aspects of the molecular simulation, such as the melting point, order parameters and average profiles are in such close agreement with the observed experimental results.

The ordering of the molecular segments in MD simulations is also examined by calculating the average z-displacement of the beads away from the graphite substrate (height), as well as the average squared displacement of the beads (mobility). Averaged mobility and height maps at different temperatures, again calculated from 50 instantaneous configurations, are shown in Fig. 8. Both observables show similar trends as P_2 parameter as a function of temperature, consistent with AFM observations.

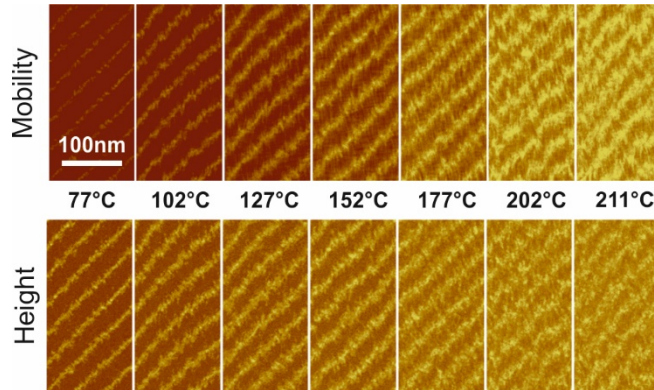


FIG. 8. Averaged mobility and height maps of $C_{390}H_{782}$ monolayer simulated below the melt, between 77°C and 211°C . Values are calculated from MD simulation *via* surface binning (1 nm^2) over 50 instantaneous configurations at 20ps intervals. In both mobility and height maps the colour goes from dark brown to yellow with increasing values.

IV. MEAN-FIELD THEORY

A mean-field model of a lamella has been constructed in order to explain the transition between the tilted and perpendicular phases (T-P) and the continuous surface melting leading to the final melting (P-M) transition. We take the perfectly ordered molecular chain of C_nH_{2n+1} as the reference ground state (Fig. 9a), whose enthalpy (H), entropy (S) and free energy (F) are all zero (the temperature effect, i.e. vibrations of the CH_2 groups are ignored). Next we consider the partially melted chain, with x disordered CH_2 groups (both ends added together), and with the remaining $n - x$ ordered CH_2 groups in the middle. In the x disordered CH_2 groups the energy and entropy levels do not jump to those of the melt immediately, instead they are assumed to increase gradually with increasing distance from the ordered C-atoms. The conformations of chain segments emerging from the crystalline layer will

be highly restricted due to the lack of lateral space, referred to as “overcrowding” at the crystal-melt interface (Fig. 10a).^{47,48} It is also expected that the initial increase in energy with distance is faster compared to the increase in entropy (the initial cost in energy from the introduced defects is not compensated by an equivalent increase in entropy from the increased number of available states). In our model, we assume that the energy of disordered CH₂ groups will be that of the 2D melt, while their entropy remains as in the crystal, jumping to that of the 2D melted chain only after another t CH₂ groups. This creates a high-energy/low entropy transition layer of thickness t . t can be taken as a measure of the overcrowding effect. The clash of many neighbouring chain suddenly becoming disordered, and the fact that all of them need to escape away from the crystalline layer, significantly reduce the number of conformations each chain end can take. It should be noted that our formulation is very similar to that previously derived by Flory *et al.*,² only with a more specific evaluation of the crystal-amorphous interface free energy, i.e. of the overcrowding effect.

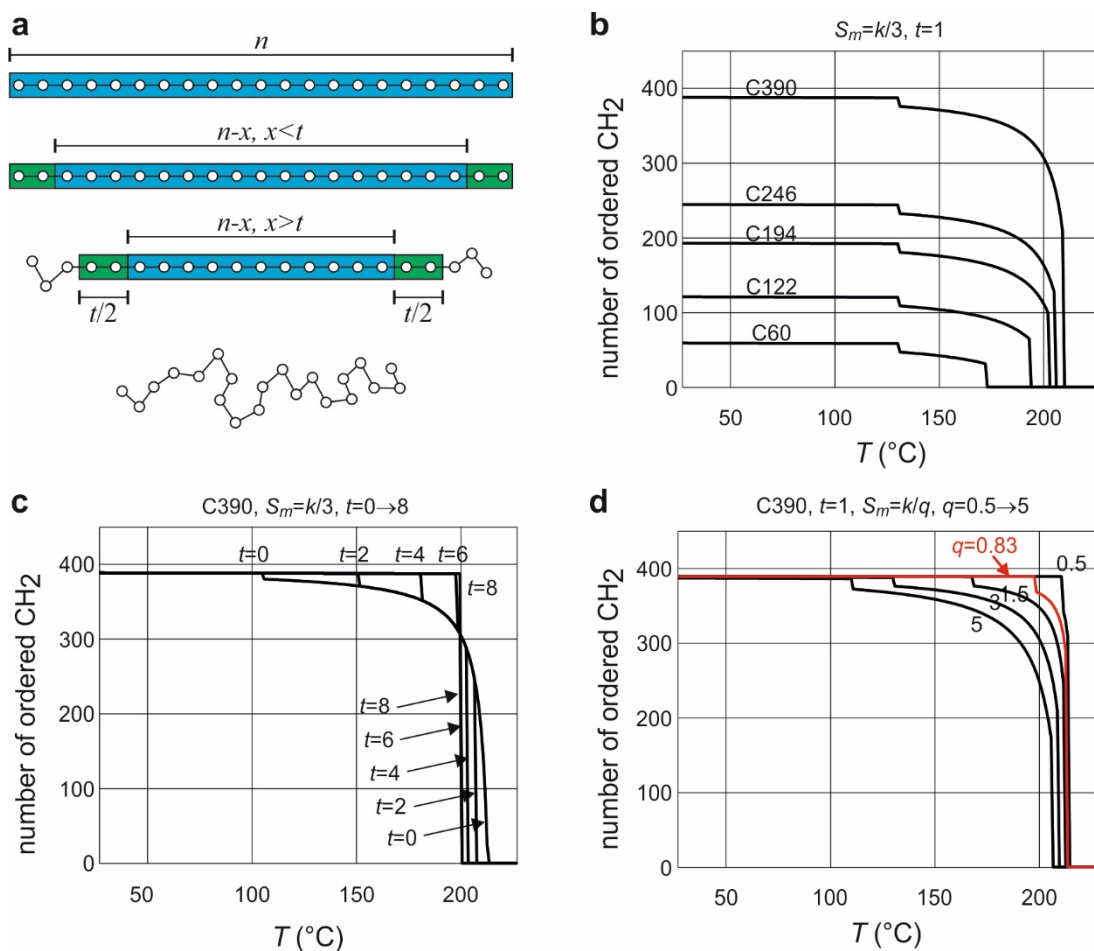


FIG. 9. Results of the mean-field theory. (a) Schematic models of chains in different states. Top to bottom: fully crystalline, no surface disorder; smooth surface with small premelting/surface disorder, $x < t$; rough surface with significant premelting, $x > t$; and melt. (b) Temperature dependence of the number of ordered CH₂ groups for different n-alkanes. (c) A 1st order smooth-to-rough surface, or tilted-perpendicular (T-P) transition, followed by the continuous melting is observed when $t=0$ (no overcrowding). When $t > 1$ (with overcrowding) the temperature range of continuous melting narrows, and is terminated by another 1st order melting transition (P-M). When $t \geq 8$ no continuous melting is predicted. (d) The higher the melt entropy S_m , the less continuous melting. Here the same ultimate melting temperature T_m^0 of an infinitely long alkane is assumed. Note that the red curve assumes the experimental S_m value for bulk n-alkanes; nevertheless, even for such high S_m a narrow but significant range of partial melting is predicted as long as the overcrowding effect is small ($t=1$).

In our model partial melting of the chain, however, does not in itself reduce the system free energy below T_{P-M} , as the increase in entropy on melting the end segments comes with an increase in enthalpy due to loss of crystallinity. Stabilization of partially melted chains should come from the extra translational entropy $k \ln(x)$ of the molecules free to slide through the crystalline layer. Our model results in two possibilities as shown in Fig. 9a: a smooth surface with the number of disordered surface segments, x , less than t , and a rough surface, where $x > t$.

Therefore we can write the free energy of the partially melted chain as

$$F_P(x) = \begin{cases} xH_m - kT \ln(x + 1) & 0 < x < t \\ x(H_m - TS_m) + tTS_m - kT \ln(x + 1) + 2\sigma_e & t < x < n - 1 \end{cases} \quad \text{(Equation 1)}$$

Here H_m and S_m are the enthalpy and entropy of melting per CH₂ group, and $\sigma_e = H_e - TS_e$ is the contribution to the free energy from the two ends of each chain. The chain sliding entropy equals $k \ln(x + 1)$: for the x units of the chain ends, there are $x + 1$ choices in selecting the position at which to separate the two ends by the $n - x$ ordered units. When the surface is rough, i.e. when $x > t$, there is an additional increase in the system free energy $2\sigma_e$ due to the disappearance of the smooth end surface (the factor 2 is used as each molecule has two ends).

The minimum free energy of a partially melted chain is therefore found at

$$x = x_0 = \begin{cases} \frac{kT}{H_m} - 1 & 0 < x_0 < t \\ \frac{kT}{H_m - TS_m} - 1 & t < x_0 < n - 1 \end{cases} \quad (\text{Equation 2})$$

In our simple model, x_0 is independent of the length of the molecule n . Interestingly, our experimental results seem to support this assumption. For example, around 130°C, for different n-alkanes the FWHM of the disordered region (Fig. 5) are all ~5 nm.

Let $H_m = T_m^0 S_m$, where T_m^0 is the ultimate melting temperature of infinitely long polymer, and Equation 2 can be rewritten as

$$x = x_0 = \begin{cases} \frac{k}{S_m} \cdot \frac{T}{T_m^0} - 1 & 0 < x_0 < t \\ \frac{k}{S_m} \cdot \frac{T}{(T_m^0 - T)} - 1 & t < x_0 < n - 1 \end{cases} \quad (\text{Equation 3})$$

So for a smooth surface the free energy of the most stable partially melted chain F_p is

$$F_p^{smooth} = kT - T_m^0 S_m - kT \ln\left(\frac{k}{S_m} \cdot \frac{T}{T_m^0}\right) \quad 0 < x_0 < t \quad (\text{Equation 4.1})$$

or for a rough surface

$$F_p^{rough} = kT - T_m^0 S_m + (t + 1)TS_m - kT \ln\left[\frac{k}{S_m} \cdot \frac{T}{(T_m^0 - T)}\right] + 2\sigma_e \quad t < x_0 < n - 1 \quad (\text{Equation 4.2})$$

The transition from a smooth ($x_0 < t$) to a rough ($x_0 > t$) surface (T-P) happens at

$$T = T_m^0 - T_m^0 \exp\left[-\frac{2\sigma_e + (t + 1)TS_m}{kT}\right] \quad (\text{Equation 5})$$

The free energy of an n-alkane in melt can be written as

$$F_m = n(T_m^0 - T)S_m - kT \ln(n) + 2\sigma_e$$

(Equation 6)

Here the term $kT \ln(n)$ comes from the entropy due to chain sliding. Here we assume that the free energy of the ends is the same for the rough surface lamella and for the melt.

The phase transition between the partially melted chain and full melt (P-M) occurs at

$$F_p^{rough} = F_m$$

$$\left[\left(n + t + \frac{k}{S_m} + 1 \right) + \frac{k}{S_m} \left(\ln n - \ln \frac{T}{T_m^0 - T} - \ln \frac{k}{S_m} \right) \right] T = (n + 1)T_m^0$$

(Equation 7)

Alternatively the melting occurs before the surface roughens, in which case

$$F_p^{smooth} = F_m$$

$$\left[\left(n + \frac{k}{S_m} \right) + \frac{k}{S_m} \left(\ln n - \ln \frac{T}{T_m^0} - \ln \frac{k}{S_m} \right) \right] T = (n + 1)T_m^0 + \frac{2\sigma_e}{S_m}$$

(Equation 8)

If there is no premelting at all, the direct transition from the perfectly ordered crystal ($S=0$) to the melt occurs at

$$\left(n + \frac{k}{S_m} \ln n \right) T = nT_m^0 + \frac{2\sigma_e}{S_m}$$

(Equation 9)

Comparing equations 7 - 9, it is evident that continuous partial melting will occur more easily when t is smaller, i.e. when a segment exiting the crystal is able to attain melt-like disorder abruptly; this implies less overcrowding. The other important parameter is the melt entropy S_m . The lower the S_m , the more important the chain sliding entropy, leading to more significant partial melting.

The parameters in our theory are estimated as follows. The heat of fusion of bulk PE is ~ 300 J/g, or 4.2 kJ mol⁻¹. Since $T_m^{PE} = 415$ K, the melt entropy in bulk is about 10 J K⁻¹ mol⁻¹ of CH₂. Assuming that in 2D the heat of fusion is roughly one third of that in the bulk (the number of neighbouring chains changes from 6 to 2), so $H_m = 1.4$ kJ mol⁻¹, and 2d melt temperature for an infinite chain $T_m^0 \sim 500$ K (C₃₉₀H₇₈₂ monolayer on

graphite melts at 484K), $S_m = 2.8 \text{ J K}^{-1} \text{ mol}^{-1}$, or $4.7 \times 10^{-24} \text{ J K}^{-1}$ per CH_2 group, hence $k/S_m \sim 3$. The end surface free energy is chosen so that the $T_{\text{T-P}}$ is close to experimental observations, and a value of $2\sigma_e/k = 430 \text{ K}$ is used, which is $6.0 \times 10^{-21} \text{ J}$ per chain or $1.6 \times 10^{-6} \text{ J cm}^{-2}$.

On the basis of the mean-field theory we were able to reproduce the T-P transition, the continuous partial melting and the final melting (Fig. 4a). As shown in Fig. 9b for n-alkanes from $\text{C}_{60}\text{H}_{122}$ to $\text{C}_{390}\text{H}_{782}$, at low temperatures in all cases the lamellae are nearly 100% crystalline with a small amount of end disorder; this corresponds to the tilted form. A first-order transition to what corresponds to the perpendicular form is observed with rising temperature, accompanied by a small drop in crystallinity. The crystalline fraction then decreases continuously with increasing temperature, reaching around 50% before final melting. Furthermore, the calculated P-M transition temperatures ($T_{\text{P-M}}$) agree very well with experimental ones (Fig. 4a and Table 2). The T-P transition temperature ($T_{\text{T-P}}$) is independent of chain length n according to our model, but experimentally it increases with n as shown in Table 2; this discrepancy is probably due to the neglect of long range end-to-end interactions.

Table 2. Comparison of experimental and calculated phase transition temperatures for different n-alkanes. The parameters used for the theoretical calculation are $t=1$, $S_m = k/3$. T-P: tilted to perpendicular phase transition; P-M: melting of the perpendicular form.

<i>n</i> -alkane	$T_{\text{T-P}}$ (exp.) °C	$T_{\text{T-P}}$ (calc.) °C	$T_{\text{P-M}}$ (exp.) °C	$T_{\text{P-M}}$ (calc.) °C	T_m (bulk) °C
$\text{C}_{60}\text{H}_{122}$	95±10	131	160	173	95.0
$\text{C}_{122}\text{H}_{246}$	125±5	131	189	194	120.0
$\text{C}_{194}\text{H}_{390}$	140±5	131	185	202	126.5
$\text{C}_{246}\text{H}_{494}$	135±5	131	214	206	128.5
$\text{C}_{390}\text{H}_{782}$	165±5	131	212	210	132.0

Fig. 9c shows that the best-fit value of the “overcrowding” parameter t is only 1. For $t = 0$ melting (the P-M transition) becomes completely continuous. However, an increase in t increases $T_{\text{T-P}}$ and decreases $T_{\text{P-M}}$. The continuous part of the melting transition disappears when $t \geq 8$.

V. DISCUSSION

At the crystal-amorphous interface in 3D systems the effective chain cross-section increases by a factor g of 2-3 according to theory^{47,48} and 2.3 according to experiment (Fig. 10a).⁴⁹ Due to solvation g is even larger at the crystal-solution interface. Therefore, in order for a polymer lamella to grow large a fraction $(1-g^{-1})$ of all chains must end at the interface, or re-enter the crystal through a sharp fold. Where chain-folding is kinetically unattainable, as in a cold-drawn polymer, lamellar growth is arrested early, resulting in microfibrils containing crystallites no more than 10-20 nm wide (Fig. 10b).⁵⁰ Regarding melting, there would be no thermodynamic advantage in a bulk lamella melting gradually by crystal thinning and thereby having to increase the number of energy-costly chain folds.

However if not a continuous, then a two-step melting does actually occur in the bulk under special circumstances, with a thermodynamically stable intermediate semicrystalline form (SCF, Fig. 10c).⁵¹ This form is stable within a $\sim 20\text{K}$ interval below the final T_m in a series of co-crystallizing binary mixtures of ultra-long alkanes of disparate length. Their lamellae contain fully crystalline shorter, and only partially crystalline longer chains, whose dangling ends form a liquid layer. Translational entropy of the longer chains was also thought to stabilize the phase. Qualitatively, this two-step melting can also be described by the schematic free-energy diagram in Fig. 1b if G_{LC} for the liquid crystal is replaced by G_{SCF} . Another example of a nearly stable semicrystalline phase is the “non-integer form” (NIF) of pure long alkanes, which crystallizes from melt below T_m^{fold} of the once-folded-chain form (Fig. 10d).^{27,49} NIF lamellae can only grow when enough chains are folded exactly in two to make room for the remaining protruding non-folded chains.

Generally, surface overcrowding has been accepted as the main cause of chain-folded crystallization of polymers, but its role in preventing continuous melting has not been recognized until now.

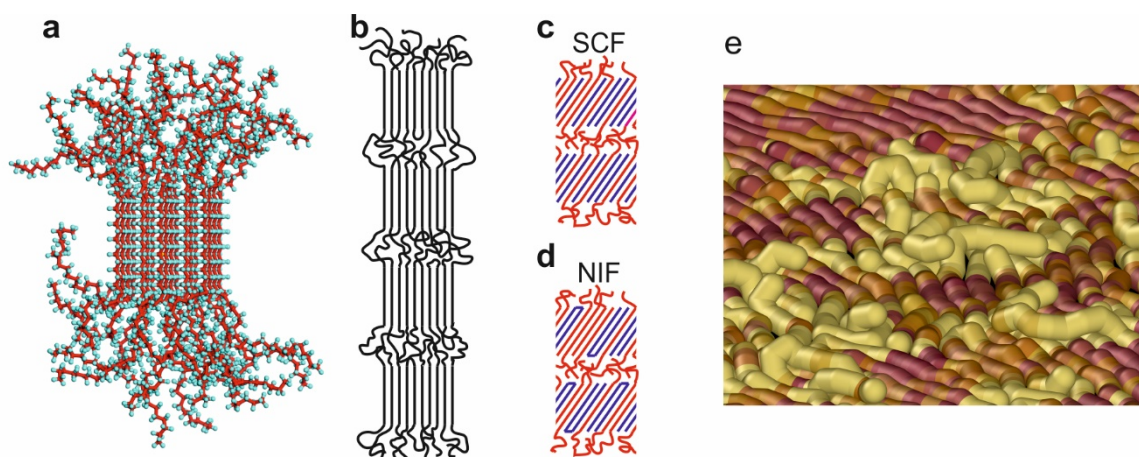


FIG. 10. Surface overcrowding and its relief in bulk system and in thin film. (a) A “fringed-micelle” crystal without chain folding: Lateral growth of the lamella is unsustainable as emergent chains expand at the crystal-amorphous interface. (b) A microfibril in drawn polymer where insufficient chain folding prevented further lateral growth of small crystal blocks. (c) Semicrystalline form (SCF) can be thermodynamically stable in binary mixtures of ultra-long n-alkanes (blue: shorter n-alkane; red: longer n-alkane) with only the chain ends of the longer alkane (red) melted.⁵¹ (d) Tight chain folding and tilting are needed to allow growth of metastable semicrystalline NIF lamellae in pure ultra-long alkanes (blue: folded n-alkane; red: non-folded n-alkane).⁴⁹ (e) A MD simulation snapshot, showing how chain segments detach from the substrate and cross over each other to resolve the overcrowding problem at the crystal-melt boundary in thin film. The chain segments are colored by their P_2 parameters, with yellow/white being more disordered.

A key question to answer is why the near-continuous melting is possible in a thin film but not in the bulk. Our results point to, firstly and most importantly, the surface overcrowding problem is solved in thin film by “escape in the third dimension”, with chain segments detaching from the substrate and occasionally crossing over each other, as evidenced by the simulation results (Fig. 10e). In terms of the above mean-field theory, this means a greatly reduced t in the 2D case. Unlike the SCF in alkane mixtures, where overcrowding is alleviated only at one particular crystal thickness that is equal to the length of the shorter chains, in thin film the uncrowded interface is free to move, enabling continuous melting.

Another parameter leading to a more significant continuous melting for alkane monolayers on graphite is their low value of melt entropy S_m (the best-fit has $S_m =$

$k/3$), as the molten chains are pinned to the substrate and nearly two-dimensional. The entropy of chain sliding (proportional to $k \ln x$) therefore becomes relatively more effective in stabilizing the partially melted states. The theory thus predicts a wide temperature range of continuous melting – see Figs. 4a and 9b. The higher the S_m , according to Eq. 3, the length x of the melted chain ends at the same supercooling ΔT is reduced. However, even if the value of melt entropy was as high as in the bulk, i.e. if it adopted the experimental value $S_m = 1.2k$ ($k/S_m = 0.83$) for bulk PE, the premelting range would be narrower but still significant if the overcrowding effect were as small as in 2D ($t=1$) (Fig. 9d). This points to the presence of overcrowding being the dominant factor preventing continuous melting of long-chain crystals in the bulk.

VI. CONCLUSIONS

Continuous melting, as predicted long ago for polymers but never witnessed, has now been observed on a series of long-chain *n*-alkanes absorbed on graphite (001) surfaces. Our experimental observations, molecular dynamics simulation, and theoretical analysis show that such behavior is mostly resulted from the nearly eliminated overcrowding effects at the crystal-melt interface, and aided by the much reduced entropy of an essentially 2D melt. The theory predicts that melting would become fully continuous if surface overcrowding was eliminated completely. The reversal of such conditions, particularly the presence of severe surface overcrowding, is the reason behind the almost negligible premelting in bulk polymers and other chain systems.

VII. MATERIALS AND METHODS

VII.A. Materials

$C_{60}H_{122}$ was purchased from Sigma Aldrich, while the long chain *n*-alkanes $C_{122}H_{246}$, $C_{194}H_{390}$, $C_{246}H_{494}$, $C_{294}H_{590}$ and $C_{390}H_{782}$ were kindly provided by Dr. G. M. Brooke of Durham University. HOPG wafers were obtained from Mikromasch, Germany. Ultrathin alkane films on HOPG were prepared by spin-coating, whereby one droplet of a toluene solution of the alkane (1-10mg/ml) was deposited on a freshly cleaved surface of HOPG at 2000 rpm with an Ossila spin coater. All sample films were subsequently dried in a vacuum oven for 2 hours.

VII.B. AFM

The AFM experiments were performed using a Cypher ES AFM instrument (Asylum - Oxford Instruments), which was equipped with a heating stage allowing heating of sample in air from ambient to 250°C in a sealed environment. AFM images were taken in the tapping mode, as commonly used for soft matter such as polymers and liquid crystals. Scanning was carried out in the repulsive force regime by keeping the phase shift less than 90°, and a 90% set point ratio was used. The drive amplitude was gently increased for scanning at higher temperatures in order to prevent the tip from sticking to the sample surface. AFM scanning was carried out typically at 10°C intervals on heating to detect changes in morphology.

VII.C. MOLECULAR DYNAMICS SIMULATION

All of the simulations conducted for this study corresponded to isothermal, isochoric (NVT) simulations, and were performed using Large-scale Atomic/Molecular Massively Parallel Simulator (LAMMPS).⁵² Each simulation used a timestep of 5 fs, and temperature was regulated using a four-member Nosé-Hoover^{53,54} chain thermostat⁵⁵ with 1-ps coupling constants. Particle positions were temporally evolved according to the velocity Verlet algorithm.⁵⁶ Full non-bonded interactions were included for all intramolecular neighbouring beads separated by more than two bonds (i.e., 1-4 interactions were not scaled) in accordance with the SDK model.³⁷ Simulation times were not scaled in contrast to earlier work using the SDK model to study polyethylene systems and processes.⁴⁰⁻⁴²

The system was initially heated from 10 K to 350 K over the course of 5 ns (simulation length: 1,000,000 time steps) under constant volume conditions. The heating process was achieved by ramping the set point of the chain thermostat as internally implemented in LAMMPS^{Error! Bookmark not defined.} via the fix NVT command. The final configuration at 350K (77°C) was then annealed at a series of different temperatures both below and at the melt temperature (211°C) for a further 3,000,000 time steps and the last 50 configurations taken at 20ps intervals were used for analysis. Above the melt (>211°C), the 77°C configuration was first annealed at 212°C for 2,000,000 time steps, and then annealed for a longer time at 227°C for 6,000,000 time steps to simulate the melt phase. The final configuration generated

from the previous run, annealed at 227°C, was extended for a further 2,000,000 time steps at 227°C, 277°C and 327°C and the last 50 configurations taken at 20ps intervals were then used for analysis.

The P_2 value of each polymer chain bead (segment) was calculated according to $P_2(i) = (3\langle \cos^2\alpha \rangle - 1)/2$, where α represents the angle between the backbone of the i th polymer bead and the backbone of a neighbouring bead. The angular brackets indicate averaging over all of the neighbouring beads within 6.1 Å of the i th bead excluding the i th bead itself and its immediate intramolecular neighbours (i.e., its bonded neighbours). Note that 6.1 Å corresponds to the approximate location of the second minimum in the bead-bead radial distribution functions for simulated monolayers considered in this study. The backbone direction of each bead was estimated using the vector connecting its intramolecular neighbouring beads (i.e., bonded neighbours) except for the beads at the end beads of the chain for which bond vectors were used instead. P_2 values of 1.0, 0, and -0.5 indicate that a polymer segment is parallel, randomly oriented, and perpendicular to its neighbouring segments, respectively.

The tilt-perpendicular transition was not probed in this study since the T-P transition relies on fine details not present in the current representation; the SDK CG beads of the alkane chains (3 CH₂ groups) are larger than the longitudinal shear associated with the tilted phase (1-2 CH₂ groups), and the SDK model approximates graphene using a cubic representation.

ACKNOWLEDGMENT

We are grateful to Professor Michael L. Klein at Temple University for providing the resources and support for the Molecular Dynamics Simulation work, and helpful discussions in manuscript preparation. We are most obliged to Drs. Gerald Brooke and Shahid Mohammed of University of Durham for providing the long alkane compounds. This work used the ARCHER UK National Supercomputing Service (<http://www.archer.ac.uk>). The authors acknowledge funding from EPSRC (EP-P002250, EP-T003294), the 111 Project 2.0 of China (BP2018008), and from NSFC (grant 21674099).

References

- ¹ S. Chandrasekhar, *Liquid Crystals* (Cambridge University Press, Cambridge, 1992).
- ² P. J. Flory and A. Vrij, *J. Am. Chem. Soc.* **85**, 3548 (1963).
- ³ H. G. Zachmann, *Z. Naturforschg.* **19a**, 1397 (1964).
- ⁴ H. Baur, *Colloid & Polymer Sci.* **256**, 833 (1978).
- ⁵ B. Wunderlich, *Macromolecular Physics* (Academic Press, New York, 1976-1980).
- ⁶ Y. Tanabe, G. R. Strobl, and E. W. Fisher, *Polymer* **27**, 1147 (1986).
- ⁷ H. E. Bair, R. Salovey, and T. W. Huseby, *Polymer* **8**, 9 (1967).
- ⁸ G. Ungar, J. Stejny, A. Keller, I. Bidd, and M. C. Whiting, *Science* **229**, 386 (1985).
- ⁹ G. M. Brookes, S. Burnett, S. Mohammed, D. Proctor, and M. C. Whiting, *J. Chem. Soc. - Perkin Transactions 1*, 1635 (1996).
- ¹⁰ K. S. Lee and G. Wegner, *Makromol. Chem.-Rapid Comm.* **6**, 203 (1985).
- ¹¹ S. J. Organ, G. Ungar, and A. Keller, *Macromolecules* **22**, 1995 (1989).
- ¹² G. Ungar and X. B. Zeng, *Chemical Reviews* **101**, 4157 (2002).
- ¹³ G. Ungar, E. G. R. Putra, D. S. M. de Silva, M. A. Shcherbina, A. J. Waddon, *Adv. Polym. Sci.* **180**, 45 (2005).
- ¹⁴ R. B. Zhang, W. S. Fall, K. Wm. Hall, G. A. Gehring, X. B. Zeng and G. Ungar, *Phys. Rev. Lett.*
- ¹⁵ J. P. Rabe and S. Buchholz, *Phys. Rev. Lett.* **66**, 2096 (1991).
- ¹⁶ J. P. Rabe and S. Buchholz, *Science* **253**, 424 (1991).
- ¹⁷ L. Askadskaya and J. P. Rabe, *Phys. Rev. Lett.* **69**, 1395 (1992).
- ¹⁸ K. Morishige, Y. Takami, and Y. Yokota, *Phys. Rev. B* **48**, 8277 (1993).
- ¹⁹ K. W. Herwig, B. Matthies, and H. Taub, *Phys. Rev. Lett.* **75**, 3154 (1995).
- ²⁰ F. Y. Hansen, K. W. Herwig, B. Matthies, and H. Taub, *Phys. Rev. Lett.* **83**, 2362 (1999).
- ²¹ A. J. Bourque and G. C. Rutledge, *Eur. Polym. J.* **104**, 64 (2018).
- ²² A. Diama, B. Matthies, K. W. Herwig, F. Y. Hansen, L. Criswell, H. Mo, M. Bai, and H. Taub, *J. Chem. Phys.* **131**, 084707 (2009).
- ²³ A. -K. Löhmann, T. Henze, and T. Thurn-Albrecht, *PNAS* **111**, 17368 (2014).
- ²⁴ S. N. Magonov and N. A. Yerina, *Langmuir* **19**, 500 (2003).
- ²⁵ S. N. Magonov, N. A. Yerina, G. Ungar, D. H. Reneker, and D. A. Ivanov, *Macromolecules* **36**, 5637 (2003).
- ²⁶ A. Tracz and G. Ungar, *Macromolecules* **38**, 4962 (2005).
- ²⁷ I. L. Hay, A. Keller, *J. Mater. Sci.* **1**, 41 (1966).
- ²⁸ X. B. Zeng and G. Ungar, *Polymer* **39**, 4523 (1998).
- ²⁹ M. G. Broadhurst, *J. Res. Natl. Bur. Stand.* **66A**, 241 (1962).
- ³⁰ W. Piesczek, G. R. Strobl, and K. Malzahn, *Acta Cryst.* **B30**, 1278 (1974).
- ³¹ G. Zerbi, R. Magni, M. Gussoni, K. Holland-Moritz, A. Bigotto, and S. Dirlikov, *J. Chem. Phys.* **75**, 3175 (1981).
- ³² J. -P. Gorce, S. J. Spells, X. B. Zeng, and G. Ungar, *J. Phys. Chem. B* **108**, 3130 (2004).
- ³³ X. B. Zeng, G. Ungar, S. J. Spells, G. M. Brooke, C. Farren, and A. Harden, *Phys. Rev. Lett.* **90**, 155508 (2003).
- ³⁴ D. S. M. de Silva, X. B. Zeng, G. Ungar, and S. J. Spells, *Macromolecules* **35**, 7730 (2002).
- ³⁵ D. S. M. de Silva, X. B. Zeng, G. Ungar, and S. J. Spells, *J. Macromol. Sci. -Phys.* **B42**, 915, (2003).
- ³⁶ N. Mullin and J. K. Hobbs, *Phys. Rev. Lett.* **107**, 197801(2011).
- ³⁷ W. Shinoda, R. DeVane, and M. L. Klein, *Mol. Simul.* **33**, 27 (2007).
- ³⁸ R. DeVane, M. L. Klein, C. -c. Chiu, S. O. Nielsen, W. Shinoda, and P. B. Moore, *J. Phys. Chem. B* **114**, 6386 (2010).

-
- ³⁹ C. -c. Chiu, R. DeVane, M. L. Klein, W. Shinoda, P. B. Moore, and S. O. Nielsen, *J. Phys. Chem. B* **114**, 6394 (2010).
- ⁴⁰ K. Wm. Hall, T. W. Sirk, M. L. Klein, W. Shinoda, *J. Chem. Phys.* **150**, 244901 (2019).
- ⁴¹ K. Wm. Hall, T. W. Sirk, S. Percec, M. L. Klein, and W. Shinoda, *J. Chem. Phys.* **151**, 144901 (2019).
- ⁴² K. Wm. Hall, S. Percec, and M. L. Klein, *J. Chem. Phys.* **150**, 114901 (2019).
- ⁴³ P. Yi, C. R. Locker, and G. C. Rutledge, *Macromolecules* **46**, 4723 (2013).
- ⁴⁴ T. Yamamoto, *J. Chem. Phys.* **115**, 8675 (2001).
- ⁴⁵ C. Liu and M. Muthukumar, *J. Chem. Phys.* **109**, 2536 (1998).
- ⁴⁶ A. Stukowski, *Modelling and Simulation in Materials Science and Engineering* **18**, 015012 (2009).
- ⁴⁷ C. M. Guttman and E. A. DiMarzio, *Macromolecules* **15**, 525 (1982).
- ⁴⁸ S. Balijepalli and G. C. Rutledge, *Macromol. Symp.* **133**, 71 (1998).
- ⁴⁹ X. B. Zeng and G. Ungar, *Macromolecules* **34**, 6945 (2001).
- ⁵⁰ D. C. Prevorsek, P. J. Harget, R. K. Sharma, and A. C. Reimschuessel, *Journal of Macromolecular Science B: Physics* **8**, 127 (1973).
- ⁵¹ G. Ungar, X. B. Zeng, G. M. Brooke, and S. Mohammed, *Macromolecules* **31**, 1875 (1998).
- ⁵² S. Plimpton, *J. Comp. Phys.* **117**, 1 (1995).
- ⁵³ S. Nosé, *Mol. Phys.* **52**, 255 (1984).
- ⁵⁴ W. G. Hoover, *Phys. Rev. A* **31**, 1695 (1985).
- ⁵⁵ G. J. Martyna, M. L. Klein, and M. Tuckerman, *J. Chem. Phys.* **97**, 2635 (1992).
- ⁵⁶ W. C. Swope, H. C. Andersen, P. H. Berens, and K. R. Wilson, *J. Chem. Phys.* **76**, 637 (1982).

Bibliography

- [1] G. Ungar, J. Stejny, A. Keller, I. Bidd, and M. Whiting. *Science*, 229(4711):386–389, 1985.
- [2] X. Zeng and G. Ungar. *Polymer*, 39(19):4523–4533, 1998.
- [3] G. Ungar and X.-b. Zeng. *Chemical reviews*, 101(12):4157–4188, 2001.
- [4] X. Zeng and G. Ungar. *Macromolecules*, 34(20):6945–6954, 2001.
- [5] S. N. Magonov, N. A. Yerina, G. Ungar, D. H. Reneker, and D. A. Ivanov. *Macromolecules*, 36(15):5637–5649, 2003.
- [6] A. Tracz and G. Ungar. *Macromolecules*, 38(12):4962–4965, 2005.
- [7] H. G. Zachmann. *Zeitschrift für Naturforschung A*, 19(12):1397–1403, 1964.
- [8] W. Shinoda, R. DeVane, and M. L. Klein. *Molecular Simulation*, 33(1-2):27–36, 2007.
- [9] K. W. Hall, T. W. Sirk, M. L. Klein, and W. Shinoda. *The Journal of Chemical Physics*, 150(24):244901, 2019.

Chapter 7

Conclusions and Future Work

A variety of soft self-assembled systems, including LC's formed from compounds with novel shapes and the melting-crystallisation processes in polymeric systems have been studied using theory and simulation working closely alongside experimental colleagues. The primary aim set out in Section 1.0.1 has been met by improving the understanding of complex LC phases, which have remained relatively untouched until now, by directly tackling specific aspects of their phase behaviour. A tight feedback loop between experimental and theoretical colleagues alike has accelerated progress in understanding these systems. In the same way that models on different length scales can be used to inform each other so too can experimental and theoretical colleagues through joint research studies. Techniques such as mean field theory, Monte Carlo and molecular dynamics simulation were employed in order to gain molecular level insights into the morphology of these systems and test and refine theoretical models which quantitatively describe the important processes. The results have provided a theoretical understanding of soft self-assembled systems and in some cases point to interesting results yet to be uncovered in experiment as well as confirm existing ones. Section 7.1 provides a summary

of the chapters in this thesis and future work will be discussed in Section 7.2.

7.1 Conclusions

A new type of phase transition between two columnar phases of the same hexagonal symmetry, self-assembled from taper-shaped minidendrons was reported in Chapter 3. A clear first-order drop in the lattice constant was seen experimentally on heating, which suggested a sudden reduction in the number of molecules comprising the column. It was proposed that an integer number of minidendrons self-assemble to form discs which then stack into columns and this number was calculated from experimental data. Next, the transition was described quantitatively in terms of the most significant energetic contributions responsible for forming the columns. This was achieved by likening the self-assembled column to a 1d spin chain in magnetic systems in an external field, where the individual spins are replaced by discs of 3 or 4 molecules. Since 1d spin chain could not produce a first-order transition, small mean field terms were added to approximate the surrounding columns. The energetic terms in the model, such as the free energy of the terminal chains were calculated using simulation by employing a coarse-grained representation. Calculated parameters were then fed into the theory which was then solved self-consistently and small adjustments were made to better fit the experimental data. The characteristic transition shape seen in experiment was successfully reproduced and the model demonstrated that the transition was being driven by the ever increasing entropy of the terminal chains. As the terminal chains gain sufficient entropy at high temperatures, the free energy may overcome that of the Coulomb interactions holding the supramolecular discs together and molecules are suddenly forced out. At this point the attractive interactions between discs with an equal number of molecules is lost and destabilises the column which compounds this effect and a first-order transition ensues.

The results were published in [1], see Section 3.2.

Further experimental results now show similar transitions in compounds with longer terminal chains and heavier ions, namely 12K^+ and 14Na^+ . In Section 3.3 the model is extended to make a prediction of the behaviour of these compounds by including phonon vibrations to account for heavier ions as well as longer chains with mixed results.

In Chapter 4 an unusual transition between two chessboard tilings in cross-shaped bolaamphiphiles was reported. The molecule comprised of a rod-like π -conjugated core with glycerol groups at either end of the rod and two flexible and incompatible chains attached either side of its centre. The molecules self-assembled to form a square array with the rod-like cores forming the walls and the flexible chains filling the nano-compartments. An order-disorder transition was seen between a two-colour chessboard at low temperatures, where the side chains segregate forming chemically different cells to a single-colour mixed phase at high temperature. Previous studies had already probed the ordering phenomena of an hexagonal tiling formed by these molecules using MC simulation. The same model was applied to this system in 3d and it was recognised that the system was exactly analogous to the 3d Ising Model under Kawasaki spin flip dynamics, where spin flips in the original magnetic system are replaced by 180° rotations of the molecules around their backbone axis. Since the degrees of freedom and dimensionality are identical to the Ising Model, universal scaling relationships were tested. When compared with experimental data it was found that the finite sized MC simulations were in closer agreement with the experiment and that the 3d Ising exponents γ and ν did not agree with experiment. This suggested that large scale fluctuations of the local two-colour patches were kinetically restricted above the transition in experiment. In a spin model flipping molecules at the boundary between local two-colour patches has no energy barrier but in reality there is always some energy involved in exchanging the side groups of the molecules. The results were published in

[2] see Section 4.2.

The crystallisation behaviour of i-PP at large undercoolings was studied in Chapter 5. Specifically the metastable form of i-PP was found to accompany the formation of the more ordered α -phase form at very large undercoolings. It was suggested in [3] that the more rapid formation of the mesophase may significantly reduce the rate of crystallisation when competing with the α -phase form, this is thought to be another example of self-poisoning in polymers. A 1d theory was devised to test this hypothesis by modelling the growth of the more stable α form in the vicinity where the mesophase is unstable and demonstrate its growth is diminished as the temperature of the mesophase is reached. Using a solid-on-solid model, incoming mesophase chains were allowed to attach to the growing α -phase crystal front and either desorb or convert to the more stable α -phase form. This rate of conversion was significantly reduced for an α -phase stem covered by mesophase chains, α -phase chains were allowed to backward convert to mesophase chains in this model by similar means. Semi-quantitative agreement was found with the experimental data in [3] and provided clear proof of the viability of self-poisoning occurring in i-PP. Both growth rate peaks however were much narrower than those of the experiment and so neighbouring interactions were introduced in order to broaden the peaks and better fit the experimental data by flattening the α -phase growth in the high temperature region. A line of 1d interacting growth stems was modelled using MC simulation and a neighbouring interaction scheme devised to adjust the 1d growth rate according to the neighbouring configuration at a given stem. The 2d model successfully reproduced the 1d model results and provided visual confirmation of the poisoning process. However the introduction of neighbouring interactions did not have the desired effect of broadening the growth over a wider temperature range and pointed to two important model modifications necessary to improve the quantitative fit of the experimental data. Firstly the fixed crystal width should be temperature-dependent,

such that the optimum crystal width is stable at each temperature and secondly that direct attachment of α -phase chains is required to allow the growth of the α -phase to proceed above the melting temperature of the metastable mesophase.

Chapter 6 addressed the commercially important phenomenon of polymer melting and the concept of pre-melting first predicted by Zachmann in the 1960's. Ultra-long n-alkanes from $C_{60}H_{122}$ to $C_{390}H_{782}$ were studied as monolayers adsorbed on graphite by high resolution AFM and were found to melt from their ends inward. This continued until over half the molecular length had disordered before the whole monolayer melted well above the bulk melting temperature. It was surprising that an essentially 2d melt should remain crystalline up to 80K above its bulk melting temperature. In collaboration with Dr Kyle Hall from Temple University, MD simulation was employed to study the monolayers using a coarse-grained representation of the alkane chains and graphite substrate in order to provide insights at a molecular level. Pre-melting was observed at all temperatures below the experimentally determined melt temperature and the results matched closely the experimentally observed AFM images. It was found that this behaviour resulted from the reduced overcrowding at the interface between the crystalline and melt portions and the much reduced entropy of a quasi-2d melt. Snapshots from the simulations captured this process in action where chains left the surface of the graphite and climbed over one-another to alleviate the overcrowding problem. This is the main reason why pre-melting is not observed in 3d. The results have been submitted for publication [4], see Section 6.2.

7.2 Future Work

In Chapter 3 the model devised for $12Na^+$ (Sodium - $C_{12}H_{25}$) provided a remarkably accurate description of the experimentally observed transition and captured some of the

important characteristics in 14Na^+ (Sodium - $\text{C}_{14}\text{H}_{29}$) and 12K^+ (Potassium - $\text{C}_{12}\text{H}_{25}$) but further experimental data is required to draw any significant conclusions [5]. In particular a more accurate determination of the transition temperatures and d-spacings for compounds with heavier ions is desirable since this data is crucial for determining the number of molecules in a disc from the volume of the unit cell. Accurate data for 12K^+ would allow for a model fit to be performed and the fitted parameters could provide insights into why the model does not provide a good fit for 12K . Speculatively this could result from a slightly larger d-spacing in 12K^+ resulting from larger ions and weaker inter-disc interactions. Recalculating these parameters with a revised d-spacing could resolve this. Vibrations are clearly important for the larger ions, it may be useful to perform additional calculations taking into account discs above and below. It was noticed that the discs prefer an offset 45 degree stacking, which places an O ion from neighbouring discs directly above/below the metal ion, this would significantly enhance the favourability of vibrations. Studying longer chains would also be interesting with different core sizes for larger ions such as Rb or Cs. Ribbon phases have also been discovered in compounds with 2 instead of 3 chains attached which show several transitions between rectangular and hexagonal columnar phases with oblate cores [6]. This would require considering different core configurations with $n > 4$ molecules in a disc as well as further simulations of the end chains in restricted geometries with $\theta < 90$. The model would also have to be extended to introduce further states for $n > 4$. Studying the 3d cubic phases at higher temperatures would also be desirable.

Chapter 4 provided insights into how kinematic effects are important in highly dynamic liquid crystals. In particular the importance of the energy barrier involved when flipping a molecule in reality when compared to that in an MC simulation. It may be interesting to insert an energy barrier in flipping a molecule in an MC simulation to study the effect on the ordering phenomena and its effect on domain size. The model could also

be extended to other tilings such as triangular and kagome tilings or even the recently discovered snub-square tiling [7]. A snub-square tiling consists of triangular and square cells, see Figure 7.1, it is not possible on this lattice for the chains to fully segregate into their respective nano-compartments. The snub-square tiling could be another example of frustration in liquid crystals [7].

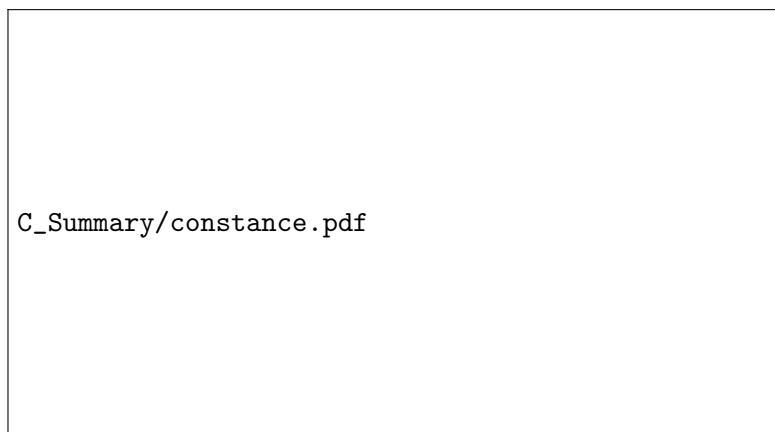


Figure 7.1: Electron density map showing the suggested structure of the frustrated p4gm phase (left), blue, yellow and green circles represent glycerol groups, carbosilane chains and semi-perfluorinated chains respectively. Tiling pattern and unit cell (right), reproduced with permission from [7].

In Chapter 5 the possibility of self-poisoning occurring in i-PP at large undercooling was investigated and clear evidence was found which supported this using a 1d solid-on-solid growth model. The introduction of neighbouring interactions pointed to some necessary model improvements in order to achieve an improved quantitative fit to the experimental data. Firstly studying the effect of a temperature-dependent stem width to allow the most stable stem width to grow at the optimum temperature. This could be achieved by varying the surface energy terms, with a small linear dependence on temperature for example, in order to see how the double peak structure is smoothed out. In addition, the direct attachment of α -phase stems needs to be introduced, in order to broaden the high temperature region of the growth curves, allowing for α -phase growth to proceed above the melting temperature of the metastable mesophase. This should provide a

much improved quantitative fit to the experimental data in [3].

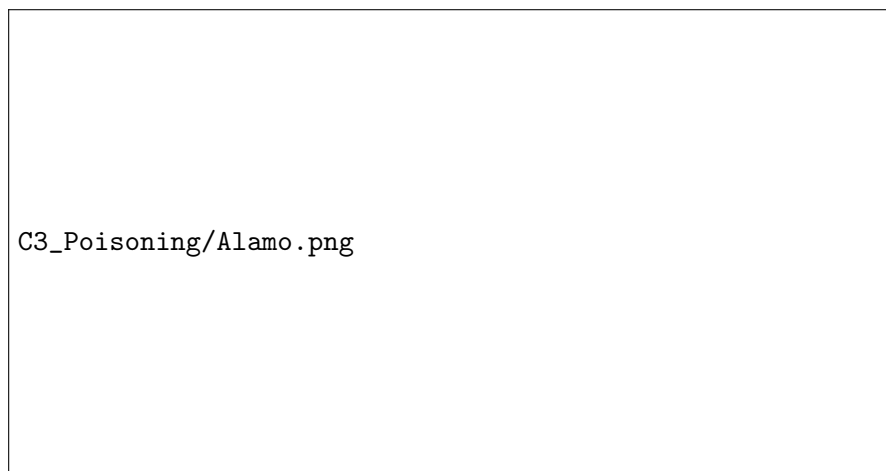


Figure 7.2: Growth rate of high molar mass polyethylenes with bromine atoms substituted on every 21st carbon site along the chain, the poisoning minimum is seen at 64°C (337K) and the glass transition temperature is around -77°C (195K) which is at least 140K below the growth minimum observed. Alongside is an example schematic of the extended chain form blocking the herringbone crystal structure. Reproduced with permission from [8].

Finally a recent study has revealed a similar growth minimum in high molar mass polyethylenes where bromines are substituted periodically along the chain in regular intervals [8]. Two different phases are observed, the ordered extended chain crystal and an additional zig-zag (herringbone) form where the bromine atoms sit at the apex of the saw-tooth structure, which forms at higher temperatures than the extended chain form, see Figure 7.2. This system is interesting because it provides a much cleaner system to study due to the much reduced temperature of the glass transition. For example in [3] the glass transition occurs at around 250K which is within 70K of the observed poisoning temperature but in [8] the poisoning temperature appears at around 337K which is nearly 142K above the glass transition at 195K. In fact a theoretical study of this system could provide even stronger evidence of self-poisoning in polymers than that performed in Chapter 5.

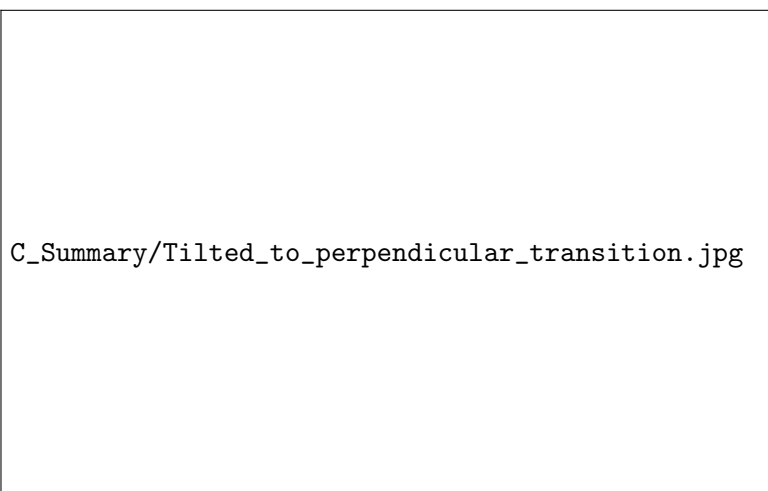


Figure 7.3: AFM image taken at the tilt to perpendicular transition reproduced from [4], yellow/white areas indicate soft amorphous regions.

In Chapter 6 MD simulations captured pre-melting in action and explained why extended pre-melting is observed in 2d-monolayers and not in bulk. One key characteristic of the simulation not reproduced by the simulation was the correct structure of the perpendicular form because it was unstable, instead chains were tilted inside the lamellae. There are two possible reasons for this, the first is that the coarse-grained nature of the model requires that the end beads have slightly larger VdW interactions than the central beads and accommodating them may facilitate the tilt. More likely though the coarse-grained graphite is responsible due to its lesser 4-fold symmetry compared to the true 6-fold symmetry of graphite, it is known that the close match between the bond length in alkanes and the graphite lattice is crucial to stabilising the lamellae. Overcoming this problem requires either re-parameterising the coarse-grained model or more likely performing smaller all atomistic simulations. In particular gauche bonds between methylene units in the coarse-grained representation used in Chapter 6 have been lost. The origin of the tilt to perpendicular transition, as depicted in Figure 7.3, is still not clear and simulating it could provide some insight into what causes it to form. If the perpendicular form could be stabilised then it may be possible to study the transition

but large timescales would be necessary because of the significant rearrangement of the chains when moving between both forms. This is no more prominent than in Figure 7.3 where it can be seen that above the transition (165°C) the number of lamellae has reduced from 14 to 13. The large timescales required and the all atomistic detail likely required to study this transition renders it a difficult problem to tackle but it is not impossible. Further calculations on the existing coarse-grained system, such as swapping out the substrate for silica or diamond or varying the graphite interaction could show the importance of graphite as a substrate to facilitate pre-melting. By reducing the graphite interaction the chains will melt at a lower temperature since $T_c \propto \frac{\Delta U}{\Delta S}$. This is due to their increased ability to gain entropy by leaving the surface, ΔS which is much larger than energy lost in order to do so ΔU when the attraction to graphite is weaker. Swapping out the substrate for another less strongly interacting material would likely have the same effect and if the symmetry of the underlying substrate is different the pre-melting behaviour may be lost altogether. Studying the interaction on a diamond substrate however could have the opposite effect since the C-C bond length is identical to the C-C bond length in n-alkanes.

Further experiments on mixed alkanes of different lengths i.e. $C_{120}H_{242}$ mixed with $C_{390}H_{782}$ show crystalline $C_{120}H_{242}$ monolayers sitting on top of the $C_{390}H_{782}$ layer as it melts [9]. The $C_{120}H_{242}$ monolayer melts around 20K above the bulk melting temperature but still below that when adsorbed as a monolayer on graphite. This could be studied in two ways, by performing simulations with additional shorter alkanes sitting on top of the pure $C_{390}H_{782}$ monolayers studied previously or by weakening the graphene interaction to something akin to the interaction between the chains themselves. Wishbone shaped alkanes with a single short-stubbed branch sitting in the central portion of the chain have also been synthesised, this prevents the extended form crystallising and would also be an interesting system to study.

Bibliography

- [1] W. S. Fall, M.-H. Yen, X. Zeng, L. Cseh, Y. Liu, G. A. Gehring, and G. Ungar. *Soft Matter*, 15(1):22–29, 2019.
- [2] W. S. Fall, C. Nürnberger, X. Zeng, F. Liu, S. J. Kearney, G. A. Gehring, C. Tschierske, and G. Ungar. *Molecular Systems Design & Engineering*, 4(2):396–406, 2019.
- [3] D. Cavallo, L. Zhang, G. Portale, G. Alfonso, H. Janani, and R. Alamo. *Polymer*, 55(15):3234–3241, 2014.
- [4] R. Zhang, W. S. Fall, K. W. Hall, G. A. Gehring, X. Zeng, and G. Ungar. *Submitted To: Science*, 2019.
- [5] Y. Liu. *Two-and three-dimensional liquid crystalline structures in self-assembled supramolecular dendrimers*. PhD thesis, University of Sheffield, 2004.
- [6] M.-H. Yen. *Self-Assembly of Minidendrons in 2D and 3D Liquid Crystal Lattices and Superlattices*. PhD thesis, University of Sheffield, 2015.
- [7] C. Nürnberger, H. Lu, X. Zeng, F. Liu, G. Ungar, H. Hahn, H. Lang, M. Prehm, and C. Tschierske. *Chemical Communications*, 55(29):4154–4157, 2019.
- [8] X. Zhang, W. Zhang, K. B. Wagener, E. Boz, and R. G. Alamo. *Macromolecules*, 51(4):1386–1397, 2018.
- [9] X. Zeng and G. Ungar. Personal Communication.